DEVELOPMENT OF NANO-GRAPHENE

CEMENTITIOUS COMPOSITES (NGCC)

A thesis submitted for the degree of Doctor of Philosophy

By

Muhammad Ilyas

Department of Mechanical, Aerospace &

Civil Engineering,

Brunel University London

November 2016

ABSTRACT

Ordinary Portland cement (OPC) is the main constituent of concrete works as a principal binder for aggregates and intrinsically transmits the brittleness into concrete through the formation of hydration crystals in the cement microstructure. A number of nano cementitious composites were developed in recent years to offset the brittleness with newly discovered nanomaterials and the most prevalent among those is the graphene oxide (GO).

The main objective of this PhD research work is to develop nano graphene cementitious composites (NGCC) using low cost, two dimensional (2D) graphene nanoplatelets (GNPs) and one dimensional (1D) graphited carbon nanofibres (GCNFs) with unique conical surface morphology. The GNPs were sourced synthesised in an environmental friendly way via plasma exfoliation whereas, GCNFs were manufactured through catalytic vapour grown method. The project further investigated the effect of these nanomaterials in regulating the distinctive microstructure of cement matrix leading to enhance its mechanical properties. Three different types of high-performance NGCC namely NGCC-Dot, NGCC-Fnt and NGCC-CNF, are developed by activating pristine GNPs (G-Dot), functionalised GNPs (G-Fnt) and graphited nanofibers (G-CNFs) into the cement matrix respectively.

It is found through various characterization and experimental techniques that both GNPs and GCNFs regulated the cement microstructure and influenced the mechanical properties of NGCC uniquely. A remarkable increase in the flexural and the tensile strength of newly developed NGCC has been achieved and that could be attributed to the formation of distinctive microstructure regulated by catalytic activation of these nanomaterials. The shape (1D, 2D) and unique morphology of these nanomaterials played a vital role in the mechanism of crystal formation to regulate the cement microstructure.

Based on the observations of test results and comprehensive characterization, the possible mechanisms of crystal formation and development of distinctive microstructure of NGCC has been established which has then proceeded to the development of a physical model for NGCC development.

ACKNOWLEDGEMENTS

Table of Contents

LIST OF TABLES

LIST OF FIGURES

xiii

LIST OF ABBREVIATIONS

0D	Zero-Dimensional
1D	One Dimensional
2D	Two Dimensional
AFm	Monosulfoaluminate
AFM	Atomic Force Microscope
AFt	Calcium Sulfoaluminate Hydrate
Al_4O^-	Aluminate Ions
ASTM	American Standards for Testing Materials
ATR	Attenuated Total Reflection
BET	Brunauer, Emmett and Teller
BWOC	By Weight of Cement
C2S	Dicalcium Silicate
C_3A	Tricalcium Aluminate
C_3S	Tricalcium Silicate
C_4AF	Tricalcium Aluminoferrite
Ca^{2+}	Calcium Ions
$CaCO_3$	Calcium Carbonate
CaO	Calcium Oxide
CCD	Charged Couple Device
CH	Calcium Hydroxide
CNFs	Carbon Nanofibers
CNTs	Carbon Nanotubes
CO_2	Carbon Dioxide
-COOH	Carboxylic Group
COSSH	Control of Substances Hazardous to Health
COV	Coefficient of Variation Percentage
C-S-H	Calcium Silicate Hydrates
CVD	Chemical Vapour Decomposition
DEF	Delayed Ettringite Formation
EDAX	Energy Dispersive Analysis By X-Rays
EDS	Energy Dispersive Spectrometer
FFT	Fast Fourier Transform

FTIR	Fourier Transform Infrared
GCNFs	Graphited Carbon Nanofibers
G-Dot	Pristine GNPs
G-Fnt	Functionalised GNPs
GNMs	Graphene Nanomaterials
GNPs	Graphene Nano Platelets
GO	Graphene Oxide
Gpa	Giga Pascal
H&S	Health and Safety
HR	High Resolution
I_D/I_G	D-Peak to G-Peak Ratio
IR	Infrared
ITZ	Interfacial Transition Zone
IUPAC	International Union of Pure and Applied Chemists
K^+	Potassium Ions
KEV	Kilo Electric Volts
Kg	Kilogram
KN	Kilo Newton
KO	Potassium Oxide
LPE	Liquid Phase Exfoliation
LTESP	Long Lever Tapping Etched Silicon Probe
m^2/g	Meter Square Per Gram
mA	Mili Ampere
MC	Micromechanical Cleavage
MgO	Magnesium Oxide
MIP	Mercury Intrusion Porosimetry
MWCNTs	Multi-Walled Carbon Nanotubes
NGCC	Nano Graphene Cementitious Composites
NGCC-CNF	Nano Graphene Cementitious Composites with G-CNF
NGCC-Dot	Nano Graphene Cementitious Composites with G-Dot
NGCC-Fnt	Nano Graphene Cementitious Composites with G-Fnt
$-NH_2$	Amine Group
nm	Nano Meter
O.S	Organic Solvent

-O$_2$	Oxygen Group
OH$^-$	Hydroxyl Ions
OPC	Ordinary Portland Cement
PC	Polycarboxylate
PEI	Poly Ethyleneimine
PP	Poly Propylene
PPE	Personal Protective Equipment
Psi	Per Square Inch
rGO	Reduced Graphene Oxide
RS	Raman Spectroscopy
SE	Secondary Electron
SEM	Scanning Electron Microscope
SEM	Scanning Electron Microscope
SO$_4^{2-}$	Sulphate Ions
SWCNTs	Single-Walled Carbon Nanotubes
TEM	Transmission Electronic Microscope
UTM	Universal Testing Machine
VGCF	Vapor-Grown Carbon Nanofiber
VP	Variable Pressure
W/C	Water Cement Ratio
XRD	X-Ray Diffraction

LIST OF SYMBOLS

Å	Angstrom
-F	Compressive Force at the Fracture Point
σ_c	Compressive Stress
θ	Contact Angle
σ_f	Flexural Stress
h	Hydration Rate
μm	Micrometre
Δ	Mid Span Deflection
E_{mod}	Modulus of Elasticity
D	Pore Diameter
k	Porosity
L	Span Length
γ	Surface Tension
+F	Tensile Force at the Fracture Point
σ_t	Tensile Stress
d	Thickness
v_{vc}	Vacuum in the Capillary Pores
v_{pc}	Volume occupied by Capillary Pores
v_{ac}	Volume of Water in Capillary Pores
v_s	Volume of Solids in Cement Paste

CHAPTER 1 Introduction

1.1　Research Background

Concrete is one of the essential and most universally used cement-based construction materials that still hold its vital importance in the construction industry. Ordinary Portland Cement (OPC) is used as the main binder of concrete constituents. Concrete is widely used due to its high compressive strength, resistance to water, easy to mould and economical production as an engineered construction material. However, quasi-brittle nature of concrete is the major disadvantage when it is used to build structural members subjected to complex loadings. The brittleness in concrete is attributed to its low resistance to crack formation, low flexural, low tensile strength and low strain capabilities. To overcome this deficiency, concrete is generally reinforced with steel rebars (Mehta et al., 2013). Portland cement represents almost 80% of the total CO_2 emissions of concrete, which in turn, are about 6-7% of the planet's total CO_2 emissions. This is particularly serious in the current context of climate change and gets even worse considering Portland cement demand is expected to increase almost 200% by 2050 and will reach 6000 million tons/year (Davalos, 2012)

Many successful efforts have been made to enhance the performance of cement-based materials by adding mineral admixtures, supplementary cementitious materials, synthetic and natural fibres. The Nanotechnology driven advancement in nanomaterials has now paved the new ways to enhance the performance of cementitious composites further. In recent years some studies were conducted to develop cementitious composite with newly recognised nanomaterials in the powder forms such as nano-silica, nano-alumina, nano-iron (Oltulu and Şahin, 2013) and nano-titanium oxide (Kawashima et al., 2013). Also, the materials from nanocarbon family such as carbon nanotubes (CNTs), Single-Walled Carbon Nanotubes (SWCNT), multi-walled carbon nanotubes (MWCNT) (Abu Al-Rub et al., 2012), and newly emerged graphene oxide (GO) sheets were used extensively (Gong et al., 2015). According to (Scrivener and Kirkpatrick, 2008) these are called nano reinforcement in the cementitious matrix and are more useful than the conventional reinforcement (steel and other fibres of millimetre scale) because the cracks developed at the nanoscale in cement paste are arrested before they propagate into micro-level cracks by these nano reinforcement materials. However, achieving intrinsic strength properties and dispersion of these nanomaterials into cement matrix remains the biggest challenge for the researchers.

GO has currently remained a focal research nanomaterial to enhance the mechanical properties of cementitious composites. GO in its different forms have been used for catalysing cement matrix with different methodologies, w/c ratios and admixtures, and with as little as 0.03 wt.% of cement, the profound effect of GO on mechanical properties has been observed (Gong et al., 2015). Moreover, GO was found to be dispersed effectively in aqueous solution due to its unique 2D layered structure by using physical and chemical surface modification in combination with mechanical efforts as compared to the nanomaterials belong to CNT's family. However, using extra mechanical efforts through sonication and chemical surface modification via functionalization by treating them with the harsh chemical may result in structurally and mechanically degraded graphene sheets which may cause re-agglomeration in the cement matrix. Further using surfactants for physical surface modification can also retard cement hydration process (Chuah et al., 2014; Garg and Sinnott, 1998).

The GO has been characterized most commonly as a few nanometer thick single layer of graphene sheet that contains carbon atoms in its honeycombed crystal structure. Its wrinkle morphology stitched with oxygen groups is considered capable of making a stronger bond with cement hydration products due to mechanical interlocking and superior interfacial strength (Pan et al., 2015). Despite the better bonding capabilities with cement matrix, a few nanometer thick GO sheets can easily be crumbled into the cement matrix and lose their 2D planetary shape which may adversely affect the bond strength and produce large variations in strength values (Romani and Gronchi, 2015). Moreover, functionalised graphene other than containing oxygen such as carboxyl (–COOH) and amine (-NH$_2$) is rarely used in the previous research.

The flexural and compressive strengths of GO cementitious composites have been reported improving mostly with the increased rate of hydration and formation of denser microstructure due to the improved pore structure and nucleation effect of nanoscale graphene sheets into the cement matrix. The increase in flexural and compressive strength, as an example, reached by 68.5% and 46.5% respectively at the age of 7 days when the 0.05 wt.% of GO with a small amount of Polycarboxylate (PC) was used (Wang et al., 2015). However, it is most difficult to scale out the physical interaction of GO sheets with cement hydration products through SEM and other characterization techniques. The improved mechanical properties of GO cementitious composites have been linked with the increased rate of hydration, reduction of pores, increased nucleation and GO as nano-reinforcement bridging cracks at the nanoscale (Wang et al., 2015; Pan et al., 2015; Gong

et al., 2015a). However, very few studies have been focused on the investigation of crystal formation and microstructure development regulated by GO into the cement matrix. Perhaps the shape, geometry and size of nanomaterials can play a vital role in the growth mechanism of hydration crystals.

Since the advent of graphene into the nanomaterials world, an incessant evolution has been witnessed in its different types and synthesis due to nanotechnological advancements. For example in the family of newly emerged nanomaterials, Graphene Nanoplatelets (GNPs) 30-50 nm thick unique in their 2D shape and morphology are synthesised more effectively and economically with plasma exfoliation instead of using harsh chemicals as compared to GO (Haydale Graphene industries plc, 2016). Moreover, with sophisticated nanoindentation techniques, a new generation of vapour grown 1D graphited carbon nanofibers (G-CNF) 100 nm in diameter with GNPs inserted into 20-200 μm long fibrous skeleton could be the potential candidates for developing nano cementitious composites (Aldrich, 2016).

In this research different nanographene cementitious composites (NGCC) has been developed using GNPs and G-CNFs with the main motivations to investigate the effect of these nanomaterials on the mechanism of crystal formation and to identify those hydration crystals favourable for the formation of distinctive microstructure in the cement matrix, leading to enhance its mechanical properties. These composites have been examined analytically and tested mechanically using sophisticated characterization techniques. The remarkable increase in the mechanical properties instigated with the formation of distinctive microstructure in these composites has been achieved. Together the observations of test results and characterization data, the possible mechanism of crystal formation and development of distinctive microstructure has proceeded to the establishment of a physical model for NGCC.

1.2 Research Objectives

The main aim of this research was to develop the nano-graphene cementitious composite (NGCC) with enhanced mechanical properties. Three main types of graphene nanomaterials, namely i) Pristine GNPs (G-Dot), ii) Functionalised GNPs (G-Fnt) and iii) Graphited carbon nanofibers (G-CNFs) were used to investigate the effect of shape and surface properties of nanomaterials on the formation and growth of hydration crystals. Those hydration crystals are favourable for the development of denser and stronger microstructure leading to enhance the mechanical properties of NGCC. Three different

types of NGCC have been developed called NGCC-Dot, NGCC-Fnt and NGCC-CNF by using pristine GNPs (G-Dot), functionalised GNPs (G-Fnt) and graphited nanofibers (G-CNFs) into the cement matrix respectively.

The main specific objectives of this research are:

1. To review the processes, procedures, properties and performances, and to understand the formation of the microstructure of cementitious nanocomposite developed recently with the aid of different forms of nano-materials.

2. To investigate structural composition and surface properties of GNPs and GCNFs those are most likely to interact with the cementitious matrix and to make the difference in the microstructural development.

3. To identify the optimal concentration of GNPs and GCNFs to synthesise aqueous solution to be used for the uniform dispersion of these nanomaterials into cement matrix, and to develop the processing technologies for these developments.

4. To develop nano-graphene cementitious composites NGCC-Dot, NGCC-Fnt and NGCC-CNF both formulations and processing technologies, and to experimentally investigate their main mechanical properties including flexural, compression and tensile strengths for establishing their correlations with the processing parameters.

5. To examine the possible formation mechanisms of hydration crystals and their growth regulated with physical interaction of 2D shape GNPs and 1D shape GCNFs into the cement matrix, and hence to derive the model for the NGCC

1.3 Research Scope

This research firstly identified three main types of graphene nanomaterials, namely i) Pristine GNPs (G-Dot), ii) Functionalised GNPs (G-Fnt) and iii) Graphited carbon nanofibers (G-CNFs) and then developed nano-graphene cementitious composite (NGCC) with enhanced mechanical properties, called NGCC-Dot, NGCC-Fnt and NGCC-CNF. The mechanical properties, mainly flexural, compressive and tensile strength of developed NGCC, were measured extensively. The preparation, curing and testing of representative samples from NGCC have been carried out using procedure, standards and equipment mentioned in Chapter 3. Chemical and physical hydration characteristics of NGCC were determined using analytical characterization techniques, such as XRD, FTIR, RAMAN,

EDAX and SEM. Moreover, the pore structure and surface areas of NGCC were also investigated through MIP and Nitrogen absorption/adsorption tests. The nanomaterials used in the research were analysed for their structural properties using the state of the art equipment such as TEM, AFM and RAMAN. To get the high-resolution SEM images at nanoscale of highly charged cement composites, SEM was operated in variable pressure mode.

1.4   Thesis Structure

In **Chapter 1** an introduction to the research topic of the thesis is presented along with the main aim and objectives of this research.

In **Chapter 2** a comprehensive review of basic cement chemistry related to the hydration process, crystals formation and microstructure development has been presented. The use of various nanomaterials in the cement matrix has been reviewed, research gaps are identified, and design philosophy of NGCC is presented.

In **Chapter 3** research methodology, processes, standards and equipment are proposed for testing, and experimentally performance evaluation of GNMs and NGCC using TEM, SEM, EDAX, AFM, FTIR, RAMAN, XRD and UTM techniques are described in details.

In **Chapter 4** material genome, that is the analysis of fundamental structural and surface properties of graphene nanomaterials (GNMs) used in the development of NGCC with the help of sophisticated characterization techniques, has been described.

In **Chapter 5** the processing of NGCC using G-Dot with various contents of 0.01% to 0.05% by weight of cement, dispersed in aqueous solution, is described. The effect of G-Dot on phase change, chemical composition, for microstructure development and optimum dose of G-Dot for strength enhancement of cement matrix is investigated through analytical and experimental techniques.

In **Chapter 6** the seeding effect of functionalised GNPs with 0.04 wt. %, grafted with -O_2, -NH_2, -COOH chemical groups, on the cement hydration kinetics is described. The possible mechanisms of dissolution of cement ions, nucleation, crystal formation and patterned growth regulated by the plasma processed functionalised GNPs (G-Fnt) are investigated. Results obtained from experiments are analysed and discussed to correlate the

effects of G-Fnt on the development of microstructure and enhancement in the mechanical properties of NGCC.

In **Chapter 7** the development of NGCC-CNF by using G-CNFs with various contents has been discussed. The physical and chemical interactions of G-CNFs with cement hydration due to their unique 1D shape geometry products were observed, and the experimental data obtained through XRD, FTIR, EDAX, SEM, MIP and UTM characterization techniques were analysed to correlate the possible mechanism of crystal formation and their reinforcing effect on the cement hydration products

In **Chapter 8** based on experimental results and characterization data and SEM micrographs, the physical models of microstructure regulated by GNPs and GCNFs are derived.

Finally, in **Chapter 9** the overall conclusions of the thesis and recommendations for future work are presented.

1.5   Contribution to Knowledge

The main contributions of this research to knowledge are summarised as follows:

High strength cementitious composites (NGCC) were developed via a simple technique using plasma exfoliated GNPs. The formation and growth of hydration crystals with the catalyst effect of graphene nanomaterials, favourable for the development of denser and stronger microstructure, leading to enhance the mechanical properties of NGCC were illustrated; and NGCC characteristics were determined in terms of mechanical strength and mechanism of crystal formation regulated by 2D shapes of GNPs.

Journal Publications:

"Use of plasma treated graphene nano-platelets (G-Dot) for fastening the microstructure of cementitious composite to enhance mechanical properties"   *under submission*

 "Seeding effect of functionalised GNPs, grafted with various chemical groups, on the cement hydration kinetics by stimulating the growth of hydration products in a distinctive way, leading to enhance its mechanical properties"   *under submission*

"Genome of plasma exfoliated graphene nanoplatelets (GNPs) and vapour grown graphited carbon nano-fibres (G-CNFs) useful for the development of nano cementitious composites"   *under preparation*

"Physical and chemical interaction of 1D unique shaped vapour grown graphited carbon nano-fibres (G-CNFs) with cement hydration products leading to enhance mechanical properties of cementitious composites"   *under preparation*

"Formation mechanisms of cement hydration crystals and their growth regulated by physical interaction of 2D geometry of GNPs and 1D geometry of GCNFs in the nano-graphene cementitious composites (NGCC)"   *under preparation*

Conference Publications:

"Use of Nano-Technology and Nanomaterial in the Development of Nanocomposite Cementitious Materials" NanoPT 2015 International Conference held in Porto (Portugal): February 11-13, 2015.

"Structural Analysis of Plasma Exfoliated Graphene Nanoplatelets (GNPs) for the Development of Nano-Cementitious Composites" Trends in Nanotechnology International Conference TNT2017 held in Dresden (Germany): June 05-09, 2017.

CHAPTER 2 Literature Review

2.1 Introduction

Concrete is the second most consumable material by mankind in the world after water (Mehta, 2006). It is widely used due to its advantageous properties such as high compressive strength, economical use, hardened at ambient temperature, ability to cast in shapes, energy efficient, excellent resistance to water, high-temperature resistance, ability to be modified, strong bonding with steel reinforcement, and less maintenance. The compressive strength is a mostly dominant factor on other advantageous attributes for its selection as an engineered construction material. However, brittleness in the concrete attributed to its low resistance to crack formation, low flexural, low tensile strength and low strain capabilities is a major disadvantage. Ordinary Portland cement (OPC) is the main constituent of concrete, works as a principal binder of aggregates intrinsically transmitted brittleness in the concrete through the formation of hydration products and crystals in the microstructure around the interfacial transition zone (ITZ).

In the recent past, many efforts had been made to enhance the performance of cement-based materials by adding mineral admixtures, supplementary cementitious and pozzolanic materials, synthetic and natural fibres. Also, a number of cementitious composites were developed in recent years with newly discovered nanomaterials such as nanoparticle (nano-SiO_2, nano-Fe_2O_3, nano-Al_2O_3 and nano-TiO_2), a family of carbon nanomaterials (CNTs, SWCNTs and MWCNTs) and derivatives of graphene (GO, rGO). These nanomaterials performed better than the conventional fibrous reinforcement (at millimetre scale) by arresting the cracks and improving the pore structure due to the nucleation effect of these materials at nano-scale. The enhanced effect on the toughness, compressive and tensile strength of cement composites by using these nano-sized materials with high specific surface area reported in recent researches has opened the corridors for the development of graphene cementitious composites for nano-engineered concrete (Fig.2.1) for future construction applications. However, strength improvement due to the incorporation of these nanomaterials is regarded as reinforcing and bonding effect with cement hydration products.

Research regarding microstructural changes due to crystal growth in the cement matrix responsible for the strength enhancement is still infancy; perhaps the shape of nanomaterials played an important role in the growth of hydration products during

hydration. These recent nanomaterials used in the cement matrix can be categorized according to their geometric dimensions and morphology. For instance, nanoparticles of silica can be termed as zero-dimensional (0D), carbon nanofibers like CNTs and CNFs as one dimension (1D) and sheets and plates like GO and GNPs as two dimensional (2D).
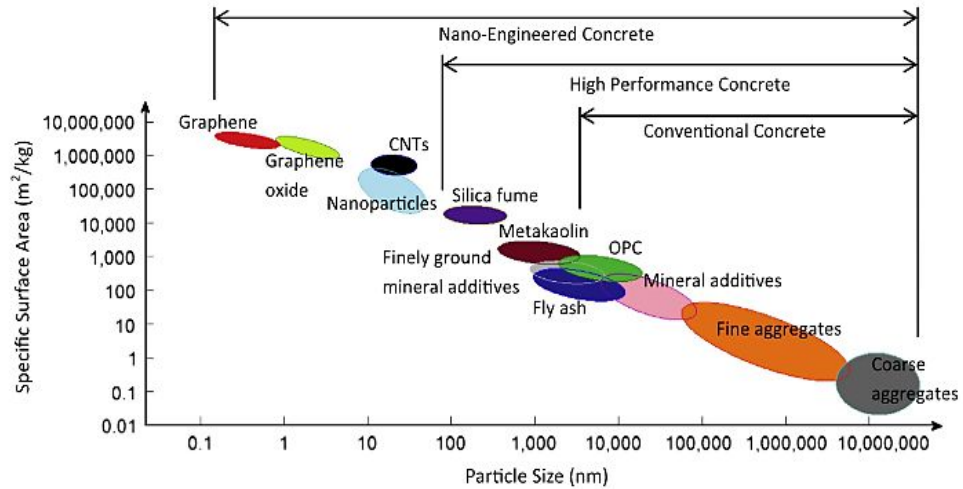
Figure 2.1 Development of nano-engineered concrete with supplementary cementitious materials (Chuah et al., 2014)

Moreover, The hydration growth and crystal properties of individual hydration products (CH, C-S-H, AFt, AFm) are understood quite well when investigated in isolation, but their co-effect is very complex when hydrated together during hydration reaction and still need to understand clearly. Before understanding cement hydration reaction in the presence of nanomaterials, it is essential to understand the chemistry of cement because constituents present in the cement changes its physical and chemical properties. Also, latest development in the field of cementitious composite up till now is needed to review.

2.2 Cementitious Materials

Cementitious materials were used since ancient times when Greeks, Romans and Egyptians made it by heating the limestone and then adding sand and gravel to make concrete.

$$CaCO_3 + \quad Heat\ 850^oC \quad \rightarrow \quad CaO \quad + \quad CO_2$$
(lime stone) (Quick Lime) (Carbon dioxide) $\qquad$ (2.1)

$$CaO \quad + \quad H_2O \quad \rightarrow \quad Ca(OH)_2 \quad + \quad Heat$$
(Quicklime) (Water) (Calcium hydroxide) $\qquad$ (2.2)
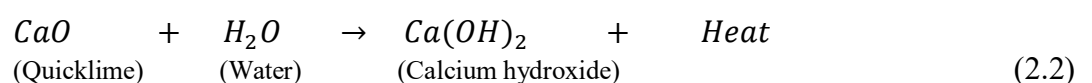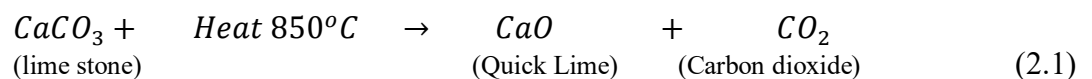
The limestone decomposes into lime (Calcium Oxide) by calcination (eq. 2.1), and then calcined lime is added in water and converted into calcium hydroxide (CH), the process

called slaking (eq. 2.2). Romans were the first who made the pozzolanic cement by adding volcanic ash with lime and used this cement widely in the marine construction. In 1824 Joseph Aspdin made a patent for the cement, he produced by calcination the limestone first and then mixed it with the clay. The mixture obtained was heated again and the product called "Portland Cement" because the colour of concrete made out of this material cement was similar to Portland stone used in England. In 1845, Isacc Johnson had improved the cement by burning chalk and clay at temperatures between 1400°C-1500°C. The Portland cement made at that time was quite similar in major contents with the cement used today except for three main developments in the processing that made it modern Portland cement. This includes clinker formation through rotary kilns during1885-1895, the addition of small amount of gypsum to control setting time and grounding clinkers, raw material through ball mills were used at the end of 19th century. Rotary kilns became widespread at the start of the 20th century for the production of cement in large quantities (Blezard, 1998). There are mainly two methods for manufacturing cement, wet process and more modern dry process.

In the wet process, the raw material is mixed together in the form of water suspended slurry using wash mills, hard and large particles are separated using mesh and then grounded by using tube mill. The slurry containing about 40% water is pumped to large storage tanks where it is continuously agitated to avoid settling down the large particles. After blending to obtain specific chemical composition the raw meal is fed into kiln unheated as slurry. Drying and heating of slurry take place while it passes through the kiln (Fig. 2.2a)
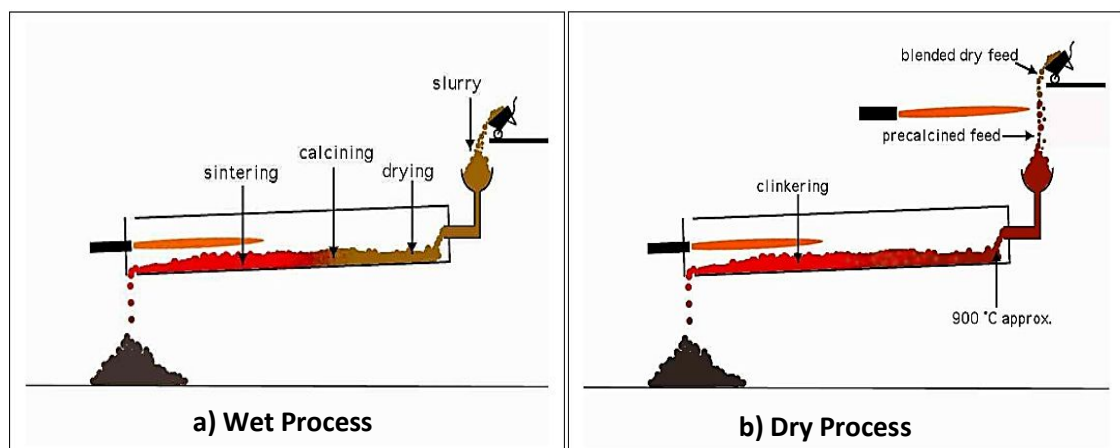
Figure 2.2 Basic principle of cement manufacturing a) wet-process kiln b) dry-process kiln with precalciner (Winter, 2009)

Whereas, in modern dry manufacturing the mixed raw material crushed and reduced to a fine meal. The meal passed through and stored in silos to the preheated tower, and then it moves down through the rotary kiln 6 m diameter and up to 250 m long. There are two types of burners in the kilns used for making clinkers in a dry process. The raw meal is almost dry in the form of fine powder is heated by the first burner called precalciner (Fig. 2.2b) further raw meal is heated through hot gases where it burnt to $1400^{o}C$ and turned into the form of clinkers. Clinkers are lumps or nodules having a diameter of 3-25 mm consist of calcium silicate, calcium aluminate, calcium aluminoferrite and metal oxides (MgO, KO, etc.) in a small amount.
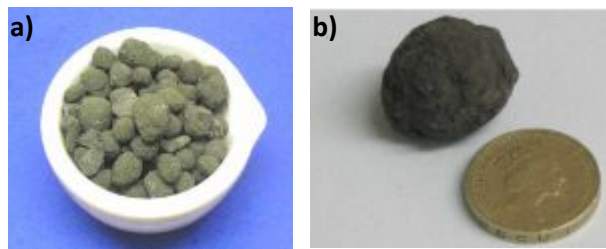
Figure 2.3 a) Typical Portland cement clinkers and b) Single clinker with 23mm dia. coin for scale (Winter, 2009)

Table 2.1 Main chemical and physical reactions taken place in the kiln

Temp.(^{o}C)	Reaction	Description
˜500	$Al_2O_3.2SiO_2.2H_2O \rightarrow Al_2O_3 + 2SiO_2 + 2H_2O$	Clay decomposition
600-950	$MgCO_3 \rightarrow MgCO + CO_2$ $CaCO_3 \rightarrow CaO + CO_2$	Carbonate decomposition
600-1000	$2CaO + SiO_2 \rightarrow 2CaO.SiO_2$ $CaO + Al_2O_3 \rightarrow CaO.Al_2O_3$ $2CaO + Fe_2O_3 \rightarrow 2CaO.Fe_2O_3$	Reaction between the decomposition product
1000-1200	$2CaO + CaO.Al_2O_3 \rightarrow 3CaO.Al_2O_3$ $2CaO + SiO_2 \rightarrow 2CaO.SiO_2$	Formation of C$_3$A and C$_2$S
1200-1250	$2CaO + SiO_2 \rightarrow 2CaO.SiO_2$	Max. Concentration of C$_2$S
1250-1450	$CaO + 2CaO.SiO_2 \rightarrow 3CaO.SiO_2$	Formation of the liquid phase and C$_3$S
Cooling	$Liquid\ phase \rightarrow 3CaO.Al_2O_3 + 4CaO.Al_2O_3.Fe_2O_3$	Formation of C$_3$A and C$_4$AF

In Table 2.1 main physical and chemical reactions are mentioned which take place in the kiln. In the next stage, these clinkers are rapidly cooled and stored until grounded into tube or ball mills where gypsum of about 3-5% is added to control setting time.

Today cement industry is manufacturing a wide variety and different types of cement to meet the end user demands according to their use in different types of projects. The cement industry is continuously making efforts to reduce carbon footprint by altering cement processing and choosing alternative cementitious composites with the desired strength.

2.3 Cement Constituents

Cement constituents decide the chemical reactions, including nano enhancement, and the performance of end products. Ordinary Portland cement (OPC) mainly consists of silicates (tricalcium silicate and dicalcium silicate) and aluminates (tricalcium aluminate and tricalcium aluminoferrite). In cement chemistry, a special notation is used to simplify formulae of oxides, for example, C= CaO, S=SiO_2, A= Al_2O_3, F= Fe_2O_3, S= SO_3, H= H_2O. The notations for the main constituents of OPC with their name known in cement chemistry are listed in table 2.2.

Table 2.2 Main constituents of OPC clinkers

Constituents	Chemical formula	Notation	Mineral Name	Weight %
Tricalcium silicate	$3CaO.SiO_2$	C_3S	Alite	50 %
Dicalcium silicate	$2CaO.SiO_2$	C_2S	Belite	25 %
Tricalcium aluminate	$3CaO.Al_2O_3$	C_3A	Celite	12 %
Tricalcium aluminoferrite	$3CaO.Al_2O_3.Fe_2O_3$	C_4AF	Ferrite	08%

When water is mixed with the cement and hydration reaction started, silicates and aluminates react with water simultaneously but with different rates and form different hydration products. Silicates react slowly as compared to aluminates and produce hydration products mainly responsible for strength development, and do not influence on setting and hardening process while aluminates react faster with respect to silicates and are mainly responsible for the setting and hardening the cement paste.

In reality, these phases are not pure but contain ions in relevant mineral phases like C_2S / C_3S contains Mg^{2+}, Al^{3+}, Fe^{3+} and C_3A contains Si^{4+}, Fe^{3+}, Na^+, K^+ while C_4AF contains varying ratios of Al and Fe. In general purpose Portland cement the constituents are in the form of oxides, and typical oxide composition is presented in Table 2.3. From these oxide

weight percentages we can calculate weight percentages of Alite, Belite, Celite and Ferrite in a Portland cement by using Bogue's equation later adopted by ASTM C150 as follows;

Table 2.3 Typical oxide composition of ordinary Portland cement (Li et al., 2011)

Oxide	Notation	Common Name	Weight Percent (%)
CaO	C	lime	64.67
SiO_2	S	silica	21.03
Al_2O_3	A	alumina	6.16
Fe_2O_3	F	ferric oxide	2.58
MgO	M	magnesia	2.62
K_2O	K	alkalis	0.61
Na_2O	N	alkalis	0.34
SO_3	$\bar{S}$	sulfur oxide	2.03
CO_2	C	carbon dioxide	—
H_2O	H	water	—

$$C_3S(\%) = 4.071C - 7.600S\text{-}6.718A\text{-}1.450F\text{-}2.852\,\bar{S} \qquad (2.3)$$

$$C_2S(\%) = 2.867S - 0.754C3S \qquad (2.4)$$

$$C_3A(\%) = 2.650A - 1.692F \qquad (2.5)$$

$$C_4AF(\%) = 3.043F \qquad (2.6)$$

In above equations C, S, A, F and $\bar{S}$ represents the weight % of oxides present in a Portland cement. The above equations can be used when A/F $\geq$ 0.64 which is mostly true for general Portland cements. The microstructure and amount hydration reaction products depend on the proportion of major constituents.

2.3.1 Alite (C_3S)

Alite is one of the most important and main constituents of OPC and hydrates differently in the presence of nanomaterials. It reacts very quickly with water during hydration reaction, and it is regarded as an essential constituent for strength development. Alite hydration produces less amount of calcium silicate hydrate (C-S-H) gel as compared to calcium hydroxide, portlandite (CH). These hydration products have strong influence on the

microstructure development of nano- cementitious composite especially interacting with graphene.

2.3.2 Belite (C$_2$S)

Belite is a second main constituent in the OPC and normally present in the form of β-polymorph, a mineral named larnite. It is mainly responsible for producing C-S-H at later stage of hydration. The nanostructure development of C-S-H depends on the hydration of C$_2$S, and it represents 80% of the final volume of the cement microstructure. Therefore, the microstructure of cement matrix regulated by nanomaterials is greatly influenced by the hydration of C$_2$S.

2.3.3 Celite (C$_3$A)

Celite commonly known as aluminate phase is a most reactive constituent. It is mostly reported that hydrates of C$_3$A do not contribute towards strength development in the final product (Taylor, 1997). However, experimental results and characterisation data regarding the hydration of aluminates presented in the subsequent chapters revealed that hydration of aluminates in the presence of graphene nanomaterials is unique and makes the difference in the development of high early strength. Furthermore, aluminates have very strong influence on setting and hardening of cement paste at early stages due to its quick reactivity with water. This quick set is undesirable in cement hydration and controlled by adding very small amount of sulphate containing substance usually gypsum in the cement during grinding. Aluminate has a cubical crystal structure containing calcium ions surrounded by six-membered alumina rings as shown in Fig. 2.8.

2.3.4 Ferrite (C$_4$AF)

Ferrite reacts with water moderately; the rate of hydration is quick at the start but slows down later even unhydrated ferrite contents can be found in very older concrete. Ferrite is black, and its presence gives cement its characteristic grey colour. Ferrite phases also produce the same hydration products as aluminates or Celite. In the hydration of graphene nano-cementitious composites, the hydration of ferrite is mostly dominated by aluminates and silicates with traces of iron in their crystals.

2.3.5 Minor Components

The important minor components which are present in the Portland cement are MgO, gypsum and alkali sulphates. To avoid a flash set of cement, due to the quick reaction of

C_3A, gypsum ($CaSO_4.2H_2O$) is grounded with clinkers at grinding stage in the production of Portland cement. In the hydration, process gypsum reacts with C_3A and forms hydration crystals named ettringite (AFT). These ettringite crystals grow on the surface of C_3A which act as a barrier and retards the fast hydration reaction of C_3A. Normally 3-5% gypsum is added to the cement, and when the percentage is more than 3% ettringite and monosulfoaluminate formation are guaranteed. The presence of alkalies (MgO, Na_2O, K_2O) increases the pH value of the cement matrix up to 13.5 and may cause leaching effect during curing. (Li et al., 2011)

2.4 Cement Hydration

Cement hydration which includes some chemical and physical processes is a chemical reaction between cement grains and water. Properties of fresh as well as hardened cement paste such as setting time and strength development are also depend on the hydration process. Therefore, before knowing that how the properties and behaviour of cement paste can be altered and optimised, some basic knowledge of cement chemistry and hydration is required.

2.4.1 Mechanism of Hydration

Considering the hydration reaction of cement, broadly the main constitutes of cement are aluminate and silicates with different chemical compositions of calcium reacting with water. The chemical reaction started soon after mixing with water and the main chemical compounds present start taking part in chemical reaction simultaneously. This makes it a very complex chemical reaction and has to be fully understood yet. It is understood commonly that the aluminates react faster as compared to the silicates and are responsible for initial setting, whereas silicates participate in hardening of cement. To understand the reaction mechanism the hydration of individual compounds of cement is studied separately and translated for overall combined hydration process. The study of individual compounds of cement assumes that the hydration takes place separately without the interaction of any other compound which is in reality not true. Although this assumption may mislead to understand the changes occurred at micro and nano level due to the combined interaction of compounds taking part in the chemical reaction, to initiate the study and understanding of complex hydration process this is the only approach that has been adopted so far. Let's start with the hydration process and chemistry of individual compounds to understand basics and then build-up new scenarios for the interface of nanomaterials in the complex hydration process.

2.4.2 Hydration of Aluminates

The hydration of C_3A starts immediately when reacts with water and produces rod-like crystal structures AFt. The reaction of C_3A with water is highly exothermic and so fast that needs to be slowed down otherwise cause a flash set in the cement paste. In OPC gypsum ($CaSO_4.2H_2O$) is added to slow down the reaction of C_3A with water and to avoid flash set. Gypsum reacting with water releases sulphate (SO^-_4) and calcium (Ca^+) ions and these ions react with aluminates ion (Al_4O^-) to form calcium sulfoaluminate hydrate more commonly called ettringites (AFt). The general chemical formula of ettringite (AFt) containing 6 calcium aluminate sulphate and 32 hydrates is ($3CaO. Al_2O_3. 3CaSO_4. 32\,H_2O$) and the main chemical reaction in cement chemistry notation is

$$C_3A + 3(C\bar{S}H_2) + 26H \rightarrow C_6\,A\bar{S}_3\,H_{32}\,(AFt) \qquad (2.7)$$
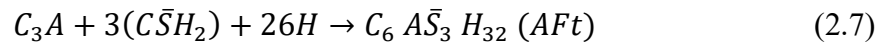
Ettringite is naturally occurring mineral with the same composition produced with a hydration of C_3A in the presence of gypsum. Ettringites are needles or rod-like crystal structures form on the surface of C_3A particles and act as a diffusion barrier to avoid flash set. Moreover, these needle or rod-like crystal structures are shown in fig. 2.4 slow down the chemical reaction of C_3A and become the reason for the initial setting of cement paste. However, recently the formation of ettringite in the cement paste has been revisited, and classical view of retardation stated as more complex.
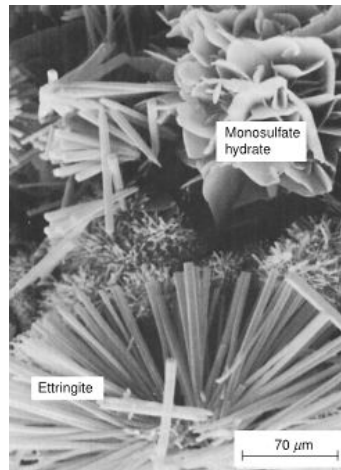
Figure 2.4 SEM image of ettringite and monosulphate (Mehta, 2006)

Role of ettringite formation in the microstructure development by filling the pores and increasing the molar volume of the cement paste is regarded as a source of early strength development. Ettringite initially forms an acicular crystal structure and subsequently transformed into the layered crystal structure of monosulfate (AFm) due to the reaction of C_3A with ettringite and calcium hydroxide (CH) when all the gypsum present is consumed.

16

The crystal structure of ettringite (Fig. 2.5) is different from the crystal structure of monosulphate; it consists of channels build-up of $Al(OH)_6^{3-}$ and Ca^{2+} ions. These channels have a net positive charge because with each ion of aluminium hydroxide there are three calcium ions associated with it. There are other channels in ettringite crystal structure build-up with sulphate and water ions due to which a net negative charge is attained on ettringite structure. All the channels present in the ettringite crystal structure are arranged in a hexagonal shape surrounded by water molecules. A cluster of ettringite is shown in Fig. 2.5 b.
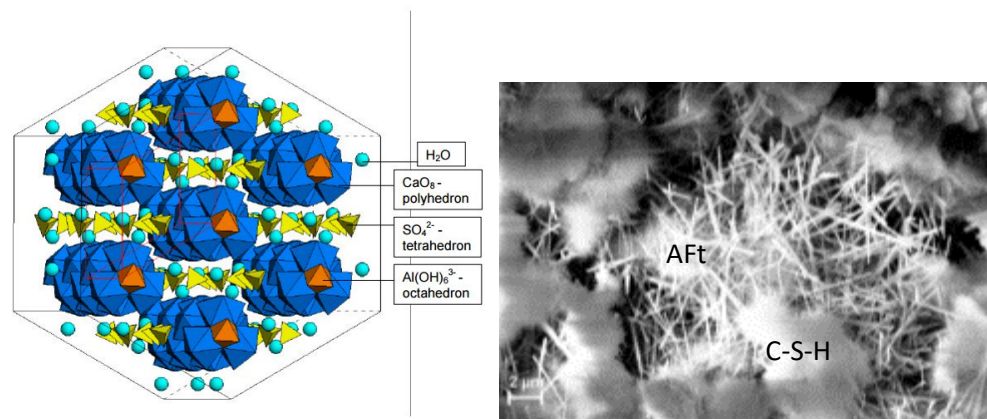
Figure 2.5 a) Crystal structure model of AFt (ettringite) b) SEM image of cement composite showing cluster of ettringites and C-S-H gel (This research work)

Ettringite grow aggressively during hydration especially when there are pores and spaces are available to grow. The effect of ettringite formation on the strength development has been reviewed and considered in two scenarios. In the first scenario, the formation of ettringite before the hardening of cement paste is taken as advantageous for the early strength development because its needle or rod-like crystal structure may act as reinforcement for the encased C-S-H gel and the expansion of ettringite structure is not significant. In the second scenario, if ettringites are formed after the cement paste is hardened then it may produce cracks by breaking other crystals to make room for their growth, which is called delayed ettringite formation (DEF). Ettringite crystals are sensitive to temperature and amount of sulphate present. They are unstable at higher temperatures above 60°C and transformed into monosulfoaluminate (AFm) when all the sulphate is consumed before the complete hydration of C_3A. The reaction of formation of AFm is mentioned in eq. 2.8. Ettringites are formed again (eq. 2.9) when AFm reacted with new sulphate ions

$$2C_3A + C_6 A\bar{S}_3 H_{32} + 4H \rightarrow 3C_4\bar{S} H_{12} \qquad (2.8)$$

$$C_4\bar{S}\,H_{12} + 2C\bar{S}H_2 + 16H \rightarrow C_6A\bar{S}_3\,H_{32} \tag{2.9}$$
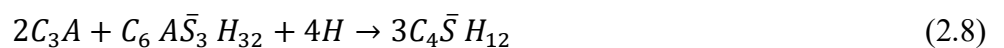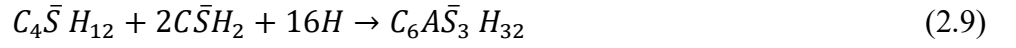
If there is no sulphate available, C_3A react quickly with water

$$2C_3A + 21H \rightarrow C_4A\,H_{13} + C_2A\,H_8 \tag{2.10}$$

The hydrates further converted into following products and reaction so fast that flash set occurs in cement paste.

$$C_4A\,H_{13} + C_2A\,H_8 \rightarrow 2C_3AH_6 + 9H \tag{2.11}$$

The hydration of C_4AF is quite similar to the hydration of C_3A. However, the rate of reaction is slower in case of C_4AF. When it is reacted with gypsum following reaction takes place,

$$C_4AF + 3(C\bar{S}H_2) + 21H \rightarrow C_6(A,F)\bar{S}_3\,H_{32} + (F,A)H_3 \tag{2.12}$$
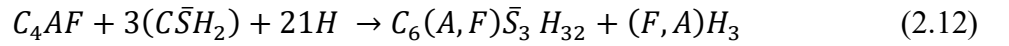
In the eq. 2.12, the expression $C_6(A,F)\bar{S}_3\,H_{32}$ contains both A and F components, means that alumina and iron oxide are present interchangeably in the compound and it can further react with water and C_4AF as follows,

$$C_4AF + C_6(A,F)\bar{S}_3\,H_{32} + 7H \rightarrow 3C_4(A,F)\,\bar{S}H_{12} + (F,A)H_3 \tag{2.13}$$
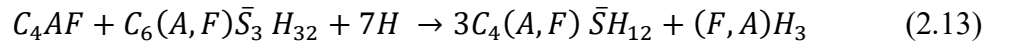
Most of the sulphate present in the form of gypsum consume due to quick hydration of C_3A at early stages and retards the hydration of C_4AF, and most of its quantity remains unreacted till late ages of hydration. Therefore, the effect of C_4AF on the cement hydration at early stages is not significant as compare to hydration of C_3A and C_3S (Scrivener, K.L. 2004)

2.4.3 Hydration of Silicates

Tri-calcium silicates (C_3S) and di-calcium silicate (C_2S) the main reaction compounds of ordinary Portland cement are stoichiometrically similar, but they form the different amount of calcium hydroxide (CH) also called Portlandite, releasing a different amount of heat with a different rate of reactions. The chemical reactions are mentioned below;

$$2C_3S + 11H \rightarrow C_3\,S_2\,H_8 + 3CH \tag{2.14}$$

$$2C_2S + 9H \rightarrow C_3\,S_2\,H_8 + CH \tag{2.15}$$

For a given quantity the C_2S generates more amount of C-S-H with respect to C_3S, whereas C_3S produces a higher amount of CH crystals. In general, both C_2S and C_3S contribute to

produce CH and C-S-H but react at a different rate. C_3S is more reactive and releases more heat than C_2S and determines the early strength of cement paste. C_3S starts hydrating within few hours of hydration while C_2S hydrates at a later stage of hydration generally after 7 days responsible for later strength in the cement paste. Another important aspect related to the growth of C-S-H and CH is that they very "gentle" and grow by passing across anything come across their way or stop their growth if there is no free space for them to grow. CH is a plate-like hexagonal shape good crystalline structure formed due to crystallisation and about 25 % of the cement microstructure is composed of it. CH increases the pH value of the cement paste over 12 which good for corrosion resistance. However, an excessive amount of CH is not desired in the cementitious materials used for construction which may cause durability issues due to leaching, carbonation, alkali reaction and sulphate attack. CH crystal is brittle and detrimental to the compressive strength of cement paste. It has definite stoichiometry and perfect morphology with hexagonal plate shape crystals and tends to crystallise in the pores, and empty spaces otherwise encased with C-S-H and cant observed in the dense microstructure.
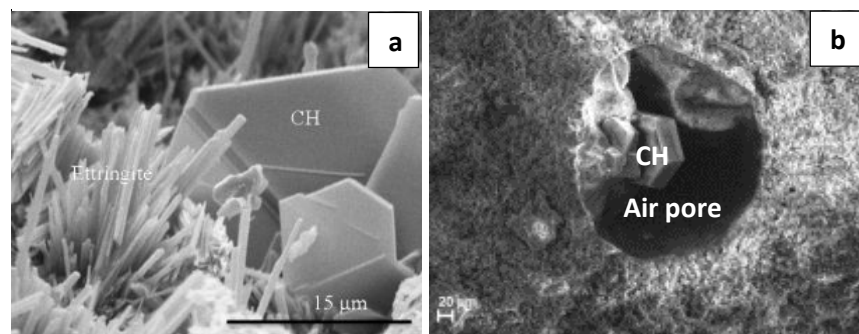
Figure 2.6 SEM micrographs showing the hexagonal plate crystal structure of CH a) size between 15-20 microns around ettringite (Stutzman, 2001) **b) size between 50-75 microns grown in air pore** (This research work)

The main hydration product in both chemical reactions mentioned above is calcium silicate hydrate ($C_3 S_2 H_8$) which is commonly designated as C-S-H non-stoichiometrically. C-S-H forms circumferentially on the surface of cement grains during hydration and about half of the structural components in the cement paste are composed of it. C-S-H is formed at nano level and grows up to micro level in the microstructure of cement paste. With its nano size and higher contents, it is believed to be the major strength source in the Portland cement. The nanoscale structure of C-S-H is still not well defined and the formula mentioned above ($C_3 S_2 H_8$) gives only an approximation values of the elements present in it. C-S-H initially grows in the form of gel-like structure and then transforms into an amorphous solid structure which is not easily detected by x-ray diffraction (XRD) investigation. Recently

structure of C-S-H has been reinvestigated to understand its binding properties in the microstructure. In the Portland cement paste, the Ca/Si ratio in C-S-H is variable and not same even in the different areas of same paste but approximately 2:1 which is same as Ca/Si ratio of C_2S (Belite). It is considered that C-S-H is the principal product of C_2S hydration and forms a small amount of CH. On the other hand, C_3S has approximately Ca/Si ratio of 3:1. The hydration of C_3S (Alite) if produces C-S-H with Ca/Si ratio of 2:1 then the excessive calcium produces calcium hydroxide (CH) reacting with water. C-S-H is considered as a main component of strength development in the Portland cement (Nicholas, 2009). Morphology of C-S-H also differs within the paste and varies from poorly crystalline fibrous structure to reticular networks. The microstructure developed by C-S-H crystals can be viewed and characterized fully through scanning electron microscope (SEM) because of their tendency to cluster and colloidal dimensions. (Paulo J. M. Monteiro P. Kumar Mehta, 2013). The usually described term microstructure of cement is used a magnified portion of macrostructure by using microscopy. With the use of advanced experimental techniques such using transmission electronic microscope (TEM), scanning electron microscope (SEM) and atomic force microscope (AFM) it is possible nowadays that the resolution of cement microstructure can be observed to up fraction of nanometres as shown in Fig. 2.7. With the progress and advancement in the field of materials engineering, it has been widely and primarily recognised that properties of materials are based on their micro and nanostructure. Therefore, the properties of materials can be improved by altering or modifying its internal micro or nanostructure.
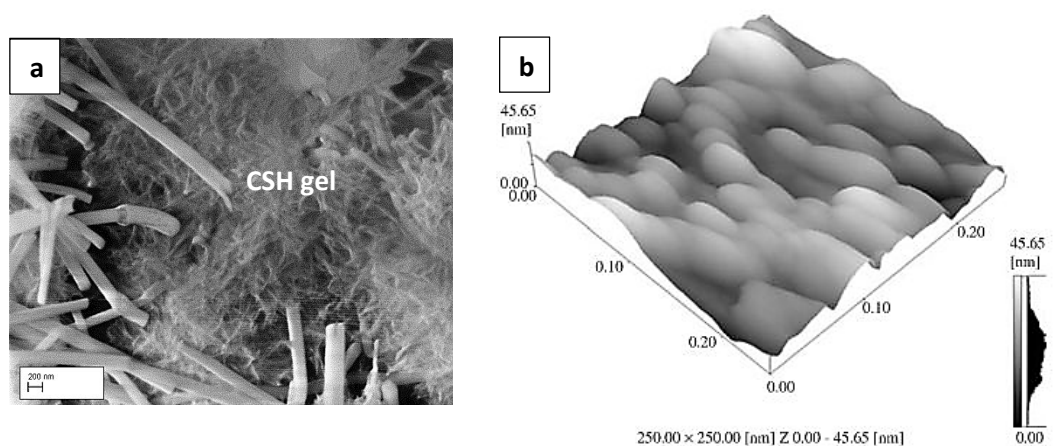
Figure 2.7 a) Morphology of C-S-H (This work) **b) AFM scans of C-S-H at nanometre scale** (Li et al., 2011)

Unfortunately, having modern tools, advanced technology and decade-long research, the structure of C-S-H is still not clear because it is difficult to characterise amorphous

structure and the varied amount of Ca/Si ratio from one area to another area within same cement paste. Therefore, it even becomes harder and more difficult to propose C-S-H structure when some additive or nano-material is added into the cement matrix.

2.5 Microstructure Development in Hydration Process

The microstructure is probably the single most important parameter when discussing nanotechnology for cementitious composites. The mechanisms of hydration, chemical reactions and development of hydration products for individual major cement compound have been discussed above in detail. These chemical reactions are exothermic, and heat release rate measured during hydration of cement is frequently used to understand the dynamics of hydration process. A typical calorimetric curve for the hydration of Portland cement is depicting the rate of heat evolution with respect to time shown in Fig. 2.8. There are many characteristic points on the curve leading to differentiate the hydration process into five different stages. These five stages are 1) dissolution, 2) dormant, 3) acceleration, 4) deceleration and 5) steady state
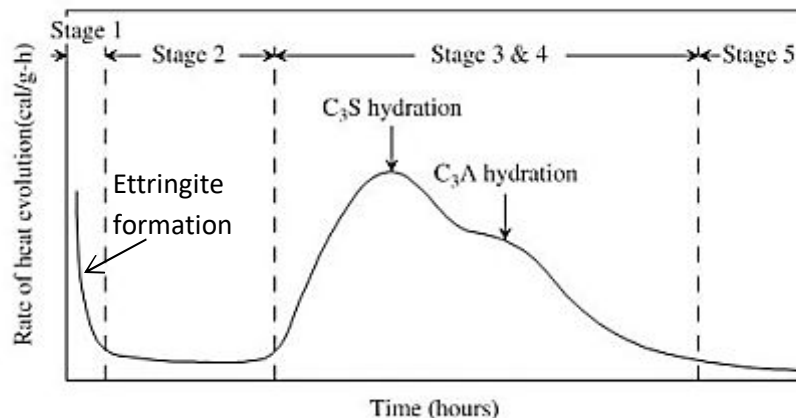
Figure 2.8 Typical calorimetric curves during hydration of Portland cement (Li et al., 2011)

In the stage-1 "dissolution" of calcium and hydroxide ions takes place during initial hydrolysis and the calorimetric curve indicates the sudden release of heat in the start when C_3A reacts with water and possible formation of short length ettringites AFt of 100 to 200 nm length (Fig. 2. 9) as a gel layer. It is believed that the gel layer formed on the surface of cement particles hinders the contact of water with unhydrated cement particles, thus slows down the hydration process of cement (Bullard et al., 2011). This is indicated by the downward trend of the calorimetric curve at the end of stage-I and leads to stage-2 called "dormant period" where the temporary retardation of hydration of C_3A takes place, and

calorimetric curves indicate very low rate of heat evolution during this stage which lasts between one and two hours. Mainly nucleation and growth hydration products like C-S-H and CH take place during this stage while the cement paste remains workable and these nucleates initiate the hydration of C_3S in the next stage. The end of the dormant period is correlated with the initial setting time of cement paste, refers the point during the hydration of cement when paste begins to solidify and becomes inflow able. In stage-3 called "acceleration" which lasts for 4 hours to 10 hours the calorimetric curve trends upward very steeply indicating a higher amount of heat evolved, possibly due to the hydration of C_3S forming hydration products such as C-S-H gel and CH. C-S-H gel formed during this stage called "outer products" precipitates on the ettringites AFt formed during stage-1 as shown in Fig. 2. 9(c).
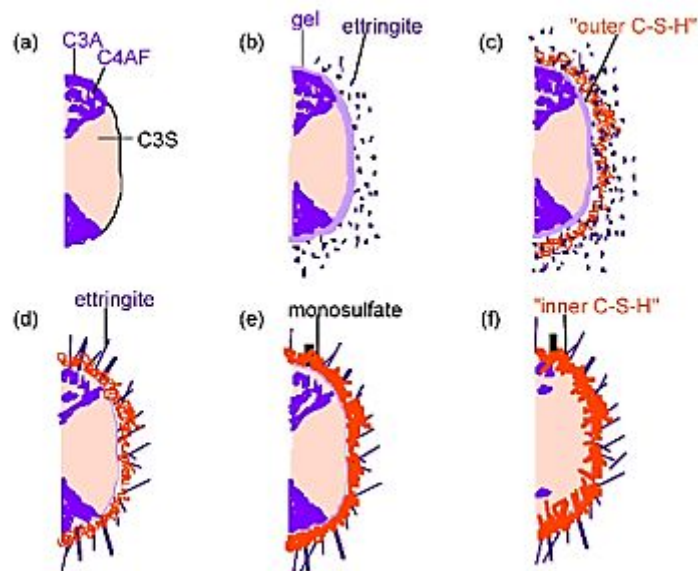
Figure 2.9 Microstructural developments during hydration of Portland cement
(Scrivener, 1989)

This outer C-S-H gel precipitates away (~1µm) from the surface of reacting cement particles leaving pores between unhydrated grain and hydrated shell (Hadley et al., 2000; Scrivener, 2004; Kjellsen and Lagerblad, 2007). Further hydration takes place in two ways inward and outward the direction of the hydrated shell. The "outer" C-S-H gel grows with the honeycombed and acicular morphology (Fig 2.7a), while CH precipitates in the pores with hexagonal plate-like crystals (Fig. 2.6a). These crystals and C-S-H gel form a network of interconnected crystals and give strength to the cement paste upon complete solidification and this point of hydration indicated by the first peak in a calorimetric curve which is referred as final setting time. In the stage-4 "deceleration" a very low rate of heat

evolution brings the calorimetric curve trend decreasing downwards. Also, the rate of hydration is very slow at this stage. After the first peak, the calorimetric curve goes down and rises again to form a second peak (Fig. 2. 8) indicating the hydration of C_3A with the formation of long rod-like ettringites AFt and plate-like AFm crystals shown in Fig. 2. 9 (d and e). The hydration of C_3S carries on, and the formation of "inner" C-S-H gel takes place which fills up the gaps between hydrated shell and unhydrated grains. Later in this stage around 14 days, the "inner" C-S-H sufficiently fills the gap between hydrated and unhydrated grains while "outer" C-S-H grows further into fibrous morphology and densifies the cement paste (Rodger and Groves, 1989; Taylor, 1997; Richardson, 1999).The formation of the large plate-like CH crystals also continues by precipitating in capillary pores. In the final stage-5 "steady state" hydration remains to continue for years with very slow rate because C-S-H gel formed around the unhydrated cement particles blocks the way of water towards the nucleus unhydrated grains.

The development of microstructure of a well-hydrated cement paste comprises the hydration growth of individual phases when sufficient spaces and pores are available for their growth and their accumulative interwoven growth when hydration products itself fill pores and gaps. The physical, chemical and mechanical properties are derived from the formation of microstructure which itself depended on many other factors. Many physical models of the microstructure of hydrated cement paste are developed to understand the growth mechanism as shown in Fig.2.10 with essential phases of hydration in a well-hydrated cement paste.
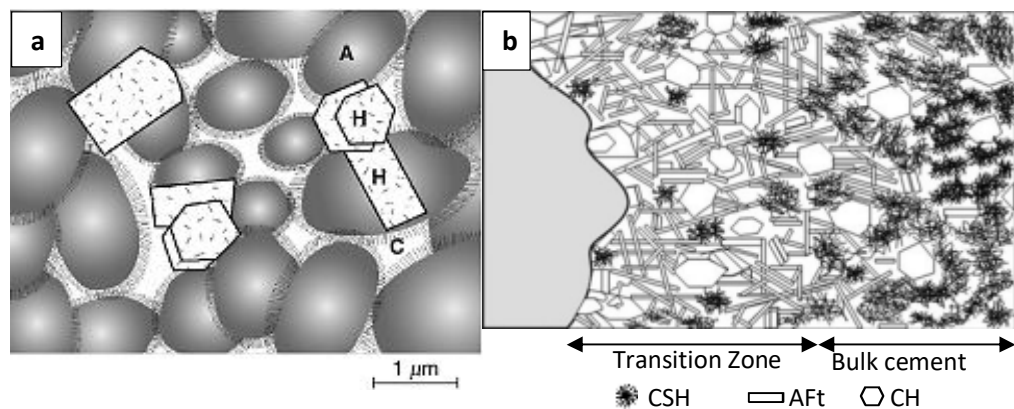
Figure 2.10 Microstructural model of well-hydrated cement paste a) essential phases of hydration products in a bulk cement paste (Mehta, 2006) **b) with unevenly dispersed system of essential hydration products near ITZ** (Li et al., 2011)

Fig. 2.10a represents the model of a well-hydrated paste of Portland cement. In the model, poorly crystalline particles of C-S-H are represented by letter "A" having one smallest colloidal dimension of 1 to 100 nm with an average inter-particle spacing of 1.5 nm. Large

hexagonal crystals of CH are represented by "H", and "C" is representing the capillary voids ranging from 10 nm to 1 μm originally filled by water. The formation of rod-like ettringite AFt and lamellar AFm phases are not mentioned in this model (Mehta, 2006).

It can be noted that size and morphology of various phases shown in the model are not uniform and not well distributed in the cement paste. This microstructural inhomogeneity in the cement paste can affect the strength and other mechanical properties because strength properties in the cement paste are governed by the well-integrated microstructure developed by the crystalline and amorphous hydration products. Many factors can affect the shape and growth of crystalline and amorphous hydration products and could be the most important aspect for the nano-enhancement that is to be carried out in this study.

Another model of the uneven distribution of cement hydration products around the interfacial transition zone (ITZ) in concrete shown in Fig. 2.10b described by (Li et al., 2011) which is based on the work of Maso (Maso, 1980). ITZ in the cement concrete is the region which is prone to failure due to the weaker microstructure around large aggregate particles. The formation of the weaker microstructure is due to the formation thin water film around large aggregates in the fresh concrete and lead to increase water-cement ratio in the region that is in bulk cement paste. With increased water contents in the region there is less number of cement particles around the aggregate surface and during the hydration process dissolution of calcium silicates (C_3S) produces calcium and hydroxide ions in the region. When critical saturation of these ions takes place, they form relatively large crystals of calcium hydroxide (CH) in the vicinity of aggregate. Due to evaporation of excessive water around the aggregate region a more porous microstructure forms as compared to the region of bulk cement paste (Fig.2.10 b). Further, with the hydration of C_3A and C_2S rod-like AFt and more plate-like crystals of CH grows with poorly crystalline C-S-H to densify the area by filling pores and hence improves the strength. Denser microstructure around aggregate strengthens the cement matrix. Therefore, the strength of ITZ depends on the microstructure developed in the region and development of dense microstructure itself depends on many factors.

In fact, there is a possibility to modify the microstructure of final hydration products of cement matrix by adding chemical admixtures, pozzolans, supplementary cementing components, adding nanomaterials and nano-fibres. How we can modify the microstructure of cement paste to develop a controlled, engineered microstructure having superior characteristics is to be discussed in the next paragraphs.

2.6   Factors Affecting Microstructure

The mechanical properties of cement paste are intrinsically linked with the development of microstructure of the paste; a denser microstructure reflects the superior while a porous microstructure yielded the poor strength. In fact, factor influencing the microstructure is indirectly related to the strength of the cement paste. Some of the factors made the microstructure of cement paste porous are water-cement (w/c) ratio, mixing technique, compacting method, temperature and curing regime. These may be controlled during the time of mixing, but pores and water at the micro and nanoscale are inevitable in the making of normal cement paste unless it is prepared under laboratory controlled conditions. These difficulties to control factors, have great influence on the strength, and not only make the cement paste microstructure porous but also link to the durability issues, because the penetration of chloride ions and carbon dioxide from the environment through channels may form the interconnectivity of pores in the microstructure.

A concise amount of water in the cement paste is essentially required to start the hydration reactions and any excess water added may cause the formation of pores and flocculation (clot like masses) of cement particles which forms porous microstructure and leads to strength reduction, resistance to deterioration and other durability issues. Formation of voids or pores largely depends only on w/c ratio in the cement paste. The formation of the porous microstructure is the main cause of deterioration by allowing penetration of chloride ions, water and carbon dioxide from the environment. The decrease in durability in terms of chlorine diffusion, moisture diffusion and air permeability in cement paste with higher w/c contents cement paste was observed (Kim et al., 2014). Various types and size of water and air pores or voids are present in the hydrated cement paste which influences the properties of cement paste. These are discussed below.

2.6.1   Voids in Hydrated Cement

i) Interlayer Spaces in C-S-H. According to the Powers (Powers and Brownyard, 1946) in solid C-S-H, 28% porosity is accounted for the interlayer spacing between the C-S-H layers. Power assumed that interlayer spacing is 18 Å, whereas, according to Feldman and Sereda (Feldman and Sereda, 1968) it may vary from 5 to 25 Å. This void size is extremely small and can be negligible for any effect on strength and porosity. However, the presence of water due to hydrogen bonding is possible and when this water evaporates under certain conditions may initiate shirking and cracking in the hydrated cement paste (Mehta, 2013).

ii) Capillary Voids. Capillary voids in a given cement paste mixture are the spaces that are not occupied by the solids (hydration products, cement grains and interlayer spacing between C-S-H) rather remain empty. The bulk density of hydrated products of cement is quite less than the anhydrous cement grains; approximately 1cubic centimetre of anhydrous cement requires double the volume after complete hydration of cement. The water takes most of the spaces in cement paste mixture. In well-hydrated cement paste with low w/c ratio may contain the capillary voids ranging from 10 – 50 nm, while in a high w/c ratio cement paste these may be range from 3-5 μm. Pore size distribution is typically measured by mercury intrusion porosity meter (MIP). Figure 2.11 shows typical curves of pore size distribution with different w/c ratios, higher w/c ratios leads to the formation of large pore sizes. Capillary voids which are larger than 50 nm size are referred as *macropores,* and these voids may be considered for effecting the strength and permeability of cement paste. The capillary voids ranging between 2-50 nm are called *mesopores* may be responsible for the porosity and capillary voids less than 2 nm are referred as *microspores* may lead to developing cracks at nano level due to drying and shrinkage. Moreover, capillary pores are interconnected with each other having irregular shapes.

iii) Air Voids. Air voids or pores generally of spherical shape are formed unconnectedly due to the air trapped during mixing of cement paste, inappropriate compaction or sometimes entrained intentionally by adding admixtures.
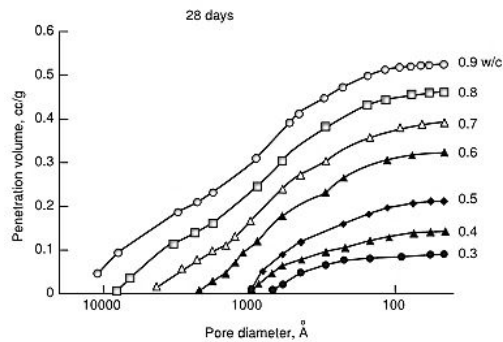
Figure 2.11 Effect on pore diameter on penetration volume at different w/c ratio
(Mehta, 2011)

They generally range from 50μm to few mm in size. These pores are quite bigger than capillary voids and can adversely affect the mechanical strength of cement paste.

2.6.2 Water in Hydrated Cement

Also an addition to solid and void phases, a typical cement paste also contains a large amount of water which exists in various states. Classification of various types of water present in the saturated cement paste is framed on the criteria that how easily present water

can be removed from the cement paste. Following are the various states in which water exists in the typically saturated cement paste.

i) Capillary Water. The water contained by the voids of a size larger than 50 Å is called capillary water and not influenced by the attractive forces generated by solids. Capillary water can be divided into two categories: *free water* present in the voids larger than 50 nm sizes and its removal does not affect the change of volume, and the water held by very small capillary voids between 5–50 nm sizes, removing it from the system may cause shrinkage.

ii) Absorbed Water. Absorbed water exists close to the surface of solids, present in cement paste, and remains under the direct influence of attractive forces exerted by surfaces of solids. The surface of solids physically absorbs the water molecules up to six water molecular layers (15 Å) by hydrogen bonding. Removal of absorbed water from the system of saturated cement paste may cause shrinkage.

iii) Interlayer Water. Interlayer water is related to the water present between the layers of the C-S-H structure. Hydrogen bonding strongly holds the monomolecular water layers between the C-S-H layers. In strong drying conditions interlayer water losses, and considerable changes in the structure of C-S-H takes place.

iv) Chemically Combined Water. The water integrally present or bonded with the different hydration products present in the microstructure of cement paste, like in AFt and AFm phases. Chemically absorbed water only evolves out of hydration products when heating decomposes them. Feldman and Sereda's model presented in Fig. 2.12 shows various types of water associated with C-S-H.

The presence of water and voids in the cement paste defines the architecture of microstructure because hydration products in the form of crystals and amorphous solids are grown under the direct influence of water and pores. The presence of pores and water molecules at the macro level can produce a poor microstructure due to disconnected hydration crystal's network while pores and water molecules present at micro and nano level may help in the growth of hydration products and develop more interconnectivity leads to enhanced mechanical strength.
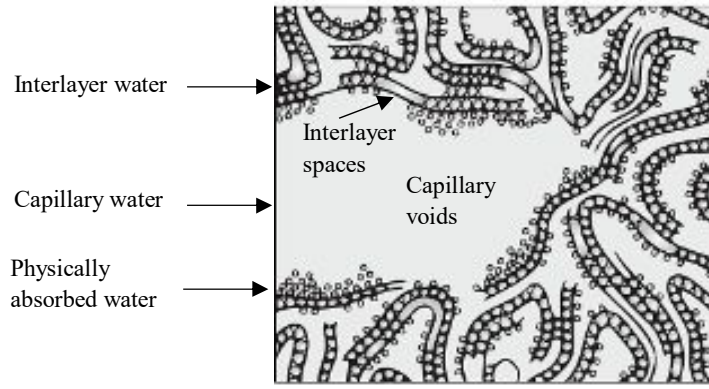
Figure 2.12 Model presented by Feldman and Sereda for types of water related to C-S-H structure

Therefore, the porosity of cement paste plays an important role in defining the mechanical strength of cement paste. There is a fundamental inverse relationship exists between porosity and mechanical strength. The established relationship between compression strength (R) and porosity (p) is (Powers, 1946);

$$R = k(1 - p)^3 = k\left[1 - \left(\frac{V_{pc}}{V_s + V_{pc}}\right)\right]^3 \qquad (2.16)$$

Where k is strength of voidless mortar, V_s is represents the volume of solids in the cement paste and V_{pc} is the volume that is occupied by the capillary pores, which is defined by another power law equation (2.17)

$$V_{pc} = V_{ac} + V_{vc} = [w/c - 0.36h] \qquad (2.17)$$

Here, V_{ac} represents the volume of water in capillary pores and V_{vc} represents the vacuum in the capillary pores, w/c is the water cement ratio and h is the hydration rate. From the equation 2.17, it can be deduced that the volume of capillary pores decreases with the increase of hydration rate and decrease of w/c ratio.

2.7 Micro-/Nano-Technology Enhanced Cementitious Composites

As aforementioned, the mechanical strength and microstructure development of cement paste is significantly linked with the porosity. It is because, the propagation of cracks, due to excessive stresses, in the microstructure initiates at the pores. In the recent past microfibers and nanomaterials are widely used in the cement composites as micro and nano reinforcement to bridging the cracks and to refining the pore structure, ultimately leading to the formation of stronger and denser microstructure.

2.7.1 Microfiber Cementitious Composite

Microfibers used in the cement composites for improving the microstructure range of steel fibres, glass fibres, carbon and polypropylene fibres. These microfibers are used in cement composites due to their large aspect ratios ranging from 10 to 1000 but have a small surface area ranging from 0.02 to 0.134 m^2/g. On the other hand, nanomaterials such as, CNTs, GO and graphene has large aspects ratios (10,000 to 600,000) as well as high surface areas ranging from 70 to 2600 m^2/g. The material properties of some microfibers and nanomaterials are given below in Table. 2.4.

Table 2.4 Material properties of microfibers and nanomaterials (Chuah et al., 2014)

Material	Shape	Elastic modulus (GPa)	Tensile strength (GPa)	Density (Kg/m³)	Dia./ thickness (nm)	Surface area (m²/g)	Aspect ratio
Graphene	2D	1000	~130	2200	~ 0.08	2600	6000-600,000
GO	2D	23-42	~0.13	1800	~0.67	700-1500	1500-45,000
CNTs	1D	950	11-63	1330	15-40	70-400	1000,10,000
Nano-silica	0D	-	-	2400	6-15	170-200	-
Carbon fibre	3D	7-400	0.4-5	1770	6000-20,000	0.134	100-1000
PP fibre	3D	3-5	0.3-0.9	900	18,000 - 30,000	0.225	160-1000
Glass fibre	3D	72	3.45	2540	5000-10,000	0.3	600-1500
Steel fibre	3D	200	1.50	7800	50,000-900,000	0.02	45-80

The bridging mechanism of microfibers strengthens the microstructure of cement composites by arresting the cracks and connecting the pores, and also works as reinforcement by carrying the partial stresses due to applied loads. Microfibers due to their excellent intrinsic mechanical strength, large aspect ratio and easy to mix have been extensively used for reinforcing the cement and concrete in the past decades. Fibres with varying material properties have been used in the cement composites for various proposes like carbon fibres with its high elastic modulus around 400GPa used for retrofitting of

structures and glass fibres with its high tensile strength (3.45GPa) used to improve the tensile and flexural strength of cement. Although the addition of microfibers improves the tensile and flexural strength of cement composites but does not enhances its compressive strength. Furthermore, the addition of microfibers degrading the workability of cement composites by entrapping small air voids attached to their surface. Functionalised carbon and polymeric fibres can make a strong covalent bond with cement hydration products but with the limited interfacial strength due to their small surface areas. Moreover, it has been reported that microfibers bridges the large cracks and forms dense system of microcracks (Fig. 2.13), but they cannot stop the initiation of cracks and nanoscale (Chuah et al., 2014)
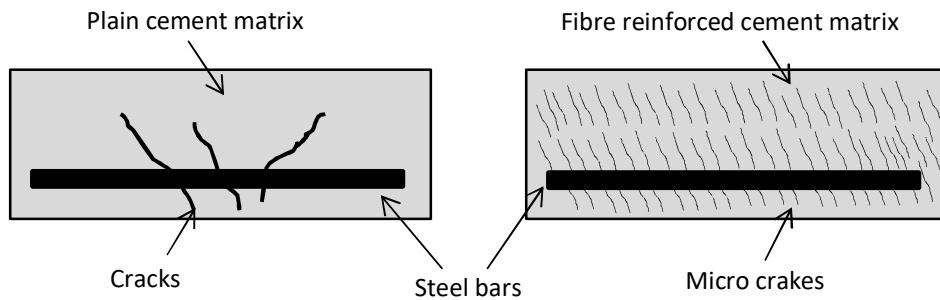
Figure 2.13 Crack pattern in plain and fibre reinforced concrete

Whereas, nanomaterials performs quite better as compared to microfibers by modifying and reinforcing cement matrix at the nanoscale. Nanomaterials which include nanoparticles, nanofibers, CNTs, GO and a new form of graphene nanoplatelets (GNPs) have the great potential to improve the microstructure of the cement matrix. These nanomaterials being so small in dimensions and having strong Van der Waal's forces between them are not easy to incorporate directly into the cement composite but require systematic and sophisticated techniques to disperse into the cement matrix fully.

Figure 2.14 various forms of fibres a) steel fibres b) glass fibres c) PP fibres and d) carbon fibres

2.7.2   Nanoparticles Cementitious Composite

Nanoparticles such as nano silica (nano-SiO_2), nano-iron (nano-Fe_2O_3), nano-alumina (nano-Al_2O_3) in the powder form with a particle size 10 nm to 70 nm have already been

used in the cementitious composites. The use of nano-titanium oxide (nano-TiO_2) and nano calcium carbonate (nano-$CaCO_3$) are also found in the recent research discussion for enhancing the microstructural properties of cement composites.

These nanomaterials proficiently accelerate the degree of hydration, leading to form denser microstructures with the formation of hydration crystals contributing to strength. It has been reported that the pozzolanic characteristics of nanoparticles consumes the CH crystals and produces C-S-H with new dimensions that improve the interface structure and develop the compact and homogeneous microstructure (Qing et al., 2007). Performance of nano silica has also been reported (Said et al., 2012) to refine the pore structure by consuming CH crystals when added with an increased dosage from 3% to 6% in cement paste. The fine nano-silica particles of 12 nm sizes are proven to be more expediting in cement hydration as compared with the coarse silica fume particles of 150 nm diameter (Zhang and Islam, 2012) (Fig. 2.15). The refinement produced in the microstructure of cement composite with the added nano silica not only explains the filling effect of nano-sized particles but also highlights the expedite degree of hydration due to its pozzolanic characteristics (Jo et al., 2007). The consumption of CH crystals and formulation of the more C-S-H gel by adding nano-silica into the cement increases the compressive and flexural strengths (Jo et al., 2007).
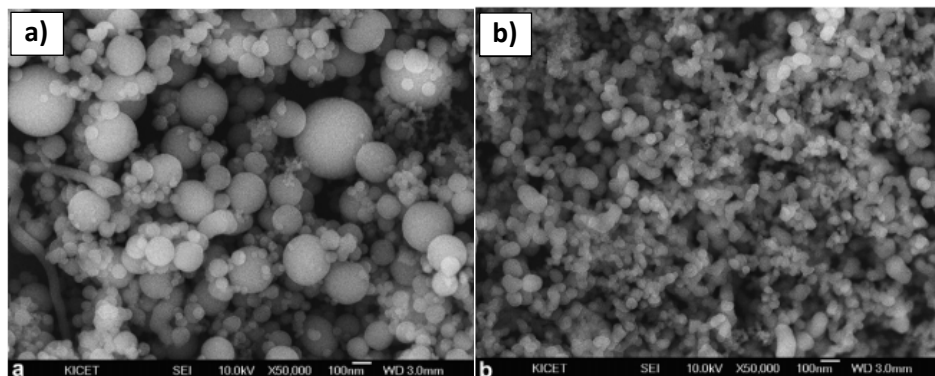
Figure 2.15 SEM micrographs of nanoparticles a) silica fumes b) nano silica particles (Jo et al., 2007)

It has been reported that adding 4% nano silica particles by weight of cement into the concrete has improved the compressive, flexural and tensile strength by a factor of 1.7, 2.2 and 1.6 times respectively as compared to the control concrete sample at the age of 28 days (Nazari and Riahi, 2011). Using both nano-SiO_2 and nano-Fe_2O_3 particles in cement mortar has also been reported to improve compressive and flexural strength with more compact and denser microstructure of hydration products with the absence of large crystals of CH

(Li et al., 2004). Furthermore, nano-sized silica particles work as filler and leave fewer weaker zones leading to develop denser microstructure (Fig. 2.16). However, it increases the water demand for further hydration as the degree of hydration retarded after few days with the absorption of water by nano silica particles (Madani et al., 2012).
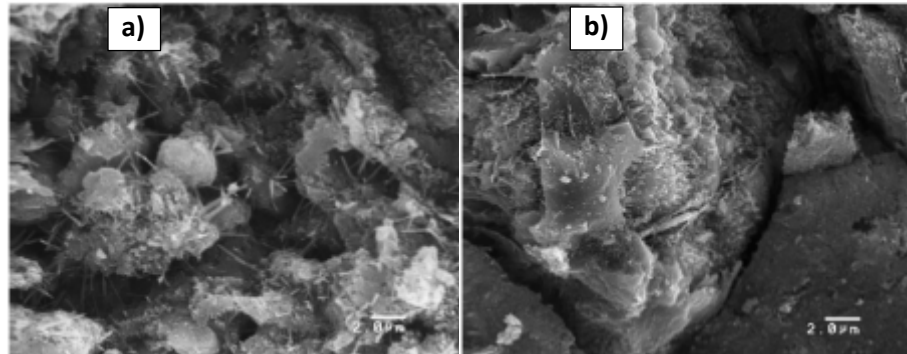
Figure 2.16 SEM micrographs of nanoparticles a) controlled cement sample b) cement paste containing nano-SiO$_2$ particles (Jo et al., 2007)

2.7.3 CNT Cementitious Composite

In nano carbon family, carbon nano tubes (CNTs) are carbon allotropes considered having one-dimensional (1D) geometry with cylindrical nanostructure in the rolled up to form the single planner graphene sheet. CNTs used in the cement composites are essentially divided into two types; 1) single wall carbon nanotubes (SWCNTs) and 2) Multiwall carbon nanotubes (MWCNTs).
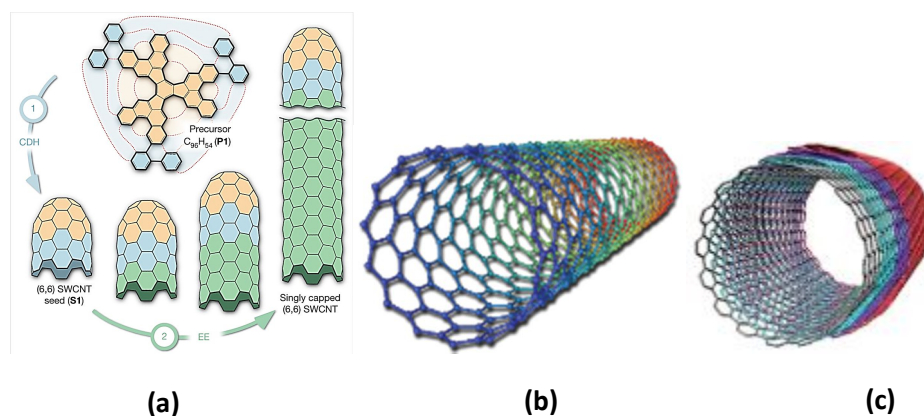
Figure 2.17 Computer simulated structures of a) growth of SWCNT on platinum surface with end cap b) rolled up SWCNT from graphene sheet c) rolled up MWCNT from multilayer graphene sheets (Sanchez et al., 2014)

SWCNT are difficult to grow in large numbers as compared to MWCNT and capped at the end (Fig. 2.17 a). However, these caps can be detached. These are easy to handle and can be twisted around without damaging its structure. While MWCNT made up of concentric

cylindrical sheets of graphite, have more defects in its structure and make it difficult to get its desired properties (Siddique and Mehta, 2014). CNTs attracted by the researchers to incorporate in cement composite due to its excellent mechanical properties, with tensile strength approximately of 11-63 GPa and elastic modulus nearly 1 TPa. However, its multifunctional properties such as excellent thermal properties and electrical conductivity enable it to be used as smart material in the cement composites (Chuah et al., 2014). Regarding physical reinforcement in the cementitious composites, both SWCNT and MWCNT are reported beneficial for the enhancement of mechanical strength due to their high aspect ratio (~1000) and their large surface area (100-2600 m^2/g) which promote the reactivity in the hydration process. Makar et al. first reported the accelerated rate of hydration in the cement composite due to the incorporation of CNTs. They used the Vickers hardness method to find out the improvement in the hardness of cement paste during early 14 days and mentioned that CNTs through nucleation effect accelerated the growth of cement hydration products (Makar et al., 2005). The nucleating effect of SWCNTs providing sites for hydration of C_3S and C-S-H grows preferentially along the surface of SWCNTs as shown in the Fig. 2.18 (Makar and Chan, 2009). The growth of dense C-S-H around the entire length of CNTs appears to be bonded strongly, resulting reinforcing effect. The similar nucleating and reinforcing effect has also been observed in MWCNT by (Li et al., 2007).
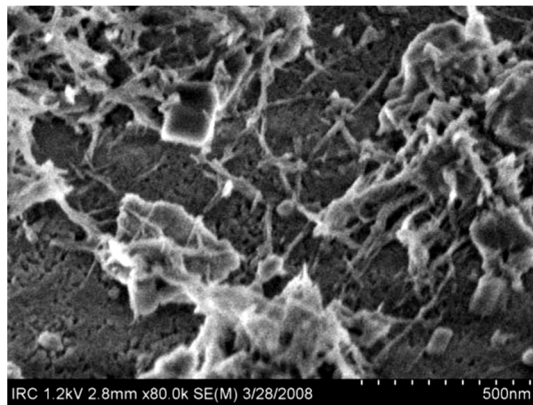
Figure 2.18 Nucleation effects of CNTs on the growth of C-S-H during hydration of cement composite loaded with SWCNTs

Further, CNTs were also reported by many authors for improving the pore structure of cement composites by filling the voids between the hydration products. Through MIP test by using the functionalised MWCNT with 0.5 wt.% in the cement composite has demonstrated a very refined pore structure. This pore structure obtained with the reduction in the total porosity of cement matrix by 39% and in the pore sizes (> 50 nm) by 45% (Li

et al. 2005). A similar study where 0.3 wt.% MWCNT were dispersed into the cement composite using two admixtures resulted in reducing total porosity by 21.6% and average pore diameter by 31.3% (Melo et al., 2011). Therefore, advantages of incorporating functionalised CNTs into the cement composites are clear in terms of improving the durability by reducing the total porosity and voids in the cement matrix and with nucleation effect with an increased amount of C-S-H gel produced to further densifies the microstructure.

The increased growth of C-S-H gel not only densifies the microstructure by bonding CNTs with hydration products but also contributes to increasing the flexural and compressive strength. Presence of CNTs in the cement matrix reinforces the cement hydration products with its 1D geometry and accelerates the hydration reaction due to its nucleating effect similar to 0D nano-silica. Initial studies of cement composite using CNTs showed that MWCNT performed very well as compared to SWCNT because of the defects presents in their structure and became a reason to provide more interactive sites for cement hydration products (Campillo et al., 2004). It was observed that hydration products secured the better anchorage due to the increased number of intersection points on the surface of MWCNT. A strong covalent bonding between the interface of CNTs and cement matrix has also been observed due to the functionalization of CNTs with chemical groups attached to its surface resulting better load transfer capabilities from cement matrix into CNTs (Li et al. 2005). The 50% enhancement in compressive strength cement nano-composite has also been demonstrated by adding 0.045 wt.% of MWCNTs functionalised with COOH (Cwirzen et al., 2008).

The nucleation effect C-S-H preferred to grow preferentially on CNTs surface rather than encapsulating nearby cement grains thus provides more chances for unhydrated cement grains to react with water and produce denser microstructure reinforced by CNTs (Makar and Chan, 2009). A test result of three-point bending test on cement composite samples loaded with MWCNTs showed a substantial increase both in flexural strength and Young's modulus of 25% and 45% respectively (Konsta-Gdoutos et al. 2010).

The major mechanical properties of CNT cementitious nanocomposite were evaluated in an experimental study by using long and short MWCNTs of different aspect ratio with various wt.% concentrations. The long MWCNTs 0.1 wt.% with an aspect ratio of 1250-3750 and the short MWCNTs 0.2 wt.% with an aspect ratio of about 157 was used in the cement paste samples and cured for 7, 14 and 28 days.

Results from the test data (Fig. 2.19) showed a remarkable increase in flexural strength and ductility of the CNT cement composites as compared to plain cement samples. Though the flexural strength increased in CNT cement composites, large variation and inconsistency in strength were observed especially at 28 days. It was concluded that reinforcing capabilities exhibited by a low concentration of longer MWCNTs are comparable to that of high concentration of short MWCNTs. Furthermore, short MWCNTs are also capable of filling nanopores while increasing the packing density (Abu Al-Rub et al., 2012).
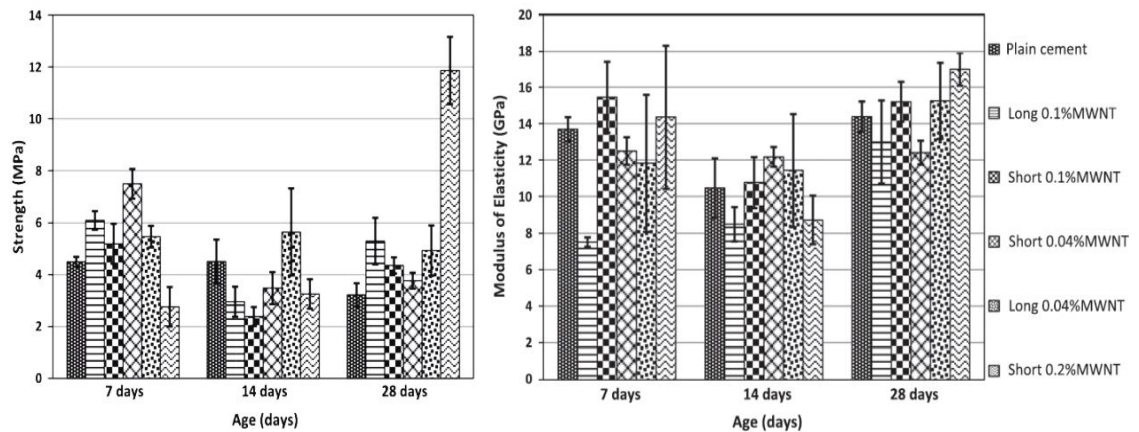
Figure 2.19 Results for various MWCNTs composites a) average flexural strength b) average modulus of elasticity (Abu Al-Rub et al., 2012).

Dispersion of nanomaterials especially CNTs into the cement matrix is challenging and without uniform dispersion full advantage of these nano-reinforced materials cannot be harnessed. The uneven distribution of CNFs in some areas of hardened cement paste was observed (Fig.2.20) when prepared by reinforcing CNF 0.4wt.% of cement (Yazdanbakhsh et al., 2010).
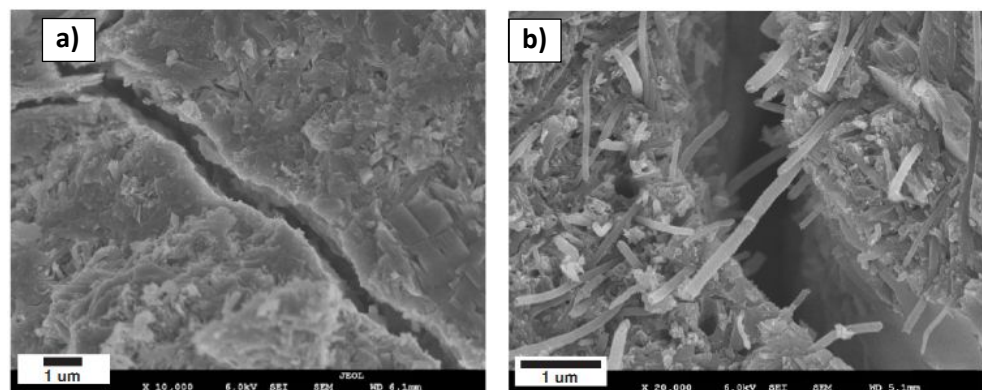
Figure 2.20 SEM images showing fractured surfaces of hardened cement mixed with 0.4wt.% CNF with nonuniform distribution a) fractured surface showing CNFs do not appear b) CNFs closely packed and agglomerated in some areas of cement paste (Yazdanbakhsh et al., 2010)

To counteract the dispersion issues of CNTs in the cement matrix applied Gum Arabic to disperse 0.08 wt.% and .10wt.% MWCNTs in the OPC as shown in Fig. 2.21(Wang et al., 2013).
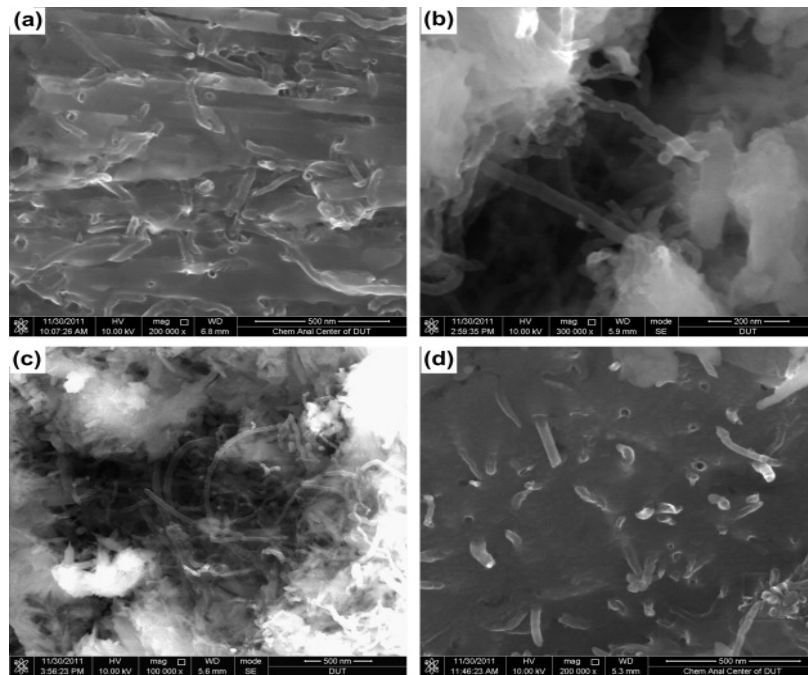
Figure 2.21 (a and b) SEM micrographs of cement composites 0.08wt.% MWCNTs (c and d) 0.10 wt.% of MWCNTs.

They observed the improved fracture energy and flexural toughness in the cement composite through a network of MWCNTs connecting cracks and pores acting as a bridge (Fig. 2.21b) to transfer the loads in tension. Various techniques including the use of surfactants in combination with sonication were commonly adopted by researchers for successful dispersion of nanomaterials and CNTs into the cement matrix. Nevertheless, most of the surfactants were found not compatible with the cement hydration process and cause the formation of poor microstructure by retarding hydration, entrapping air voids and reacting adversely with water reducing agents. Functionalization of CNTs is an alternative approach for their better dispersion into the cement matrix by attaching polar impurities or chemical groups such as hydroxyl (OH) or carboxyl (COOH) groups at the end of their surfaces.

2.8 Graphene Cementitious Composites

The Recent discovery of a wonder material graphene has sparked the cement researchers to use it as nano reinforcement into the cement matrix by shifting their attention from CNTs. Graphene in different forms based on their synthesis, structure, morphology and

functionalization is attributed to its high strength, increased surface area, unique 2D morphology and the most important its hydrophilic nature disperse it into the water. Plenty of work has been done for developing graphene-based cement composites in very recent years, but 95 % of the work is based on harnessing GO into the cement matrix. There are other forms of graphene, such as nano graphene platelets or graphene nanoplatelets (GNPs) which are more integrated structurally, easy to disperse resulting in more seeding and ribbed effect on cement microstructure. In the subsequent section, a brief about the graphene-based cement composite is discussed to extend research objectives and set specific research goals.

2.8.1 Graphene Forms

There are various forms of graphene-based on its synthesis and extraction from raw graphite. Many scientists had theoretically structured the graphene and with many years of their research they could produce graphene with 50 to 100 layers until in 2004, when two researchers from Manchester University UK were successful to obtain single layer of graphene and were awarded Nobel Prize in 2010 for extracting single layer of graphene from pure graphite using scotch tape (Novoselov, 2004). Since the familiarity of graphene in the field of material science many forms of graphene are available both commercially and synthesis in labs as shown in the Figure 2.22.

Most commonly known graphene derivate, GO attributed with its multifunctional properties, such as high thermal and electrical conductivity, is rapidly recognised as very interesting and attractive material for its application in numerous electronic devices. Pristine graphite is chemically oxidized for the production of GO, then exfoliated and dispersed into suitable solvent or water. GO is a single layer of graphene having honeycombed crystal structure of hexagonal carbon items functionalised with an oxygen-containing epoxide, hydroxyl and carboxyl groups.

Another recent form graphene material is graphene aerogel, and it is claimed to be the lightest materials in the world. Graphene aerogel is attributed to extraordinary low density, high electrical conductivity, high surface area, superior mechanical properties coupled with hydrophobic nature (Supermarket, 2009). Graphene aerogels are also produced by using 3D extrusion using graphene materials as inks.

Reduced graphene oxide (rGO) is chemically reduced from GO. These are not the pristine graphene layers because few oxygen-containing groups remained stitched with their

surface despite reduction. The treatment of harsh chemicals or unsuitable thermal treatments may harm their structure.
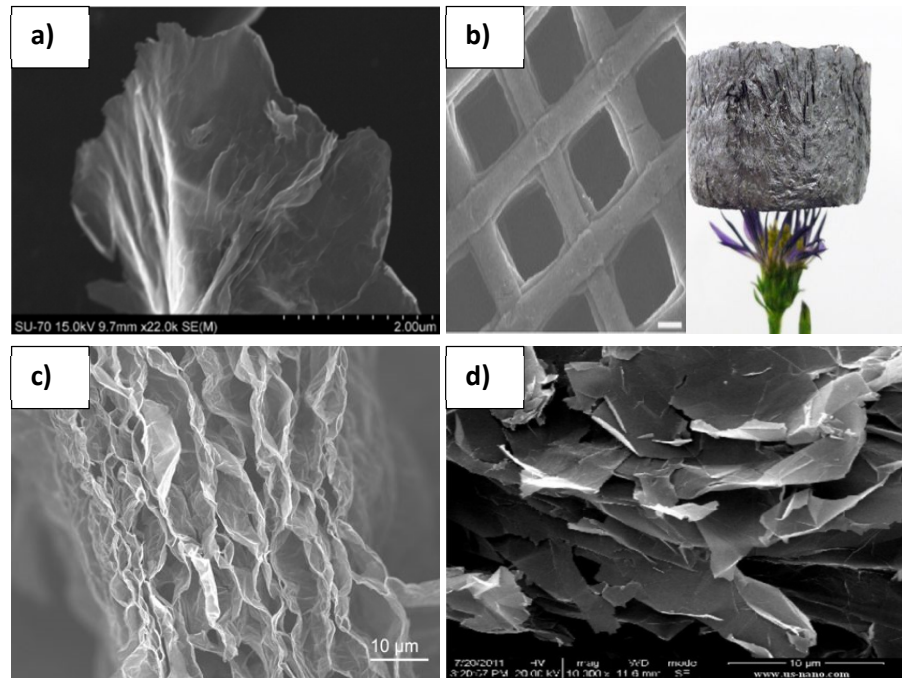
Figure 2.22 Various forms of graphene a) single layer of graphene oxide GO (Goncalves et al., 2009) **b) SEM micrograph of 3D printed microlattice of graphene aerogel** (credit: Cheng Zhu et al./nature Communications **c) SEM image of reduced (rGO) cross section** (Image: Dr. Chen, Nanyang University) **d) SEM micrograph of commercially available graphene nano platelets (GNPs)**

Graphene nanoplatelets (GNPs) when exfoliated have a similar chemical structure as CNTs, but advantageously they can be modified chemically at their edges more easily than CNTs. Typically GNPs is in range of 1µm to 100 µm in lateral dimension and less than 5 nm thick but depends on its synthesis procedure. The exfoliated GNPs are mostly used in new applications of electrical and thermal conductivity, but their use and effect on the development of microstructure in the cement are in their infancy (Alkhateb et al., 2013).
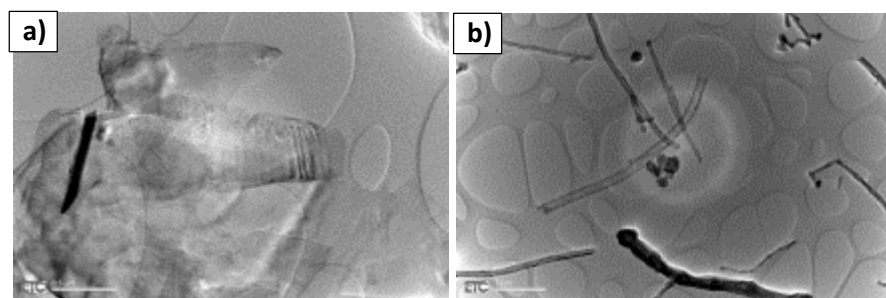
Figure 2.23 Emerging forms of graphene a) plasma exfoliated GNPs b) graphited carbon nanofibers (GCNF) (current work)

Since the emergence of graphene in the material world, a continuous evolution in its forms has been witnessed and it is progressing extremely fast due to nanotechnological advancements. Nanotechnological enhanced techniques make it possible to synthesise large quantities of emerging graphene forms stitched with tailor-made properties such as plasma exfoliated GNPs functionalised with various chemical groups and graphited carbon nanofibres with conical graphene sheets inserted into their hollow structure as shown in Figure 2.23b.

2.8.2   Synthesis of Graphene

There are several routes invented for the synthesis of graphene and its derivative. Also, much research is underway to include more novel routes for commercial production. The few well-known routes are

    i)   Micromechanical cleavage (MC)

    ii)   Chemical vapour decomposition (CVD)

    iii)   Liquid phase exfoliation (LPE)

    iv)   Hummers and Offeman method

    v)   Reduction of graphene oxide (RGO)

    vi)   Plasma exfoliation (new)

i) Micromechanical cleavage (MC) was breakthrough experiment also famed with "peel off" or the "scotch tape" method of extracting the single layer of graphene from pure graphite (Novoselov, 2004).

ii) Chemical vapour decomposition (CVD) is commonly used method for synthesis of graphene presented in early research. The graphene films are used to grow on substrates such as Ni(111), Cu and Si by providing a temperature controlled gas sources enriched with carbon atoms such as methane or ethane (Lahiri et al., 2011).

iii) Liquid phase exfoliation (LPE) referred to an ultra-sonication process of graphene exfoliation. In this process, graphite in water or suitable organic solvent is dispersed, and exfoliation takes place due to cavitation produced by controlled hydrodynamic shear forces in the form of tiny air bubbles (Bonaccorso et al., 2012).

iv) Hummers and Offeman is also most widely used method to chemically synthesis graphene oxide in early research and used with some modifications in recent years. In this method graphite is oxidised using a chemical mixture made up of sodium nitrate ($NaNO_3$),

potassium permanganate ($KMnO_4$) using concentrated sulfuric acid ($H2SO_4$) and then oxidised graphene exfoliated in water through ultra-sonication (Hummers and Offeman, 1958).

v) As described in earlier that exfoliated single layers of GO can be obtained through oxidation of pure graphite, then these exfoliated GO are reduced by using chemical, electrochemical, thermal or sometimes a combination of these methods. Reduced graphene oxide (rGO) is obtained upon reduction (Fig. 2.24) but still different from pristine graphene because of oxygen atoms stitched with its surface. (Sarkar et al., 2014) & (Stankovich et al., 2007)
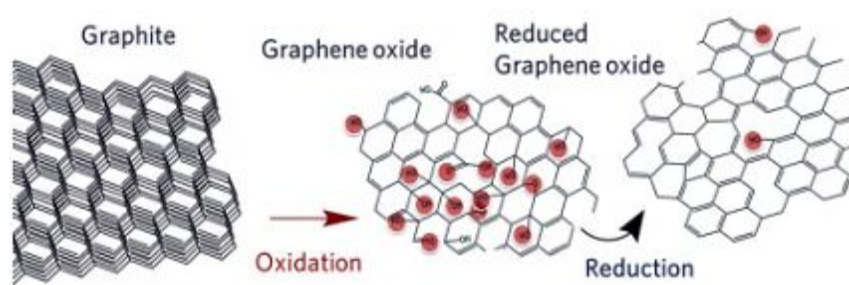
Figure 2.24 Process for reduction of rGO from pure graphite (Materials chemistry research group, 2015)

vi) Plasma exfoliation is a new sophisticated technologically enhanced method of graphene synthesis without using any harsh chemicals and acids, which can degrade the structure and surface properties of graphene. In a recent experimentation illustrated by (Lee et al., 2014) the plasma was generated (Fig. 2.25) between two carbon electrodes while immersing their tips into distilled water.
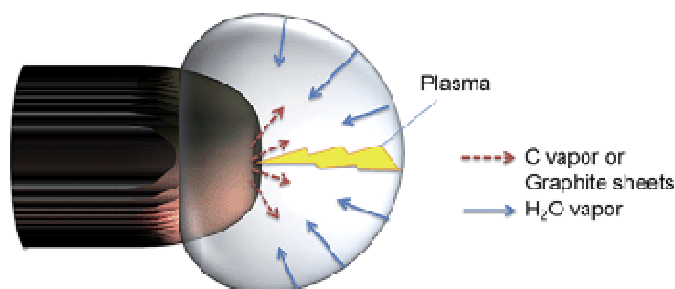
Figure 2.25 Plasma exfoliation of graphene (Lee et al., 2014)

A continuous energy accumulation production approach in which accumulated energy is induced by focusing the plasma steamers on the surface of electrodes. This accumulated energy further produces thermal gradient zones producing proper energy level. This energy

is sufficient for the extraction of graphene layers out of the graphite without breaking covalent bond between C-C atoms in the graphene sheet. TEM and RAMAN characterization confirmed the characteristics of graphene exfoliated through plasma method.

2.8.3 Characterization of Graphene Material

Graphene is widely researched for its unique properties regarding geometrical shape, aspect ratio, surface morphology, lattice structure, and capability of attaching functional groups. However, to fully utilise the capabilities of graphene in a particular application its material properties need to be determined. A number of characterization techniques are used to determine exact material properties of graphene.

2.8.3.1 Structural and Morphological Characterization using TEM

TEM microscopy is a characterisation technique used to observe internal structure of the material up to atomic scale to ascertain their structural and morphological properties. The working principle of TEM is based on the scattering of an electron through the material interaction. The electrons in the form of the beam are emitted from the electron-emitting gun and focused towards the sample. After interacting with the material, some of the electrons from the accelerated beam pass through the material, and some are scattered making certain angles. These scattered electrons are again focused on the objective lens and form an image. This transformed image can be viewed and magnified on a fluorescent screen and can be recorded (Akhtar, 2012).
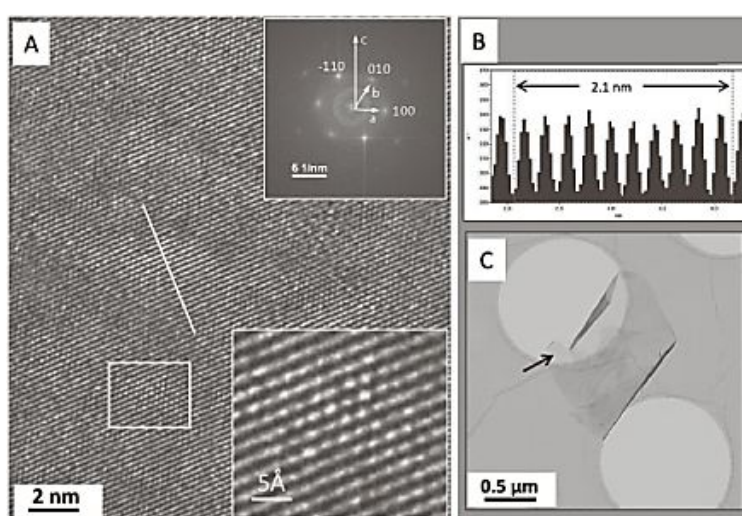
Figure 2.26 HR-TEM imaging of graphene A) TEM image showing few layers of graphene with the magnified area in the lower inset. FFT is shown in the upper right inset. B) Intensity profile of graphene along the white line drawn in the image "A" C) bright field (BF) TEM image of graphene indicating area of HR-TEM image by an arrow (Akhtar, 2012)

The high resolution (HR) TEM image is obtained due to contrast generated by scattering electrons when then interact with the specimen. Crystalline planes of the material diffract electrons, if they satisfy the Bragg scattering condition, produces a diffraction pattern of periodic potential in the form of Fast Fourier transform (FFT). The FFT can be used efficiently to decode the pattern of values into discrete frequencies.

In the literature related to graphene cement composite mostly BR-TEM images, which are limited to characterize the surface morphology and not the crystal structure of graphene, are discussed by authors. (Lin et al., 2016) has recently demonstrated the catalytic behaviour of GO in the hydration of cement and characterized the GO sheets having wrinkled morphology resulting from effective exfoliation through TEM image (2.27a).
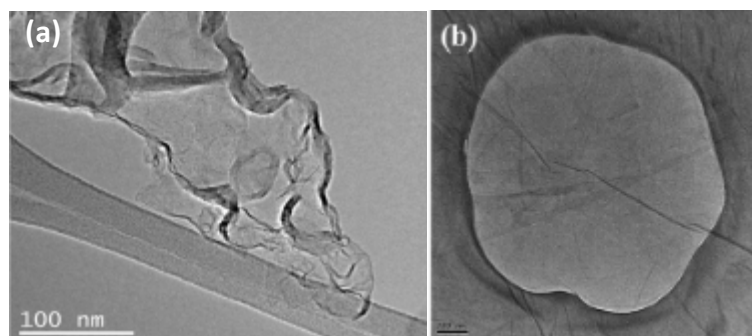
Figure 2.27 BF-TEM images a) TEM image by using JEOL JEM-2010F (Lin et al., 2016) **b) BF- TEM image of GO sheet on lacy carbon grid using Philips CM20 analytical TEM** (Pan et al., 2015)

Pen et al. also characterized GO sheets using TEM to observe wrinkle surface morphology (Fig. 2.27b). In the study, they mentioned that due to wrinkling morphology a better bond strength could be achieved between GO and the cement matrix with enhanced interfacial strength provided by mechanical interlocking (Pan et al., 2015). To probe further and to ascertain the morphology such as thickness and lateral dimensions of graphene other characterization techniques are required.

2.8.3.2   *Dimensional and Dispersion Characterization using SEM*

Secondary electron microscope (SEM) is a substantial tool for material characterization. In the SEM electrons are emitted from an electron gun source under high vacuum to form an image of the object under observation. The electrons are emitted in the form of a focused beam generated by high electric potential difference ranging from hundreds of volts to tens of kilovolts. The generated beam of electrons made focused when travelled through the arranged geometry of magnetic lenses and apertures in the microscope. When this focused

beam of electrons interacts with the atoms, present at or near the surface of the sample, it generates various signals to scans the surface in the raster data and transforms the information into an imaging device.

SEM characterization technique can be used for a very wide range of analysis such as surface dimensions, surface morphology, and dispersion etc. of nanomaterials. SEM is a vital tool to characterize the microstructure and crystallography of cement microstructure, and most of the findings in the current research are also based on the SEM characterization. Further, the list of analysis of materials we can perform using SEM can be long enough, but limited areas are mentioned here related to the current research. For example, SEM characterization was also used to evaluate the dispersion of GO sheets into the water by depositing them on a silicon substrate (Fig. 2.28), and FE-SEM images were used to measure the thickness (20 nm) of GO flakes. The AFM is preferred to determine the thickness of graphene sheets (Gong et al., 2015b; Babak et al., 2014).
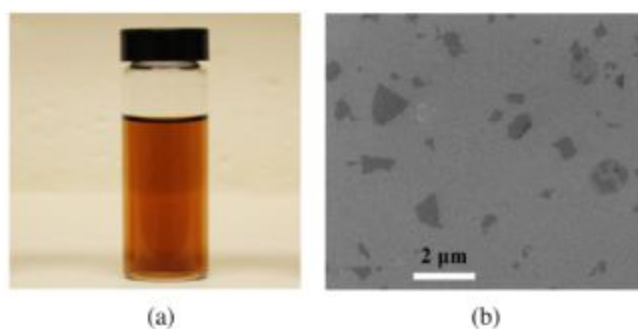
Figure 2.28 (a) GO solution (b) SEM image of dispersed GO on silicon substrate

2.8.3.3   Topographical and Surface Characterization using AFM

Atomic force microscope (AFM) is a powerful tool to generate images of the material surface at atomic resolution with angstrom scale, and it requires minimal sample preparation. In AFM the topography of a material surface is obtained by scanning through a highly sophisticated cantilever tip over an area of interest. The elevated and depressed structures on the sample surface affect the deflection of the cantilever, which is monitored by a controlled laser and optical system. Through the controlled laser and optical system, the movement of the cantilever is constantly observed and through the feedback of positioning data of cantilever the AFM can produce a precise topographic map of the material surface. For example, the topography of GO was estimated by using AFM (Nanoscope V Multimode 8, Bruker) and significant changes found in the initial graphite

sheets ranging from 156-171 nm to finally oxidised graphene sheets of 0.89 nm thickness as shown in the Fig.2.29 (Horszczaruk et al., 2015)
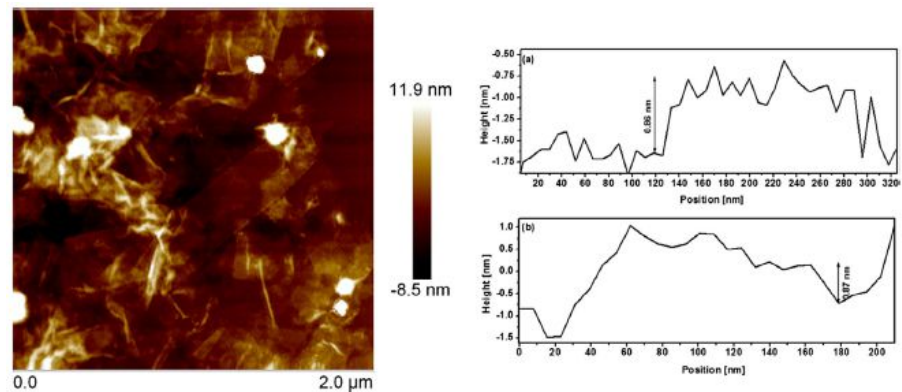
Figure 2.29 AFM image showing topography of prepared GO
(Horszczaruk et al., 2015)

2.8.3.4 Crystallographic Characterization using XRD

X-ray diffraction is a characterization technique by which atomic and molecular structural characteristics of the crystalline material can be identified. A beam of x-rays is emitted from gun diffracted into many specific angles after interacting with the crystal structure of the material in question. A diffraction pattern can be drawn by measuring the intensities and diffraction angles of these diffracted x-rays. These diffraction patterns are the fingers prints of that material which are unique to every material.

Few XRD studies for graphene harnessed into cement matrix were found in previous literature. For example, the two broad peaks of GO at angles 23° and 43° corresponding to the planes (002) and (100) were observed in the XRD pattern shown in Fig.2.30a (Lin et al., 2016). In another study in which XRD pattern of pure graphite and graphene oxide were compared (Lv et al., 2013), are shown in Fig. 2.30b.
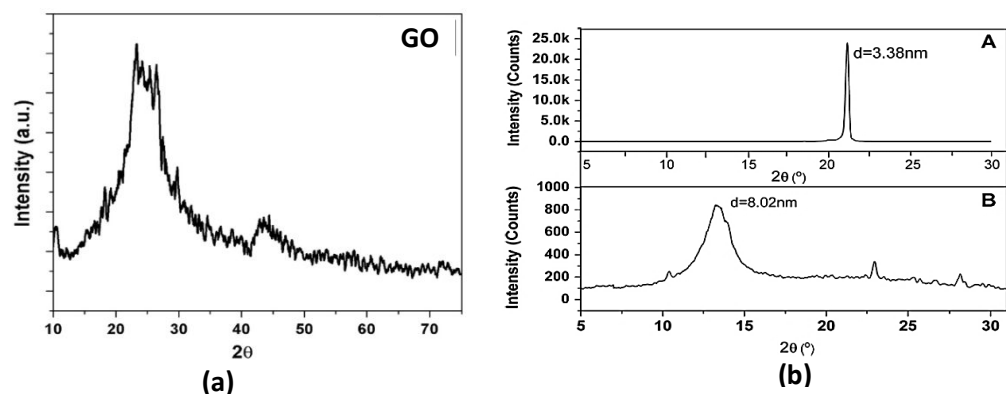
Figure 2.30 a) XRD pattern obtained through XDS 2000 powder diffractometer (Lin et al., 2016) **(b) XRD pattern of pure graphite (Gr) and GO** (Lv et al., 2013)

XRD pattern of pure graphite showed a sharp peak near diffraction angle of 20° with d= 3.38 nm whereas, in GO the main peak is shifted near diffraction angle 14° with expanded interlayer distance d=8.02 nm

2.8.3.5 *Chemical Structure Characterization using FTIR*

Fourier Transform Infrared (FTIR) spectroscopy is used to determine the chemical structure of materials and compounds. It is used for both qualitative and quantitative analysis to identify the functional groups attached to the structure of materials. The main structure of a compound is determined by infrared (IR) energy absorbed by its chemical bonds and at the definite wavelength (frequencies). Strength and amount of chemical bonds present in the compound can be mapped through the IR absorptions at specific spectral locations.

For example, FTIR on the GO nanosheets was performed and compared it with the spectrum obtained for graphite as shown in the Fig. 2.31a. The results from spectrum indicated that GO stitched with oxygen-containing groups attached to its surface exhibiting absorption peaks at 3350, 1730 cm-1 corresponding to -OH, -COOH and 1360, 1102, 1025 cm-1 corresponding to the presence of –O. Whereas, in graphite peaks at 1624 and 1661 cm-1 are related to C=C carbon double bond, and 1442 cm-1 is peak related to C-C carbon single bond (Lv et al., 2013).
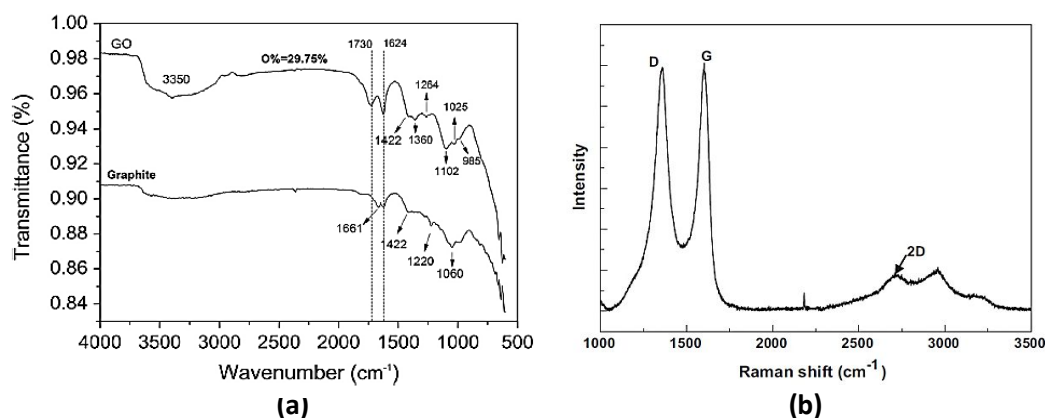
Figure 2.31 (a) FTIR spectrums of graphite and GO (Lv et al., 2013) **(b) RAMAN spectrum showing typical D,G and 2D bands of graphene** (Pu et al., 2012).

2.8.3.6 *Structural Disorder Characterization using RAMAN*

RAMAN spectroscopic (RS) technique is used to study vibrational, rotational, and usual low-frequency modes in a compound structure (Gardiner, 1989). In RS technique, the material sample is illuminated with a laser source from the visible, near infrared or near ultraviolet range. Laser with specific frequency excites the molecules of the material

sample and convert them into oscillating dipoles. These dipoles further emit light with three different frequencies out of which two provides useful information about energy shift. The energy shifts, also known as "Raman shift" provide information about the oscillating or vibrational modes in the molecules of a compound (Princeton Instruments, 2012).

Pu et al. used the RAMAN characterization technique for graphene structural disorder and observed the typical features such as G-band, D- band and 2D- band near 1580 cm^{-1}, 1350 cm^{-1} and 2700 cm^{-1} respectively as shown in the Figure 2.31b. They found ID/IG ratio higher than 1 for the graphene they use indicating a high defect in the graphene structure due to strong chemical oxidation and use of higher temperatures for thermal reductions (Pu et al., 2012).

2.8.4 Dispersion of Graphene

Processing graphene cement composite is not complex but requires minute detailing and extra care. Dispersion of graphene into the water and ultimately into cement matrix is a key issue. Graphene also agglomerates and makes clumps due to the presence of Van der Waal's forces, which is added to cement may cause poor microstructure by developing large pores. Compared to CNTs the dispersion of graphene is easy due to its 2D layered structure and can be done by using following routes or their combinations, mechanical dispersion, physical surface modification, chemical surface modification and plasma surface modification.

2.8.4.1 Mechanical Dispersion

Graphene can disperse uniformly into an aqueous solution or directly into cement matrix by using various mechanical techniques such as ultra-sonication, shear mixing, ball milling and stirring but ultrasonication method is widely for dispersion in water (S. Chuah et al., 2014). Graphene oxide is available in solution form synthesised from the oxidation of graphite and then exfoliated using ultrasonication water. Extra ultrasonication may harm the graphene structure resulting re-agglomerate in a cement matrix.

2.8.4.2 Physical Surface Modification

Various surfactants can be used to lower the surface energy of nanomaterials and facilitate dispersion into the water. Polycarboxylate (PC) water reducing agent can also facilitate the dispersion of nanomaterials Wang and Lv used PC 0.5% and 0.2% by wt.% of cement respectively in preparing the GO cement composites (Wang et al., 2015; Lv et al., 2014). It

has been observed that surfactants may produce incompatibility with cement and retarding cement hydration (S. Chuah et al., 2014)

2.8.4.3   Chemical Surface Modification

Functionalization is a term used for the chemical modification of nanomaterials attaching various chemical functional groups to their surface by covalent bonding. Nanomaterials are treated with harsh chemicals to attach functional groups such as –O (oxygen), –OH (hydroxyl), –COOH (carboxyl), etc. Functionalised groups render GO to hydrophilic nature make it possible to disperse uniformly into the water has attracted many researchers to use them without any surfactant as an alternative to CNTs into the cement matrix (Qiu et al., 2010). However, mechanical properties such as elastic modulus and tensile strength are degraded due to the grafting of various functional groups on the surface of nanomaterials treating with harsh chemicals (Garg and Sinnott, 1998).

2.8.4.4   Plasma Surface Modification

The synthesis of graphene using plasma exfoliation method is discussed above in the section 2.8.2 the same technique is also used for surface modification. Plasma modification is relatively new technique and produces bulk quantities of graphene functionalised with various chemical groups without damaging the structure. For the dispersion of plasma functionalised graphene requires simple sonication for a short period. GNPs used in the current work are also functionalised through plasma treatment is discussed in chapter 6.

2.8.5   Processing of Graphene Cement Composites

Uniform dispersion of graphene into water leads to prepare cement composite according to the mix design following some standard mixing procedure. In previous literature mostly ASTM C305, equivalent to EN 196-1, is quoted for mixing graphene with cement using standard Hobart mixer. However, Pan used a shear mixer with high speed of 12,000 rpm to effectively disperse graphene into cement matrix (Pan et al., 2012).

2.8.6   Moulding and Curing

Graphene cement nanocomposite is required to cast into moulds of desired shape and sizes and then compacted or vibrated to remove air voids. After removal of air voids samples are required to cure to accomplish hydration process under controlled moisture and temperature conditions up to certain time for which further testing and characterization is

desired. In the previous literature, most of the graphene cement composites were moulded and cured with controlled conditions as mentioned in Table 2.6.

2.8.7 Characterization of Cementitious Composite

Characterization techniques such as XRD, FTIR, SEM, EDX and UTM testing are very useful to investigate chemical composition, identification of crystalline hydration products, phase change, microstructure development, and strength enhancement of graphene cement composites. The impact of graphene oxide on cement hydration and Young's modulus was recently investigated by using XRD, FTIR and RAMAN for identification of crystalline hydration products and to reveal the phase composition of both references and GO cement nanocomposite samples. XRD pattern, FTIR and RAMAN spectrums of reference and GO samples are depicted in Fig. 2.40 and used to demonstrate the differences between two due to the effect of GO on producing hydration products. The effect of GO on the cement hydration can be seen clearly in the XRD pattern (Fig. 2.32a) with higher peak intensities of "p" and "e" in GO sample indicating the increased formation of portlandite (CH) and ettringite (AFt) respectively (Horszczaruk et al., 2015).
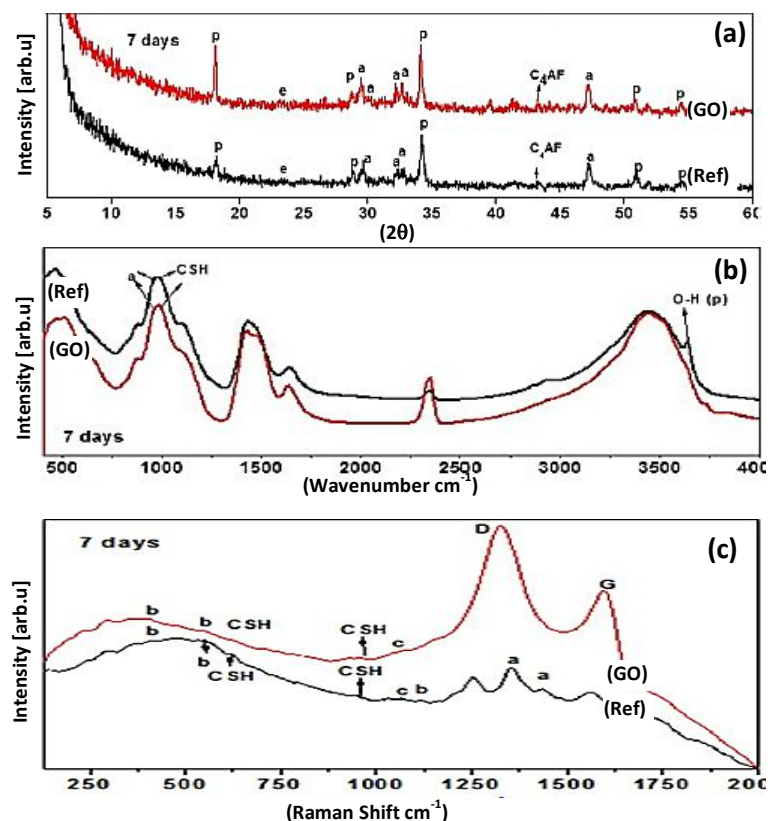
Figure 2.32 Characterization of GO cement nanocomposite at 7days (a) XRD pattern (b) FTIR spectra (c) Raman spectra (Horszczaruk et al., 2015)

FTIR spectrum of both reference and GO cement nanocomposite (Fig. 2.32b) couldn't demonstrate the hydration kinetics in favour of GO indicated by the lower intensity of bands than the reference samples. However, RAMAN spectra of GO nanocomposite (Fig. 2.32c) distinguished with a higher band of D and G indicating the increase formation of C-S-H.

Analytical studies of graphene cement composite using FTIR, XRD and especially RAMAN spectroscopy is very limited in the previous research. In a very recent study, the catalytic effect of GO on the hydration of cement composite was evaluated by using FTIR and XRD (Lin et al., 2016). In the XRD pattern, they observed the increased contents of CH, AFt and C-S-H with increased concentration of GO up to 2.5 wt.%. The enhanced peak intensity of FTIR spectra of GO cement composite as compared to control cement composite confirmed the acceleration in the hydration of cement due to the presence of GO.

In another study, a comparison was made between GO cement composite loaded with graphene flakes 1.5 wt.% and control sample. Apparently, there was no difference observed between XRD pattern of both, but upon a closer look, the growth of C-S-H in the nanocomposite sample was observed due to nucleation effect of GO flakes.

Element	Series	Unn. C (wt.%)	Norm. C (wt.%)	Atom. C (at.%)
Carbon	K series	0.61	0.59	1.03
Oxygen	K series	54.40	52.40	68.80
Magnesium	K series	0.24	0.23	0.20
Aluminium	K series	0.80	0.77	0.60
Silicon	K series	24.99	24.07	18.00
Sulfur	K series	0.44	0.43	0.28
Calcium	K series	20.99	20.21	10.60
Iron	K series	1.36	1.31	0.49

(a)

Element	Series	Unn. C (wt.%)	Norm. C (wt.%)	Atom. C (at.%)
Carbon	K series	0.00	0.00	0.00
Oxygen	K series	59.22	52.77	68.08
Magnesium	K series	0.55	0.49	0.41
Aluminium	K series	0.97	0.86	0.66
Silicon	K series	36.91	32.89	24.17
Sulfur	K series	1.06	0.94	0.61
Calcium	K series	12.36	11.02	5.67
Iron	K series	1.16	1.03	0.38

(b)

Figure 2.33 Chemical compositions of cement composites using EDAX (a) Sample with 1.5 wt.% of GO sheets (b) control sample without GO sheets (Babak et al., 2014).

Cement composite prepared with comparatively higher contents of GO flakes as compared to other studies (Table 2.5) higher contents of GO fail to depict any diffraction peak related to the presence of graphene (Babak et al., 2014). Therefore, they used the energy

dispersive analysis by X-rays (EDAX) as shown in the Fig.2.33 to identify the graphene contents in the cement composite.

In another study, Lv et al. also obtained the chemical element composition (Table. 2.5) by energy dispersive spectrometer (EDS) of different shape hydration crystals formed as a result of cement hydration process regulated by harnessing GO sheets. They used low contents of GO, ranging between 0.01 to 0.05 wt.% into the cement matrix (Lv et al., 2013). Their study extensively based on SEM and EDS to develop the relationship between mechanical properties and development of microstructure and they observed the distinct shape change of hydration crystals with increasing dosage of GO contents through SEM images as shown in Fig. 2.33. The shape of hydration crystals and their arrangement to develop microstructure determines the mechanical strength of cement composite. The formation of many rod-like (AFt), CH and AFm crystal structure were found stacked disorderly in the samples without having GO sheets.

Table 2.5 Chemical composition of GO- cement composite using EDS (Lv et al., 2013)

Cement hydration crystals Fig 2.34 (A-F)	Element percentage (%)								
	C	O	Ca	Al	Si	S	Mg	K	Fe
A: needle-like crystals	1.98	25.08	56.75	3.02	6.04	1.96	0.63	1.81	1.72
B: flower-like crystals	1.62	55.35	27.47	2.99	6.39	2.13	0.46	1.86	1.73
C: flower-like crystals	1.82	56.11	26.6	2.77	6.65	2.19	0.61	1.65	1.6
D: flower-like crystals	1.96	55.52	26.25	2.41	6.82	2.12	0.64	1.67	2.62
E: polyhedron crystals	1.62	57.57	23.71	2.44	6.64	2.23	0.59	1.41	1.79
F: polyhedron crystals	1.63	56.42	24.53	2.62	6.69	2.22	0.67	1.48	1.74
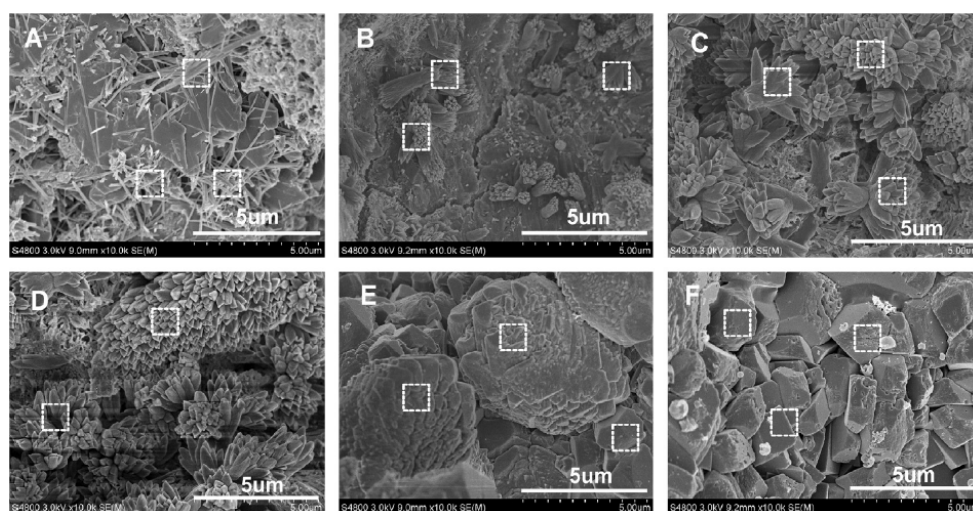
Figure 2.34 SEM images of GO-cement composite with different shape hydration crystals at 28 days (A) sample without GO (B) with GO contents 0.01% (C) 0.02% (D) 0.03% (E) 0.04% and (F) 0.05%. White squares in SEM images indicating areas studied for EDS (Lv et al., 2013)

With the increase contents of GO from 0.01% to 0.03%, they observed the formation of denser flower-like crystals structure (Fig.2.34 B-D) believed to be transformed from rod-like (AFt), plate-like (CH) and lamellar (AFm) cement hydration crystals. By further increasing the dosage of GO sheets by 0.04 and 0.05% into the cement matrix, the shape of cement hydration crystals transformed into irregular to regular polyhedral shapes loosely stacked as shown in the Fig. 2.34F. By analysing EDS, SEM and mechanical test data collectively they concluded that flower-like crystal structures are beneficial to increase flexural strength (toughness) while polyhedron crystals are responsible for enhancing the compressive strength of GO cement composite.

Contrary, in a preliminary study of GO as an additive for reinforcing cement matrix, Romani and Gronchi (Romani and Gronchi, 2015) affirmed through SEM images that flower-like and polyhedron crystal structures were not present in their samples of GO cement composite loaded with various contents of GO sheets. They used GO sheets with concentration 0.02%, 0.04% and 0.06% and up to 100 μm long while Lv et al. used Go sheets of nanoscale (72 to 430 nm). Despite functionalization and good dispersion of GO sheets into the cement matrix in their case, GO sheets few nanometre thick crumbled into the cement paste and lost the planetary shape. This might be due to the length of GO sheets (100 μm), not effective to increase the hydration of cement matrix by arranging and transforming the shape of hydration crystals rather they observed the large standard of deviations in the mechanical strength test. Further, even with the very good quality of SEM images (Fig. 2.35a), they were unable to scale out GO sheets interacting with cement hydration crystals. However, carbon contents in their EDS analysis verified the presence of GO sheets in the cement matrix, but from the elemental percentage data, they were not able to describe the contribution of GO sheets in the hydration of cement composite.

(a)   **(b)**
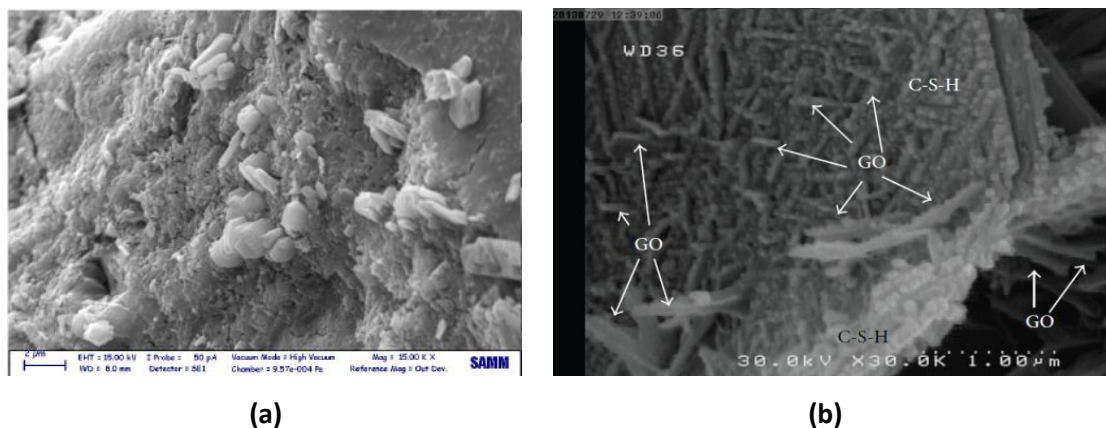
Figure 2.35 SEM micrographs cement composite after 28 days curing (a) with 0.02 wt.% GO (Romani and Gronchi, 2015) (b) with 1.5 wt% GO. (Babak et al., 2014)

On the other hand, SEM images were taken by (Babak et al., 2014) marked the profiles of GO sheets with arrows interacting with C-S-H (Fig. 2.35b). Perhaps comparatively large contents of 1.5 wt% GO in cement composite made it possible to characterize GO sheets in the complex microstructure in this case. Otherwise, it is very difficult and needs lots of efforts to indicate nanosized GO sheets interacting with cement hydration products in the SEM micrographs showing the morphology of hardened cement paste.

SEM micrographs can be used effectively to observe the morphology of cement composite and improvements in its microstructure due to the presence of GO sheets. Wang et al. studied the influence of the varied amount of GO sheets (0.01 % to 0.05%) on the microstructure and mechanical strength of cement composite. Through SEM micrographs they observed the increased amount of flower-like crystals and decreased a number of the harmful pores leading to develop more compact microstructure with increase contents of GO sheets into cement composites (Wang et al., 2015). Pores in cement matrix can develop poor microstructure. Poor sizes and their distribution within the microstructure can be analysed by MIP and nitrogen gas sorption/adsorption techniques.
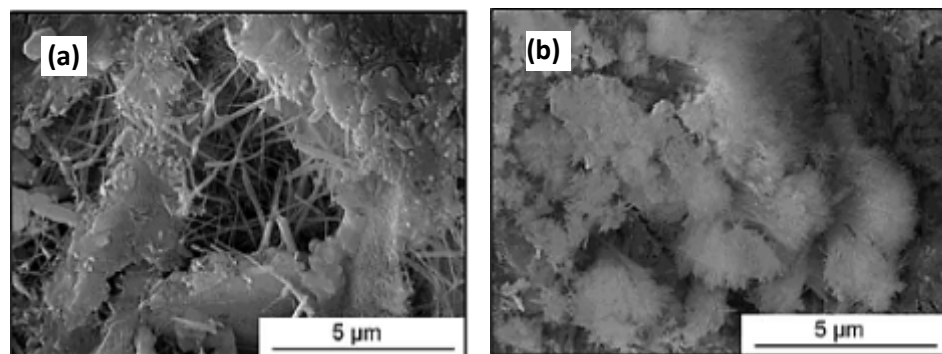
Figure 2.36 SEM micrographs showing effect of GO sheets in hardened cement composite at 28 days (a) control cement composite (b) cement composite loaded with 0.04 % of GO

2.8.8   Pore Structure Analysis

SEM micrographs of cement microstructure can be employed collectively with pore size distribution techniques such as nitrogen (N_2) absorption/adsorption and Mercury Intrusion Porosimetry (MIP) to evaluate a whole range of macropores to mesopores. Nitrogen absorption/adsorption technique can also be used to find out the surface area of porous materials having pores in the range of 2 to 100 nm (BS ISO 15901-2:2006). Pores with larger sizes cannot be analysed using this technique is one of the limitations. Also, it takes a long time approximately 24 hours to go through one sample.

However, MIP method is advantageous because it is quick and can measures the pores extended up to the surface of the sample. MIP method established on the basis of capillary law which governs the penetration of liquid into small pores. In case of liquids which are non-wetting and non-reacting like mercury to be intruded into cylindrical pores, this law can be expressed by equation (2.18) (Webb, 2001)

$$D = - (4\gamma\cos\theta)/P \qquad (2.18)$$

Where **D** is the pore diameter, **P** is the applied pressure (Pa), **γ** is the surface tension (Nm^{-1}) and **θ** is the contact angle in degrees.

It has been suggested that an increase in the degree of hydration in GO cement composites is also linked with the development of pore structure and corresponding surface area at the nanoscale (Pan et al., 2012). Pore size distribution and surface area of GO cement composite were analysed using nitrogen absorption/desorption test. They revealed that pore diameter increased at the nanoscale (1-80nm). Also, the formation of gel pores (1-10nm) present in C-S-H gel was increased in proportion. Therefore, GO influences the surface area and formation of pore structure in the cement composite.

An alternative approach of mercury intrusion porosimetry (MIP) was used to analyse pore size distribution and porosity of GO cement composite. The test data revealed that the formation of capillary pores reduced by 27.7% while pore volume increased by 109% while the total porosity the GO cement paste reduced by 13.5%. Therefore, microstructure refined by the incorporation of GO into the cement matrix with an accelerated degree of hydration (Gong et al., 2015).

As discussed above that the mechanical strength of cement composites is influenced by its microstructure, developed through growth and interlocking of hydration crystals and by filling the pores.

2.8.9 Mechanical Properties of GO Cement Composites

In recent years, GO due to its unique 2D structure, surface morphology and excellent mechanical properties stitched with oxygen-containing functional groups, favourable for dispersion in water, to its surface has remained a focal research nanomaterial to enhance mechanical properties of cement composites. GO in its different forms has been used by researchers into cement matrix with different methodologies, but with as little as 0.03 wt.% of cement. The profound effect of GO on mechanical properties has been observed in the

recent research. A detailed comparison in this regard, showing improvements and reasons for improvements in the mechanical properties has been tabulated in Table 2.6.

From the analysis of tabulated data (Table 2.6), it has been observed that strength in graphene cement composite instigated during the early duration of hydration (between 7 days) and mostly reported for improvements in flexural and compressive strength with few in tensile strength. Improvement in flexural strength is found higher as compared to compressive strength. Functionalised graphenes, other than oxygen-containing functional groups are such as carboxyl (–COOH) and amine (-NH$_2$), are rarely used in the previous research, while GO has been used extensively in solution form obtained commercially or synthesised by using harsh chemical methods. GO is mostly investigated into cement paste matrix with low wt.% up to 0.06% and with higher contents up to 2.5 wt.% in cement sand matrix. A higher value of flexural and compressive strengths has been observed in the graphene cement composites where PC admixture was added. In processing graphene cement composite, mixing is mostly done by using standard Hobart mixer with mixing time of 4 to 5 mins keeping the water-cement ratio between 0.3 and 0.4.

Nevertheless, the enhanced mechanical properties of GO cement composites in previous research are linked with the improved microstructure due to the increase of hydration rate, reduction of pores, nucleation effect and other factors but a limited study has been done on the investigation of crystal formation and microstructure development regulated by GO.

Table 2.6 Comparison of improved mechanical properties of graphene cement composites

Ref	Cement Matrix	GO %	w/c	Admixture/Additive	Methodology	% improvements (days)	Reasons for improvements
(Wang et al., 2015)	Paste	0.05	0.37	PC 0.5 wt. %	GO solution of 4mg/ml was used already dispersed into water. Standard mixing machine used to mould 40 x 40 x160 mm samples	Flexural strength 68.5 % (7D) 90.5 % (28D) Compressive strength 46.5 (7D) 40.4% (28D)	Nucleation Pore structure
(Wang et al., 2015)	Sand mortar	0.05	0.37	PC 3.5 gm + Antifoaming agent 2 gm	GO solution of 4mg/ml was used already dispersed into water. Standard mixing machine used to moulds 40 x 40 x160 mm^3 samples	Flexural strength 106.4 % (7D) 70.5 % (28D) Compressive strength 33% (7D) 24.4% (28D)	Nucleation Pore structure
(Pan et al., 2015)	Paste	0.05	0.5	No	Mixing is done using hand mixer at 2000 rpm for 5 min and prisms moulds of 15 x 15 x 80 mm^3 were used	Flexural strength 41-59% (7D) Compressive strength 15-33% (7D)	Nano reinforcement Production of C-S-H Pore structure
(Li et al., 2015)	Sand mortar	1.5 (GO) + 0.5 (SWCNTs)	0.3	PC 120 gm	GO (~ 3.85 mg/ml) was synthesised using modified hummers method using sonication for 48 hrs. 40 gm cement +12 gm of water +4 gm of PC +120 gm of sand was used to prepare composite+ SWCNT	Flexural strength 72.7 % (7D)	Increase of crystals
(Shang et al., 2015)	Paste	0.04%	0.4	No	GO (4mg/ml) was prepared using ultrasonication for 2 hrs. Cement composite was prepared using a high-speed mixer. With the combination of low and high speeds for approx. 5 mins.	Compressive strength 15.1% (28D)	Improve pore structure
(Gong et al., 2015a)	Paste	0.03%	0.5	No	GO (2mg/ml) was prepared using ultrasonication for 30mins. Cement composite was prepared using a high-speed mixer. With the combination of low and high speeds for approx. 4 mins.	Compressive strength 46.2 % (28D) Tensile strength 40% (28D)	Reduction of pores Enhances degree of hydration
(Lv et al., 2014)	Paste	0.04 %	0.3	PC 0.2%	Aqueous dispersion of GO was prepared using hummers method Cement composite was prepared using a high-speed mixer. Prism moulds 40 x 40 x160 mm^3 were used for samples. Cured at 20°c at 90% humidity.	Flexural strength 42.1% (28D) Compressive strength 34.5% (28D)	Formation of rod-like structure Improve pore structure Cross-linked crystals

Ref	Cement Matrix	GO %	w/c	Admixture/Additive	Methodology	% improvements (days)	Microstructural Changes
(Babak et al., 2014)	Sand mortar	1.5%	0.4	PC	Polycarboxylate (PC) was used for dispersion. GO was synthesised using hummers method and sonication is done for 40 mins. Samples were cured in water bath at 23 ± 2^oC	Tensile strength 48% (28D)	C-S-H growth Nucleation Bridging cracks
(Lv et al., 2013)	Sand mortar	0.03 %	0.36	PC 0.9 gm	The aqueous dispersion of GO was prepared by sonication of 1 hr. Cement composite was prepared using a high-speed mixer. Prism moulds 40 x 40 x160 mm^3 were used for samples. Cured at 20^oc at 95% humidity.	Flexural strength 60.5% (28D) Compressive strength 38.9% (28D) Tensile strength 78.6% (28D)	Formation of rod-like structure Regulate micro structure Cross linked crystals
(Alkhateb et al., 2013)	Paste	0.5 % GNPs	-	No	0.162 gm of GNPs are dissolved in 8.955 gm of water and sonicated for 3 mins. Simple mixing without mixer and samples moulds of 2 x 2 x 2 cm^3 were used.	Young modulus Pristine GNPs 6.5% (10D) Young modulus Func. GNPs 23.2%(10D) Shear modulus Pristine GNPs 20.9% (10D) Shear modulus Func. GNPs 37.3 % (10D)	Interfacial strength C-S-H Pore Structure

2.9 Conclusions

A comprehensive review of basic cement chemistry involved in the hydration process of crystals formation and the microstructure development regulated by nanomaterials into the cement matrix led to enhance its mechanical properties has been carried out in this chapter. The main aim was to review the processes, procedures, properties, performance and to understand the formation of the microstructure of cementitious nanocomposite developed recently with the aid of different forms of nano-materials. The purpose is to develop the simplest process, gauge performance measurement techniques and to explore the most suitable nanomaterials for the development of NGCC.

Through the review of previous research following gaps has been identified in the development of graphene cementitious composite:

2.9.1 Research Gaps

Although GO sheet synthesised through harsh chemicals and extensive sonication found to be in very thin layers of 5-6 nm range with more reactive sites, they may lose structural properties, crumble into cement matrix and re-agglomerate causing defects in the microstructure.

Graphene sheets functionalised with oxygen group were used extensively for better dispersion into the aqueous medium, but the effect of other functional groups such as carboxylic (-COOH) and amine ($-NH_2$) attached to the graphene planer structure were found very rarely in previous studies.

Most of the GO composites prepared along with Polycarboxylate (PC) suggested the remarkable enhancement in flexural and compressive strength, but limited numbers investigated the sole effect of graphene on the strength gain especially for the tensile strength.

Enhanced mechanical strength is mostly associated with improved microstructure due to nucleation effect, increased hydration rate, improved pore structure. However, the shape of nanomaterials and physical interaction with cement hydration crystals was not characterized at the nanoscale. Further, GCNFs with unique geometry were not used before. Therefore, there is a need to investigate the mechanism of hydration crystal formation regulated by geometry (2D or 1D) graphene nanomaterials and their ultimate

effect on the mechanical properties of cementitious composites with scientific rigour and in-depth knowledge of cement hydration chemistry.

2.9.2 Philosophy of NGCC Design and Development

From the extensive literature review and identified gaps, a simple process was developed for the development of NGCC. The whole process for the material research, design and development covers two main aspects: one covers the processing/synthesis, material composition and microstructure, whereas the other includes measurements/characterization, properties and raw materials. The philosophy and complete scope of NGCC design and development of this research are presented in Fig. 2.37 and 2.38 respectively.
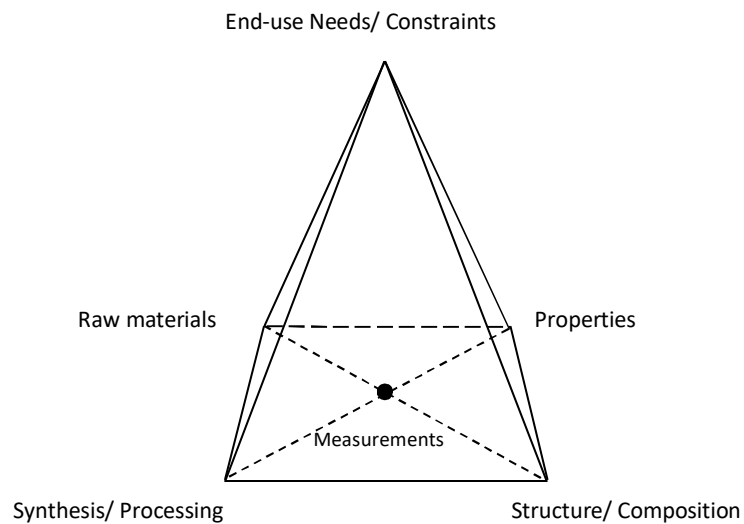
Figure 2.37 Philosophy of NGCC design and development

The whole concept of this approach is that the processing, microstructure and properties should be researched, investigated or designed according to the required performance of that material. In the main features of material research, development and design measurement or characterization is an essential part of material science and engineering.
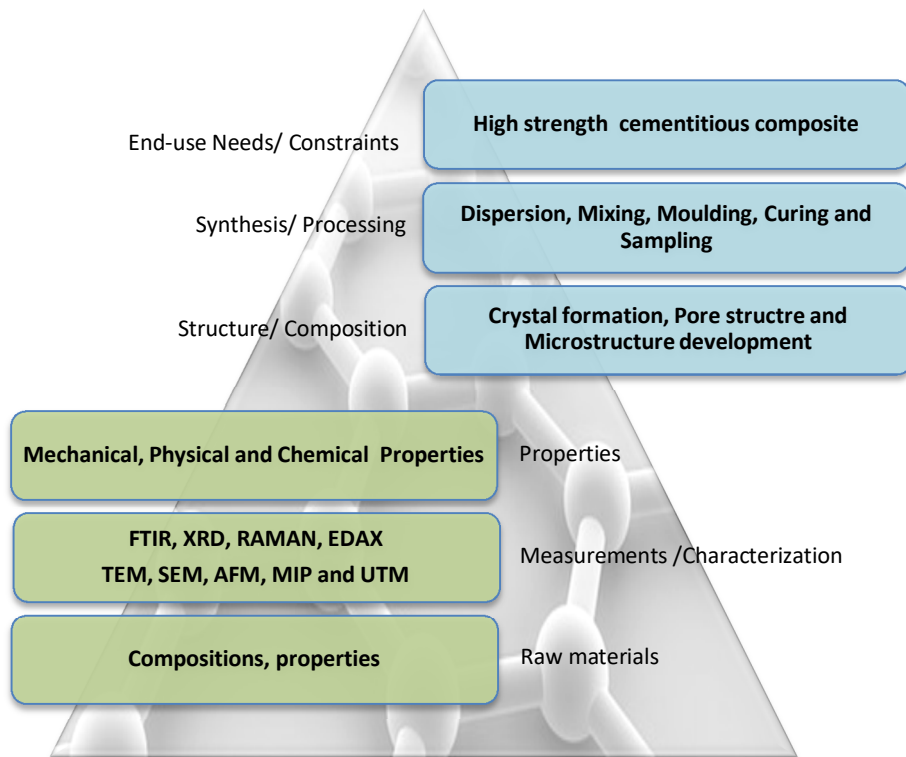
Figure 2.38 Complete scopes of design and development of Nano-graphene cementitious composite (NGCC)

CHAPTER 3 Materials, Methods and Characterization Techniques

3.1 Introduction

This chapter covers the materials and methods used for characterization and the development of three main types of nano-graphene cementitious composites (NGCC). These include NGCC-Dot, NGCC-Fnt and NGCC-CNF by activating pristine graphene nano platelets-Dot (G-Dot), functionalised graphene nanoplatelets (G-Fnt) and graphited carbon nanofibers (G-CNFs) respectively. Development of these NGCC mainly constitutes cement and graphene nanomaterial. The cement used in the development of NGCC was ordinary Portland cement (OPC) sourced from Cemex UK Ltd. Main constituents present in the cement defines its type and nomenclature. The microstructure developed in a cement matrix leads to affect its properties, primarily depends on the type and amount of constituents present in the cement. The other important constituent of NGCC is graphene available in many forms and sizes from single layer to 2-3 layers and in multilayers, with the thickness varying from 5 nm to 50nm depending on the number of layers. The nanographene used in the development of NGCC-Dot and NGCC-Fnt was graphene nanoplatelets (GNPs) sourced from Haydale UK Ltd. While for the development of NGCC-CNF graphited carbon nanofibers (G-CNFs), conical graphite sheets inserted in carbon nanofibers, were sourced from Sigma Aldrich UK Ltd.

For the processing of NGCC, standard procedures of mixing, moulding, curing and testing were adopted. Moulds of standard sizes and calibrated equipment with standard loading rates were used for mechanical testing. However, to prepare samples for tensile testing with standard dimensions, moulds and testing rig were designed and manufactured in the laboratory.

In the development of nano-cementitious composite, surface, structural and chemical characteristics of GNPs and G-CNFs are of vital importance because GNPs and G-CNF interact with cement particles at the nanoscale and pave the way towards distinctive microstructure development in the cement matrix. The nanomaterials used in this work were analysed structurally by using TEM, SEM, AFM, FTIR, RAMAN and XRD techniques for its lattice structure, morphology, thickness, size, functionality and chemical composition. While for the characterization of developed nano-graphene cement

composites, FTIR, XRD, SEM, EDX techniques were employed and strength test was carried out by using the Instron universal testing machine (UTM).

3.2 Research Materials

3.2.1 Cement

Ordinary Portland cement (OPC), compiled to BS EN 197-1 of type CEM I 52,5 N from Cemex UK, was used in the development of nano-graphene cement composites. Cement was kept in the airtight container to avoid contact with moisture at a standard temperature in the laboratory. The chemical composition and physical properties of the cement used are presented in Table 3.1and Table 3.2 respectively.

Table 3.1 Chemical Composition of OPC CEM I 52,5 N (Cement CEMEX UK, 2016)

Cement Type	Content[wt%]									
	Loss on ignition	SiO_2	Al_2O_3	Fe_2O_3	CaO	MgO	SO_3	Na_2O	K_2O	Cl-
CEM I 52,5 N	2.8	20.1	4.9	3.4	63.4	1.1	3.4	0.62	0.9	0.006

Table 3.2 Physical properties of OPC CEM I 52,5 N (Cement CEMEX UK, 2016)

Property	Value
Loss on ignition	2.80
Density (Kg/m^3)	3,140.00
Fineness (m^2/kg)	420.00
Initial setting time (mins)	125.00
Expansion (mm)	1.50
Mean particle size μm	15.01

Fig. 3.1 depicts the FT-IR of the anhydrated cement used in the development of NGCC. The carbonate peaks at 1421 cm^{-1}, 875 cm^{-1} and 714cm^{-1} are detected due to the reactions of the CO_2 present in the environment. The peak at 1145 cm^{-1} is related to the stretching of S-O indicating the presence of sulphate compound in the form of gypsum. The strong band at 928 cm-1 is associated with the asymmetric stretching of Si-O indicating the presence of C_3S and C_2S. Peak near 860 cm-1 is associated to Al-O indicating the presence of C3A. These spectrum bands are in good agreement with reported in previous studies (Omotoso, et al., 1998; Palomo et al., 1999 and Yousuf, et al., 1993).
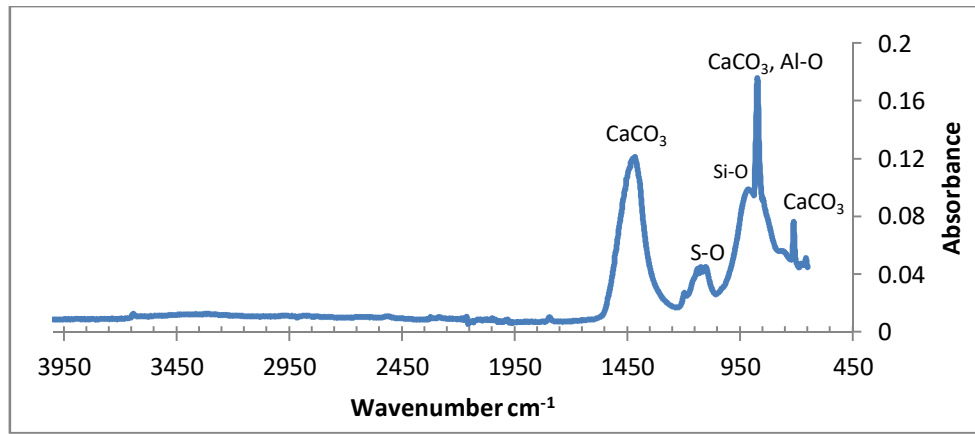
Figure 3.1 FT-IR spectrum of anhydrous cement powder

XRD pattern of anhydrous cement is shown in Fig. 3.2 confirming the presences of all major compounds. All the peaks related to alite (C3S), belite (C2S), C3A, C4AF, and gypsum are in good agreement with the typical Portland cement, and it can be seen that C3S is a very dominant phase and mostly overlapping other phases of C2S (Taylor, 1992).
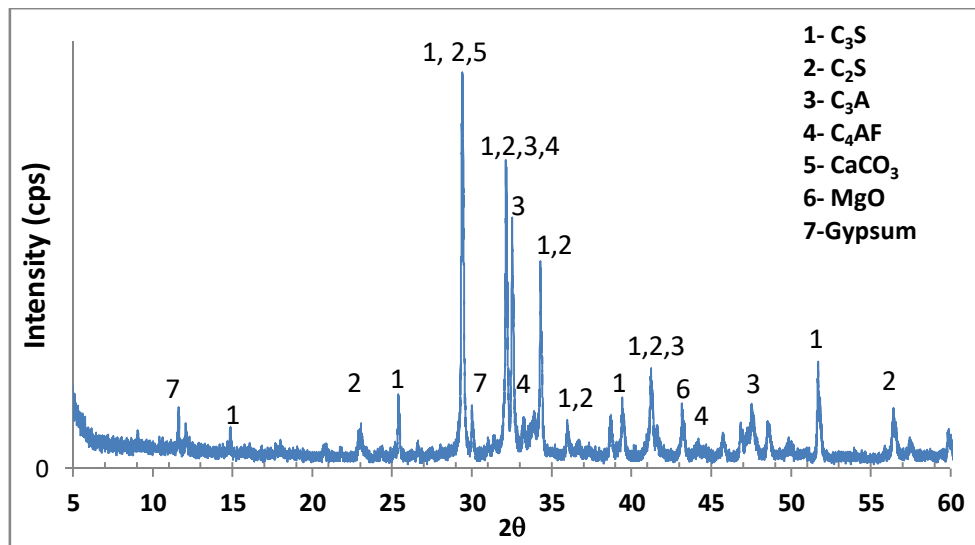
Figure 3.2 XRD pattern of anhydrous cement powder

3.2.2 Graphene Nano Platelets (GNPs) G-Dot

Graphene Nano Platelets (GNPs) trade name G-Dot was used in research for the development of nano-graphene cementitious composites (NGCC-Dot). These GNPs synthesised by using plasma exfoliated technique by Haydale UK instead of using conventional chemical exfoliation Hummers method. The G-Dot used in the development of NGCC were < 50 nanometers thick and have unique properties (Table 3.3) that make

them ideal supporting material for composite making. TEM and SEM images of G-Dot are shown in Fig. 3.3.
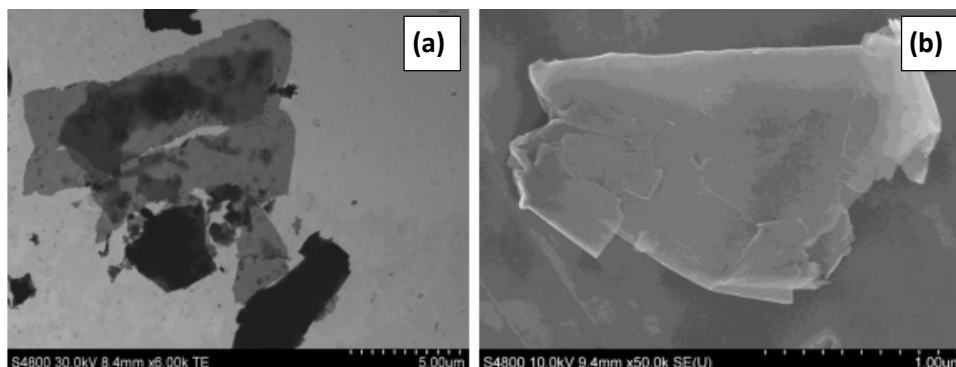
Figure 3.3 (a) TEM and (b) SEM images of G-Dot (Haydale Graphene industries plc, 2016)

Table 3.3 Typical Properties of GNPs (Haydale Graphene industries plc, 2016)

Data	Measurement	Method
Production Method		Plasma Exfoliation
Colour	Black/Gray	Visual
Bulk Density	215 Kg/m^3	EN ISO 60
True Density	2.2 g/cm^3	Theoretical
Specific Surface Area	~ 25m^2/g	BET Analysis
Typical GNP Planer Size	~5-10 μm	SEM
Typical GNP Thickness	< 50 nm	SEM

3.2.3   Functionalised Graphene Nano Platelets (GNPs) G-FNT

Three (3) types of surface modified functionalised GNPs were used to develop nano-graphene cementitious composite (NGCC-Fnt). These GNPs were functionalised through plasma exfoliation technique with functional groups -O_2, -COOH and -NH_2 attached to their surface. Functionalization of graphene using plasma technique enables to attach a desired chemical functional group on the graphene surface, providing greater ability to disperse in aqueous solution and compatibility between various matrices resulting in enhanced surface properties. The nanosize, high aspect ratio and presence of Van der Wall's forces could cause GNPs to agglomerate when mixed in aqueous solution. Therefore, the functionalisation via plasma technique can lead to disentanglement and exfoliation of these nano-sheets and stop de-agglomeration. Moreover, GNPs are

synthesised environmentally friendly and share no environmental waste. According to XPS analysis provided by the manufacturer, the atomic wt. % of oxygen in $G-O_2$ is ~7.0 %, in G-COOH is ~6% and in $G-NH_2$ is ~2.5%. Typical properties of these GNPs are also presented in Table 3.3 (Haydale Graphene industries plc, 2016).

3.2.4 Graphited Carbon Nano Fibres (G-CNF)

Graphitized carbon nanofibres were used to develop nano-graphene cementitious composite (NGCC- CNF). These graphitized carbon nanofibres with a diameter of 100 nm and length of 20-200 μm were composed of graphitic conical platelets encased by fibre structure (Fig. 3.4). These G-CNFs were produced by Pyrograf® Products Inc. using Floating Catalyst Vapour-Grown Method and were arranged from Sigma-Aldrich UK. These G-CNFs had very strong Van der Wall's forces and needed to disperse with the help of dispersing agent into the aqueous solution. Typical as received material properties of G-CNFs are presented in Table 3.4.
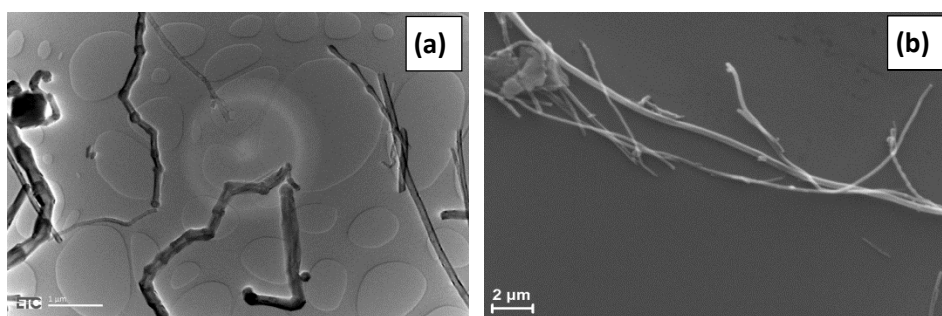
Figure 3.4 (a) TEM and (b) SEM images of G-CNF

Table 3.4 Typical Properties of G-CNF (Aldrich, 2016)

Data	Measurement
Bulk Density of Product (g/cm³)	0.008- 0.0561
*Nanofiber Density (including hollow core) (g/cm³)	**1.4 - 1.6**
Nanofiber Wall Density (g/cm³)	2.00 - 2.10
Catalyst (Iron) Content (ppm)	**< 100.00**
Outer Diameter, (nm)	125 - 150
Inner Diameter, (nm)	**50-70**
Specific Surface Area, m²/g	24.00
Average pore volume (cm³/g)	**0.075**
Average Pore Diameter(angstroms Å)	123.99

3.2.5 Isopropyl Alcohol

G-CNFs due to their structural and surface properties and presence of strong Van der Waal's forces in between them were found to be hydrophobic, and they were not well dispersed into water. Polyethyleneimine (PEI) or organic solvents (O.S) miscible in water such as isopropyl alcohol can be used to disperse G-CNF into water (Aldrich, 2016). Isopropyl alcohol was economical and easily available, therefore, used for the dispersion of the G-CNFs in water.

3.3 Equipment Used

For the processing, testing, and characterization of the NGCC, both standard and highly sophisticated state of the art equipment were used under controlled laboratory conditions. Compliance H&S were assured with risk and COSSH assessments and wearing proper PPE. The details of equipment used for testing and characterization are discussed in the subsequent sections.

Following standard equipment were used for the processing of NGCC

    a) Mortar mixer (ELE international, 5-litre nominal capacity, EN 196-1)

    b) Steel prismatic mould 40x40x160 mm^3 (ELE international, EN 196-1)

    c) Moulds for tensile test (95x45x25.4) mm^3 25.4 waist (Machine workshop made)

    d) Flexural and compression test frame (Controls, EN 196-1)

    e) Temperature-controlled curing tank

    f) Jolting machine (ELE international, EN 196-1)

    g) Digital scales (max.600g. and max.12kg.)

    h) Sensitive digital scale (accuracy 0.0000 gm)

    i) Sonication bath 42 Hz, 1000 watts (Fisher scientific)

    j) Specimen grinding machine

    k) PPE, Glassware, containers, spatulas, releasing oil, plastic sheets, etc.

Mortar Mixer   Test frame   Grinding Machine

Figure 3.5 Standard equipment used for the development of NGCC

3.4 Processing of Nano-graphene Cementitious Composite (NGCC)

Processing of all three main types of NGCC has almost followed the same procedure except their mixing ratios and synthesis of an aqueous solution with nanomaterials. The specific steps for the development of each nanocomposite are mentioned in the relevant chapters. In general following procedure was used for the processing of NGCC.

Cement from fresh supply was used and measured in accurate digital balance and kept in the airtight plastic bag until mixing time. GNPs and G-CNFs being very lightweight to be mixed in very small quantities were accurately measured in precise digital weighing scale with an accuracy of 0.0000 gm. The weighing scale was also protected from sides during weighing to avoid any interference with air and moisture. Water was accurately measured in standardised glass cylinder of 100 ml.

Table mounted mortar mixer machine unit with planetary mixing action and a steel bowl with a capacity of about 5 litres confirming to BS Standard EN 196-1 was used to mix the ingredients. Pre-weighted cement from airtight bags was poured into the bowl at the same time the graphene sonicated solution was added to start the mixing and hydration process. The standard steel mould has three horizontal chambers to mould three prismatic specimens 40 mm X 40 mm in cross-section and 160 mm in length was used. After the flexural test, the tested samples were re-trimmed for compression strength test.

Flexural / compression testing samples

Tensile testing samples
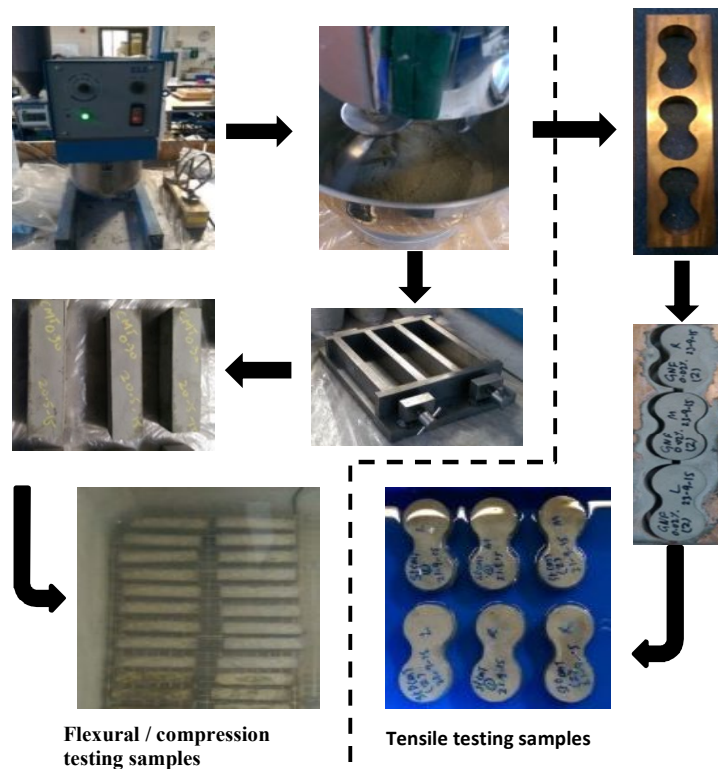
Figure 3.6 Composite processing for strength test

For tensile test, specimens were cast in 95mm x 45mm x 25.4 mm dumbbell shape moulds. These moulds with standard dimensions were designed and manufactured in the laboratory. Mixed cement composites were poured into the moulds in two equal layers; each layer was compacted on a jolting machine with 60 jolts. The surface of moulds was made smooth and cleans through a standard spreader with a straight metal edge. Soon after finishing the surface of samples a glass plate was placed to avoid any moisture loss. Samples were kept in a safe place at room temperature for 24 hours. After 24 hours samples were de-moulded with care and labelled. The samples were then cured in a water tank at 20°C under controlled conditions for 7, 14 and 28 days. The composite processing method is also briefly presented in Fig. 3.6.

Table 3.5 Mix proportions for the processing of NGCC

Sr. No	NGCC	Sample ID	Cement gm	G-NPs mg	*% BWOC	Water ml	Surfactant ml
1	**Control**	Control	1400	0	0	420	0
2		GDot 0.01	1400	140	0.010	420	0
3		GDot 0.02	1400	280	0.020	420	0
4	**NGCC-Dot**	GDot 0.03	1400	420	0.030	420	0
5		GDot 0.04	1400	560	0.040	420	0
6		GDot 0.05	1400	700	0.050	420	0
7		G-O$_2$	1400	560	0.040	420	0
8	**NGCC-Fnt**	G-NH$_2$	1400	560	0.040	420	0
9		G-COOH	1400	560	0.040	420	0
10		G-CNF 0.00	1400	0.0	0.000	370	50
11		G-CNF 0.005	1400	70	0.005	370	50
12	**NGCC-CNF**	G-CNF 0.01	1400	140	0.010	370	50
13		G-CNF 0.02	1400	280	0.020	370	50

*BWOC = by weight of cement

3.4.1   Development of NGCC-Dot

Total six sets of samples were cast, among them, control samples were in set 1 without G-Dot, and others were prepared with the varied amount (0.01% to 0.05%) of G-Dot into the cement matrix. The G-Dot was added into cementitious composites by weight of cement and keeping water/cement ratio 0.3 constant in all six sets as shown in mix proportion (Table 3.5). G-Dot used in the composite processing was mixed first with fresh tap water through a sonication process. Sonication was done with simple sonication bath with an ultrasound frequency of 42.0 Hz and ultrasonic power of 100 watts. After 30 minutes of

sonication, the G-Dot was well dispersed in the aqueous solution as shown in Fig. 3.7. The prepared aqueous solution of G-Dot was used for the development of NGCC-Dot by using process mentioned above (Fig. 3.7). Samples cast with G-Dot were tested for only flexural and compressive strength at the age of 7, 14 and 28 days.
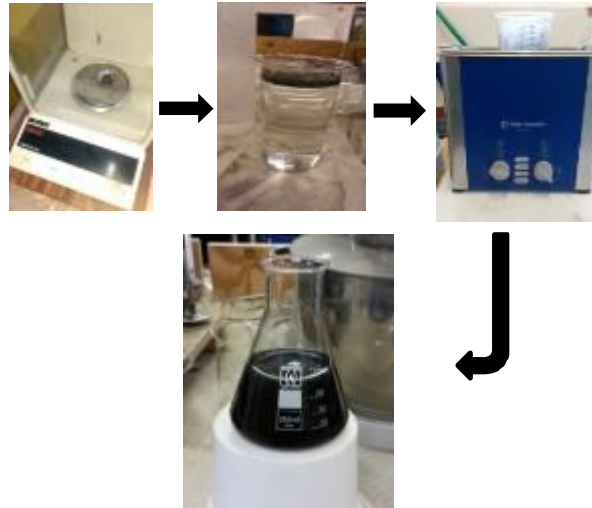
Figure 3.7 Synthesis of G-Dot Solution

3.4.2   Development of NGCC-Fnt

For the development of NGCC-Fnt, three types of G-Fnt stitched with oxygen (-O_2), amine (-NH_2) and carboxylic (-COOH) groups were used. These functionalised GNPs had almost physical properties similar to G-Dot but due to the attachment of functionalised groups to their surfaces they might have a better interface with an aqueous solution and hence have better dispersion capabilities. From the preliminary test data, it was observed that G-Fnt amount with 0.04 to 0.05% by weight of cement was also optimal in the strength test. Therefore, to compare the mechanical properties of G-Fnt with the G-Dot optimal dose of 0.04 % obtained from preceding work of NGCC-Dot was selected. Water cement ratios (w/c) of 0.3 and all other parameters of the test were kept the same as for the development of NGCC-Dot. The mix proportion for the development of NGCC-Fnt is presented in Table 3.5

3.4.3   Development of NGCC-CNF

For the development of NGCC-CNF again the same procedure was adopted used for the development of other two nano-composites, except the synthesis of aqueous solution and quantities to be mixed in the cement. The G-CNFs were first mixed in water through the same procedure as done for G-Dot and G-Fnt but they were not dispersed into the water

rather settle down after few minutes due to their hydrophobic nature (Fig. 3.8a). Through literature review, it was found that organic solvents (O.S) miscible in water such as isopropyl alcohol can be used for the dispersion of G-CNFs. Therefore, G-CNFs were first sonicated using the sonicated bath in a small quantity of isopropyl alcohol (Fig. 3.8b) and then added to required amount water and finally mix into the cement for the development of NGCC-CNF. To determine the optimum quantity of G-CNFs in the cement matrix, three mixes were used mentioned in Table 3.5.

a) Simple water   b) Isopropyl alcohol
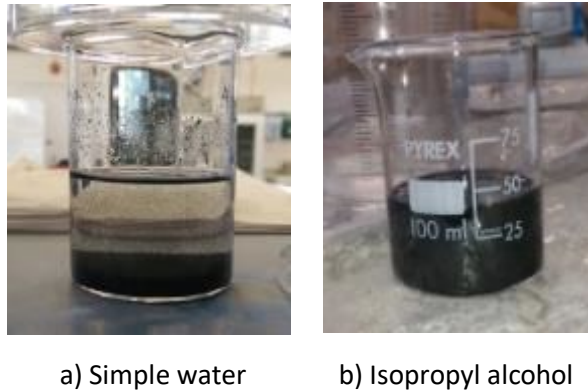
Figure 3.8 G-CNFs sonicated solution

3.5   Mechanical Strength Testing

Mechanical properties of the developed NGCC were investigated through mechanical strength tests. For mechanical strength tests, sample preparation, sample dimensions and rate of loading applied during the test were according to BS EN standards. Instron 150KN Universal Testing Machine was used for all the mechanical strength tests. Calculation of flexural strength of rectangular section under three points loading (Fig. 3.9) is done by using eq. 3.1 while compressive strength, tensile strength and modulus of elasticity are calculated using eq. 3.2, 3.3 and 3.4 respectively by the software blue hill version 3.6 linked with Instron.
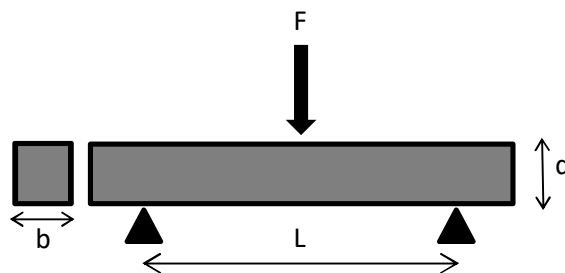
Figure 3.9 Three point loading applied to NGCC samples

$$\sigma_f = \frac{3FL}{2bd^2} , \tag{3.1}$$

$$\sigma_c = \frac{-F}{bd} , \tag{3.2}$$

$$\sigma_t = \frac{+F}{bd} , \tag{3.3}$$

$$E_{mod} = \frac{L^3 F}{4bd^3 \Delta} . \tag{3.4}$$

Where, "-F" is the compressive force at the fracture point (N); "+F" is the tensile force at the fracture point (N); "L" is the span length; "b" is the width; "d" is the thickness; and "Δ" is the maximum mid-span deflection.

3.5.1 Flexural Strength Testing

Flexural strength tests were performed according to BS EN 196-1:2005. For the flexural test, specimens were placed in standardised flexural test apparatus (Controls) (Fig. 3.10) the distance between the two supports was exactly 100 mm. Specimens were placed very carefully in the middle so that load may be applied exactly in the middle of the specimen to ensure maximum bending moment yield in the middle. A loading rate of 3.0 KN/min was applied.

3.5.2 Compressive Strength Testing

The specimens for the flexural test were re-trimmed for compression test (Fig. 3.10). A loading rate of 144 KN/min was applied in compression until the time of crushing. During the tests, parameters for all specimens were set into computer software linked to the UTM to calculate maximum load, flexural strength and flexural modulus for the analysis of the results.

3.5.3 Tensile Strength Testing

For the tensile strength test moulds and test frame attachment (Fig.3.10) was designed and manufactured for the shape similar to standards in the machine lab. Samples of dumbbell shape were used with dimensions 95mm in height, 45mm top and bottom width and 25.4 mm from the neck. A loading rate of 2.67 KN/min was applied during the test. Maximum load at failure was recorded to calculate the tensile strength at the fracture point of the sample.

Figure 3.10 Mechanical strength testing

3.6 Characterization Techniques Used

Several characterization techniques were used to investigate the material characteristics of nanomaterials used and the developed nanocomposite in the research. Basic working principle of these characterization techniques was discussed in chapter 2. A brief description of the process including the type of equipment, sample preparation and operating conditions during testing is discussed in the subsequent sections. While the detail discussion on results and characterization data of GNPs, GCNFs and NGCC are discussed in the relevant chapters.

3.6.1 TEM Analysis

Transmission electron microscopy (TEM) characterization technique was used to observe internal structure of the GNPs and GCNFs up to atomic scale to ascertain their structural and morphological properties. For this purpose, JEOL JEM-2100 F field emission electron microscope with Schottky electron gun was used for high resolution (HR) images of GNPs and GCNFs operated at electron source of accelerating voltage of 200 kV. To prepare the sample, GNPs and GCNFs were diluted in methanol and dispersed for 30 seconds through sonication. The sonicated GNPs and GCNFs were arranged, by a very small drop of sonicated solution, onto a holy carbon film having 300 mesh Cu grids supplied by Agar scientific. Prepared samples were placed very carefully into the sample holder and placed for short interval into Gatan solarus advance plasma system for surface cleaning and

71

removal of any hydrocarbon contamination. TEM characterisation process of GNPs and GCNFs is shown in Fig. 3.11.
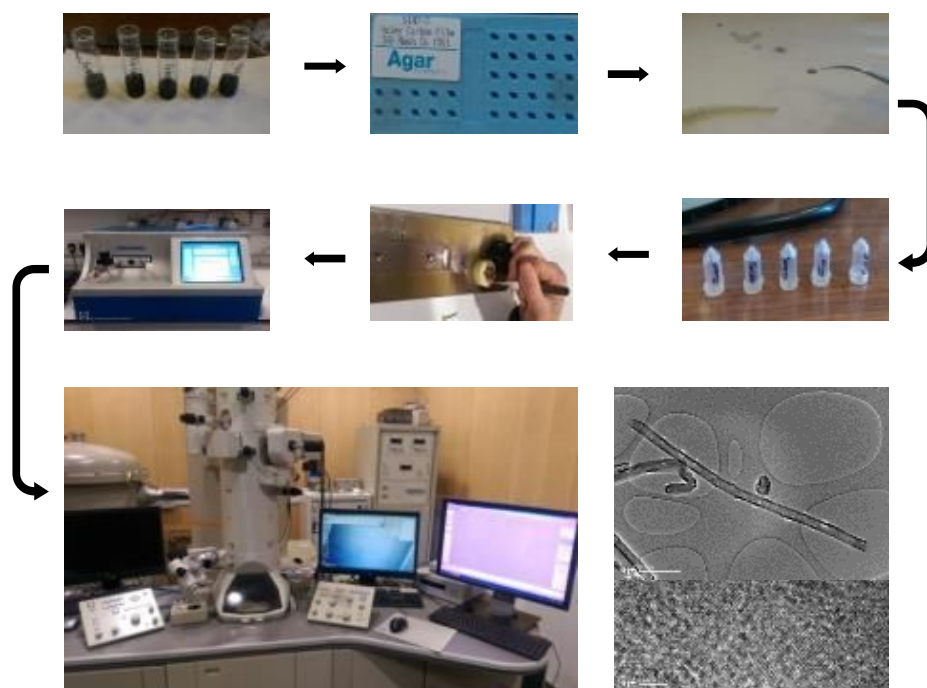
Figure 3.11 TEM characterization of GNPs and GCNFs using JEOL JEM-2100 F field emission electron microscope

3.6.2 AFM Analysis

The thickness and surface topography of nanomaterial used (GNPs and GCNFs) were also characterized to determine dispersion capabilities through atomic force microscope (AFM) Digital Instrument Nanoscope dimension 3100 with long lever tapping etched silicon probe (LTESP) attached to it. Dispersed GNPs and GCNFs through sonication were diluted in aqueous solution, and then a drop of solution was air dried on the glass slide for observation.
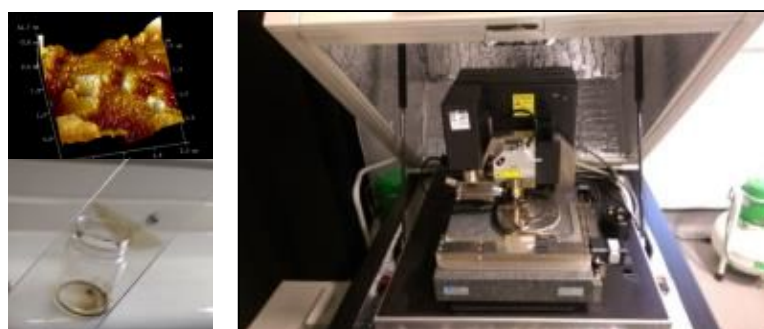
Figure 3.12 AFM characterization using Digital Instrument Nanoscope dimension 3100

The AFM was set at ambient temperature with the resonant frequency of tip 363-432 KHz. AFM image files were analysed using software NanoScope Analysis version 1.5 to acquire

3D and profile images of the material surface. Sample preparation for AFM is simple to take a short time as compared to TEM. Simple process to acquire AFM images is illustrated in Fig. 3.12.

3.6.3 SEM and EDAX Analysis

To characterize the shape, lateral dimensions and chemical composition of the GNPs and GCNFs used in the development of nanocomposites SEM image technique was adopted. This technique was also used for the high-resolution images and chemical analysis of cement hydration crystals formed during complex hydration process with resolution up to 1nm and large depth of focus. SEM images were acquired using (FEG-SEM) Zeiss Supra 35VP an ultra-high performance FEG-SEM, with both high-vacuum and variable operating pressure (VP) capability. VP mode enables imaging and analysis of specimens in their natural state, without distorting due to charge on the surface. To acquire the SEM images secondary electron (SE) detector was used. An analytical technique for material composition and phase detection was done through energy-dispersive x-ray analysis (EDAX). It was made sure that SEM was operated at 20.0 KEV to obtain EDS spectrum for point and selected area analysis using TEAM software.
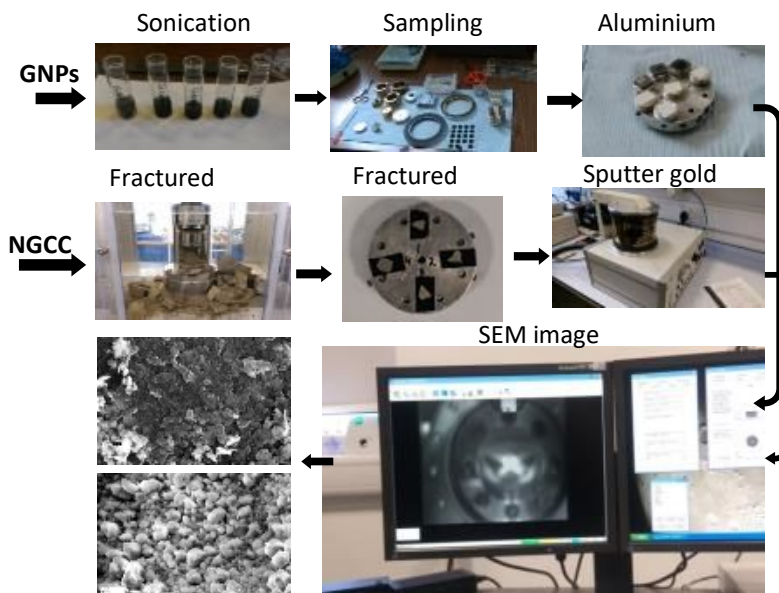
Figure 3.13 SEM Characterization process using FEG-SEM Zeiss Supra 35VP

To prepare samples a drop from diluted GNPs and the GCNFs solution was placed on monocrystalline silicon (5.5 mm x 5.5 mm x 0.45 mm) and dried in vacuum oven at 50°C for 2 hrs. Various sizes of GNPs were observed from 0.3 to 10 μm, mostly in the range of

5-6 μm. The samples from the fractured surface of NGCC were fixed on a small aluminium stub and coated with a thin layer (1nm) of gold through sputter coated technique. Samples with high surface charges were examined using VP mode. Characterisation process for both nanomaterials and nanocomposite is shown in Fig.3.13

3.6.4 FTIR Analysis

Fourier Transform Infrared (FTIR) spectroscopy technique was used to reveal the functional groups attached to the structure of GNPs, GCNFs and nanocomposite developed in the research work. FTIR spectrums were acquired using Perkin Elmer Spectrum One Fourier transform infrared spectrometer (Fig. 3.14a). Attenuated Total Reflection (ATR) technique was used, and all spectrums were collected in the range from wavenumber 4000 to 650 cm^{-1} at a resolution of 4 cm^{-1} with 25 accumulations. A small quantity of material in a thin layer subjected to infrared light was placed in between the lens and ATR crystal. A persistent pressure was applied to all the samples to acquire precise spectrums by twisting bridge screw up to specific rotation.

GNPs and GCNFs in the form of powder were used to obtain FTIR spectrums while for cementitious nanocomposite, bits of fractured samples obtained from strength test were first ground into fine powder and then sieved through 250μ size sieve (Fig. 3.14 d) for FTIR analysis. The main drawback of FTIR technique is that water presents in the samples exhibit strong absorption, and may overlap the spectrums of other compounds in the same range with low absorbance values.
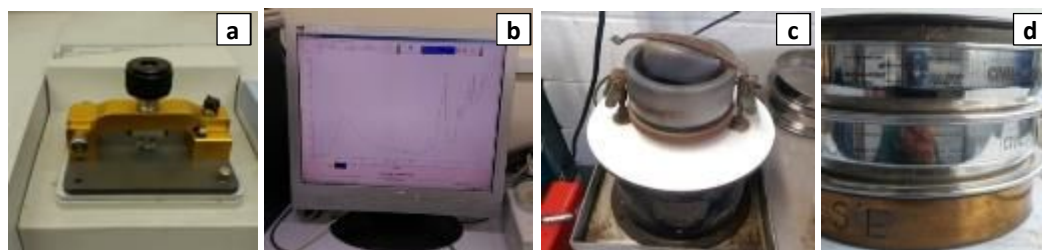
Figure 3.14 FTIR characterization process using Perkin Elmer Spectrum One FTIR spectrometer a) diamond ATR crystal b) linked software c) grinder d) set of sieves

3.6.5 RAMAN Spectroscopy Analysis

Raman spectroscopy (RS) may be used as a complementary characterization technique to FTIR, because the bands which are intense in FTIR, like water band, are often weak in RS and vice versa. This feature of RS is very useful to analyse the cementitious compounds especially at early ages of hydration. Moreover, to quantify the structural defects in GNPs and GCNF, I_D/I_G ratio can be obtained from Raman spectrums.

RS spectrums were obtained by Renishaw Invia micro-Raman spectrometer attached with charged couple device (CCD) detector. Nanomaterial and nanocomposite samples were illuminated by a 514 nm laser source. Scan range was set between values 300 to 2000 cm^{-1}. Spectrums of all the samples were taken with a 50x magnification with the exposure time of 10s. Calibration of the instrument was done by using 520.5 cm^{-1} line of the silicon wafer. WiRE 3.4 software was used for data acquisitions. A base correction was carried out after each spectrum for clear identification of peaks (Fig. 3.15)
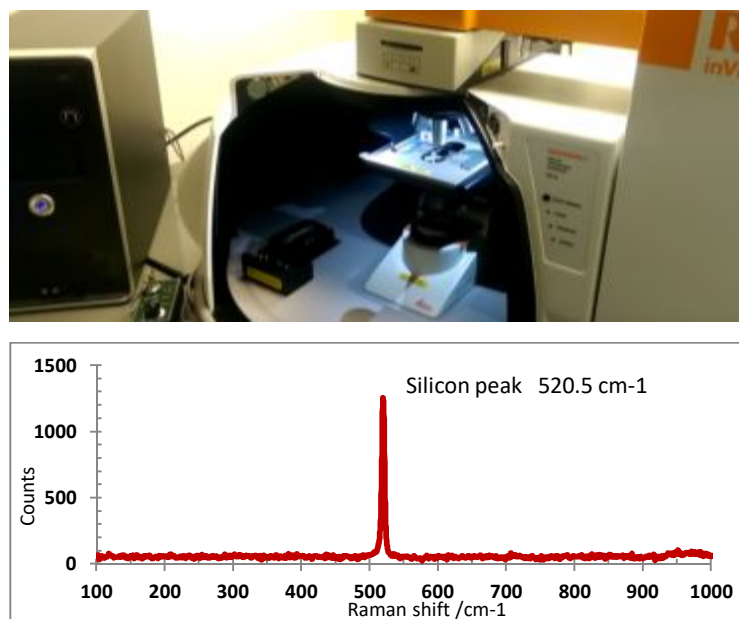
Figure 3.15 RAMAN characterization Renishaw Invia micro-Raman spectrometer

3.6.6 XRD Analysis

X-ray diffraction (XRD) characterization technique was used to identify phase composition, crystallinity and chemical composition materials under investigation. XRD patterns were collected by using Bruker D8 Advance diffractometer fitted with a Lynxeye XE high-resolution energy dispersive 1-D detector.
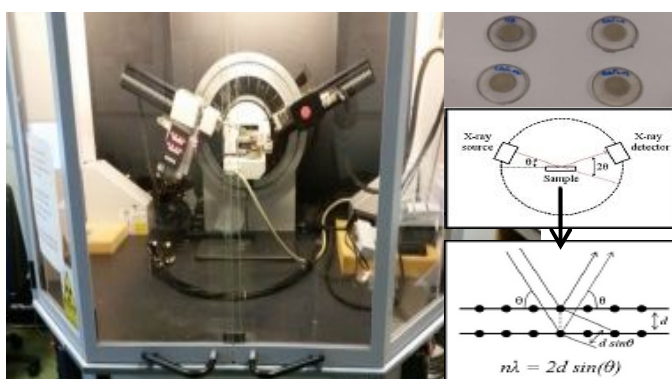
Figure 3.16 XRD characterization using Bruker D8 Advance diffractometer

75

Monochromatic CuK radiation (copper tube 40 kV/40 mA) with 0.154 nm wavelengths was exposed to samples under analysis. The analysis of samples was done by using DIFFRAC.SUITE software. The scanning range between 5 and 80° 2θ was used (Fig. 3.16)

3.6.7 Gas Adsorption Test

Pore size and surface area analysis using (BET) method of control cement composite and NGCC were carried out using nitrogen adsorption analysis at a bath temperature of 77.350 K using micromeritics Tristar II series surface area porosity analyser. Samples were degassed at 250°C for 24 hours. The weight of sample used for analysis was measured after degassing procedure. Samples were kept in a tube attached to the analysis part of the instrument. Adsorption and desorption isotherms for both samples were collected by placing the sample in a tube attached to the analysis port of the instrument. Before the measurement of adsorption isotherm, cold free space and warm free space of the sample tube were volumetrically measured 21.0484 cm3 and 8.0630 cm^3 respectively using helium. Helium was discharged, and sample tube was placed in cryogenic liquid nitrogen of known volume of N_2 at series of controlled pressures. Maximum relative pressure with a value of 0.999 was used to measure 21 adsorptions and 17 desorption at equilibrium.
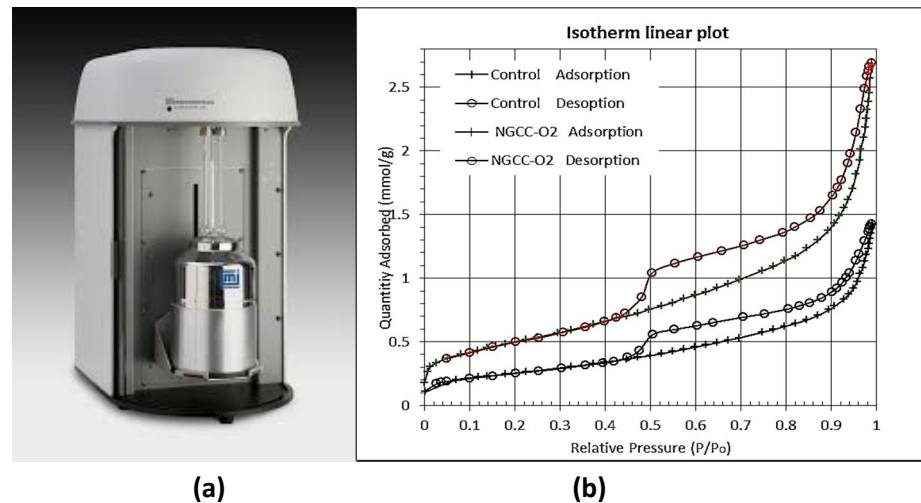
Figure 3.17(a) micromeritics Tristar II series surface area porosity analyser (b) Typical adsorption isotherm for cement composite

3.6.8 Mercury Intrusion Porosimetry (MIP) Test

Porosity, pore volume and pore sizes distribution were measured using MIP technique employing a Micromeritics Autopore V mercury porosimeter over a pressure range of 0.10 – 61,000 Psia to measure the total intrusion volume. The surface tension of 0.48 Nm^{-1}, temperature of 18.46^{o}C and a contact angle of 140° was used for mercury. Software package micro active Autopore V 9600 V 1.03 was used to calculate total pore volume by

calculating the difference of intrusion volume at a maximum pressure of intrusion volume at zero pressure. The bulk volume of samples was presumably calculated by subtracting total penetrometer volume from intrusion volume at zero pressure.

(a)   **(b)**
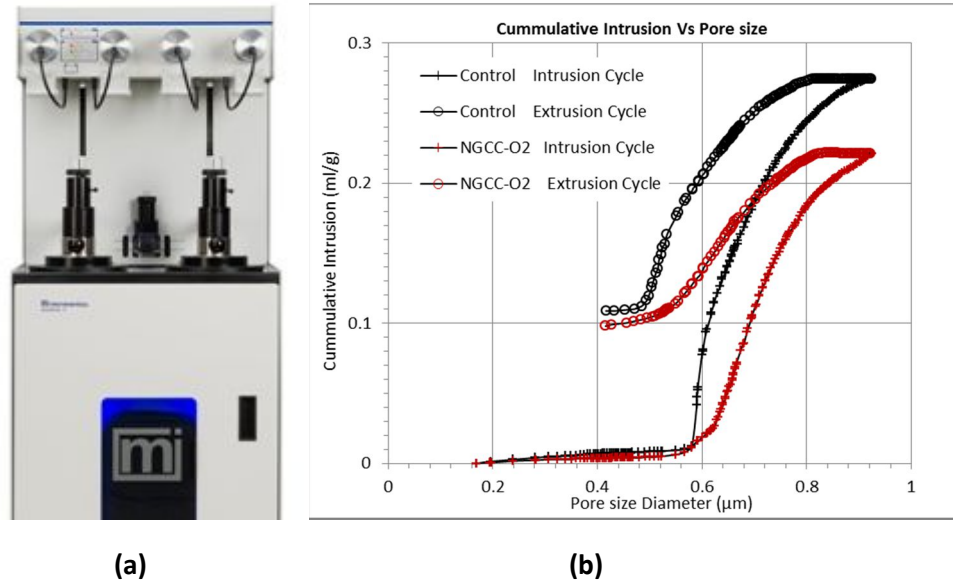
Figure 3.18 (a) Micromeritics Autopore V mercury porosimeter (b) typical cumulative intrusion (%) of mercury in cement composite

3.7 Conclusions

In this chapter, materials, methods and equipment for characterization in the development of NGCC were discussed. General procedures for the dispersion of nanomaterial and process for development of NGCC were also discussed. However, specific method and procedure for the development of a particular NGCC are discussed in the relevant chapters. Nanomaterials used in this research work were characterized for lattice structure, morphology, thickness, size, functionality and chemical composition by using TEM, SEM, AFM, FTIR, RAMAN and XRD techniques and detailed in chapter 4. Whereas, for the characterization of the developed NGCC with various graphene nanomaterials (G-Dot, G-Fnt and G-CNFs), FTIR, XRD, SEM, EDAX techniques were employed and strength test was carried out by using Instron universal testing machine through controlled software programme. The results and characterization data are correlated and discussed in relevant chapters.

CHAPTER 4   Material Genome of GNPs and GCNFs

4.1 Introduction

This chapter presents the structural and surface characteristic of graphited nanomaterial used in this research. HR-TEM and SEM images were obtained to measure the structural and morphological features of the GNPs and GCNFs. SEM and AFM characterization were employed to determine dimensional features of GNPs. Surface functionality, chemical composition, crystal structure and structural disorder of graphene nanomaterial were determined by FTIR, XRD and Raman spectroscopy. The characteristics of GNPs were correlated with the findings in the previous literature. The structural models of pristine and functionalised GNPs were also proposed. Due to hydrophobic nature of GCNFs, few properties could not be measured.

4.2 Material Genome of GNPs

As aforementioned in the previous chapters, pristine Graphene Nano Platelets (GNPs), trade name G-Dot, functionalised with different chemical groups (G-O_2, G-NH_2 and G-COOH) attached to their surface and GCNFs with graphited conical nanoplatelets inserted into fibre skeleton were used for the development of nanographene cementitious composites. Various material characterization techniques were employed to determine the structural and surface properties of both GNPs and GCNFs and explained in subsequent sections.

4.2.1 Structural and Morphological Analysis of GNPs

Graphene is a monoatomic layer of carbon atoms in the form of hexagonal lattice resembling with a honeycomb structure. To identify the lattice structure and morphology, GNPs were characterized using TEM equipment by using methodology mentioned earlier in chapter 3. HR-TEM micrographs of G-Dot and G-Fnt (G-O_2, G-NH_2 and G-COOH) were also analysed for atomic structure, surface morphology and functional groups attached at their edges.

Fig. 4.1 depicts the high resolution (HR) TEM image, Fast Fourier Transformation (FFT) and intensity profile of the selected area on the surface of the single layer of G-Dot. In Fig.4.1a dark graphitic structure on the edges of G-Dot and well defined condensed honeycombed lattice structure in the middle can be observed. This suggests the impurities of graphene in the G-Dot nanoplatelets. Further analysing the atomic structure and spacing

between lattice planes of the FFT (Fig.4.1c) and intensity profile (Fig 4.1d) of G-Dot were taken. The intensity profile of G-Dot sheets was taken along the arrow line shown in Fig 4.1b which represents the spacing between the carbon and carbon atoms. The spacing between symmetrical pairs of carbon atoms (hexagon width) was measured ~ 0.178 nm whereas the distance between atomic layers found to be 0.335 nm which is in accordance with the pure graphitic structure (Delhaes, 2000). HR-TEM micrographs of G-Dot (Fig.4.1b) further revealed the unfolded wrinkled free morphology due to the compact packing of carbon atoms into honeycombed crystal plane. The condensed hexagonal honeycombed lattice structure suggests that G-Dot nanoplatelets are structurally integrated, and wrinkle-free morphology could help them not to crumble into cement matrix. However, the graphitic impurities found at the edges may hinder their dispersion into the cement matrix and may cause agglomeration into lumps.
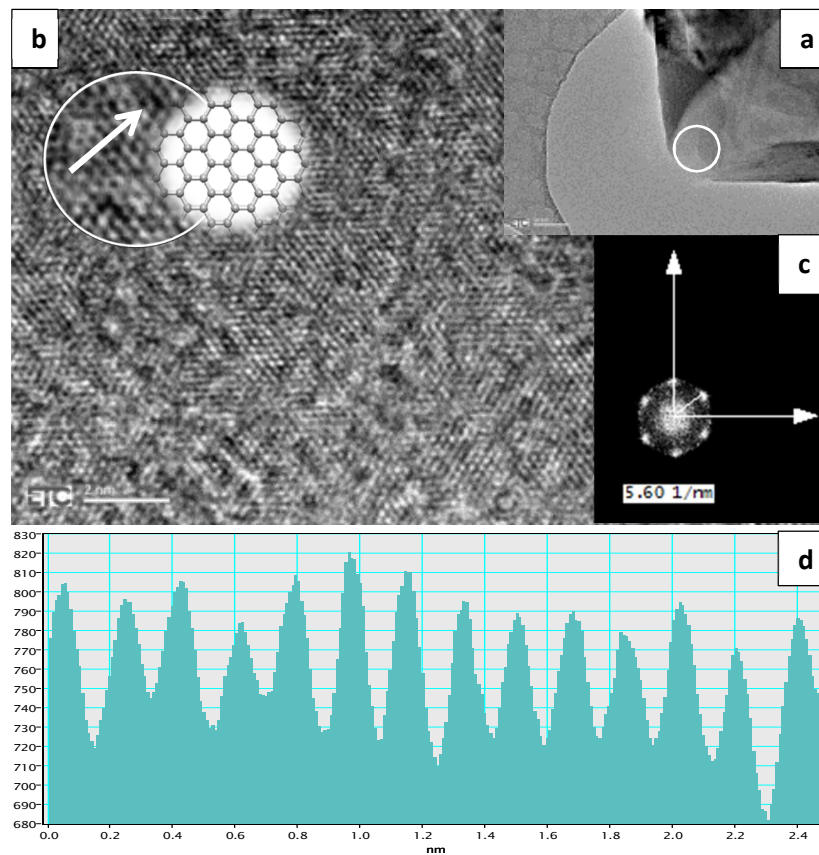
Figure 4.1 Structural analysis of G-Dot (a) single layer of G-Dot on Cu grid showing graphitic structure at the edges (b) HR-TEM of the area spotted with white circle in fig 4.1a (c) FFT for the analysis of spacing between lattice planes and (d) intensity profile taken along the arrow shown in top left of Fig.4.1b

In comparison, the smooth and defect-free surface at the edges of G-O_2 nanoplatelets can be seen in the HR-TEM micrographs (Fig.4.2a). Fig.4.2b depicts the surface morphology

and honey combe lattice structure of G-O_2 and G-NH_2 nanoplatelets. The octagonal type features (highlighted with makeup marker shapes), especially at the edges, indicate the attachment of O_2 –functional group on its surface. The FFT (Fig.4.2c) of the circled area in Fig 4.2a and the intensity profile (Fig.4.3d) taken for G-O_2 along the arrow shown on in the inset of Fig.4.2b were taken. The distance between the symmetrical pair of carbon atoms was observed 0.200 nm with an interlayer spacing of 0.335 nm. The stitching of O_2 functional group on the surface of nanoplatelets may help them disperse efficiently into an aqueous solution and provide more reactive sites to interact with the cement hydration products. Moreover, G-O_2 nanoplatelets can be observed staked over in layers (Fig. 4.2a) with unfolded and wrinkled free morphology.
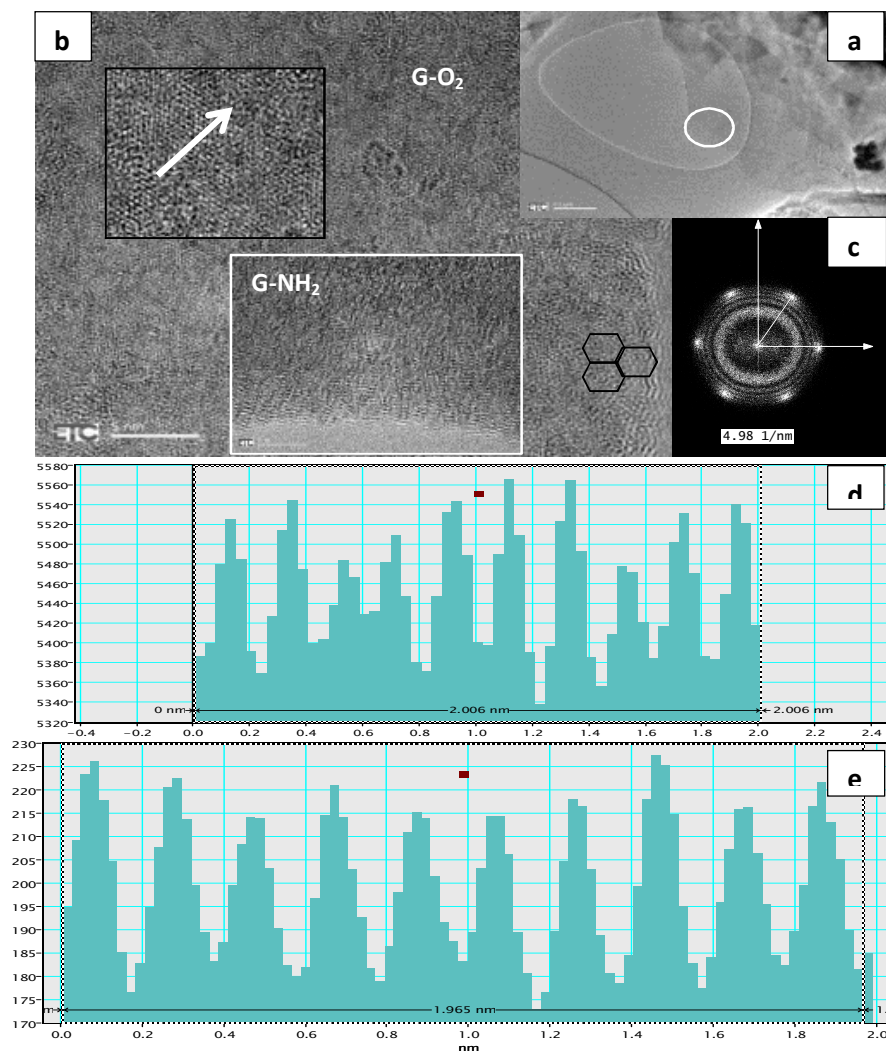
Figure 4.2 Structural analysis of G-O_2 and G-NH_2 (a) multilayers of G-O_2 on Cu grid (b) HR-TEM of G-O_2 (upper inset) and of G-NH_2 structure (lower inset) (c) FFT of G-O_2(d) intensity profile of G-O_2 taken along arrow in the top left inset of Fig 4.2 b and (e) intensity profile of G-NH_2

The atomic structure and morphology of G-NH$_2$ nanoplatelets (Fig. 4.2b lower inset) were found similar to the G-O$_2$ nanoplatelets. Smooth edges and NH$_2$ functional group attached to its surface and through intensity profile the spacing of 0.197 nm was observed between symmetrical carbon atoms (Fig4.2e). This suggests that structural and morphological properties of G-O$_2$ and G-NH$_2$ nanoplatelets are similar to each other.
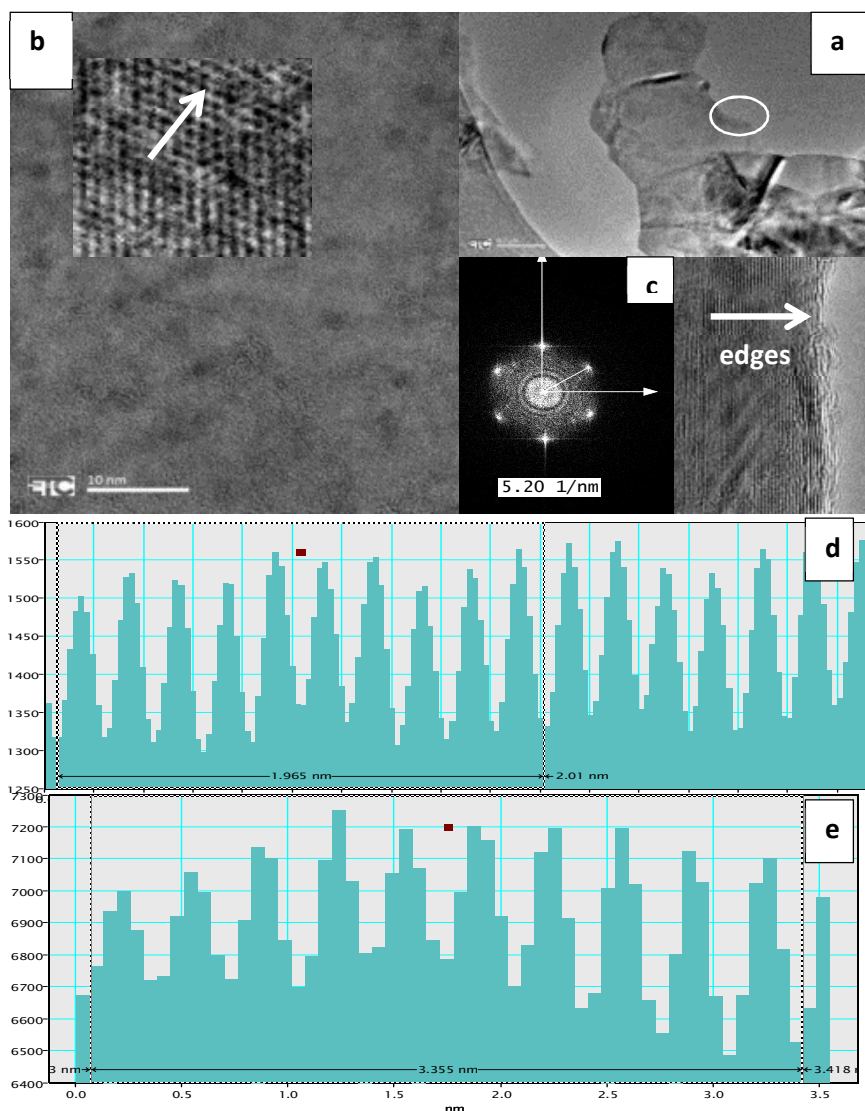
Figure 4.3 HR-TEM image of G-COOH (a) single layered G-COOH on Cu grid (b)HR TEM micrograph of spotted area (c) FFT of G-COOH for analysis of spacing between lattice planes (d) Intensity profile of area indicated by arrow in top left inset (e) Intensity profile of edges indicated by arrow in bottom right inset

Fig. 4.3 depicts the HR-TEM micrographs and structural analysis of G-COOH nanoplatelets. Through the intensity profile is taken along the line indicated by an arrow in the top left inset of Fig. 4.3b, the spacing between the symmetrical pair of carbon atoms was measured 0.197 nm. A well-defined hexagonal arrangement of carbon atoms similar to

81

honeycombed lattice structure can be seen in the high-resolution image (top left inset Fig 4.3b). However, few wrinkles and folded layers at the edges were observed in the morphology of G-COOH nanoplatelets.

The intensity profile taken at the edges, along the line indicated by an arrow revealed the inter-planner spacing of 0.355nm. This suggests the structure and morphology of G-COOH matching with G-Dot. However, no impurities were observed in case of G-COOH nanoplatelets. The condensed crystal structure and more reactive sites at the surface may provide nucleation effect in the cement hydration.

4.2.2 Dimensional and Dispersion Analysis of GNPs

For lateral size and the shape analysis of both types of GNPs, SEM characterization was adopted. SEM micrographs are shown in Fig. 4.4a and Fig.4.4b revealed that both types of GNPs have irregular rectangular to triangular shapes loosely stacked over platelets in dry form and have a lateral dimension between 0.3 and 10 microns but mostly fall in the range of 5-6 microns. To observe the instant dispersion of functionalised nanoplatelets into the aqueous medium, $G-O_2$ nanoplatelets were dispersed in water manually with a very little effort. It was observed under the SEM that the layers $G-O_2$ nanoplatelets expanded instantly and slipped over each other, forming a skeleton of aligned graphene platelets by generating gaps at nanoscale perhaps holding water molecules between them. This dispersion pattern of $G-O_2$ could be beneficial for attracting cement particles and hydrate effectively in the presence of water between the gaps.
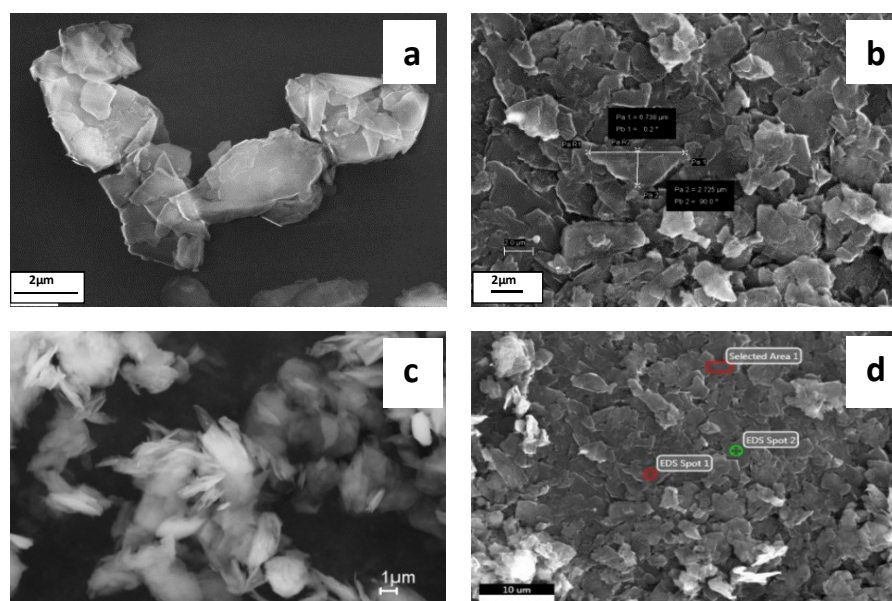
Figure 4.4 SEM micrographs of GNPs (a) high resolution micrograph of $G-O_2$ in dry form (b) G-Dot sheets spread on carbon tape (c) $G-O_2$ dispersed manually in water and (d) EDS analysis of $G-O_2$ for elemental composition

The better dispersion capabilities of functionalised GNPs can be associated with the stitching of functional group to their surface. It was found in elemental composition through EDAX analysis that G-Dot contains 99 % carbon contents whereas up to 7% oxygen and 93 % carbon contents were detected in G-Fnt nanoplatelets. SEM images were very helpful in measuring the shape and lateral dimensions of the GNPs, but it is difficult to find thickness and dispersion of nanoplatelets with it. Therefore, GNPs were further characterized using AFM.

To observe the thickness of nanoplatelets, GNPs were dispersed in water very gently through sonication, and a drop of dispersed solution was arranged on a glass slide. AFM characterization was also used to observe the dispersion of nanoplatelets in the aqueous medium. AFM images of the G-Dot solution and G-Fnt solution were analysed using Nanoscope software. For comparison between pristine GNPs and functionalised GNPs, the AFM images of G-Dot and $G-O_2$ were measured and presented in Fig.4.5 and Fig. 4.6 respectively. Dispersed G-Dot solution (Fig 4.5a) shows several flakes of nanoplatelets stacked over each other, while for the same dispersion period and effort, the dispersed $G-O_2$ solution (Fig. 4.6a) exhibited a well-dispersed pattern of nanoplatelets. As aforementioned, better dispersion capabilities of $G-O_2$ are associated with oxygen group grafted on its surface. Though, with extended sonication time and with a lower concentration, G-Dot can also be dispersed evenly in the water but functionalised GNPs with surface modification seems to have better dispersion capabilities with same sonication efforts and time.
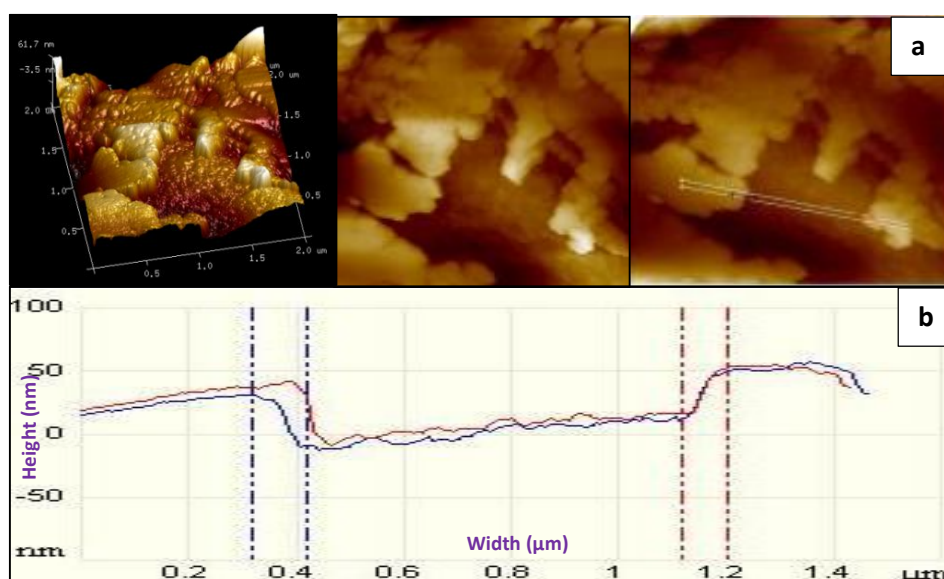
Figure 4.5 AFM Images of G-Dot Solution (a) dispersion of G-Dot into water (b) surface profile of G-Dot measuring thickness

83

The thickness of these nanoplatelets was characterized by taking profile on AFM images and found to be in between 35 and 40 nm. A number of graphene layers in these GNPs can be estimated between 7 to10 as single graphene sheets stake over each with the average thickness of 5-10 nm. This multilayer platelet morphology of plasma exfoliated GNPs differentiates them from pure graphite and graphene oxide (GO). These GNPs are economical and easy to synthesise as compared to GO, and could be more beneficial when activated in cement matrix due to its wrinkled free, unfolded morphology.
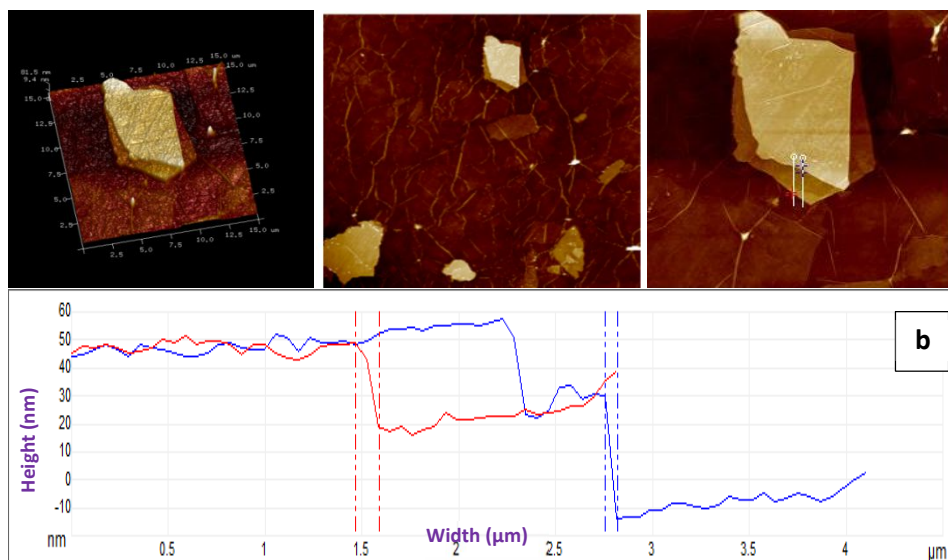
Figure 4.6 AFM Images of GNPs Solution (a) dispersion of G-O$_2$ into water (b) surface profile of G-O$_2$for measuring thickness

4.2.3   Chemical Structure Analysis of GNPs

For the chemical structure identification, GNPs were characterized using FTIR as per the procedure described earlier in chapter 3. In the combined IR-spectrum of GNPs depicted in the Fig. 4.7 a noise band appeared at 2347 cm^{-1}due to the CO_2 present in the environment. In the broad spectrum, IR of both G-Dot and G-Fnt are quite similar because oxygen contents in the G-Fnt are only up to 7% due to which major peaks difference does not appear in the spectrums. In the Fig. 4.7b and Fig. 4.7c has presented an expanded view of the spectrums of G-Dot and G-Fnt respectively for the range between 1700 and 650 cm^{-1} where we can identify the main peaks of graphite structure and the peaks of different functionalities present.

The graphene and graphitic crystal structure have two main IR spectral peaks presented as E_{1u} near to the 1587 cm-1 and A_{2u} near to wavenumber 870 cm-1 (Kostić et al., 2009). From the Fig. 4.8b the main IR bands representing graphene crystal structure can be

84

identified at 1591 cm-1 which are associated with C-C stretching of sp^2 carbon backbone and the peak at 863 cm-1 is associated with the C-O-C symmetrical stretching also the peak at 1044 cm^{-1} due to the C-O stretching confirming the graphitic structure of both G-Dot and G-Fnt. The other peaks at 1497 and 675 cm-1 can be attributed to C-C stretching and C-O stretching respectively.
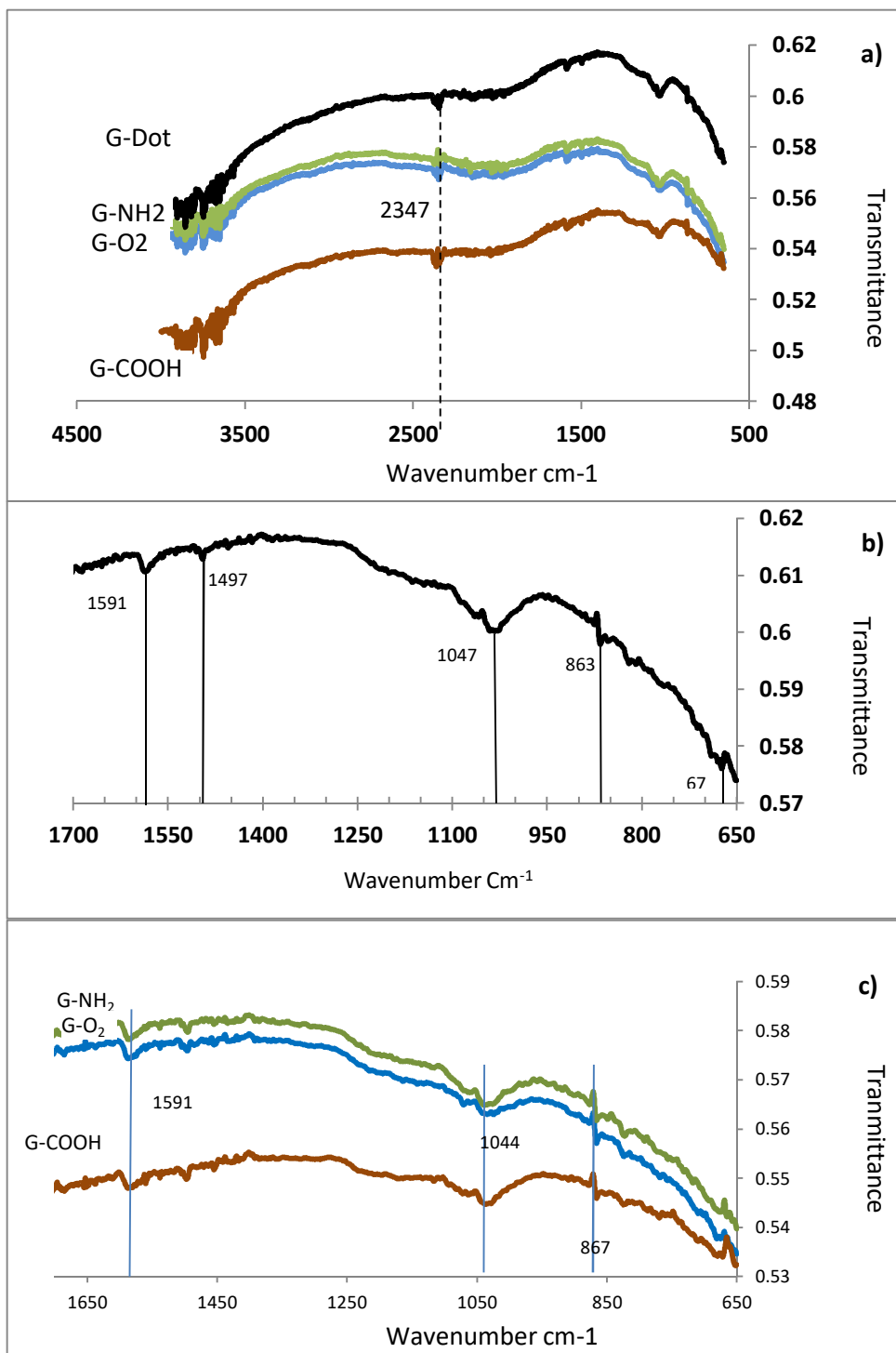
Figure 4.7 FT-IR spectrum of GNPs (a) range between 3000-650 cm^{-1} (b) expanded view of FT-IR between wavenumbers 1700-650 cm^{-1}

85

4.2.4 Structural Disorder Analysis of GNPs

Raman spectroscopy (RS) has renowned as a non-invasive characterization technique especially for graphite and graphene-related materials such as GNPs and graphene oxide. G-Dot and G-Fnt were also characterized using RS to find out the presence of edges or breathing modes of its aromatic rings and I_D/I_G ratios using equipment and methodology mentioned earlier in chapter 3. The combined spectrums of G-Dot and G-Fnt are shown in Fig. 4.8 where typical D, G and 2D bands are visible in all the spectrums. However, the spectrum of G-Dot can be distinguished with very lower intensities of D and G peaks. Further, for detail analysis of these spectrums variation in intensities and wavenumbers has been observed and used to calculate I_D/I_G ratios.
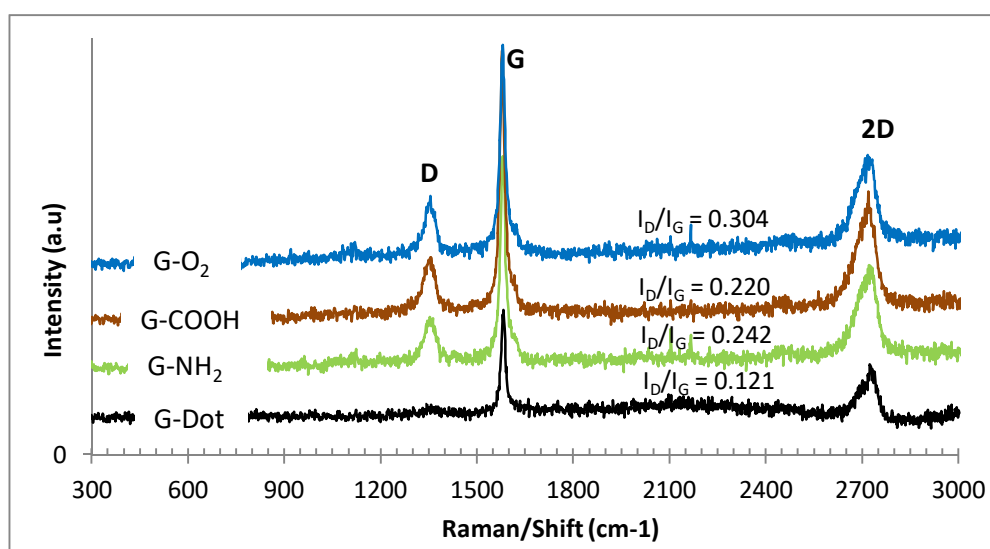
Figure 4.8 Combined RAMAN spectrum of G-Dot and G-Fnt showing typical graphitic D and G bands

Fig.4.9a represents the RS spectrum of G-Dot in which a very strong and sharp peak, referred as G-peak (graphite peak), at 1582 cm-1 which is associated to combine stretching vibration of carbon atoms and reflects good crystalline graphitic structure. Another normal broad peak referred as D-peak (disorder peak), at 1356 cm-1 which is Raman active only in the presences of edges or defects in the sp^2 carbon atoms or it is also associated with a combined breathing mode of the aromatic rings. A shoulder peak D′ at 1591 cm-1 is assigned due to the presence of edges in the G-Dot, and 2D peak at 2725 cm-1 is attributed to the overtone of D band vibration and is always present in the spectrum with varied intensity. In case of G-Fnt, a strong and sharp G-peak in the RS spectrum of $G-O_2$ (Fig. 4.9b) appeared at wavenumber 1580 cm-1, and broad normal D peak with higher

intensity as compared to G-Dot appeared at 1355 cm-1 and overtone this band in the spectrum 2D peak appeared at 2724 cm-1. A slight shift in the wavenumbers between G-Dot and G-Fnt has also been observed that might be due to the oxidation or functionalization of GNPs while a slight variation in the peak intensities of G-NH$_2$ and G-COOH has also been observed and reflected in the respective I$_D$/I$_G$ ratios.
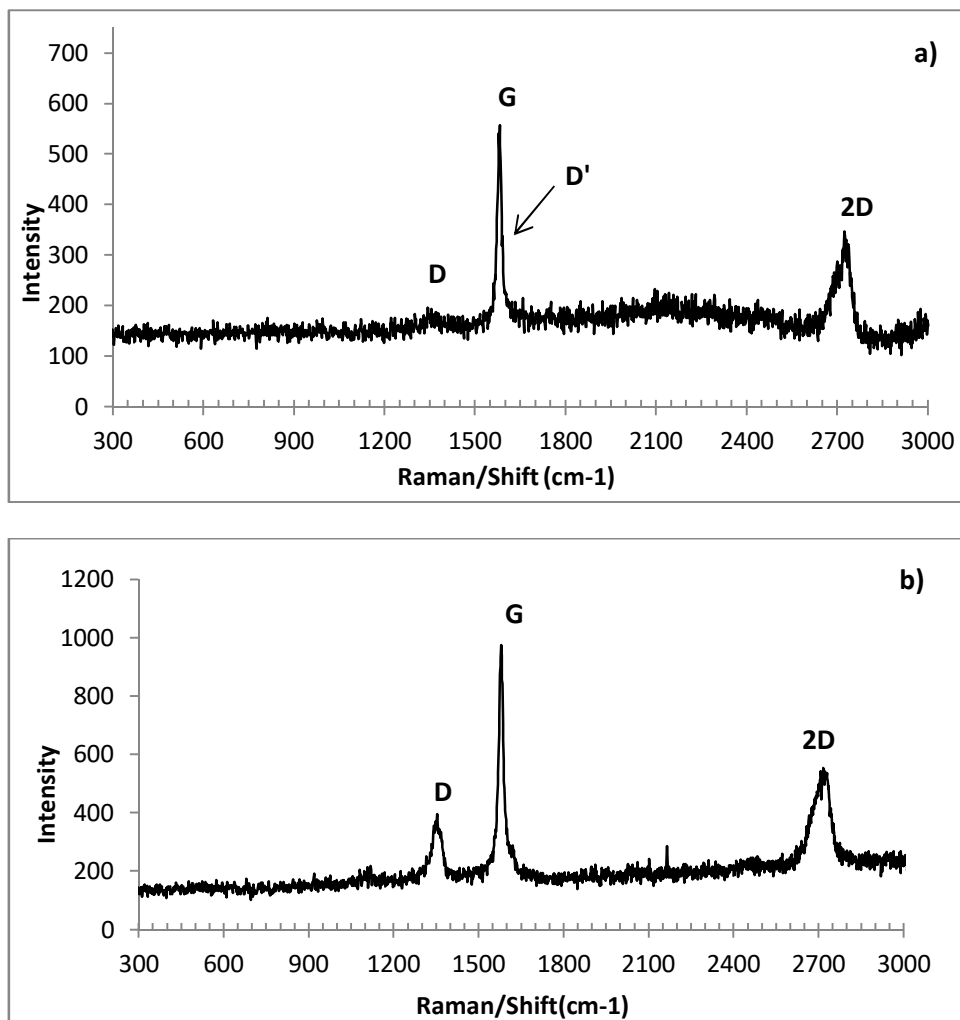
Figure 4.9 RAMAN spectrum of a) G-Dot showing typical graphitic peaks and b) G-O$_2$ with higher D-peak value

It is reported that disorder in the graphitic material can be measured by intensity ratio between D-peak and G-peak (I$_D$/I$_G$). Higher the I$_D$/I$_G$ ratio higher would be the disorder, and more oxidation would be represented by the graphite structure with higher surface energy which is a good characteristic for dispersion in aqueous solution and build active sites for nucleation in cement matrix (Tuinstra, 1970; Reich and Thomsen, 2004). The Raman spectrums were used to obtain I$_D$/I$_G$ ratio of these GNPs, and a value of 0.121 is obtained for G-Dot while 0.304, 0.242 and 0.220 were obtained from spectrums of G-O$_2$,

G-NH$_2$ and G-COOH respectively. The spectrums I$_D$/I$_G$ ratios of G-Dot and G-Fnt were found to be in between the I$_D$/I$_G$ ratio of pure graphite (0.05) and graphene oxide (0.70) reported by (Naebe et al., 2014). In chemically exfoliated graphene sheets structural characteristics are a trade-off with structural defects and show higher D-band values (Rashad et al., 2013), but these plasma treated GNPs showed the adequate value of D-band and this indicates that they have structurally integrated surface.

4.2.5 Crystallographic Analysis of GNPs

Further to determine crystalline properties of GNPs, XRD analysis was performed. The XRD features of these GNPs were found almost similar. In the Fig.4.10a the combined XRD diffraction pattern of G-Dot and G-Fnt shows a very strong peak in all near 26.41° corresponding to (002) plane related to the typical graphitic structure with a layer spacing of 3.4 A$^{\circ}$ (0.346 nm) and a very small peak at 54.12° corresponding to (004) plane. This indicates that the functionalization did not destroy the lattice parameter and crystal structure of graphene.
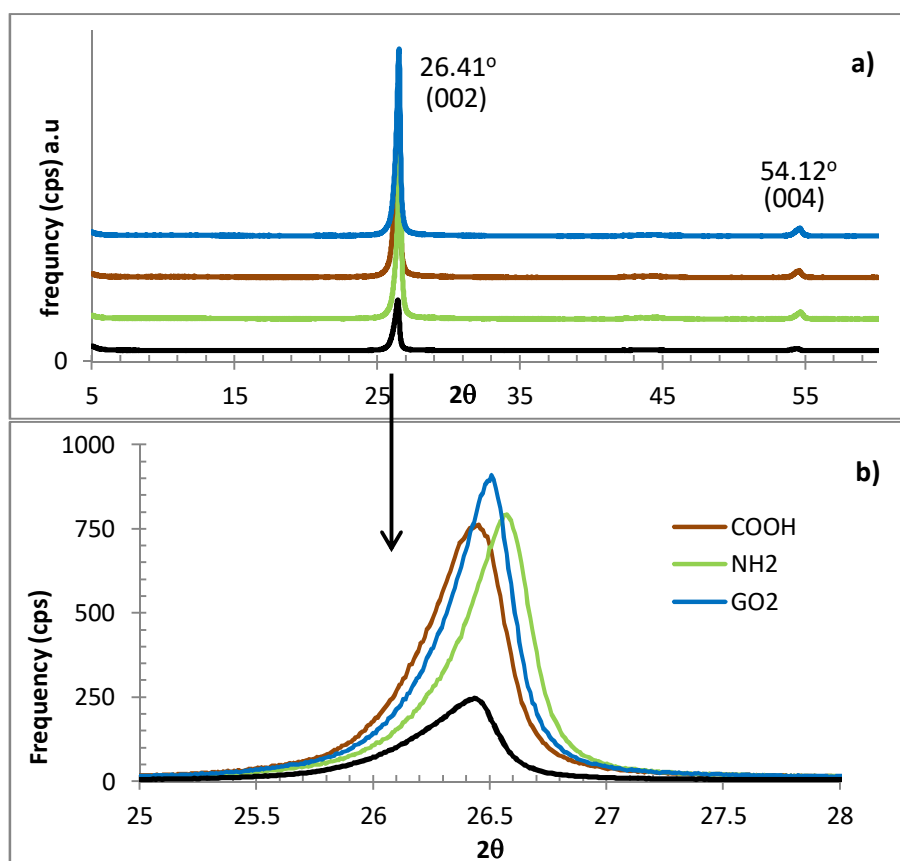
Figure 4.10 Combined XRD pattern of GNPs showing typical graphitic peaks a) near 26.5°, 54.12°and b) expanded view of area of interest near 26.5°

Therefore, the structural characteristics of plasma treated GNPs are quite similar to the pure graphite, indicating their less defective and structurally integrated surface. However, higher peak intensity and broaden peak area has been observed in the diffraction peaks of G-Fnt as shown in the expanded view of the area of interest in Fig. 4.10 b. It has been reported that higher diffraction peak intensity reflects the higher degree of crystallinity while broadening is attributed to the smaller size of crystallite (Wani et al., 2011) and disorder in the graphene structure (Zou et al., 2006). Therefore, it can be inferred that G-Fnt has better crystallite lattice as compared to G-Dot.

4.3 Genome Summary of GNPs

To understand the fundamental structural and other surface properties of GNPs various characterization techniques were employed. The measurements taken through these techniques were used to analyse the Genome of GNPs so that their potential use in the cement matrix can be realized. The summary of the measurement and analysis is presented in Table 4.2 below and the proposed model of GNPs in presented in Fig 4.11.

Table 4.1 Characterization summary of GNPs

Genome	Technique	Characterization	Measurements	
			G-Dot	**G-Fnt**
Structural and morphological analysis	TEM	Condensed hexagonal honeycombed lattice structure and wrinkles morphology	Hexagon width 0.178 nm and Interlayer spacing 0.335 nm	Hexagon width 0.200 nm and Interlayer spacing 0.335 nm
Dimensional and dispersion analysis	SEM/AFM	Irregular and triangular shape platelets staking over each other	Lateral dimension 5-10 μm	Lateral dimension 5-10 μm
Dimensional and dispersion analysis	AFM	Fine topography with angular sheets	Thickness 35- 40 nm/aspect ratio ~208	Thickness 35- 40 nm /aspect ratio ~208
Chemical structure analysis	FTIR	Graphene crystal structure observed with identification of two main graphitic peaks	Main IR bands at 1597 cm^{-1} and 897 cm^{-1}	Main IR bands at 1597 cm^{-1} and 897 cm^{-1}
Structural disorder analysis	RAMAN	In between pure graphite and GO, presences of edges detected due to higher D-peak	D-Peak to G-Peak ratio $I_D/I_G = 0.121$	D-Peak to G-Peak ratio $I_D/I_G = 0.304$
Crystallographic analysis	XRD	Similar to graphitic structure	Main peak at $2\theta = 26.41^\circ$	Main peak at $2\theta = 26.48^\circ$

Further based on structural and morphological characterization data the simple structural models of plasma exfoliated GNPs were developed and shown in Fig. 4.11. The synthesis of plasma functionalised graphene is done in a low-pressure container, attached to the main electrode that generates the plasma. The procedure gently functionalizes the graphene, environmentally friendly at a low temperature. This is unlike to acid treatment as it is a dry functionalization treatment with no hazardous waste in streams and with less damage to the surface of the graphene. The oxygen functionalization process grafts the functional or chemical groups to the surface, giving an improved dispersion and compatibility in water. This functionalization overcomes dispersion and provides enhanced bonding with the cementitious material.
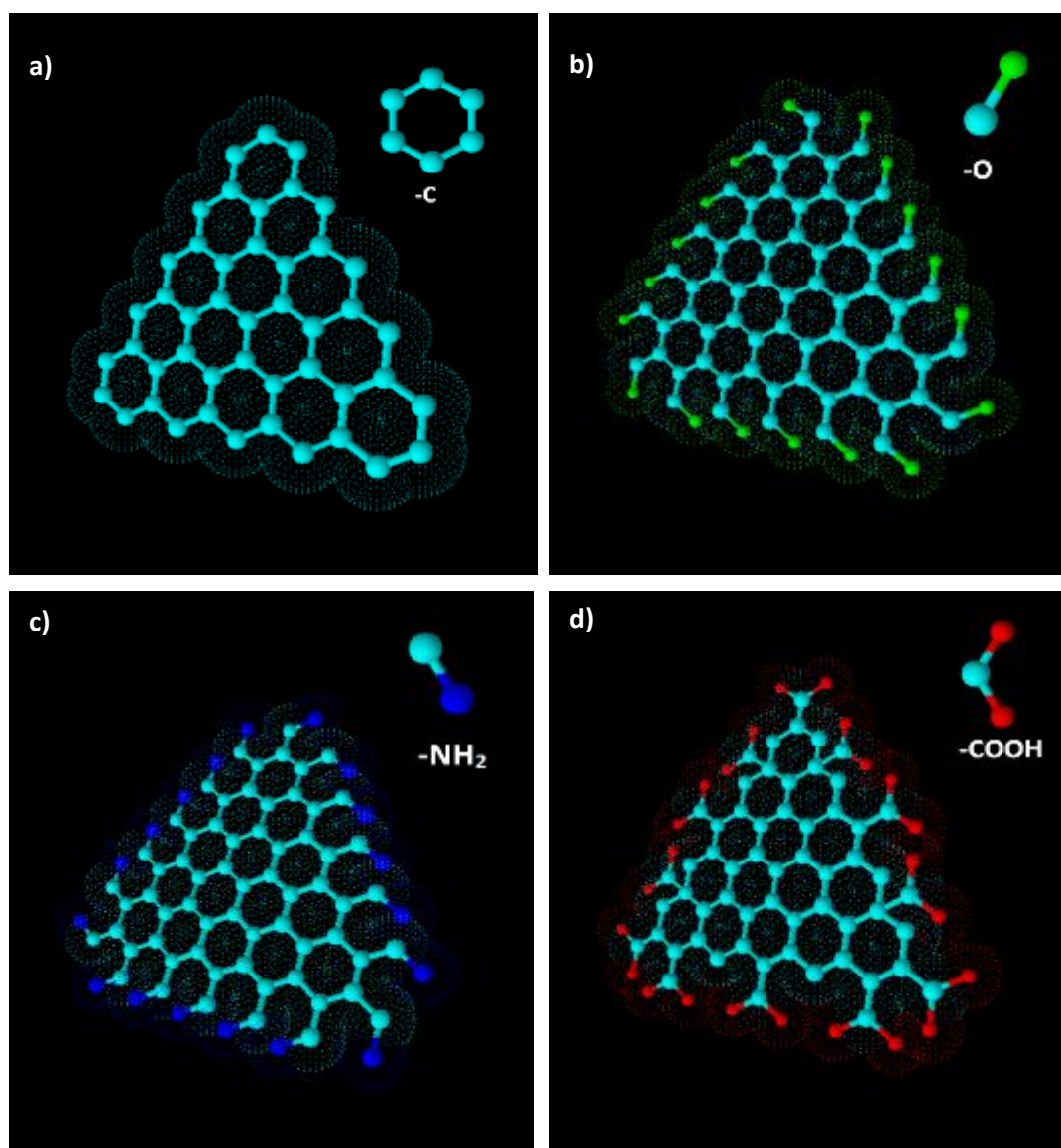
Figure 4.11 Proposed structural models of a) G-Dot b) G-O$_2$ c) G-NH$_2$ and d) G-COOH

4.4   Characterization of Graphited Carbon Nano Fibres (GCNF)

The GCNFs used in the development of cementitious nanocomposite are of vapour-grown carbon nanofiber (VGCF) grade. These GCNFs are discontinuous with length ranging 20-200 um and highly graphitic structurally. They possess excellent mechanical properties, high thermal and electrical conductivity. GCNFs have unique surface properties and can accommodate surface modification to tailor the needs via functionalization (Aldrich, 2016) Various physical and chemical properties of GCNFs were obtained from the source and presented in chapter 3. Further, structural, morphological and surface properties were determined and discussed in the subsequent section.

4.4.1   Structural Analysis of GCNFs

To determine the morphology and lattice structure, GCNFs were characterized using TEM equipment. Fig. 4.12a shows the HR-TEM micrographs of GCNFs. The discontinuous morphology with conical features can be seen clearly. The external diameter of GCNFs ranges from 120 nm to 150 nm whereas graphited conical nanoplatelets are 200 nm wide (Fig. 4.12b)
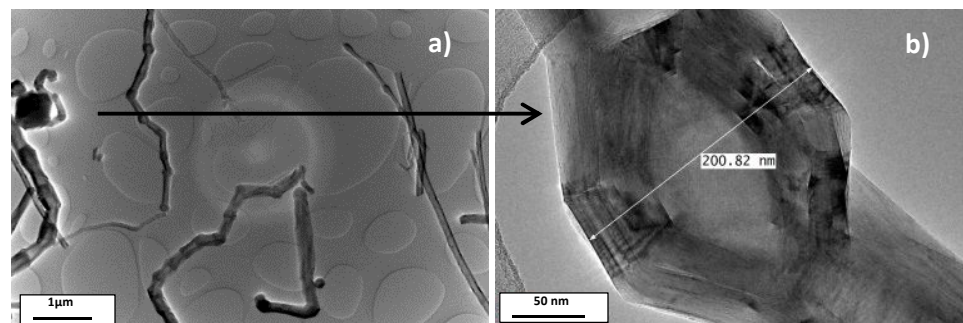
Figure 4.12 HR-TEM images of GCNFs a) discontinuous morphology with graphited conical platelets b) enlarged view of conical feature

Further FFT and intensity profile of GCNFs surface were taken along the line shown in the Fig. 4.13b. The surface of GCNFs observed rough and structured with longitudinal ridges or having a keel on it resembling with snake's skin like features as shown in Fig. 4.13a. The FFT taken was not clear (Fig. 4.13c), however from the intensity profile (Fig. 4.13d), the interlayer spacing of graphite atomic layers was found to be 0.359 nm. This is consistent with the (002) lattice plane parameter as compared to 0.335 nm for pure graphene structure (Kalbac et al., 2011). This confirms the highly crystalline graphitic structure of GCNFs. The unique structural properties of GCNFs could be beneficial to trigger the nucleation effect in the cement hydration.
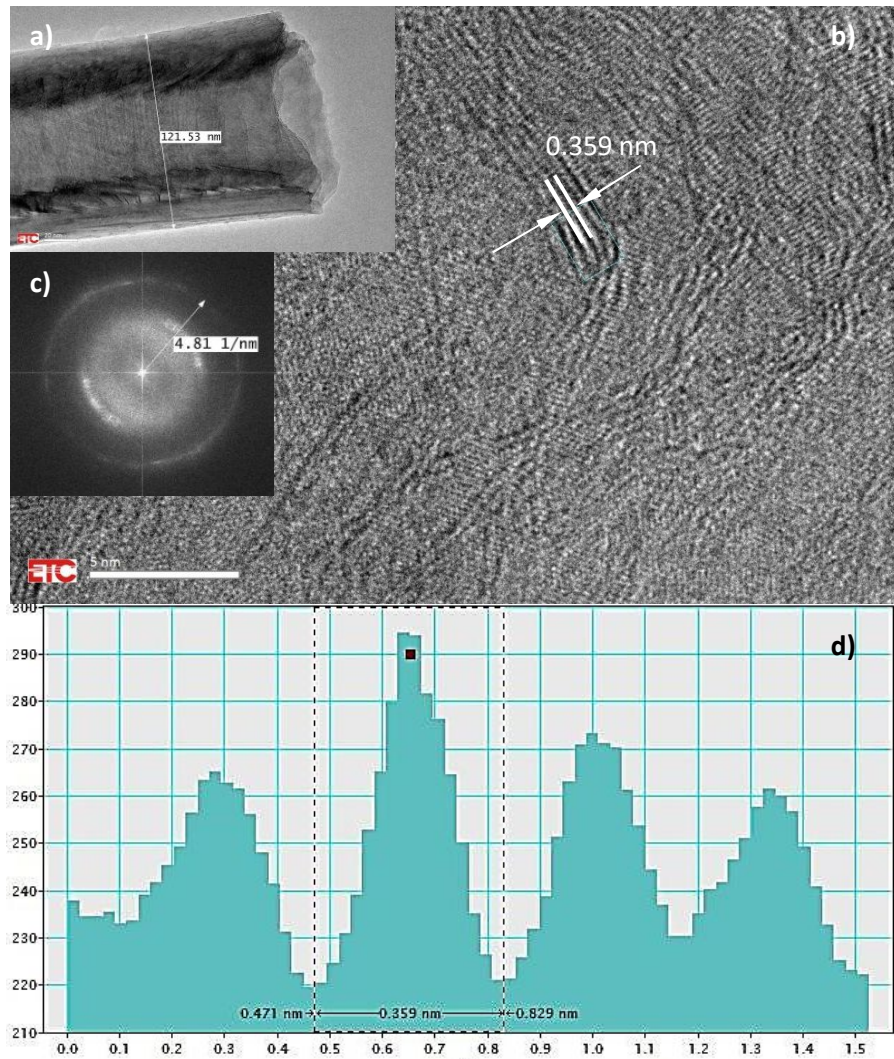
Figure 4.13 HR-TEM images of GCNFs a) rough surface with structure resembling snake skin features b) hollow tube graphitic structure showing multilayers at the edges c) FFT of selected area d) intensity profile of the area taken along the arrow

4.4.2 Morphological Analysis of GCNFs

To characterize the lateral size and physical appearance of GCNFs, SEM micrographs were measured using FEG-SEM mentioned in chapter 3. Due to high Van der Wall's forces, agglomeration in GCNFs can be seen in Fig. 4.14a. However, long profile around 200 µm of fibres structure can be seen in enlarged view indicated by the arrow in Fig.4.14b. With diameter range of 120-150 nm and length around 150-200 µm, the aspect ratios of these GCNFs comes out to be ~1300. The high surface activity, as well as the high aspect ratio of GCNFs, could be beneficial for their bonding to the cementitious matrix. It can be seen that in the bulk of fibres GCNFs are present in the pure form; few impurities were also observed indicated by the arrow in Fig. 4.14b. The closer SEM view also revealed that GCNF have a rough surface and graphited nanoplatelets are attached to the surface. This may provide more reactive sites to interact with hydration products.
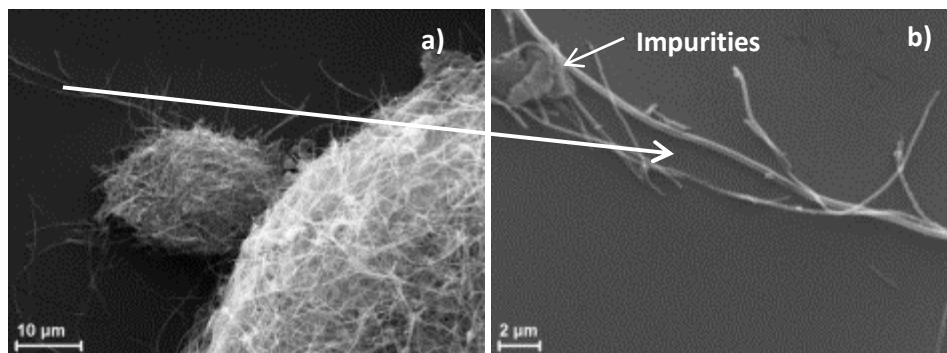
Figure 4.14 SEM images of GCNFs a) agglomeration due to Van der Wall's forces b) enlarge view of fibre profile

4.4.3 Chemical Structure Analysis of GCNFs

To analyse the chemical structure of GCNFs, FTIR characterization technique was employed with equipment and procedure similar to those used for the analysis GNPs. The obtained FTIR spectrum is shown in Fig. 4.15 was not helpful to identify the characteristic peaks associated with graphitic structure and bond formation in the GCNFs. However, peaks at 2347, 2192, 2073, 1525, 1073 and 695 cm^{-1} were observed and explained. The noise bands near 2347 cm^{-1} were due to CO_2 present in the environment, and this band was also observed in the FTIR spectrum of GNPs. The weak bands at 2192 and 2073 cm^{-1} can also be associated to double bond between carbon and oxygen groups (Nadeem et al., 2009). The peak at 1525cm^{-1} can be due to stretching of sp^2 carbon C=C atoms of graphitic domain and peaks at 1073 and 695 cm^{-1} is due to the C-O stretching.
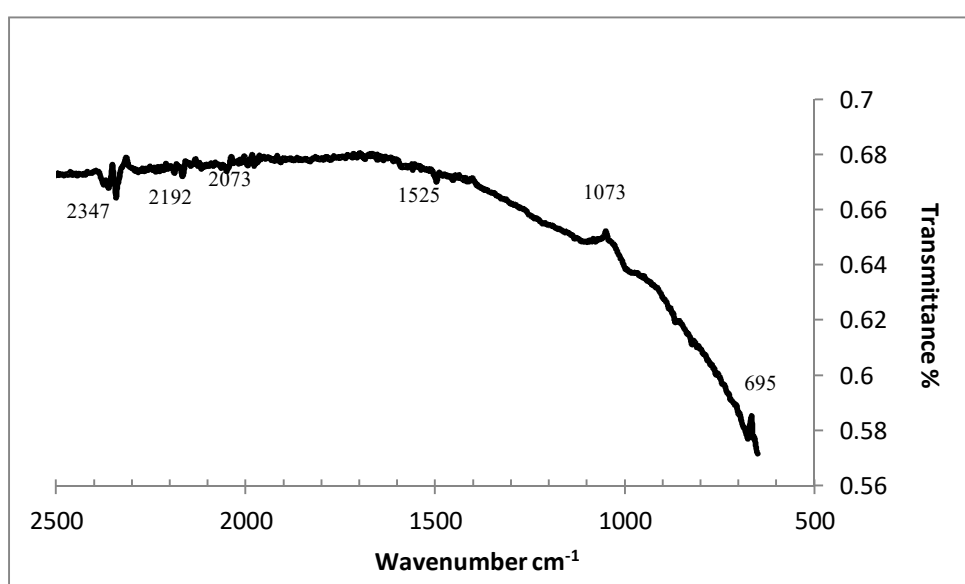
Figure 4.15 FTIR spectrum of GCNFs

4.4.3 Structural Disorder Analysis of GCNFs

To further investigate the chemical structure of GCNFs, Raman spectroscopy was employed. The representative Raman spectrum of GCNFs depicted in Fig.4.16 shows a sharp peak at 1580 cm-1, also known as G (Graphite) peak and a small D (Disorder) peak at 1360 cm^{-1}. The peak G is attributed to Raman active E_{2g} in-plane vibration mode, and D peak is attributed to A_{1g} in plane breathing vibration mode (Xiong et al., 2004). More specifically, the G peak exhibits an E_{2g} mode related to the vibration sp^2 carbon atoms bonded in in 2D hexagonal lattice of graphite layers. Whereas A_{1g} mode is related to the disorder structures caused by lattice distortion of graphite crystals, and when the degree of graphitisation decreases, the G peak shifts its position towards higher wave number also the higher D peak associated with, the higher disorder in the lattice structure. Thus, Raman peak G obtained for GCNFs at 1580 cm^{-1} is close to the 1582cm-1(Kang et al., 2004; Roy et al., 2003) indicating high graphite structure and small intensity of D peak at 1360 cm^{-1} indicates defect-free lattice structure of GCNFs. Whereas, a higher value of D peaks is associated with the structural defects in graphene (Rashad et al., 2013) and higher I_D/I_G ratios are favourable to interact with cement hydration products.
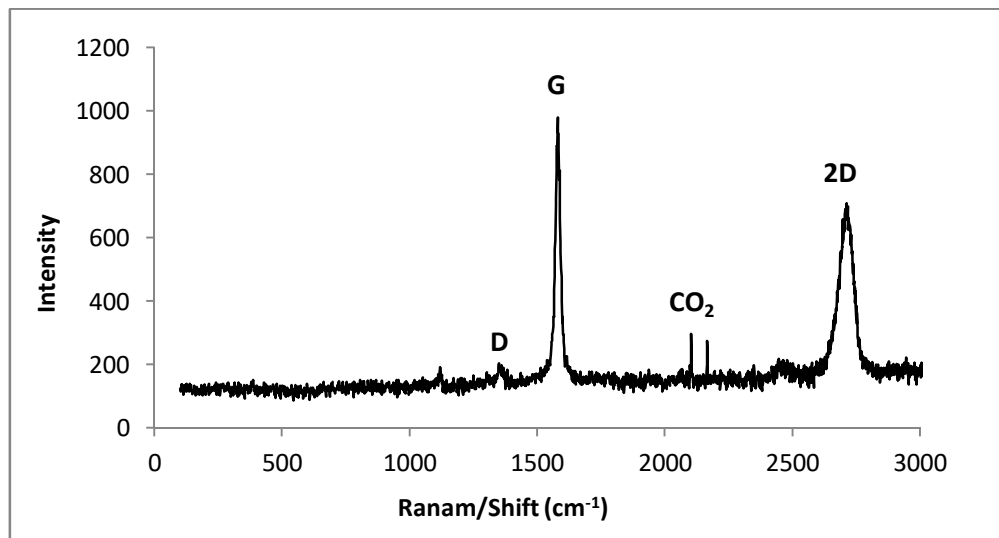
Figure 4.16 Raman spectrum of GCNFs indicating positions of various peaks

The 2D peak at 2716 cm-1 is due to the overtone of D peak and always present in the spectrum whereas small spikes near 2150 cm-1 are due to the reaction of the CO_2 present in the environment with the sample.

4.5 Conclusions

Various characterisation techniques have been successfully employed to identify the lattice structure, surface, morphology and chemical structure of GNPs and GCNFs. From the characterization data, GNPs seemed a promising candidate for the development of nano cementitious composite due to their well-defined lattice structure, wrinkled free 2D shape morphology, high surface energy and well dispersion capabilities in the aqueous solution. Whereas, graphited carbon nanofibres (GCNFs) with their unique conical structure and long fibrous 1D morphology and high aspect ratio may be able to develop a robust interaction, and strong interfacial bonding and strong interlocking between fibre structure and hydration products. This hypothesis originated the motivation to investigate the physical and chemical interaction of GNPs and GCNFs with cement matrix for the development of cement nanocomposite presented in next chapters of the research.

CHAPTER 5 Development of NGCC-Dot

5.1 Introduction

Concrete is specified as brittle material by knowing the fact that it has low flexural strength as compared to its compressive strength. This brittleness instigated in concrete is the result of a very complex microstructure formed by cement hydration crystals such as Portlandite CH, ettringite (AFt), monosulfoaluminate (AFm) and calcium silicate hydrates (C-S-H) as gel and amorphous solid (Taylor, 1992). Many factors influence crystal shapes and have a significant impact on the mechanical properties of cement matrix; perhaps import one is their assemblage and arrangement in cement matrix at nano-level.

Since the discovery of graphene and its simplest method of synthesis, many researchers have been investigating various forms of graphene into cement matrix. Graphene gained much attention due to its exceptional multifunctional properties (mechanical, electrical and thermal), high surface area to volume ratio, high aspect ratio and unique 2-dimensional atomic structure (Cooper et al., 2012). A similar atomic structure of graphene with CNT and sp2-bonded carbon atoms in its structure gives extraordinary mechanical properties, with the intrinsic strength of 60 and 130 GPa and Young's modulus of 1TPa respectively (Rafiee et al., 2009; Kuilla et al., 2010). Theses extraordinary mechanical characteristics attracted the researchers to use the graphene or its forms in the cement matrix to improve its mechanical properties. Many authors have reported the use of graphene and its forms especially graphene oxide (GO) in the cementitious composite for its positive impact on compressive and flexural strength. For example, it is reported that by introducing GO with a very low concentration of 0.05% by weight of cement has increased the compressive strength 15-33 % and flexural strength 41-59 % in the cement mortar due to improved interfacial bonding and arresting the cracks (Pan et al., 2013). In another study GO addition by 0.05% has remarkably increased the compressive and flexural strength by 46.5 % and 68.5 % respectively at the age of 7 days in the cement paste due to modification of its pore structure with increased nucleation effect of GO (Wang et al., 2015).

It has been reported mostly in previous research that an improved strength of cementitious composites is primarily due to bonding properties of nanomaterials and cement matrix. Also, the techniques of strengthening the cement matrix were on reinforcing the material elaborating bonding and arresting cracks, filling the pores by nanomaterial in the cement matrix.

In fact, the shape and arrangement of hydration crystals in cement matrix may play a vital role in the strength of cement matrix. This aspect of microstructural modifications in the cement matrix due to the interaction of graphene nanomaterial has recently been focused by researchers and in infancy phase. Also, the GO sheets are very expensive to produce commercially and synthesised by oxidation and reduction subsequently followed via chemical exfoliation and extensive sonication which can harm the inherent lattice structure of graphene. Moreover, 5-6 nm thin GO sheets may crumble into the cement matrix and can produce an adverse effect on the mechanical properties.

In this scenario, low-cost GNPs synthesised via less energy-intensive, environmentally and commercially viable plasma exfoliation method can be harnessed into the cement matrix to replace GO. These GNPs are exfoliated without using harsh chemicals and not used before into cement matrix. The extensive analysis of structural and other properties of GNPs presented in chapter 4 suggests that structurally integrated wrinkle free 2D morphology can be a promising candidate for the development of cementitious composite. In the current research work, NGCC-Dot has been developed with the motivation to explore the suitable dose and effect of GNPs on the growth of cement hydration products and to identify those hydration crystals favourable for the formation of distinctive microstructure lead to enhance its mechanical properties. The distinctive planner structure of GNPs, which is only one atom thick and flat surface of carbon atoms, can create significant contact area to reside the cement particles. These cement particles can sprout, grow and assemble during the hydration process in a distinctive manner (Cooper et al., 2012).

In this chapter development of NGCC-Dot is describe. NGCC-Dot is processed using varied contents of G-Dot 0.01% to 0.05% by weight of cement (bwoc) dispersed in aqueous solution. The effect of G-Dot on phase change, chemical composition, microstructure development and strength enhancement of cement matrix is investigated through analytical techniques (FTIR, XRD, SEM and EDAX). The developed NGCC-Dot tested for strength enhancement using the Instron universal testing machine (UTM). To understand the arrangement of cement hydration products with the activation of G-Dot, the results obtained through analytical techniques and mechanical testing along with detailed observations of the microstructure of hardened cement paste are discussed.

5.2   Composite Processing

A general procedure to develop NGCC-Dot is discussed in chapter 3. Specifically for the processing of NGCC-Dot, mix proportion of materials is mentioned in Table 5.1. In the

development of nanocomposite, no superplasticiser or polycarboxylate (PC) was used. The G-dot solution was synthesised with varying concentrations of 0.01% to 0.05% of G-Dot bwoc. G-Dot nanoplatelets in dry form were first mixed with water using simple sonication bath for 30 mins. Dispersion of G-Dot in the water was observed through SEM images using a diluted solution of varied concentrations and found well dispersed in the water (Fig. 5.1). However, in the solution with higher concentrations of G-Dot agglomeration of nanoplatelets was observed (Fig. 5.1f).
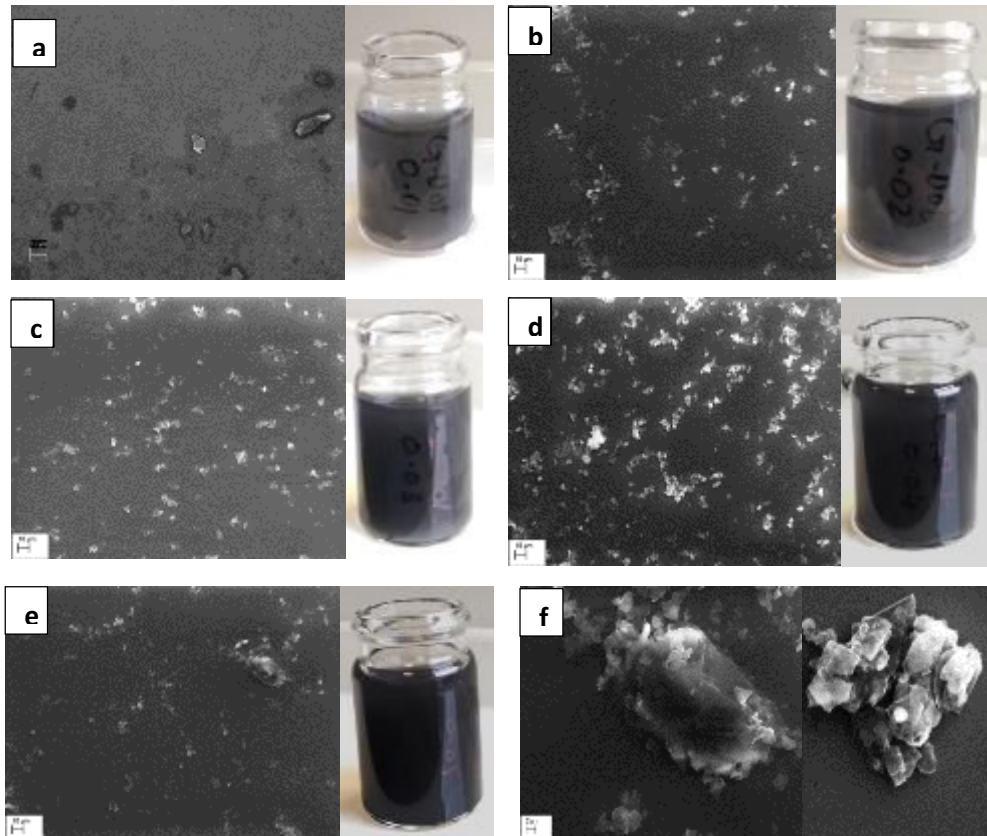
Figure 5.1 Dispersion of various contents of G-Dot using simple sonication bath for 30 mins a) concentration of 0.01 % b) 0.02 % c) 0.03% d) 0.04% and e) 0.05% f) agglomeration of G-Dot with higher contents

The obtained solution of G-Dot was then used for the processing of NGCC-Dot cementitious composite using standards and procedures mentioned earlier. After mixing, compacting, moulding, de-moulding and curing for different curing durations, the NGCC-Dot samples were tested and analysed for chemical and mechanical properties discussed in subsequent sections.

Table 5.1 Mix proportion of G-Dot nanocomposite

Sr. No	Sample ID	Cement Contents gm	GNP Contents mg	% BWOC Cement	W/C
1	Control	1400	0.00	0.00	0.30
2	GDot 0.01	1400	140	0.01	0.30
3	GDot 0.02	1400	280	0.02	0.30
4	GDot 0.03	1400	420	0.03	0.30
5	GDot 0.04	1400	560	0.04	0.30
6	GDot 0.05	1400	700	0.05	0.30

*BWOC=by weight of cement; W/C=water/cement ratio

5.3 Results and Discussion

5.3.1 Effect of G-Dot on Phase and Chemical Composition of NGCC

XRD analysis, which is performed for both controlled cement and NGCC samples with a varied amount of G-Dot at 7, 14 and 28 days of age, shows a substantial difference between the compositions with G-Dot ranging from 0.03 to 0.05% but those from 0 to 0.02%. The XRD spectrum of NGCC G-Dot 0.04 % (Fig.5.2) taken at the age of 7days has been used to compare the expected diffraction peaks with control. It is apparent that all the expected peaks related to C_3S (Alite), C_2S (Belite), CaO or $CaCO_3$ (Calcite), CH (Portlandite) and AFt (Ettringite) are distinct and clear in both control and G-Dot samples of 7 days. A scrutiny of XRD patterns indicates some clear differences between control and nanocomposite with G-Dot at 0.04%, especially the formation of main diffraction peak with other small peaks between diffraction angle $2\theta = 25^o$ and 29° (Fig.5.2b). The visible peak at 26.6^o is attributed to the presence of graphene (G-Dot) in the nanocomposite, while this peak is missing in the control sample. Some other small peaks, attributed to the formation of ettringites (AFt) and CH in the nanocomposite, are present in NGCC-Dot sample while missing in control sample. This indicates the increased number of hydration products especially AFt and CH in the NGCC sample are grown leading to develop denser microstructure.
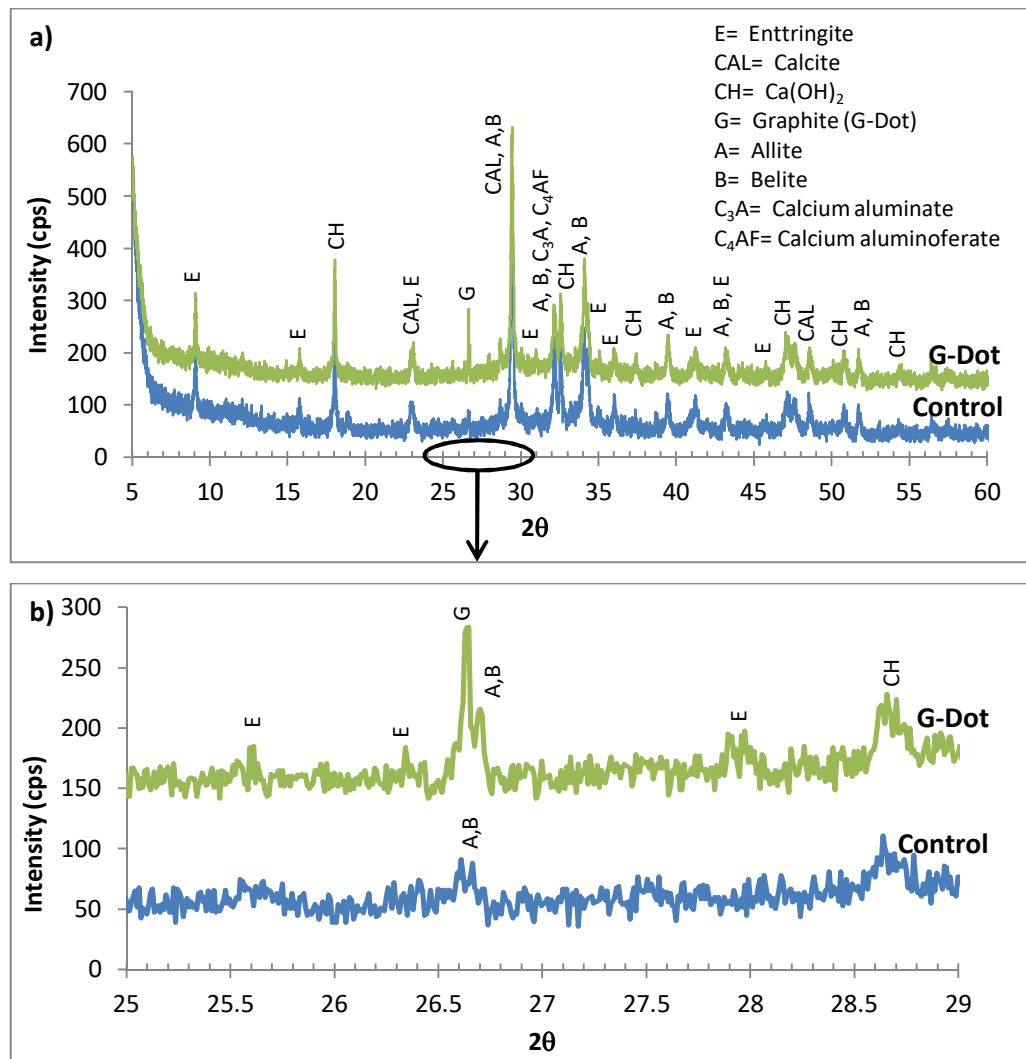
Figure 5.2 a) XRD spectrum of 7 days control and NGCC sample loaded with G-Dot 0.04%
b) Expanded area of interest between spectral angle 2θ = 25° and 29°

However, the main hydration product of cement C-S-H in amorphous solids or gel form cannot be detected in the XRD spectrum as the working principle of XRD is based on the scattering of the radiation on the crystal lattice (Horszczaruk et al., 2015). Through XRD analysis it may be inferred that major changes in phase and chemical composition of cement takes place within few days of accelerated hydration of C_3S and C_3A compounds and very small amount of 0.01% to 0.03% of G-Dot in nanocomposite cannot be mapped through XRD.

FTIR spectrums of control cement and all NGCC samples showed identical peaks with the same wavenumber, but NGCC loaded with 0.03% to 0.05% showed higher absorbance intensity at the same peak positions (Fig.5.3a). For a comparison, FTIR spectrum is shown as bands of various peaks, of both the controlled and NGCC sample, loaded with G-Dot 0.04% are presented in Fig.5.3b, which may help to understand the phase formation and

the presences of hydration products XRD can not detect those. The IR spectrum regions between bands of 3400 - 3700 cm^{-1} reflect changes in water system due to hydration, is known as water band. The band between 3400-3500 cm^{-1} is due to H-O-H stretching vibration and calcium hydroxide (CH) gives a sharp peak at 3640 cm^{-1} is due to OH present in Ca(OH)$_2$.
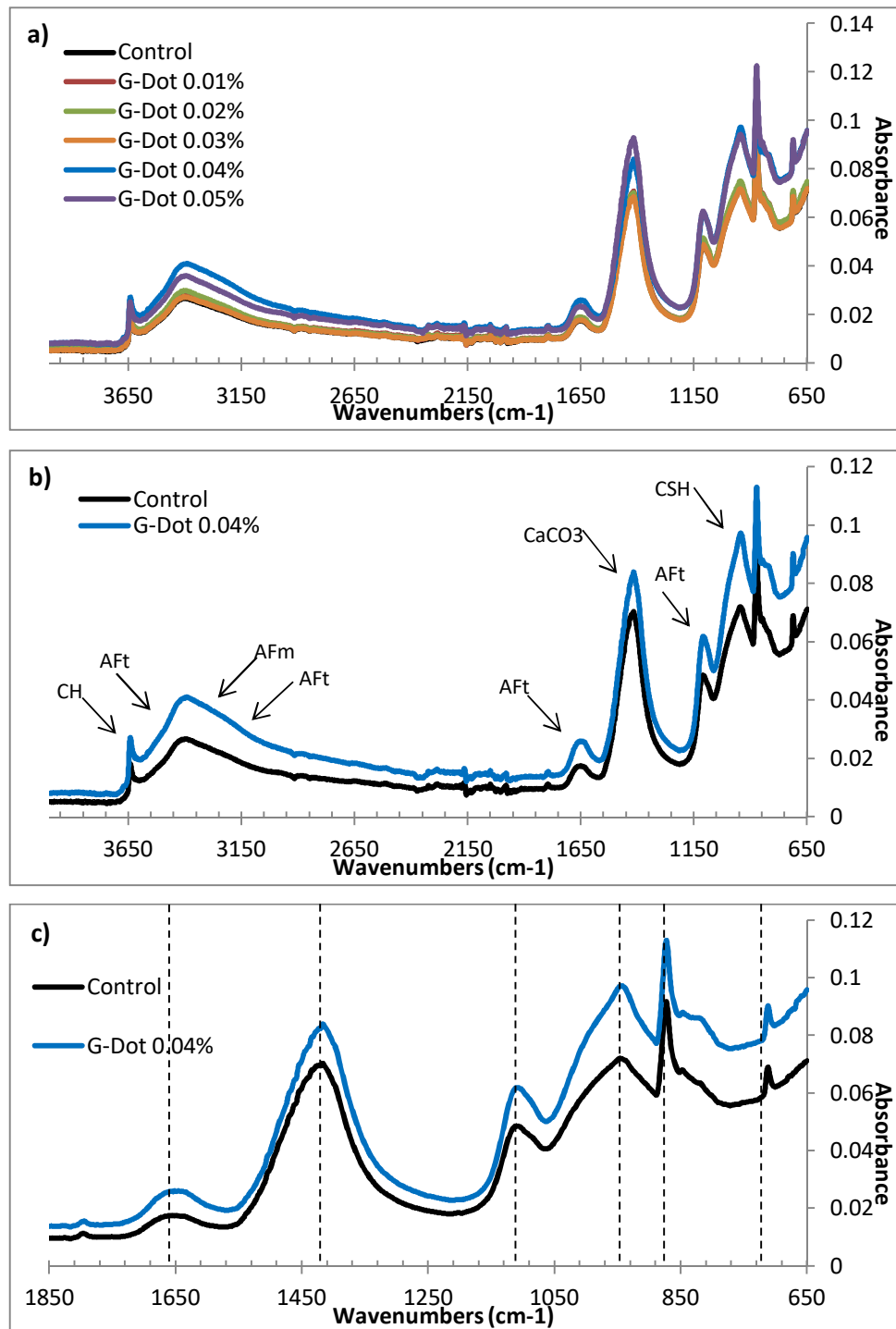
Figure 5.3 a) FTIR spectrum of controlled sample & G-Dot at 7days b) FTIR spectrums of control and NGCC with G-Dot 0.04% c) FTIR spectrum showing bands between wavenumbers 1850 cm^{-1} and 650 cm^{-1}

The formation of ettringite may be related here because more water is attached to their crystal structure (Gastaldi et al., 2009) and more stretching of H-O-H is reflected from high absorbance value indicating more ettringite formation in G-Dot nanocomposite. It has been reported that ettringite (AFt) has a strong peak at 3422 cm^{-1} and weaker one at 3545 cm^{-1} with less absorption values than OH bands, similarly monosulfonate (AFm) has bands at 3260, 3333, 3402, 3458 and 3527 cm^{-1}(Li and Liang, 2011). However, these bands are missing here in both controlled and nanocomposite samples. These peaks may be overlapped by water band, in these regions indicated by arrows in the Fig.5.3b, ranging between 3000 and 3700 cm^{-1}. Also, peak at 1650cm^{-1} related to the presence of molecular water indicating ettringite formation. While the peak regions 1415-1360 cm^{-1} and 874-885 cm-1 are related to carbonate peaks, indicating the presence of $CaCO_3$ in both samples, but its absorption value is high in nanocomposite sample. The peak at 1130 cm^{-1} to 1030 cm^{-1} related to Si-O-Si and Si-O-Al, indicating that carbonate reacted with C_3A and increased the formation of ettringite in the cement matrix (Matschei et al., 2007). The peak at 950 cm^{-1} is related to the presence of C-S-H gel, and absorbance intensity of this peak is high in case of the nanocomposite, indicating that more C-S-H is formed during the hydration process.

It may be inferred from FTIR spectrums that NGCC sample loaded with 0.04% G-Dot are comparable with the control sample and have same general spectral features indicating there is no secondary structure formation. However, the peak intensities show higher absorbance values in NGCC sample. The higher absorbance intensity signifies some changes in the composition of NGCC that might be related to chemical interaction, increased number of bonds or might be due to large dipole movement of the carbonyl group (C-O). It may also be due to change in crystallinity increased in hydrated products in the sample (Yousuf et al., 1995; Steven et al., 2013; Kongkhlang et al., 2010). Moreover, due to very small amount of graphene sheets in a very strong cement matrix and few absorptions bands may be overlapped with the bands of strong cement matrix. In this scenario, a Raman Infrared Spectroscopy may be used to get a better characterization of cement composite with graphene.

5.3.2   Effect of G-Dot on Microstructure of NGCC

To comprehend the diffraction peaks of graphene in XRD pattern and bands of higher absorbance intensities of C-S-H and other hydration products in FTIR spectrum of the

nanocomposite, further characterization of control and nanocomposite samples has been investigated through SEM images.

SEM images of control and NGCC samples with a varied amount of G-Dot from 0.01 % to 0.05% (Fig.5.4) revealed that the microstructure of cement matrix altered with the addition of various contents of G-Dot nanoplatelets. It is apparent that the control sample (Fig. 5.4a) has large pores, less rod-like crystal structure and mostly composed of standalone C-S-H gel-like structure. A similar C-S-H structure has been observed in the sample with G-Dot 0.01% and 0.02% (Fig. 5.4b and 5.4c), but more rod-like crystal emerged from the denser area in the microstructure.
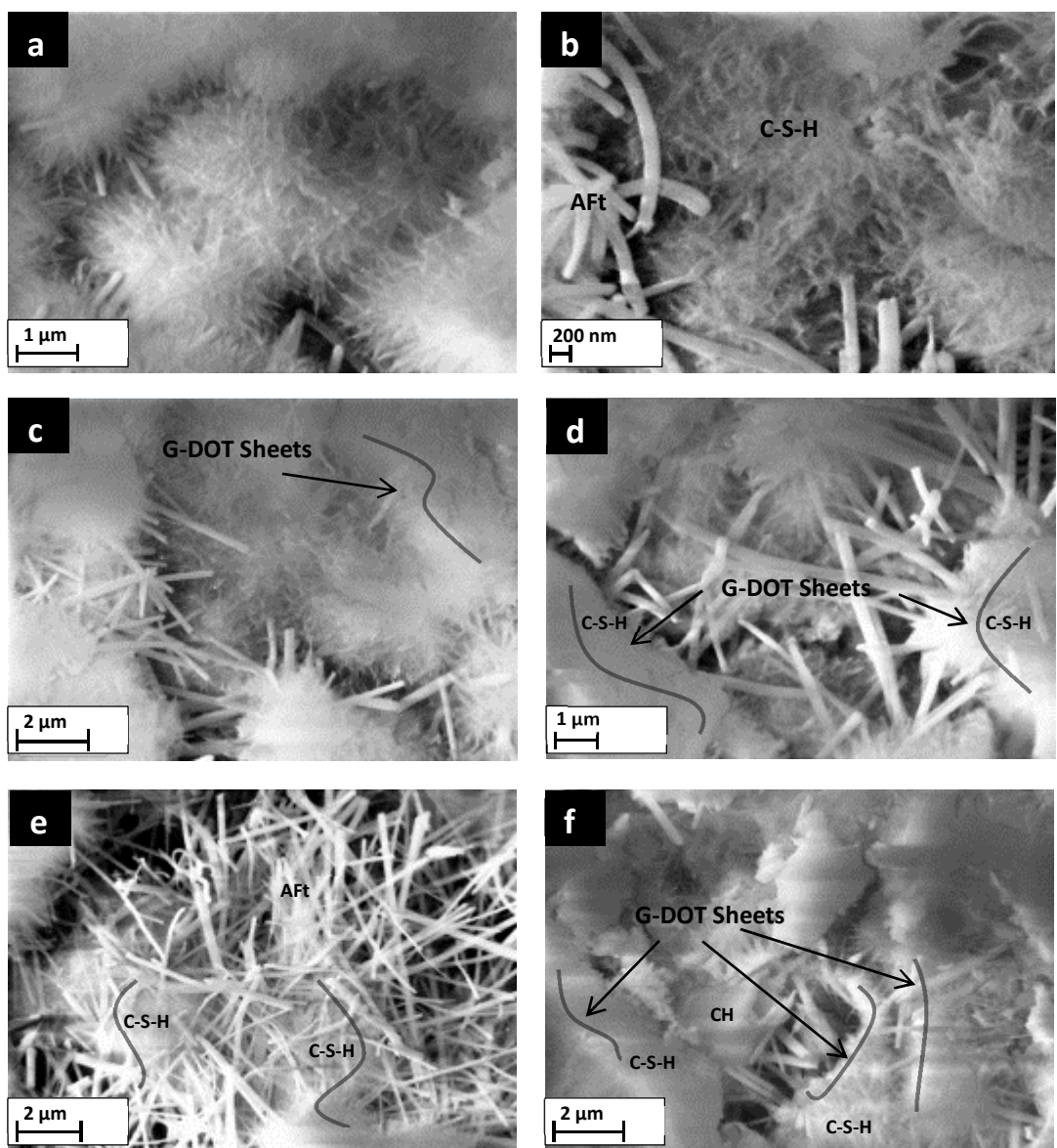
Figure 5.4 SEM images 7 days a) control b) and NGCC with G-Dot 0.01% c) G-Dot 0.02% d) G-Dot 0.03% e) G-Dot 0.04% and f) G-Dot with 0.05 %

These rod-like crystals may be calcium aluminate hydrates ettringite (AFt) 5-10 μm long with a diameter range of 100-150 nm and interlocked with each other. The main hydration product, calcium silicate hydrate (C-S-H) can be seen as gel-like structure (Fig. 5.4b) 2 to 3 μm diameter and also present in the form of amorphous solid (Winter, 2009).

A distinctive microstructure structure with increased growth of interlocked rod-like crystals emerging from denser, probably C-S-H, amorphous solid, has been observed in the SEM images of nanocomposite with G-Dot contents of 0.03% to 0.05 % (Fig. 5.4 to 5.4f). It seems that the addition of GNPs in the cement matrix has regulated the microstructure and promoted the growth of hydration products. The mechanism that could regulate the microstructure of cement matrix by adding G-Dot may act in two ways; the first may be the nucleation of G-Dot by attracting the cement particles, due to its high surface energy, on its surface. Secondly, due to the wrinkle-free morphology of G-Dot might have channelised the growth of hydration products (C-S-H, CH, AFt) by developing new pores system. It is also reported that the addition of graphene sheets support the formation of micro C-S-H clusters, CH, AFt and AFm crystals in the cement matrix. Also, these sheets introduce new pores ranging from 15 nm to 10,000 nm in the cement matrix (Mohammed et al., 2015; Sobolev et al., 2008). It can be seen that C-S-H amorphous solid grown preferentially on the surface of G-Dot due to its nucleation effect in the cement matrix, a similar effect has also been reported for SWCNT (Makar and Chan, 2009; Li, Wang, and Zhao, 2007). Moreover, other crystals (CH, AFt, AFm) are grown outwards from both surfaces of G-Dot to develop distinctive microstructure which is in agreement with that reported by Lv et al., 2013. In the SEM images of the nanocomposite denser C-S-H amorphous solid structure grownup presumably around the G-Dot nanoplatelets, indicated by arrows, can be seen in Fig. 5.4c to 5.4f. This might be due to hydration of attached cement particles. Also, the rod-like crystals (AFt) in large amount are grown in between these nanoplatelets. This growth effect of crystals is more visible in NGCC with G-Dot 0.03% to 0.05%. It is worth mentioning that G-Dot nanoplatelets not only acted as nuclei to grow C-S-H and other hydrated products on its surface but might have also acted as nano reinforcement to build stronger microstructure. The appearance of additional diffraction peaks related graphene, AFt and CH in XRD pattern and higher absorbance intensities in FTIR spectrum of the NGCC also indicated the presence of graphene and formation of denser matrix structure due to the increased number of bonds. With the continued hydration of cement particles, this pattern and arrangement of hydration crystals become further denser, and most of the crystals (AFt, CH) transformed into new crystals of

lamellar and polyhedral shapes. A lamellar structure with few nanometres layer thickness at the age of 14 days has been observed in the nanocomposite with G-Dot 0.04% as shown in the Fig.5.5. It was also reported that rod-like crystals ettringite (AFt) could transform into monosulfoaluminate (AFm) reacting with C_3A and giving rise to the layered structure (Taylor, 1992).
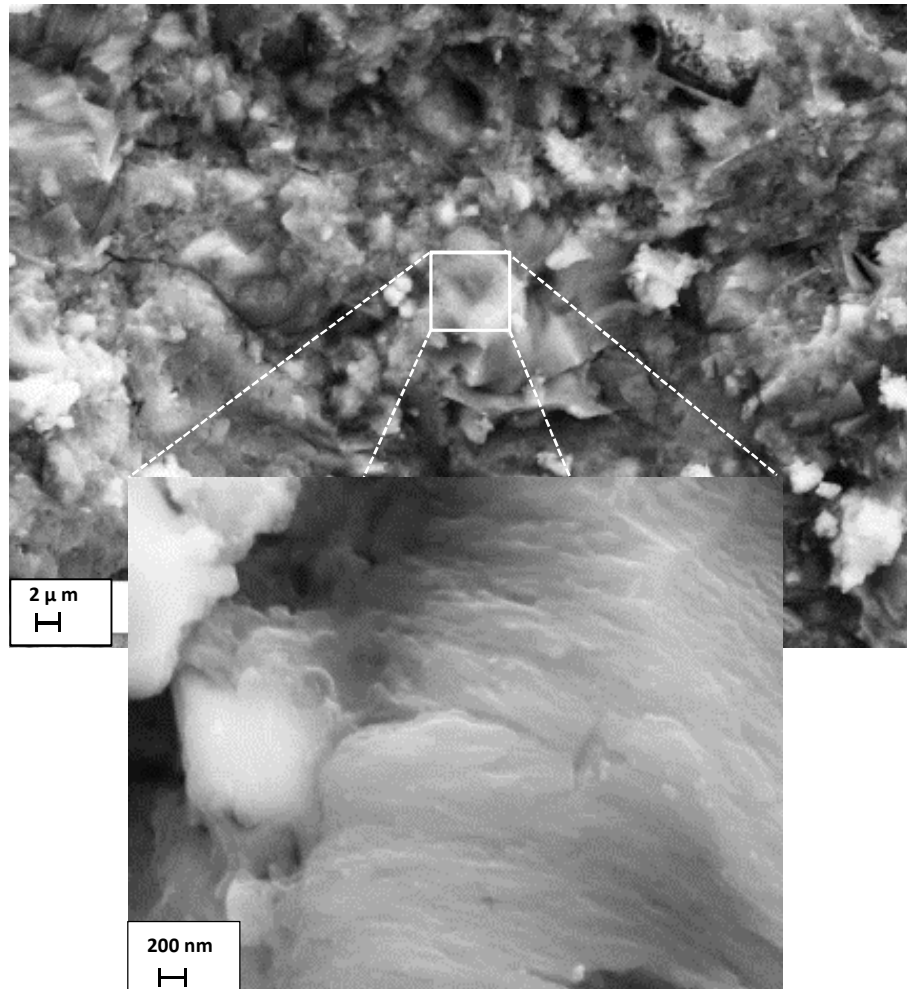
Figure 5.5 SEM micrograph of 14 days showing layered crystals structure in NGCC with G-DOT 0.04%

More solid and denser structure in controlled and NGCC samples has been observed at the age of 28 days (Fig.5.6). Most of the gaps and cracks at micro and nano level in NGCC samples seem filled up due to further growth and transformation of hydration products in the distinctive microstructure developed at the start of hydration with the nucleation of G-Dot nanoplatelets. However, cracks are apparent and wider in controlled cement sample Fig.5.6a.

Moreover, lamellar and polyhedron shape crystals have been observed at this stage in the nanocomposite especially in samples with G-Dot concentration 0.03% to 0.05% Fig. 5.6d

to Fig.5.6f. In a uniformly compact, denser and hardened cement matrix, these lamellar and polyhedral crystals of hydration products are fused together while encased with C-S-H (Fig.5.6f). Through examining SEM micrographs of both controlled and NGCC samples with a varied amount of G-Dot, it has been observed that presence of G-Dot nanoplatelets helped in assembling and regulating the growth of hydration crystals led to form a distinctive microstructure. This distinctive microstructure further matured and crystals structure transformed into lamellar and polyhedral shapes encased by C-S-H may lead to enhance the mechanical properties of the NGCC.
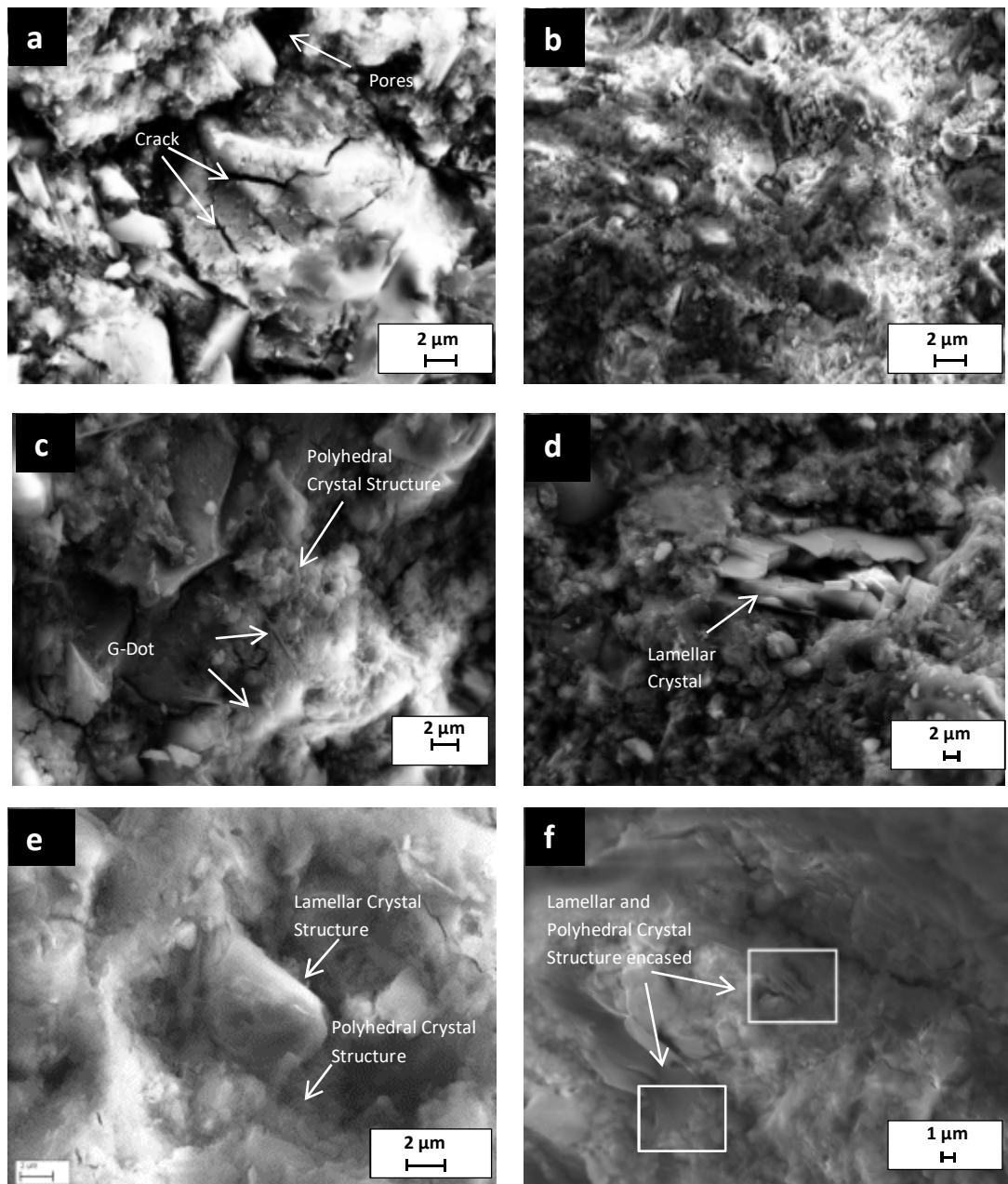
Figure 5.6 SEM micrographs of 28 days a) Control b) and NGCC with G-Dot 0.01% c) G-Dot 0.02% d) G-Dot 0.03% e) G-Dot 0.04% and f) with G-Dot 0.05%

EDAX analysis (Table.5.2) has been performed to verify the chemical and element composition of these different shaped crystals formed in the NGCC. From the element percentage, it can be seen that lamellar crystal structure (Fig.5.7a) has contents of Ca, Al, S and Fe and this element composition is close to calcium aluminate hydrates (AFt, AFm) family. The polyhedral crystal structure is shown in Fig.5.7b also contains Al and Fe content but higher contents of Ca relate them with CH crystals. The rod-like structures formed at the early stage of hydration (Fig.5.7c) has element composition close to ettringite (AFt) indicated by the presence of higher contents of Al. C-S-H gel structure also has been identified at EDS spot 2 marked in Fig.5.7c with Ca/Si ratio of 2.28.
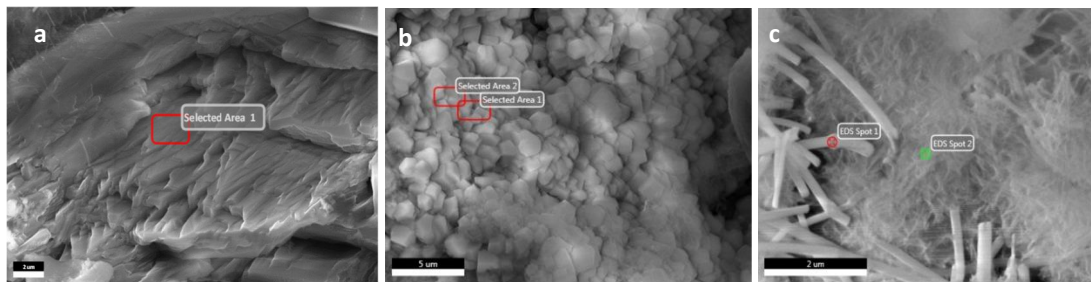
Figure 5.7 EDAX analysis of hydration crystals in NGCC a) lamellar crystal structure in NGCC with G-DOT 0.03% b) polyhedral crystal structure in NGCC with G-DOT 0.04% and c) rod-like crystal and C-S-H gel structure in NGCC with G-DOT 0.01%

Table 5.2 Chemical Composition of hydration crystals

Cement hydration crystals	Element percentage (%)								
	C	O	Ca	Al	Si	S	Mg	K	Fe
Fig 5.7a : Lamellar crystals	1.31	55.11	26.18	2.75	7.54	1.96	0.46	0.65	2.62
Fig 5.7b: Polyhedral crystals (area 1)	1.57	65.35	29.58	0.84	2.45	0.00	0.28	0.00	0.00
Fig 5.7b: Polyhedral crystals (area 2)	1.47	63.25	30.15	0.82	2.18	0.00	0.34	0.00	0.51
Fig 5.7c: Rod-like crystals (spot 1)	0.00	63.23	23.58	2.99	8.04	1.11	0.61	0.41	0.00
Fig 5.7c: C-S-H gel (spot 2)	0.00	64.39	23.41	0.62	10.24	0.79	0.53	0.00	0.00

It is important to mention that nevertheless, the nucleation and reinforcement of G-Dot nanoplatelets promoted the growth of hydration crystals and development of distinctive microstructure in cement matrix but some loose crystals structures were also observed (Fig.5.8) in some samples with a higher concentration of G-Dot. In these samples, nanoplatelets turned into rolled up structures and may cause defects in the microstructure.

These defects can develop large pores and can initiate microcracks when subjected to flexural loads consequently responsible for strength variation in NGCC composites.
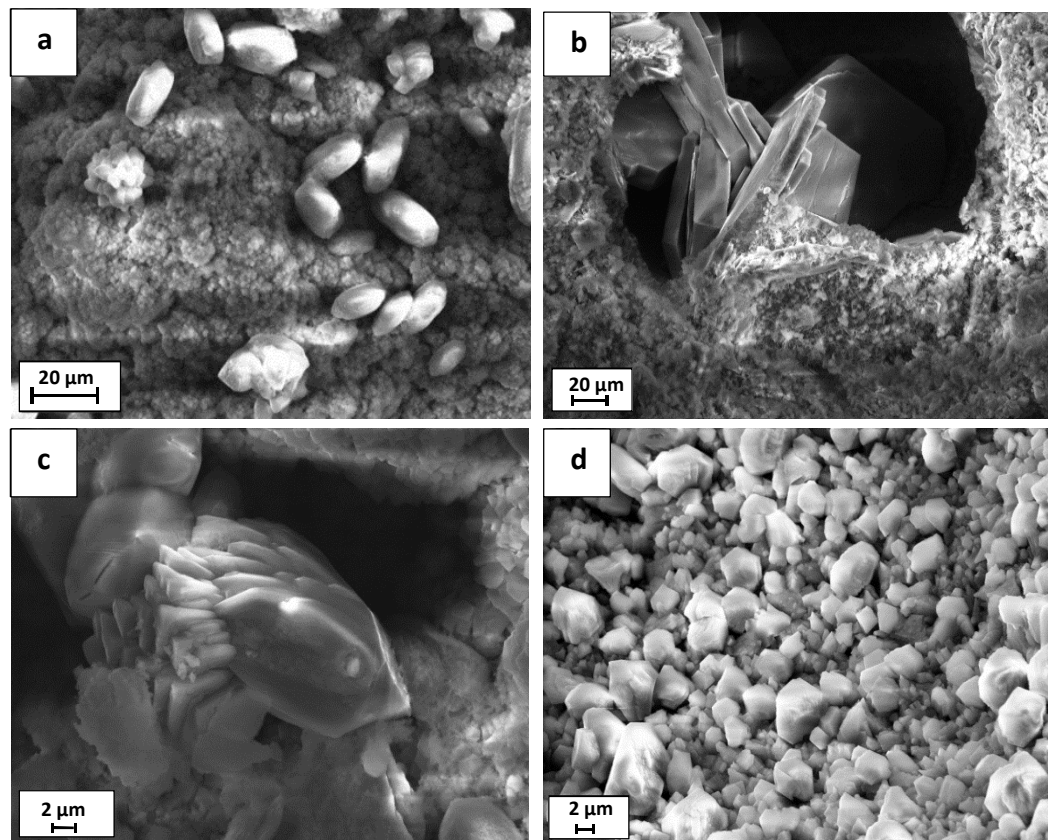
Figure 5.8 Loose crystal structure formation in nanocomposite a) rolled up G-Dot graphene found in NGCC 0.05 % b) regular hexagonal crystals of CH found in pores of NGCC 0.03% c) lamellar crystal fish like structure growth observed in gaps of NGCC 0.05% and d) loose polyhedral crystal structure in NGCC 0.04%

5.3.3   Effect of G-Dot on Mechanical Properties of NGCC

Mechanical strength test results of control and nanocomposite samples, loaded with various contents of G-Dot, are presented in Table 5.3. Samples were divided into six categories according to G-Dot contents added into cement. Further, six number of samples were tested under each category. Graphs presented in Fig.5.9 depicted the effect of adding various contents of G-Dot graphene (0.0% to 0.05%) by weight of cement in NGCC on flexural and compression strength at the age of 7, 14 and 28 days. Controlled cement composite is one with 0.0% G-Dot. The graph indicated that the flexural and compression strength increased with increased contents of G-Dot in NGCC. However, in the NGCC with G-Dot 0.05% this effect seems not protruding with sustained strength values. Increased strength in a nanocomposite with increased contents of G-Dot sheets may be due

to the acceleration of hydration process and formation of more dense and distinctive microstructure through augmented nucleation of G-Dot nanoplatelets, discussed above and shown in Fig 5.4.

Table 5.3 Mechanical strength test data

Flexural Strength									
	7days			**14days**			**28days**		
Sample ID	**MPa**	**% inc**	**% cov**	**MPa**	**% inc**	**% cov**	**MPa**	**% inc**	**% cov**
Control	6.78	0.00	5.43	7.22	0.0	4.54	7.81	0.0	4.48
G-Dot 0.01	7.09	4.57	4.27	7.81	8.2	5.57	8.81	12.7	4.55
G-Dot 0.02	7.79	14.79	6.67	8.70	20.5	6.21	9.13	16.9	5.45
G-Dot 0.03	9.93	46.35	7.54	10.17	40.9	5.97	10.42	33.3	6.57
G-Dot 0.04	10.50	54.78	5.66	10.75	48.9	5.16	11.28	44.3	4.50
G-Dot 0.05	10.51	54.90	6.67	10.72	48.5	7.31	11.25	44.0	4.22
Compressive Strength									
	7days			**14days**			**28days**		
Sample ID	**MPa**	**% inc**	**% cov**	**MPa**	**% inc**	**% cov**	**MPa**	**% inc**	**% cov**
Control	65.55	0.00	2.34	73.93	0.00	2.21	79.21	0.00	1.87
G-Dot 0.01	71.65	9.31	2.15	76.34	3.25	2.50	80.64	1.81	2.27
G-Dot 0.02	73.36	11.92	2.09	77.53	4.87	2.88	83.03	4.83	2.17
G-Dot 0.03	76.59	16.85	2.37	82.12	11.08	2.06	86.43	9.12	1.87
G-Dot 0.04	82.31	25.57	2.94	91.67	24.00	2.03	93.72	18.32	0.83
G-Dot 0.05	82.37	25.67	3.54	91.50	23.76	2.36	93.70	18.29	0.46

Graphs also indicated that NGCC with G-Dot contents of 0.04% exhibited a maximum value of flexural and compressive strength and hence regarded as optimum contents for the strength enhancement in the nanocomposite. At this optimum value, both flexural and compressive strengths are increased by 55.60 % and 25.57 % respectively at the age of 7 days as compared to the control samples. From SEM micrographs shown in Fig.5.4, it seems that rod-like AFt crystals played an important role in reinforcing the C-S-H structure and densifying overall cement matrix leading to enhance the flexural strength of NGCC especially when G-Dot contents are 0.04%. In a detailed study of hydration products, the formation of rod-like (AFt) structure in the cement matrix is revisited by researchers and found to be effective for filling spaces, reducing porosity and permeability of hardened cement paste at early days of hydration (Matschei et al., 2007). Moreover, G-Dot sheets, with its excellent mechanical properties, presumably encased by C-S-H might have also acted as nano-reinforcement in the cement matrix. Therefore, the combined reinforcing effect of G-Dot sheets, rod-like (AFt), lamellar (AFm), polyhedral and plate-like (CH) crystals encased with C-S-H might have led to the enhancement of the overall strength of

NGCC at this age of hydration. Increase in flexural and compressive strength of NGCC with G-Dot contents 0.04% is, marginalised to 44.3 % and 18.32 % respectively at the age of 28 days.
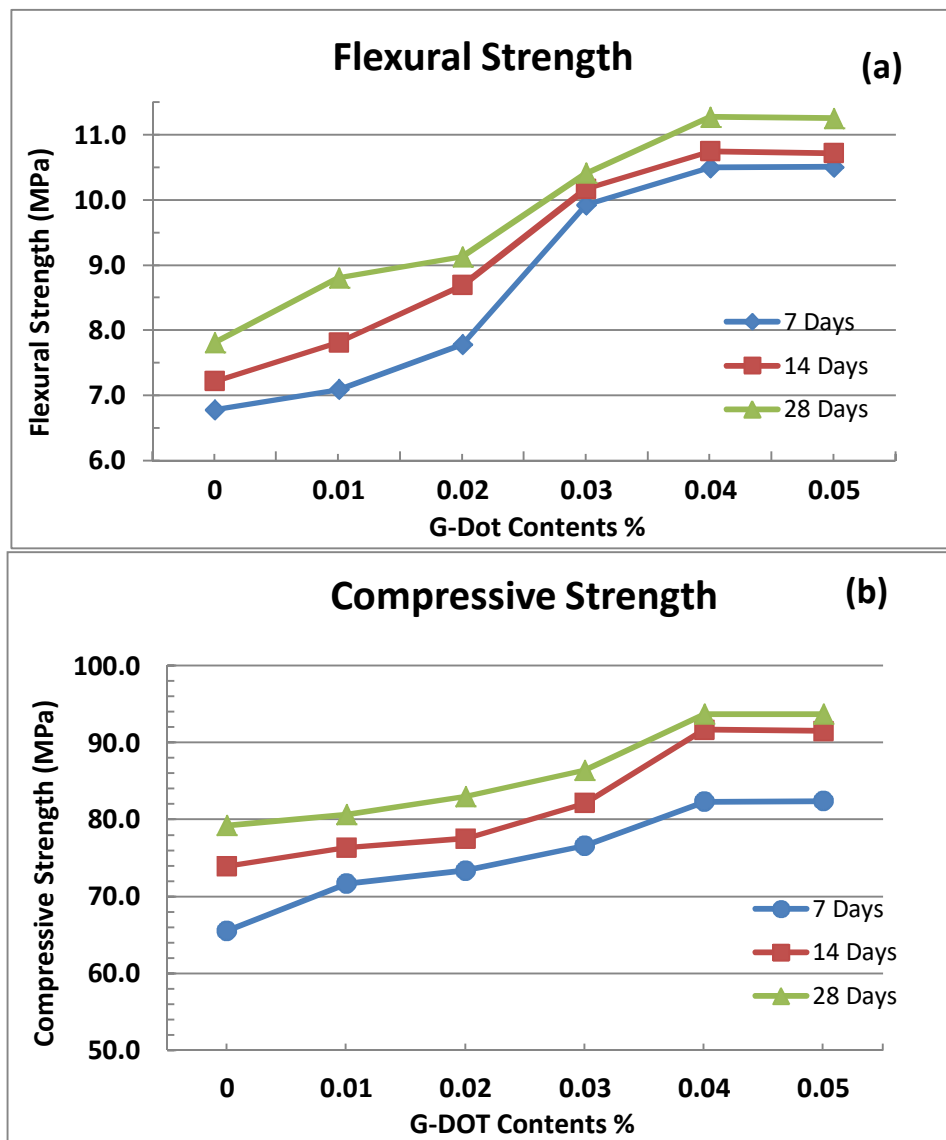
Figure 5.9 Comparison of strength of control and NGCC with varied contents of G-Dot at 7, 14 and 28 days a) flexural strength graph b) compressive strength graph

It can be justified that in control cement composite usual microstructure developed at the early age of hydration has also become denser and stronger by filling the pores with the growth of C-S-H structure and subsidised the strength deficit at this age. It can be seen from the graphs that the compressive strength increment trend is more linear and the increase is noticeable at the age of 14 days. Whereas, flexural strength increment has steeper trend and noticeable at the age of 7days. It may be inferred that both flexural and compressive strength are instigated in NGCC by different mechanism and type of hydration products.

It is more likely that the formation of AFt crystals grown at early days by hydration of C_3A and their transformation into the structure of a lamellar crystal like one observed in nanocomposite shown in Fig. 5.7a may work as a reinforcement for the C-S-H structure contributing towards the enhancement of flexural strength, while polyhedral and cube shapes denser crystals developed later with a hydration of C_3S and C_2S at a later stage of hydration encased with amorphous C-S-H like shown in Fig. 5.7b may be the reason for the increasing compressive strength of the nanocomposite.

Despite the fact that strength in nanocomposite increased remarkably with increasing contents of G-Dot, but variations in both flexural and compressive strength values were observed in each set of samples and indicated by error bars in the graphs shown in Fig. 5.9. These variations in strength values have also been calculated statistically and presented as the coefficient of variation percentage (COV%) depicted in Fig.5.10. It has been found that compressive strength results for both control and nanocomposite samples are mostly complying with the recommended COV value of 2.37 % mentioned in the C39-99 ASTM standards. Whereas, in case of flexural strength results COV values of some nanocomposite are higher than the recommended value of 5.7 % according to ASTM C8-02. The variability of strength in cement composite may be associated with the defects appeared in the microstructure due to large air pores, cracks and formation of loose CH crystals in the cement matrix. These defects are also observed in some nanocomposite with higher COV % in flexural strength and shown in Fig. 5.8. G-Dot nanoplatelets without any functional group attached on its surface might have some dispersion incompatibility in aqueous solution, also with increasing concentration of G-Dot in water solution may hinder their proper dispersion and converted them into rolled up a structure like shown in Fig. 5.8 a due to strong Van der Waal's forces.

These rolled up structures may be a cause to introduce gaps and air pores of large sizes with the weaker and defective microstructure of hydration products around them. A weaker microstructure has also been observed in G-Dot 0.05% with formation of loose regular, irregular, lamellar and polyhedral crystals shown in Fig. 5.8b, 5.8c and 5.8d which is likely to fail against applied loads particularly flexural loads. This phenomenon of weaker microstructure, near air pores, and its failure against flexural loads would equally be true for both control and nanocomposite. It is mentioned in the text (Mehta et al., 2013) that hexagonal crystal structure formed by portlandite (CH) relatively large with regular geometric shapes, can be seen when grown air pores, have less strength capabilities than C-S-H.
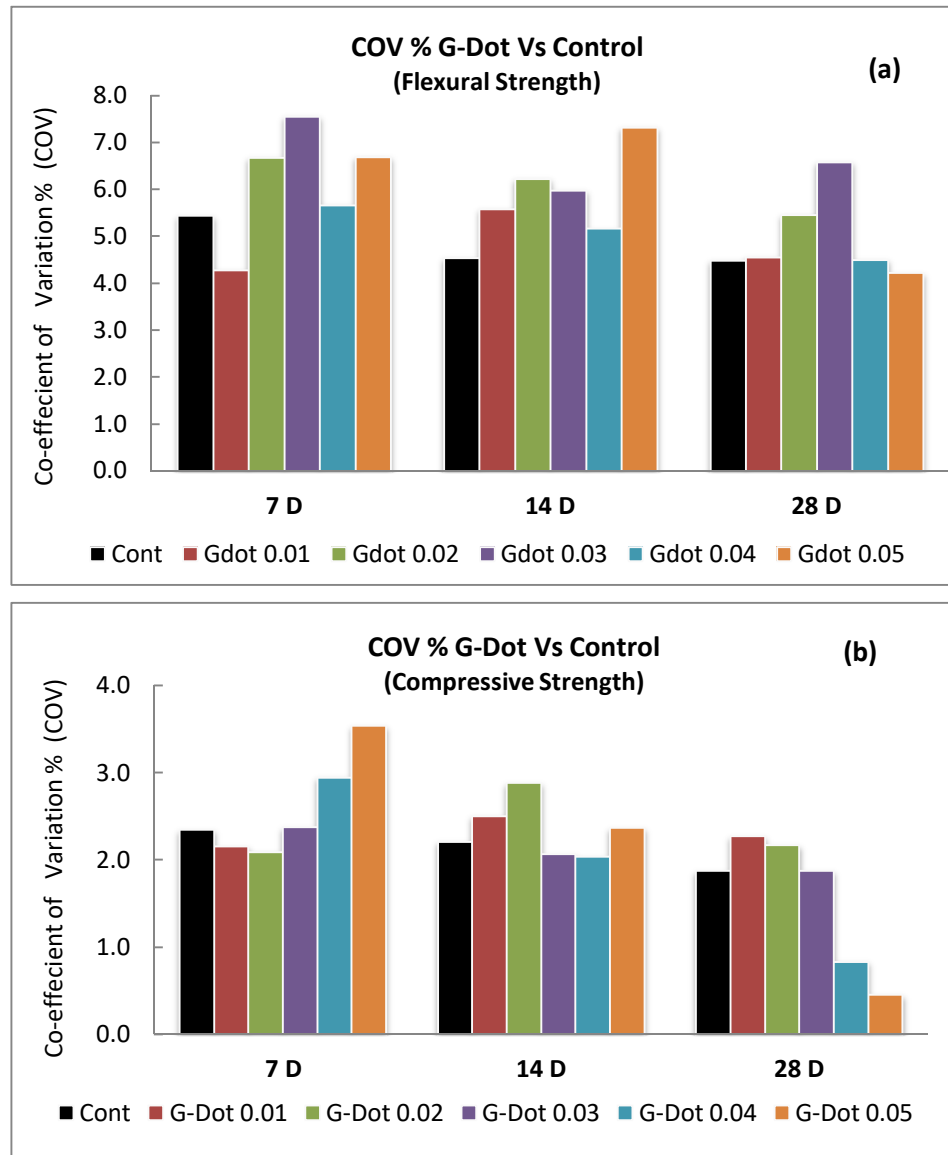
Figure 5.10 Coefficient of variation in strength values of control and NGCC-Dot at 7, 14 and 28 days a) COV % in flexural strength values b) COV % in compressive strength values

Form the mechanical test data it may be summarised that nanocomposite NGCC exhibited remarkable increase in strength especially flexural strength with G-Dot sheets contents of 0.04%. However, larger strength variations have been observed in some samples which might be due to agglomeration of G-Dot sheets causing defects in some samples. Functionalised nano-graphene sheets with better dispersion capabilities may increase nucleation effect with more reactive sites on their surface and reduce the formation of the defective microstructure to limit the strength variations.

5.4 Conclusions

Nano-graphene cement composite (NGCC) has been developed by using plasma treated nano-graphene sheets and investigated for its phase change, chemical composition and development of microstructure. It has been revealed from the test data and SEM micrographs that small amount of G-Dot nanoplatelets promoted the growth and arrangements of cement hydration crystals on or near the GNPs surface leading to develop distinctive microstructure and enhance its mechanical properties especially when G-Dot contents were 0.04% bwoc.

G-Dot initiated the nucleation effect attracting the small cement particles on or near its surface with nucleation effect due to its honeycombed structure, high aspect ratio and high surface energy. G-Dot might have acted as nano reinforcement and provided the strong interfacial bond between cement hydration products, especially with C-S-H grown along with its surface. Apart from G-dot as nano-reinforcement, rod-like (AFt) structures finally transformed into lamellar shape crystals might have also contributed to enhancing the early flexural strength, while hexagonal plate-like (CH) and polyhedral shape crystals encased with C-S-H may have contributed to the compressive strength. NGCC exhibited a remarkable increase in flexural and compressive strength at 7 days with G-Dot contents of 0.04% by 55.60 % and 25.57 % respectively. However, this margin in flexural and compressive strength mutated at a later stage but still with a significant value of 49.41 % and 24.00% at 14 days, 44.43 % and 18.32 % at 28 days, respectively.

This research is not limited or exhaustive but opens the corridors for the potential and practical application use of GNPs in the field on graphene nano-cementitious composite. Like other forms of graphene such as functionalised with $-O_2$, -COOH and $-NH_2$ functional groups with better dispersion capabilities might have more nucleation and intrinsic impact on the mechanical properties of cement composite.

CHAPTER 6 Development of NGCC-Fnt

6.1 Introduction

In the previous chapter, G-Dot nanoplatelets were harnessed in the cement matrix for the development of the NGCC-Dot. Improved mechanical properties of the nanocomposite at an early age of hydration are a testament to the effective use of the nanoplatelets (G-Dot) in the cement matrix. However, higher standard deviations in the strength values were observed may be due to agglomeration of G-Dot nanoplatelets in the cement matrix. The hydrophilic behaviour of pristine graphene can be improved with the covalent surface modification, generally termed as functionalization, by adding the desired chemical group to their surface. These functional groups not only support the dispersion of graphene sheets in the aqueous solution but also supply more reactive sites to cement particles during nucleation process to develop a strong bond with C-S-H (Lv et al., 2013).

The chemical surface modification techniques use harsh chemicals and acid for functionalization and degrade the structural and mechanical properties of graphene as discussed in section 2.8 of chapter 2. Whereas, the functionalization of graphene using plasma exfoliation technique enables to attach the desired chemical functional groups such as $-O_2$, $-NH_2$, $-COOH$, $-Ar$ and $-Br$ on graphene surface without degrading its structure. This provides greater ability to disperse in aqueous solution and better compatibility between various matrices resulting in enhanced surface and mechanical properties. Graphene nanoplatelets also termed as HARN (High Aspect Ratio Nanomaterial) because of their small size and high aspect ratio, and nano size, high aspect ratio and presence of Van der Wall's forces. These forces cause them to agglomerate when mixed in aqueous solution. Functionalization via plasma technique leads to disentanglement and exfoliation of these nanoplatelets and stop de-agglomeration (Haydale Ltd., 2016). The same sort of agglomeration has been experienced in case of G-Dot during the processing of NGCC-Dot discussed in section 5.2 of chapter 5. Moreover, as compared to GO, the plasma functionalization of GNPs is a low cost and sustainable green process leaving no industrial waste because it uses low temperatures (less than $100^{\circ}C$) and does not utilise a chemical or acid treatment which, generally degrades the functional performance of graphene.

The effect of functionalised graphene, other than GO, on the microstructure of cement matrix, is reported in very limited research, mentioned in Table 2.10 of chapter 2. This needs further investigation to probe the mechanism of crystal formation in the light of

cement hydration chemistry and requires scientific evidence through characterization techniques. The kinetics of cement hydration broadly progresses by two ways, chemical and physical hydration. Chemical hydration involves the reaction of cement and the dissolution of ions in water, and further reaction to form new chemical compounds. Whereas in physical hydration, the growth and formation of hydration products are in the form of crystals and amorphous solids which takes place to form microstructure, hence reduces porosity and densifies the cement matrix ultimately responsible for the enhanced mechanical properties (Li and Liang, 2011).

Recently a physical model was proposed for the microstructure of cement matrix with the insertion of GO sheets in which cement hydration crystals are bloomed as flower-like structure, leading to enhance mechanical properties (Lv. et al., 2013). The model was proposed by SEM micrographs obtained from the cement composite samples prepared using polycarboxylate superplasticiser (PC) that might have also influenced the growth of hydration products. Therefore, to fully understand the formation of hydration crystal and their sole interaction with homogeneously dispersed graphene nanoplatelets in the cement matrix, the development of functionalised nanographene cement composite (NGCC-Fnt.) is proposed without using any admixture.

This chapter covers the understanding of seeding effect of functionalised GNPs, grafted with various chemical groups, on the cement hydration kinetics by stimulating the growth of hydration products in a distinctive way, leading to enhance its mechanical properties. The possible mechanism of dissolution of cement ions, nucleation, crystal formation and patterned growth regulated by the plasma processed functionalised GNPs (G-Fnt) in the microstructure development of cement has been discussed. Three different types of the functionalised graphene nanoplatelets called $G-O_2$, $G-NH_2$ and $G-COOH$ synthesised via plasma exfoliation method have been used in the development of NGCC. The primary hypothesis behind this study is that the better dispersion and more reactive sites grafted on the surface of unique 2D shape G-Fnt nanoplatelets may enhance nucleation effect and growth of hydration crystals in the cement matrix. This would help understand the formation mechanism of cement hydration crystals regulated by the G-Fnt nanoplatelets and their influence on the further growth of hydration products to form a distinctive microstructure, leading to the enhancement of mechanical properties of nanographene cement composite.

The effect of G-Fnt on both, chemical and physical cement hydration was observed by using sophisticated characterization techniques such as XRD, FTIR, RAMAN, MIP, SEM, EDAX and UTM. Results obtained from experiments are analysed and discussed to correlate the effects of G-Fnt on the development of microstructure and enhancement in the mechanical properties of NGCC in the subsequent sections.

6.2 Processing of NGCC-Fnt

In the processing of NGCC-Fnt, general procedure mentioned in chapter 3 was adopted. Specifically, the mix proportions used for the processing of nanocomposites are given in Table 6.1. NGCC-Fnt was processed without using any superplasticiser or polycarboxylate (PC) in order to observe and understand the discrete interaction and effect of GNPs on the arrangement, growth and regulating the microstructure of the cement matrix. Three types of functionalised nanocomposites (NGCC-O_2, NGCC-NH_2 and NGCC-COOH) were developed using graphene nanoplatelets functionalised with three different chemical groups as mentioned above.

Table 6.1 Mixing proportion of NGCC-Fnt

Sr. No	Composite Name	Sample ID	Cement Gm	GNPs mg	% BWOC	W/C
1 ^	Control	Control	1400	0.00	0.00	0.30
2	NGCC-O_2	G-O_2	1400	560	0.04	0.30
3	NGCC-NH_2	G-NH_2	1400	560	0.04	0.30
4	NGCC-COOH	G-COOH	1400	560	0.04	0.30

^ Control samples used for NGGC-G-Dot *BWOC=by weight of cement; W/C=water/cement ratio

A specified amount of GNPs was mixed in water through simple sonication for 30 minutes, and dispersion of GNPs in water was analysed using SEM images. Graphene stitched with functional groups can disperse well in water due to electrostatic repulsion induced by functionalization (Geng, Wang, and Kim, 2009). A better dispersion of G-$O_2$was observed in water as compared to G-COOH and G-NH_2. The structural and material properties of these nanoplatelets were discussed in chapter 4. For the dose of nanoplatelets to be used in the cement, an optimised concentration of 0.04% bwoc previously obtained for NGCC-Dot was used to make a comparison later between these nanocomposites.
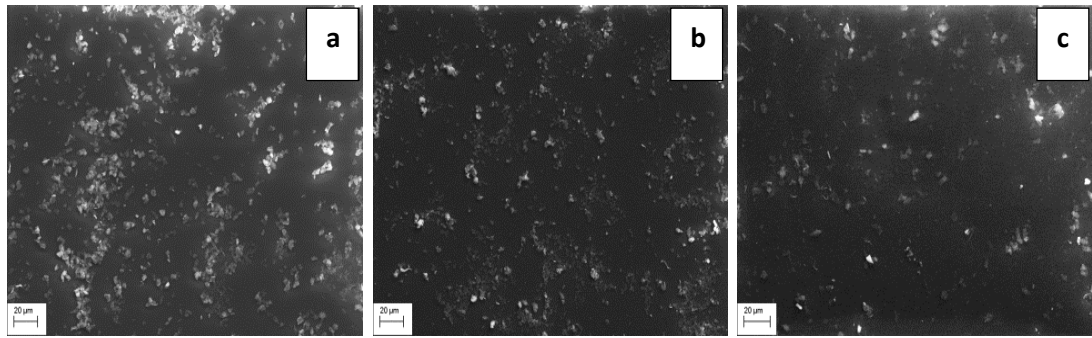
Figure 6.1 SEM images of dispersed GNPs 0.04% (a) G-O$_2$ (b) G-NH$_2$ (c) G-COOH

6.3 Results and Discussion

6.3.1 Effect of G-Fnt on Phase & Chemical Composition of NGCC

As discussed above that the chemical reaction of cement is still considered as very complex to understand due to the dynamics of dependency factors and formation of hydration products, but with the help of modern analytical techniques coupled with sophisticated computer software this complexity can be resolved up to a large extent. The XRD measurements were taken to analyse the effect of G-Fnt nanoplatelets on the phase and chemical composition of cement composite as per methodology, equipment and technique mentioned earlier in chapter 3. Fig 6.2 depicts the patterns of diffraction peaks observed in NGCC-Fnt and control cement samples at the age of 7 days. The graphite peak emerging from (002) plane near diffraction angle 26.5° in all three NGCC-Fnt samples visibly distinguished them from control cement sample. The intensities of graphite diffraction peaks vary with the type of G-Fnt and found higher for nanocomposite prepared with G-O$_2$ nanoplatelets. This suggests the uniform presence of graphene nanoplatelets being identified through XRD in the representative samples of NGCC-Fnt prepared from very small pieces of fractured part. The diffraction peaks related to C$_2$S, C$_3$S and calcite (CaCO$_3$) also appeared in all samples at their respective diffraction angles (Fig.6.2). The peaks related to C-S-H are not distinguished in XRD due to its amorphous or poorly crystalline calcium silicate hydrate structure. Whereas, during early days of hydration the most important AFt phases in cement hydration are the formation of ettringite and they form the hexagonal prismatic crystal structure. XRD readily detects these crystal structures due to their good crystallinity but sensitive to molecular water present in their structure (Taylor, 1992).

In XRD pattern of 7days (Fig.6.2) AFt phases can easily be distinguished by their strong and low angle diffraction peaks at diffraction angles 9.03°, 15.75°, 18.75°, 34.9°, 35.9° and

41.42°. It can be observed that intensity of peaks related to AFt phases is comparatively higher in NGCC-Fnt samples as compared to the control cement sample. The higher peak intensity due to AFt phases and can be related to the increased formation of ettringites in nanocomposite as compared to control cement composite sample. Moreover, the fraction of AFt peaks is greater in case of G-O$_2$ nanocomposite as compared to other two prepared with G-NH$_2$ and G-COOH. It may be due to more active sites available on the surface of G-O$_2$ due to functionalization of oxygen group.
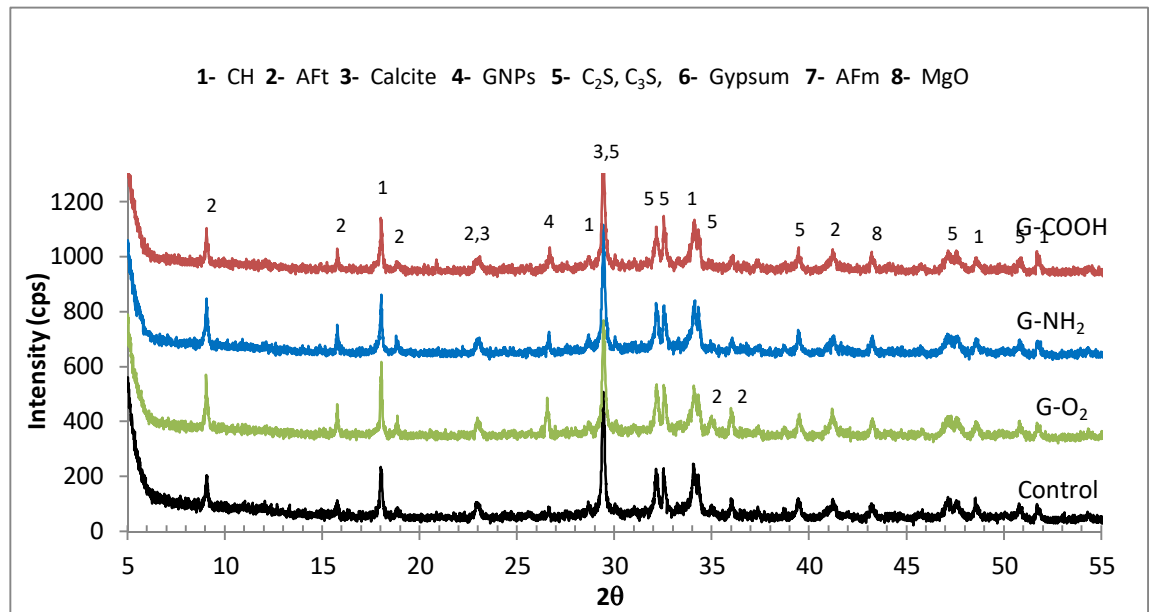
Figure 6.2 Combined XRD patterns of control and NGCC-Fnt samples at age of 7 days

The diffraction peak related to CH can be seen in all the samples (Fig. 6.2), and again its peak intensity is slightly higher in nanocomposite samples. AFm phase of cement hydration formed by the transformation of AFt phases is not detected at this stage of hydration.

The XRD patterns of NGCC-Fnt and control cement composite samples at the age of 28 days are depicted in Fig. 6.3. This indicates that the intensity of graphite peak at differential angle 26.5° diminished at this age of hydration. The reduction of diffraction peaks related to C$_3$S and C$_2$S has also been observed at this stage. This indicates the consumption of cement particles in the progress of hydration, leading to increase the contents of hydration products. The reduction in graphite peak intensity may be due to the increased growth of hydration crystals such as C-S-H and AFt in the cement matrix, which might have encapsulated the G-Fnt nanoplatelets and affected the diffraction. The two new peaks near diffraction angle 10.9° and 11.7° appeared in the samples of nanocomposites are

118

related to AFt and AFm phases, indicating that part of AFt transformed into the layered or polyhedral crystal structure. AFt and AFm crystals both provide reinforcing effect on the development of cement microstructure (Lv et al., 2013).
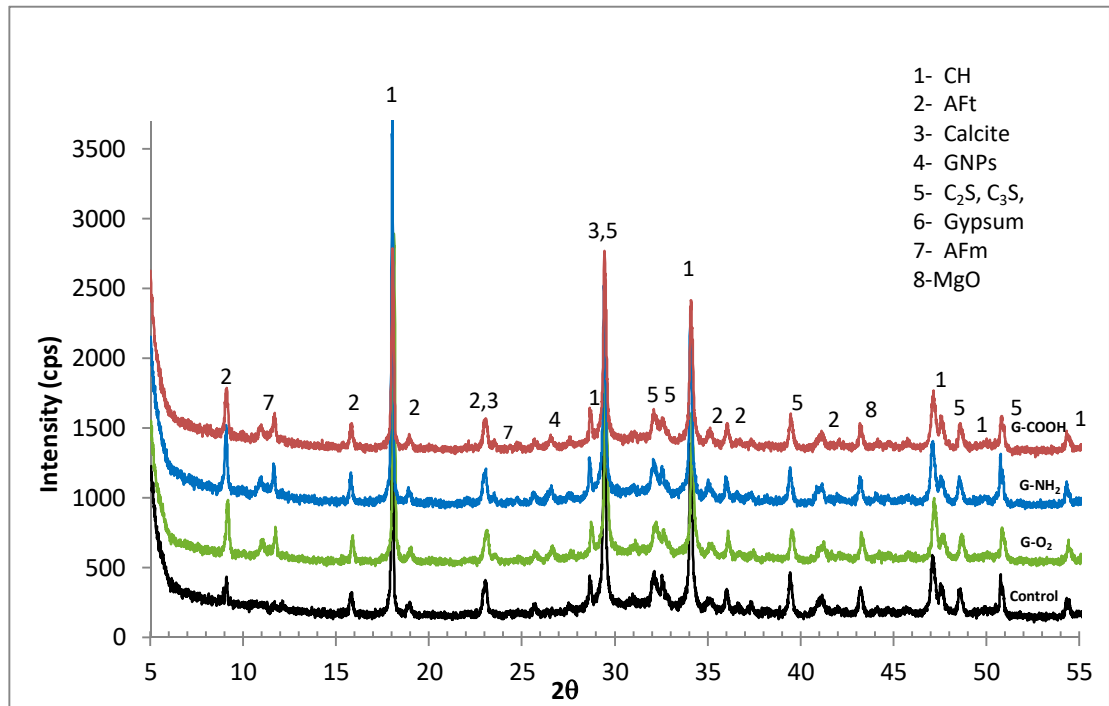
Figure 6.3 Combined XRD pattern of control and NGCC-Fnt samples at age of 28 days

The intensity of diffraction peaks related to CH at the age of 28 days has remarkably increased in the nanocomposite samples. This suggests that G-Fnt activated the growth of hydration crystals Aft and AFm, and was helpful to form the distinctive microstructure. In XRD various diffraction peaks of hydrated products are overlapped with the other higher peak intensities of anhydrous cement clinkers especially under the peaks of $CaCO_3$, C_3S, and C_2S. Therefore, to further reveal the effect of G-Fnt nanoplatelets on chemical composition and formation of bonds in a cement matrix, FTIR characterization technique was employed on NGCC-Fnt and control cement samples using the method, equipment and procedure mentioned earlier in chapter 3.

The resulting IR spectrum obtained from nanocomposite and control samples at the age of 7 and 28 days are depicted in the Fig. 6.4. The spectrums of NGCC-Fnt and control cement composite exhibits the absorption bands near 3647, 3450, 1650, 1429, 1117, 957, 876 and 714 cm^{-1} at 7 days, and comparatively with higher intensities at 28 days are shown (Fig. 6.4a and 6.4b). The absorption band at 3647cm^{-1} in both 7 days and 28 days samples is due to the stretching of OH present in CH, and this band is more intense in the case of

nanocomposite samples. The major absorption IR bands near 3450 cm^{-1} and 1650 cm^{-1} are regarded as water band area in the IR spectrum of hydrated cement due to stretching, and bending vibrations of H-O-H presented in the compound (Lucia.F et al., 2012). It is reported that ettringites exhibit a strong peak at 3422 cm-1 and a weaker one at 3545 cm-1 (Li, 2011) because AFt also contains plenty of water molecules attached with intervening channels of its hexagonal acicular crystal structure (Taylor, 1992). Therefore, the band representing the formation of AFt at early days of hydration in the spectrums of control and NGCC-Fnt may be representing these water bands at 3431cm-1 in the control sample. Whereas in NGCC samples of G-COOH, G-NH$_2$ and G-O$_2$ this band is more intense at 3430 cm^{-1}, 3412 cm^{-1} and 3413cm^{-1} respectively (Fig. 6.4a) indicating more ettringite formation.

Fig.6.4c represents the expanded view of 7 days spectrum between the range of 1850 and 650 cm^{-1} to distinguish the other characteristic bands. The band near 1651 cm^{-1} is also related to H-O-H but bending (v_2) vibration of molecular water and this band is present in all composite samples but being more intense in nanocomposite samples. The sharp band of absorption at 1117 cm^{-1} is due to stretching vibrations (v_3) of SO$_4^{-2}$ which indicates the presence of ettringites in control and particularly with more intense absorption value in the NGCC-Fnt samples. A similar absorption band near this value has been identified for the presence of ettringite in the hydrated ultrafine cement paste (Kontoleontos et al., 2013). The presence of sulphate absorption bands due to stretching of v_3 between the range of 1100-1200 cm^{-1} was also reported (Mollah et al., 2000; Hughes, 1995; Ghosh and Handoo,1980; Kloprogge et al., 2002). In the Fig. 6.4 the strong characteristic bands related to the presence of CaCO$_3$ can be seen at two locations, one between 1427-1429 cm^{-1} due to combined vibration of the v_2 and v_3 band, and another between wavenumbers 874-876 cm^{-1} due to vibration of the v_4 band. The characteristic band centred at 957 cm^{-1} is due to the strong asymmetric stretching vibration v_3 of the Si-O band, indicating the formation of C-S-H due to polymerization of SiO$_4$ in control and with intense absorption bands in NGCC samples.

Intense bands which appear in FTIR spectra are sometimes characterized as weak bands in Raman spectroscopy, and this is true vice versa. For example, FTIR bands related to silicates are intense while weak in Raman spectroscopy. Similarly, sulphates bands in Raman are sharp and well defined while in FTIR this band may be dominated by other bands between 1000 and 1200 cm^{-1}(Black et al., 2006). Using Raman spectroscopy as a

complementary to FTIR may help in analysing the formation of hydration products in a cementitious matrix. Therefore, to further investigate the growth of hydration products due to activation of G-Fnt in the cement matrix, Raman spectroscopy characterization technique was employed on NGCC-Fnt and control cement samples as per procedure, equipment and methodology laid down in section 3.6.5 of chapter 3.
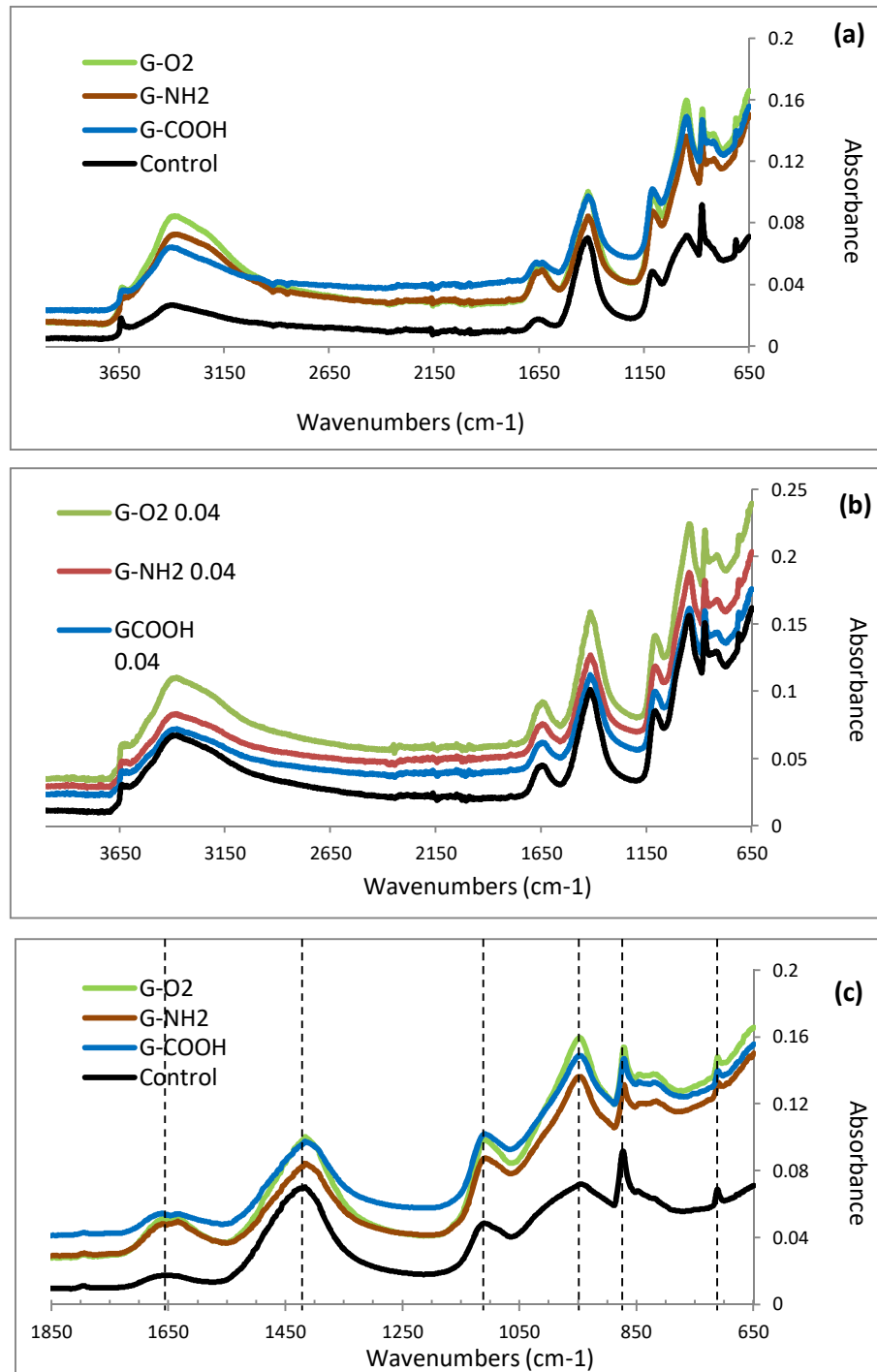
Figure 6.4 Combined FTIR spectrum of controlled and NGCC-Fnt a) at the age of 7 days (b) at the age of 28 days and (c) expanded view of 7days spectrums between 1850 and 650 cm^{-1}

Fig. 6.5 depicts the Raman spectrum (RS) of control and NGCC-Fnt cement composites loaded with G-O_2 nanoplatelets at the age of 7 days. The RS of control and NGCC-Fnt can easily be distinguished by the characteristics D and G peaks of graphene at 1362 cm^{-1} and 1584 cm^{-1} respectively (Fig. 6.5a-b). This suggests that G-O_2 nanoplatelets are homogenised with the cement matrix and activated the formation of hydration products. A similar effect has been observed in the XRD and FTIR spectrums discussed above. The peaks related to other hydrated and un-hydrated cement products can be distinguished clearly in Raman spectrums of both samples. The typical RS characteristic peaks anhydrous cement and hydrated products observed and reported by other researchers are listed in Table 6.2. The Raman spectrum of pristine G-O_2 obtained while analysing structural properties of GNPs, discussed in chapter 4, was superimposed with the spectrum obtained for NGCC-O_2 at the age of 7 days as shown in the Fig. 6.5c.

Table 6.2 Typical Characteristic RS Peaks for anhydrous cement and hydrated products observed and reported by researchers (Liu, Sun, and Qi, 2015)

Compound	Raman Shifts (cm^{-1})	Researchers
C_2S	846-864	Bensted 1976; Conjeaud and Boyer 1980; Gastaldi et al. 2007
C_3A	750-760, 504-510	Bensted 1976; Conjeaud and Boyer 1980; Torréns-Martín et al. 2013
CH	356-359	Conjeaud and Boyer 1980; Tarrida et al. 1995; Garbev et al. 2007
C-S-H	600-700, 450-500	Tarrida et al. 1995; Kirkpatrick et al. 1997; Garbev et al. 2007
AFt (Ettringite)	987-992	Sahu et al. 2002; Renaudin et al. 2007; Torréns-Martín et al. 2013
AFm	979-984	Black et al. 2007; Renaudin et al. 2007; Torréns-Martín et al. 2013

It can be seen that intensity of D-peak in the spectrum of nanocomposite has increased remarkably. This indicates the higher in-situ oxidation activity of graphene nanoplatelets and may be triggered due to chemical reactions taking place during the hydration process. As discussed earlier in the literature review, that oxidation of graphene sheets provides high surface energy to build up more active sites on its surface and can be helpful for the nucleation in the cement matrix. This view is supported by the observed increased growth of C-S-H in the nanocomposite sample when compared with control cement composite. In the RS of control cement composite (Fig 6.5a) small peaks near 414 cm^{-1} may be assigned to C-S-H, and this peak seems shifted to a smaller peak at 485 cm^{-1} and a stronger peak at 640 cm^{-1} in NGCC-GO_2 sample (Fig. 6.5b). These RS shifts are near to the corresponding

values of C-S-H also observed by (Garbev et al. 2007) and others researchers listed in Table 6.2. Moreover, the strong peak related to C-S-H in the RS of NGCC-GO$_2$ indicates higher C-S-H contents in the sample because a stronger peak corresponds to a higher concentration of the hydration products in the matrix (Liu, Sun, and Qi, 2015).
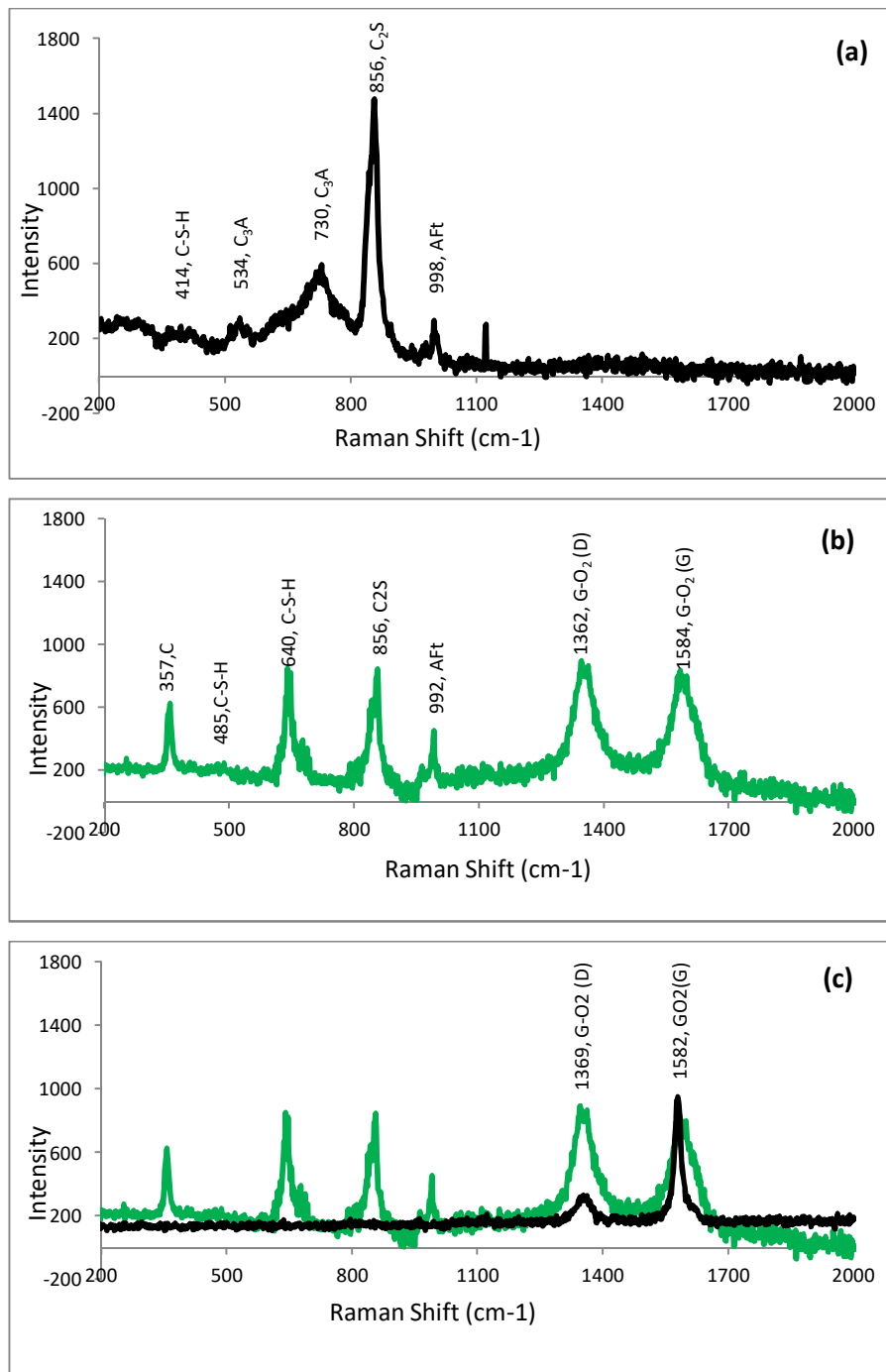
Figure 6.5 RAMAN spectra at the age of 7 days a) control b) NGCC loaded with G-O2 c) combined spectra of NGCC-GO$_2$ and pristine G-O$_2$

A sharp peak at 356 cm^{-1} in the spectrum of NGCC sample (Fig. 6.5b) is due to the absorption of OH^{-} on the surface of Ca$^{2+,}$ and this shift is also quite close to the reported value for CH (Garbev et al. 2007) and others (Table 6.2). CH is an important product of cement hydration and obviously present in control sample as detected by XRD and FTIR data, but its characteristic peak could not be mapped here in the control sample, this might be due to the scanning of a very limited area of the cement sample.

In Fig.6.5a two other peaks at 534 cm^{-1} and 730 cm^{-1} are assigned to the stretching of Al-(OH) indicates the presence of C$_3$A in control sample. These peaks seem depleted in the nanocomposite sample (Fig.6.5b) because the peak attributed to the formation of ettringite in the control cement sample (Fig. 6.5a) comparatively less intense at 998 cm^{-1} shifted to intense peak at 992 cm^{-1} in the NGCC-GO$_2$ sample (Fig. 6.5b). This shift might be due to the active chemistry of AFt phases and consumption of C$_3$A reacting with gypsum. It is mentioned in previous research (Liu, Sun, and Qi, 2015) that with the progress of cement hydration C$_3$A further reacts, after depletion of all gypsum, with AFt phases to transform them into AFm phases and these phases can be characterised by the RS peaks in the range of 979-984 cm^{-1}. The spectrum of control cement sample (Fig. 6.5a) also exhibited a strong peak at 856 cm^{-1} representing un-hydrated C$_2$S. This is also accordance with the value reported (Bensted et al.) in Table 6.2, but the peak at the same position in nanocomposite sample has shown a less intense value indicating the consumption of C$_2$S.

Test data also revealed that nanocomposite activated with G-O$_2$ comparatively yield more diffraction peaks and intense spectrums owing the formation of more hydration products of CH, AFt and C-S-H as compared to the other nanocomposite activated with G-NH$_2$ and G-COOH. Therefore, it can be suggested that G-Fnt provided the environment for generating pores and a concentration of ions where water molecules at nanoscales helped the growth of hydration crystals especially AFt during early days of hydration.

Through XRD pattern, FTIR and RS spectrum analysis it may be inferred that more ettringite (AFt) formation has been identified at the 7days and increased the growth of CH crystals between 7-14days of hydration with the activation of GNPs in the cement matrix but no peak related to new compound has been observed. Further, intense D-peak in RS of NGCC-O$_2$ suggests the nucleation effect of GNPs.

6.3.2 Effect of G-Fnt on the Pore Size Distribution of NGCC

Cement based composites have high porosity due to the pore structures developed with disorder growth of hydration crystals. The addition of graphene nanoplatelets into the cement matrix can improve the pore structure by regulating the growth of hydration crystals in an ordered fashion, which helps in filling the gaps, reducing porosity and increasing the molar volume of the paste (Lv et al., 2014). Similar ordered formation of rod-like AFt crystals and preferential growth of C-S-H due to the nucleation of G-Dot platelets has been observed in SEM micrographs discussed in chapter 5. In order to investigate the effect of graphene nanoplatelets on the pore structure of cement matrix, nitrogen gas absorption/adsorption and MIP test were employed in both control and nanocomposite activated with 0.04% contents of functionalised $G-O_2$ nanoplatelets. These tests were carried out in accordance with the methodology and procedure laid down in chapter 3.

Figure 6.6 shows the nitrogen adsorption-desorption isotherms of control and nanocomposite prepared with $G-O_2$. Adsorption isotherms of both samples exhibit shape characteristic of type IV adsorption isotherm classified by the International Union of Pure and Applied Chemists (IUPAC) and are related to mesoporous materials containing pores 2-50 nm. These Isotherms are similar to type II at low pressure allied with macroporous material containing pores > 50nm and show monolayer which is followed by capillary condensation. Nitrogen gas method does not cover the whole range of the macroporous system. Therefore, MIP has also been applied to these samples. Cumulative intrusion (%) of mercury in control cement composite and GO_2-nanocomposite samples over a range of pore size in nm is shown in Fig. 6.7

The test results of both nitrogen gas and MIP methods of control and composite with-GO_2 sample are shown in Table 6.3. From the test data, it can be seen that the total volume of mercury intruded into control and nanocomposite-GO_2 samples were 0.2745 ml/g and 0.2211 ml/g respectively showing that with the addition of $G-O_2$ into cement total intrusion volume decreased. This suggests that there is a decrease in porosity with activation of $G-O_2$ into the cement matrix. With the decrease in porosity from 39.80% to 34.38 % there is a corresponding increase in bulk density from 1.44 g/ml to 1.55 g/ml in the nanocomposite, $G-O_2$ composite, sample as compared to control composite sample. Average pore diameter (4V/A) is reduced from 59.59 nm to 36.1 nm in the nanocomposites, and this shows improvements in the developed pore structure due to the addition of GO_2.
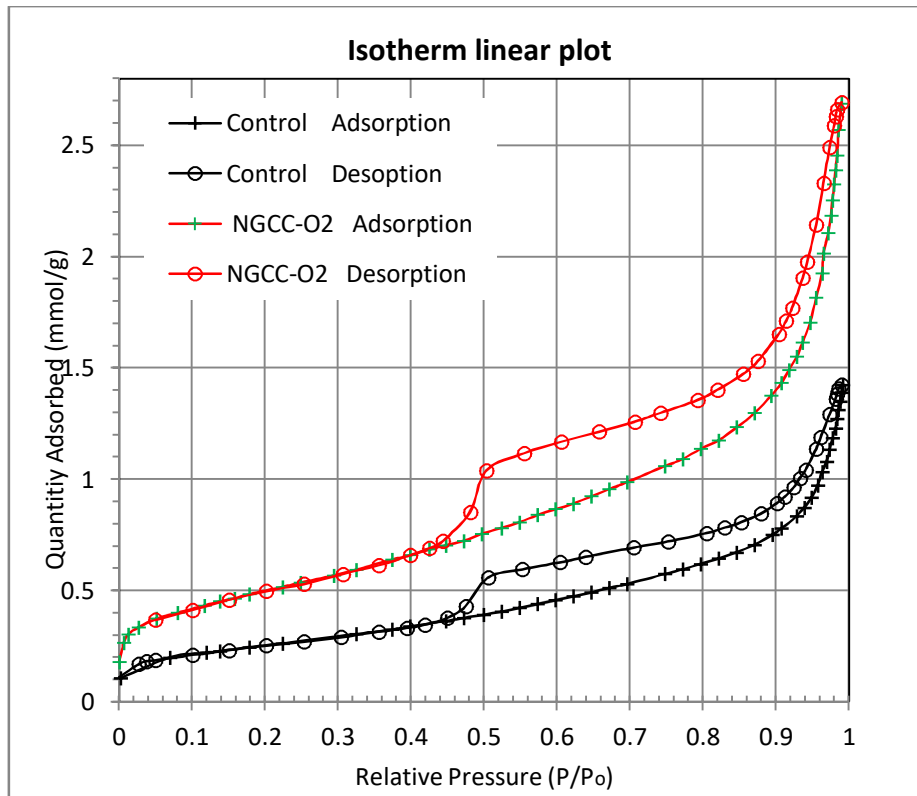
Figure 6.6 Linear plot of nitrogen adsorption-desorption isotherms of control and NGCC-O₂ cement composite samples.
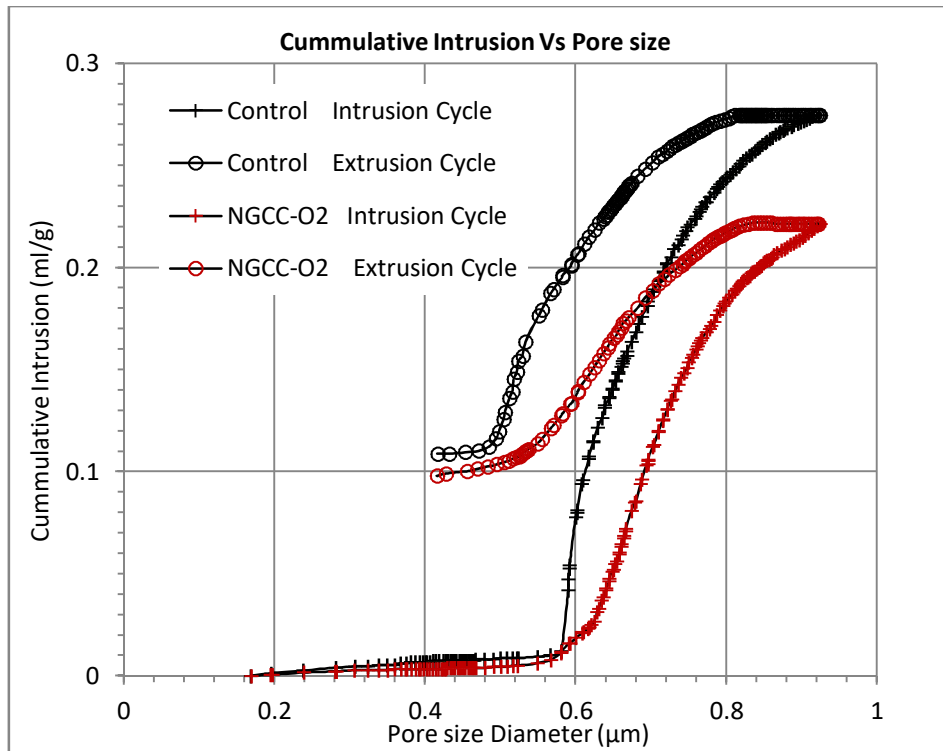
Figure 6.7 Measured distribution of cumulative intrusion (%) of control sample

Further, with the addition of GO_2 surface area measured through (BET) has increased from 20.55 m^2/g to 40.24 m^2/g as shown in Table 6.3. It is largely accepted that C-S-H gel is mainly responsible for influencing the surface area of cement paste and has a significant effect on the development of porous phases (Thomas et al., 1998). The previous researches on the microstructure development of cement paste demonstrated that the degree of hydration highly increased with the increased surface area (Garci and Jennings, 2001). Therefore, it can be suggested that the increased surface area indicates an accelerated hydration reaction in the cement matrix. It can also be ascertained that the presence of G-O_2 in the cement matrix affects pore size distribution on the microstructure development.

Table 6.3 Intrusion data and nitrogen gas adsorption/desorption summary

Parameters	Samples	
MIP Test		
	Control	**NGCC-O_2**
Total Intrusion volume mL/g	0.274	0.221
Total pore area m^2/g	18.430	24.459
Average pore diameter (4V/A) nm	59.590	36.100
Median pore diameter nm	13.040	10.010
Bulk density g/mL	1.445	1.555
Apparent (skeletal) density g/mL	2.409	2.371
Porosity %	39.804	34.389
Nitrogen gas absorption/adsorption Test		
Surface area (BET) m^2/g	20.548	40.240
Cumulative volume of pores between 5 Å and 3000 Å width (cm3/g)	0.050	0.094
BJH Adsorption average pore width (4V/A) Å	81.673	71.740
BJH Desorption average pore width (4V/A) Å	43.982	41.699

From the test data of pore size distribution (Table 6.3), MIP curves and nitrogen desorption isotherms analysis, it can be suggested that the presence of GNPs in the cement matrix influenced the pore structure development of nanocomposite. Uniformly dispersed G-Fnt can reduce the total pore area, average pore diameter and total porosity of hardened cement matrix, whereas, the increased surface area in the NGCC-O_2 indicates the high degree of hydration.

6.3.3 Mechanism of Crystal Formation in NGCC-Fnt

The mechanism of crystal formation controlled by G-Fnt nanoplatelets in the development of cement microstructure was investigated through high-resolution SEM images and EDAX characterization techniques. To obtain EDS spectrums, SEM was operated at 20.0

KEV using secondary electron (SE) detectors under high vacuum mode as mentioned in section 3.6.3 of chapter 3. SEM images of nanocomposite samples prepared with the fixed dose of 0.04 % functionalised GNPs in cement matrix are shown in Fig. 6.8. These high-resolution SEM images represent the microstructure and possible interaction of cement hydration crystals with functionalised nanoplatelets (G-Fnt) at the age of 3 days. It took many efforts to locate the area in densely packed nanocomposite samples where the interaction of GNPs with cement hydration crystals can be observed, and clear presentable SEM micrographs may be obtained. EDS spectrums obtained for the areas shown in the SEM images (Fig6.8) are discussed later in this section.

Fig. 6.8a depicts the area where graphene nanoplatelets (G-O_2) can be seen aligned in the vertical direction with hydration products grown around its periphery. It appears that amorphous solid C-S-H has grown along the peripheral surface of nanoplatelets while rod-like (AFt) crystals and CH in the amorphous form precipitated between the spaces of nanoplatelets. Perhaps these spaces between the nanoplatelets contain nano-sized water molecules attracted the mobile cement ions as shown in Fig.6.8b. It seems that C-S-H tended to grow along the surface of GNPs rather than on the cement particles. This indicates that the high surface energy of nanoplatelets attracted the cement ions near its surface. Spherical shape features with the diameter size ranging between 250nm – 300 nm close to the surface of nanoplatelets can be seen in the Fig.2.8c. This suggests the initiation of nucleation effect of G-Fnt by attracting ions liberated from cement grains. It has been reported that cement grains hydrated in two ways, one by dissolution of ions process in the large available water-filled gaps and secondly, with the nucleation effect of fine particles present in the cement matrix (Sakai et al., 2004).

It is understood from the chemical and phase composition analysis of NGCC-Fnt coupled with the SEM characterization micrographs at the nanoscale (Fig. 6.8c) that G-Fnt did not react chemically with the cement matrix. It induced a co-effect of nucleation and regulation of hydration products by developing a pore system of water filled gaps (Fig. 6.8b) in the cement matrix due to its unique 2D shape, structural and surface properties. Perhaps at the time of dissolution stage, mobile cement ions like Ca^{2+}, K^+, Na^+, OH^- and $SO4^{2-}$ dissolved in the water solution and interacted with G-Fnt nanoplatelets due to more active sites and their high surface energy. Moreover, functional groups attached to the unique 2D surface of G-Fnt provided more reactive sites during nucleation and developed strong bonds with the C-S-H structure. Nucleation effect of functionalised graphene in the C-S-H has also been reported in previous research (Lv et al., 2013; Gong et al., 2015).
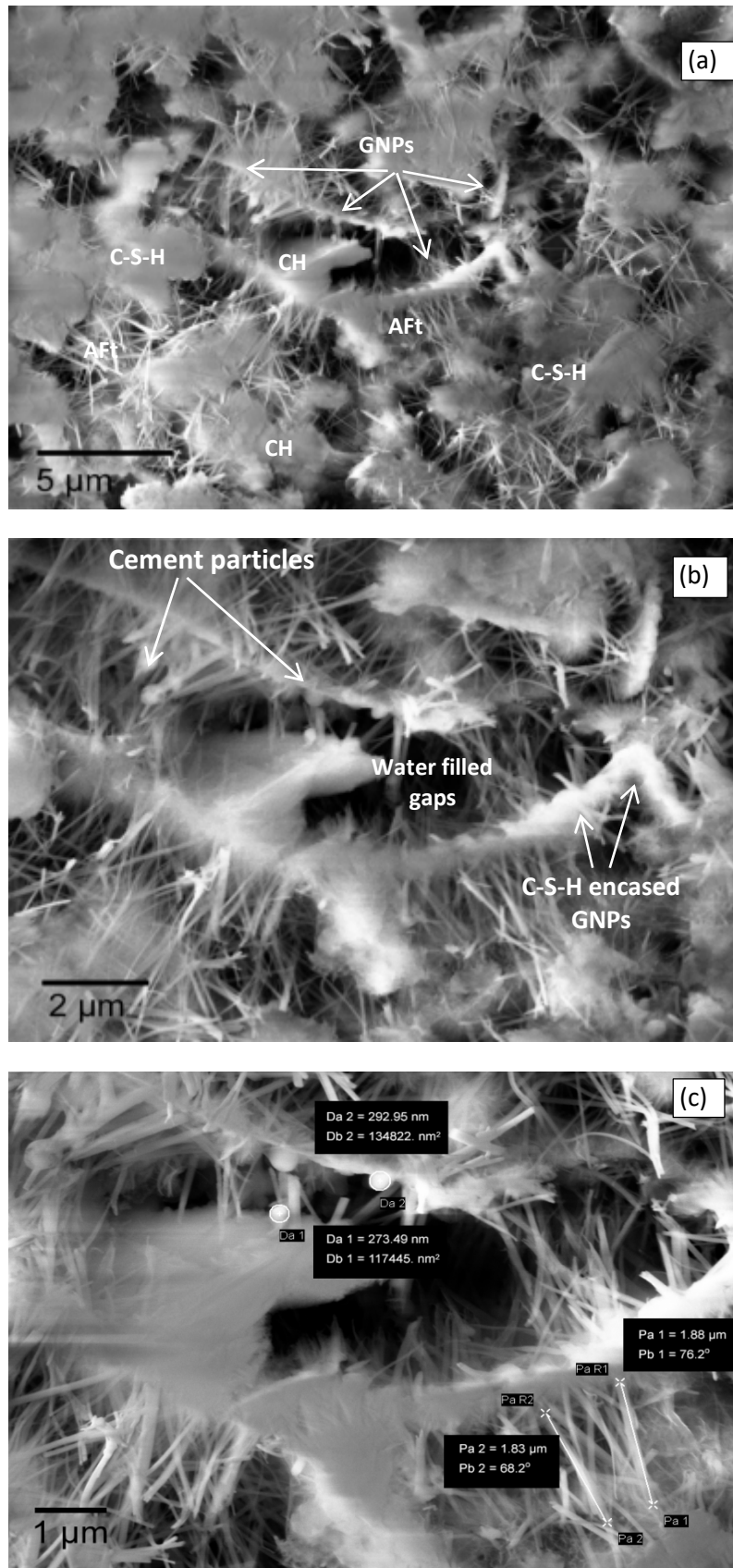
Figure 6.8 SEM micrographs of NGCC-Fnt showing formation of cement hydration crystals at the age of 3 days a) GNPs functionalised with-O_2 forming a network pores b) AFt, CH crystals grown in water-filled gaps C-S-H grown along peripheral edges of G-O_2 c) nano-sized spherical features attracted by G-O_2 surface

In the progress of hydration C_3A being most active compound hydrated quickly and reacted with sulphate ions, liberated from gypsum, to form ettringites (AFt). Ettringites are found with increased numbers in the microstructure of NGCC mostly grown in water-filled gaps as shown in the SEM images Fig.6.8b. It seems that nanoplatelets provided the support to sprout these rod-like AFt crystals on both sides of its surface. It can be seen in the Fig.6.8c that average gap of 1.88µm – 2.0µm between nanoplatelets tends to fill by aggressive growth of ettringites and other amorphous hydration products. This indicates that hydration crystals grow aggressively in water-filled spaces to attain certain shapes and proportion. This explanation appears similar to the previous report that cement hydration crystals require a particular pore system which can provide growth spaces to them so that they can attain certain structure and shape and later with the increased growth. These crystals will fill the pores and spaces to develop a dense microstructure (Lv et al., 2014). Therefore, the growth, shape and proportion of cement hydration crystals can be influenced under certain conditions and can have a significant impact on the microstructure development. From the SEM images (Fig.6.8) it seems that the pore system developed by 2D shape GNPs regulated the growth of cement hydration crystals especially AFt out of its surface and in the water-filled gaps between them.

In the cement chemistry, the formation of rod-like AFt crystal regarded as negative in the development of microstructure of cement paste due to large contents of water attached to its structure. Also, AFt transforms into AFm phases in the absence of sulphates (Li and Liang, 2011) but there is sufficient evidence available where the presence of AFt phases has shown improved microstructural properties, compactness, reduced permeability and increased molar volume. Moreover, it has induced the high early strength in cement paste by reinforcing C-S-H structure (Lv et al., 2013; Sakai et al., 2004). From the SEM micrographs measured at the nanoscale (Fig.6.9), it can be seen that rod-like AFt crystals in the form of interwoven network surrounded by amorphous C-S-H and CH hydration products have improved the microstructure at the nanoscale. Also, AFt crystals approximately 2-6 µm long and 120-200 nm in diameter can be seen in the Fig. 6.9d providing nano reinforcement by twisting around C-S-H gel structure (300-500 µm in size).

The effect of superplasticiser on the cement hydration products has been observed in previous works, and it was found that ettringites AFt produced densely on the cement particles are one of the main reasons for the increased compactness and anti-carbonation of cement matrix (He et al., 2012). It seems the presence of G-Fnt sheets has yielded the

similar effect as of superplasticizer in the cement matrix, as it has been observed that their presence triggered the hydration of C_3A and C_3S, resulting in an increased crystal amount, growth and distribution of hydration products especially AFt.
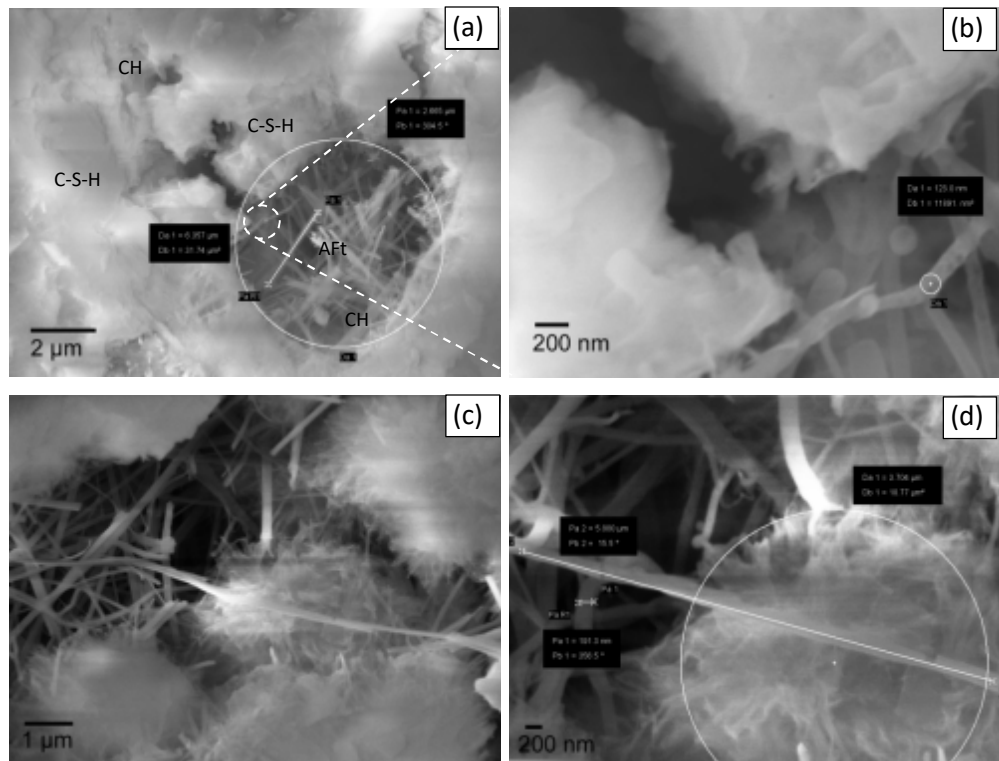
Figure 6.9 SEM images NGCC-Fnt at the age of 3 days a) hydration crystals AFt showing interwoven growth around CH and C-S-H b) nanoscale SEM of Fig.6.9a showing 120 nm dia of AFt crystals c) AFt crystals reinforcing other hydration crystals and d) AFt reinforcing C-S-H at nanoscale by twisting around its gel-like structure

SEM images measured to understand the mechanism of crystal formation influenced by G-Fnt in the cement matrix were also used for EDS analysis. The EDS analysis was used to determine the chemical element composition of the areas where C-S-H has grown with, and without the possible presence of nanoplatelets, such areas are marked as "Selected Area1" and "EDS Spot1" respectively as shown in the Fig.6.10. The EDS spectrum and element percentage % data of the marked areas are presented in Fig. 6.10 and table 6.4 respectively. Presence of $G-O_2$ nanoplatelets has been verified by the carbon and varied contents of Ca and Si for the area where C-S-H apparently grew preferentially along the nanoplatelets as shown in EDS spectrum (Fig. 6.10) and element % data (table 6.4).

Therefore, it may be concluded that insertion of G-Fnt developed a unique network of graphene nanoplatelets in the cement matrix consisting system of pores, water molecules

and aligned ions liberated from cement constituents. The network of these graphene nanoplatelets at this stage of hydration might act like an elementary skeleton for the development of microstructure with the progress of hydration process.
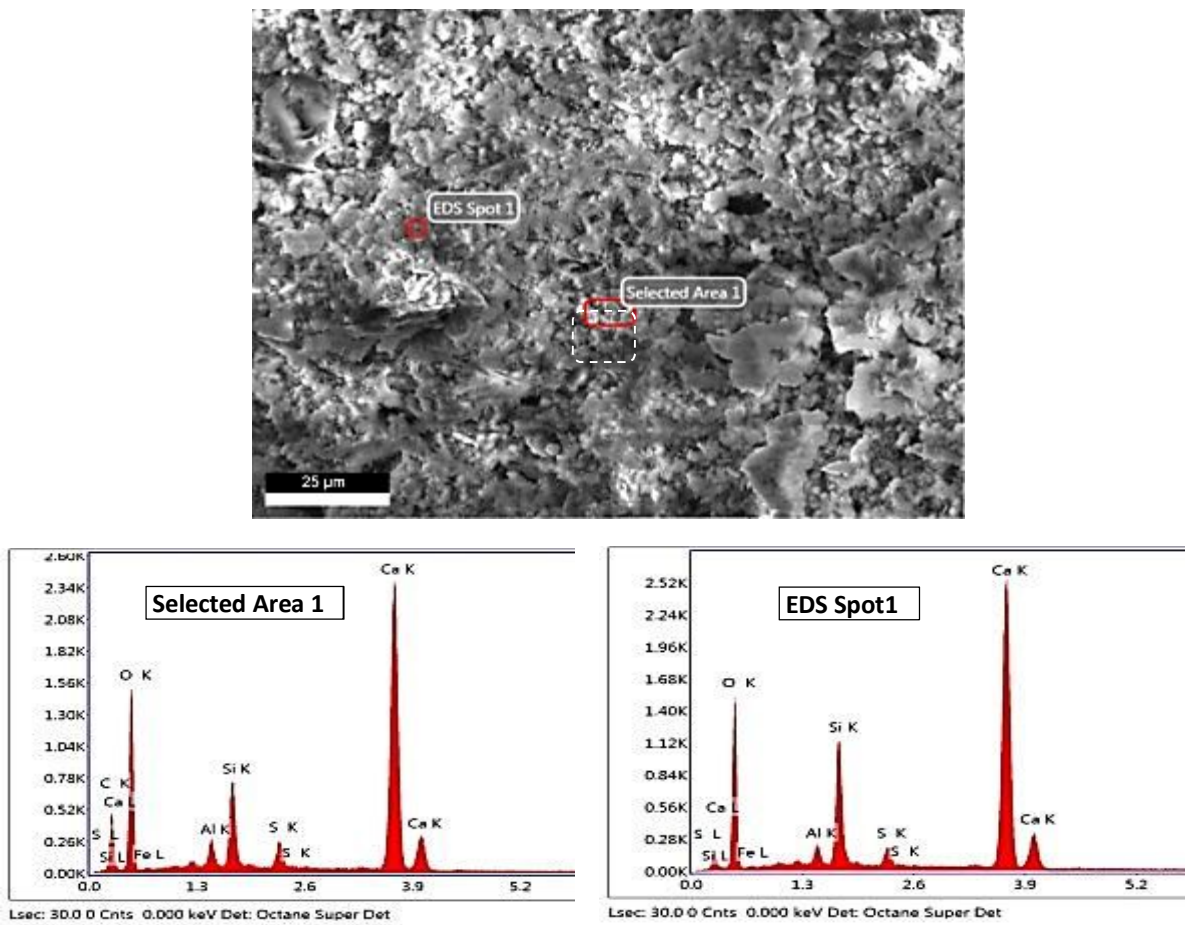
Figure 6.10 EDS analysis of NGCC-O₂ at the age of 3 days lower inset windows showing spectrums of marked areas in the SEM image shown above

Table 6.4 Chemical composition of C-S-H in NGCC-O₂

C-S-H growth in NGCC-O₂	Element percentage (%)								
	C	O	Ca	Al	Si	S	Mg	K	Fe
Fig.6.10: C-S-H encased GNPs (Selected Area 1)	10.96	46.97	33.48	1.40	4.47	1.68	0.64	1.68	1.03
Fig.6.10: C-S-H without GNPs (EDS spot 1)	0.00	49.36	39.07	1.19	7.69	1.43	0.61	1.48	1.26

6.3.4 Effect of G-Fnt on Microstructure of NGCC

To further investigate the microstructural development due to the influence of G-Fnt nanoplatelets with increased hydration duration in the cement matrix, SEM images of

control and NGCC-Fnt cement composite were obtained at the age of 7, 14 and 28 days. The microstructure developed at the age of 7 days in the control and NGCC-Fnt composite can be distinguished through SEM images shown in Fig. 6.11. It is clear from Fig. 6.11a that the microstructure of control cement composite comprises of pores and more gel-like C-S-H and amorphous CH structures with very less amount of AFt crystals. Whereas, a denser microstructure with an increased number of hydration crystals AFt, CH and amorphous solid C-S-H around the GNPs can be observed in the SEM images of NGCC-Fnt nanocomposite (Fig. 6.11 b-d). This differentiation of increased hydration products between control and nanocomposite samples has also been identified in the XRD pattern, and spectrums obtained through FTIR and RS at the age of 7 days as shown in Fig.6.2, Fig.6.4a and 6.5b respectively.

Through the detailed observation of SEM micrographs (Fig. 6.11) and the presumed interaction of G-Fnt graphene nanoplatelets with the cement matrix, it appears that G-Fnt activated the growth of hydration products by developing a unique network of graphene nanoplatelets as a skeleton at early days of hydration. This skeleton led the formation of different shapes of crystals and amorphous solids arranged in a distinctive pattern to develop a denser microstructure at the age of 7 days. In SEM images of NGCC-O_2 at the age of 7 days (Fig. 6.11b), a dense microstructure composed of G-O_2 sheets encased with C-S-H amorphous solid intermixed with rod-like AFt, plate or lamellar shape CH structures can be seen. It seems that nanoplatelets dispersed in the nanocomposite has now encased with more C-S-H amorphous solid and ribbed into the microstructure. This distinctive microstructure of interwoven crystals arranged uniquely due to the presence of G-Fnt nanoplatelets may be responsible for enhancing the strength of nanocomposite. Otherwise, these crystals were also present in control cement composite but less and in disorder fashion mostly dominant by irregular C-S-H and leaving pores and gaps as shown in Fig.6.11a.

The similar structure of interwoven crystals and GNPs encased with C-S-H solid has been observed in the NGCC-NH_2, and NGCC-COOH nanocomposite samples (Fig. 6.11c-d) but more rod-like AFt crystals and well-dispersed nanoplatelets have been observed in the NGCC composites composed with G-O_2 and G-NH_2. This composition might be due to the better dispersion and augmented nucleation effect as their structural properties were also found close to each other in FTIR, XRD and Raman spectroscopy analysis mentioned in chapter 4.
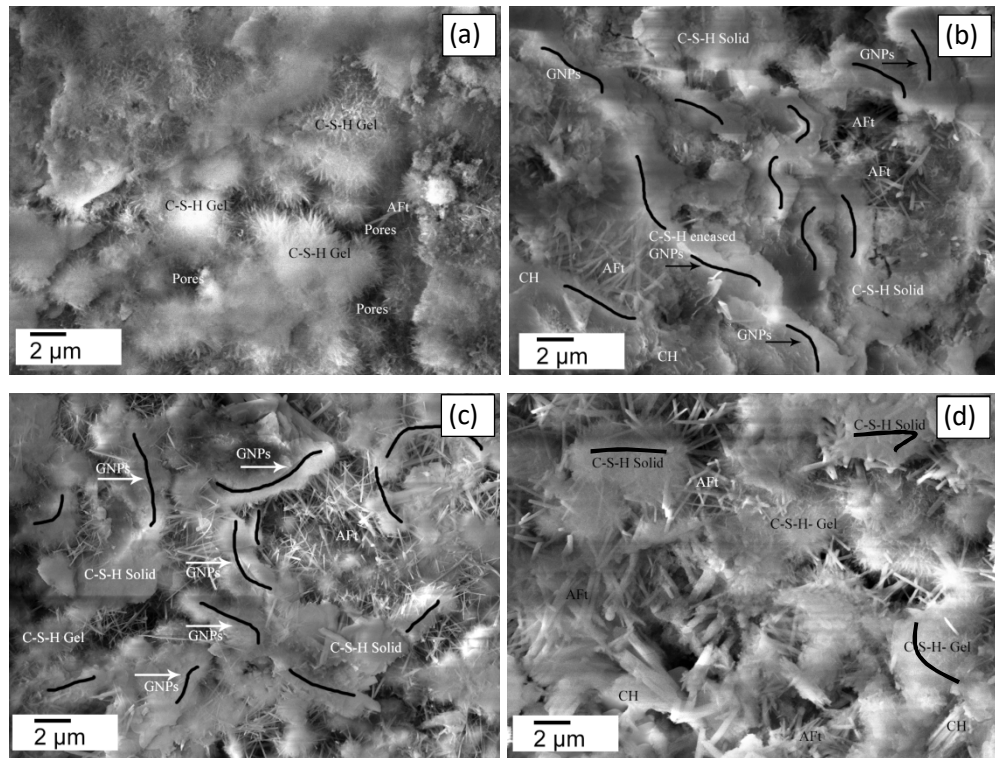
Figure 6.11 SEM micrographs of cement composites at 7days a) control b) NGCC-O₂ c) NGCC-NH₂ and d) NGCC-COOH

In the progress of hydration perhaps after 7 days, some of AFt phases might have reacted again with C_3A and converted the AFt phases into AFm phases due to the consumption of sulphate ions. AFm lamellar shape crystals in nanocomposite were also detected by XRD and visible in diffraction pattern (Fig. 6.4) at the later days of hydration. This observation indicates that C_3A hydrated extensively and formed the ettringite even after 7 days due to the availability of sulphate ions. These ions might be available in water-filled gaps developed due to the presence of graphene nanoplatelets, otherwise surrounded by C-S-H bundles. The rod-like AFt and lamellar shape AFm crystals have grown up continuously in the favourable environment of ions and pores developed by G-Fnt nanoplatelets. Perhaps at the same time, Ca^{2+} and OH^- ions liberated from the C_3S present in water-filled gaps started the formation of CH of polyhedral and other shape crystals to densify the microstructure. It has been observed through SEM images taken at the age of 14 days that with the increased hydration time the skeleton of ribbed G-Fnt nanoplatelets interwoven with rod-like and plate-like crystals, further hardened and covered with the dense skin of C-S-H to give a uniform whole. It is difficult to observe the microstructure developed by cement hydration crystals at this stage of hydration, but it can be estimated by observing crystal shapes near large pores and voids.
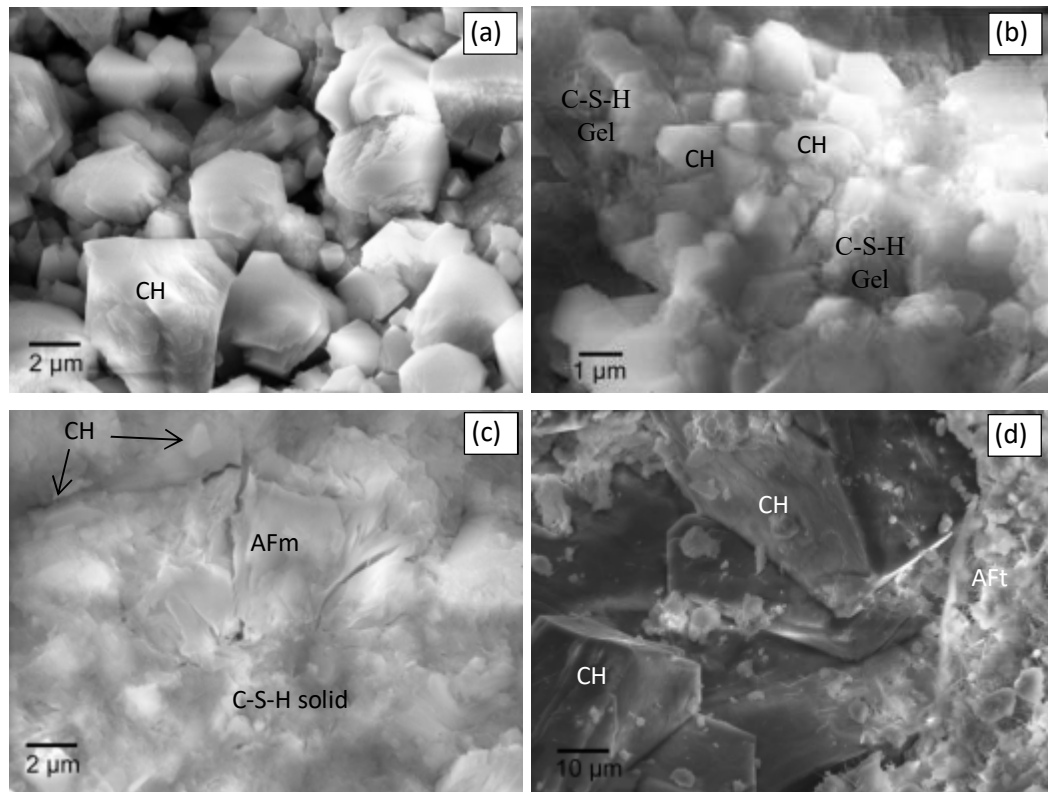
Figure 6.12 SEM micrographs cement composites at 14 days a) control b) NGCC-O$_2$ c) NGCC-NH$_2$ and d) NGCC-COOH

Fig.6.12 depicts the formation of different shapes of polyhedral and lamellar crystals in both control and NGCC-Fnt nanocomposites. The formation of loosely attached CH crystals of polyhedral shape in the control composite sample at the age of 14 days has been observed as shown in the Fig.6.12a. Whereas, the formation of densely packed CH polyhedral shape crystals encased with C-S-H gel has been observed in the NGCC-Fnt nanocomposites at the same age as shown in the Fig. 6.12b. It has been discussed in the previous chapter that plate-like or polyhedron shape crystals of CH might have contributed to increasing the compressive strength while rod-like AFt and lamellar AFm in the flexural strength of G-Dot nanocomposite. Lamellar shape crystals of AFm and plate-like CH crystals covered with C-S-H solid can be seen the Fig. 6.12

The hydration of C$_3$S and C$_2$S progresses continuously and growth of hydration products mostly CH and C-S-H largely increased the solid contents in the cement matrix and microstructure developed earlier further densified with the growth of these hydration products by filling pores and gaps. The formation of CH and C-S-H in the nanocomposite is also confirmed through the XRD patterns (Fig. 6.2), FTIR (Fig. 6.4b) and RS spectrum (Fig. 6.5b).
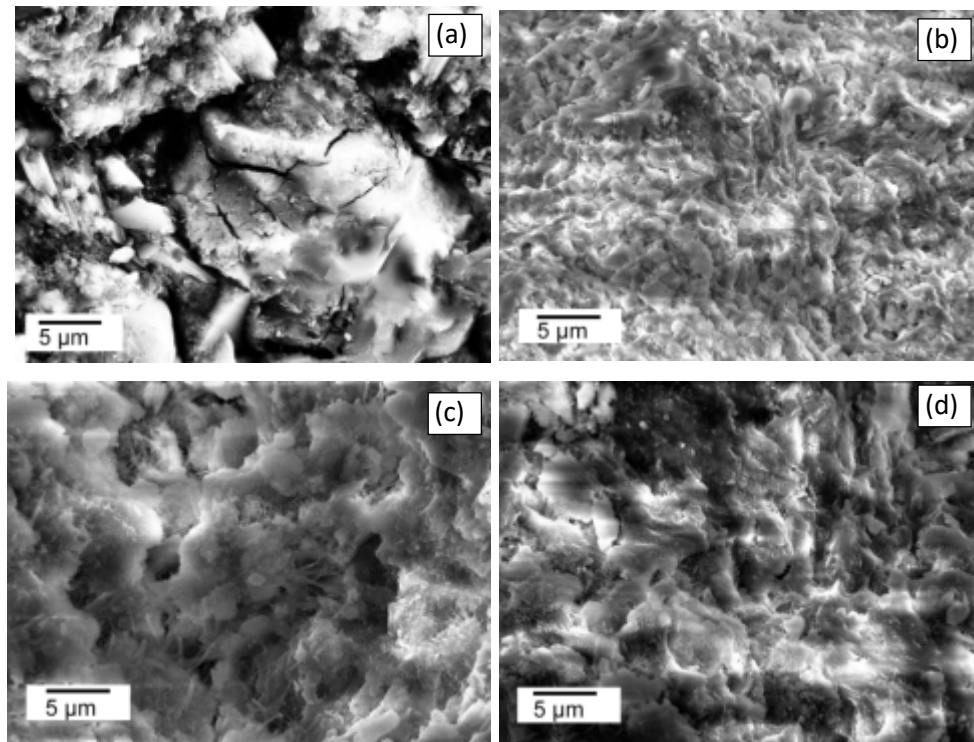
Figure 6.13 SEM micrographs cement composites at 28 days a) control b) NGCC-O$_2$ c) NGCC-NH$_2$ and d) NGCC-COOH

SEM images of controlled and NGCC-Fnt nanocomposite at the age of 28 days has been presented in Fig. 6.13. It can be seen in SEM image of the control cement sample (Fig. 6.13a) that C-S-H densely produced leaving with pores and cracks in the microstructure whereas, a well-integrated, dense and hardened microstructure has been observed in the nanocomposites as shown in Fig. 6.13b to 6.13d. It can be seen in Fig. 6.13c that rod-like AFt crystals are interwoven with the C-S-H, like reinforced bars in concrete, to develop a strong and dense microstructure. From the SEM images of NGCC-Fnt nanocomposite, a compact, dense microstructure free from cracks has been observed. This suggests that presence of G-Fnt nanoplatelets in the cement matrix might not only trigger the growth of crystals, but their presence also hinders the propagation of cracks initiate and nano-scale.

From the SEM micrographs the microstructure of nanocomposites appeared at the age of 28 days apparently build up with C-S-H solids only, but there must be ettringites AFt, AFm and CH hydration products interwoven and densely packed within the microstructure. The presence of these products was verified with their distinctive diffraction peaks in the XRD pattern of 28 days (Fig. 6.3).

To summarise above discussion, it is stated that the uniformly dispersed G-Fnt in the cement matrix initially developed an elementary skeleton of platelets and activated the

growth of hydration products. This elementary skeleton provided a platform to support AFt, CH crystals C-S-H in a unique way that results in the development of distinctive microstructure lead to enhance the mechanical properties of the cement matrix.

6.3.5   Effect of G-Fnt on the Mechanical Properties of NGCC

To investigate the effect of G-Fnt on the mechanical properties of cement composites, both control and NGCC-Fnt with a fixed dose of 0.04% were tested for flexural, compressive and tensile strength at the age of 7, 14 and 28 days of hydration. Samples were prepared and tested using procedure, methodology and equipment mentioned in chapter 3. Test results with the percentage increase in strength of control and nanocomposite samples loaded with functionalised graphene (G-O$_2$, G-NH$_2$ and G-COOH) are presented in Table 6.5. The coefficient of variation percent (COV %) was also calculated for all values and presented in the same table to evaluate that how strength values varied in each sample.

It has been observed from the test data (Table 6.5) that the strength values (flexural, compressive and tensile) increased with significant margin at early days of hydration in the nanocomposite as compared to the control cement composite samples. However, this margin of increase diffused slightly in the nanocomposites at the later stage of hydration but remained very promising to justify the role of GNPs in the cement matrix.

For example, the flexural, compressive and tensile strength of nanocomposite with G-O$_2$ has increased 63.73 %, 25.88% and 26.13% respectively at the age of 7 days and with slightly reduced margin at 28 days, increased with 55.3 %, 18.74% and 22.20 % respectively as compared to the control cement composite. Similarly, strength values of other two types of nanocomposites NGCC-NH$_2$ and NGCC-COOH have also increased in the same fashion. Flexural, compressive and tensile strengths increased by 59.8%, 25.97% and 22.56% at 7 days and by 49.7%, 18.25% and 20.60% at 28 days respectively in NGCC-NH$_2$. Whereas, in NGCC-COOH these strength values increased by 54.30%, 23.90% and 19.77% at 7 days and by 46.3%, 16.49% and 14.85% at 28 days respectively. It is evident from the test data that presence of G-Fnt in the cement matrix has a remarkable impact on the strength of nanocomposite which is due to the formation of distinct microstructure developed through activation of G-Fnt sheets discussed in section 6.3.4 and shown in Figures 6.11 b-d and 6.13 b-d.

Table 6.5 Mechanical strength test data

Flexural Strength									
	7days			14days			28days		
Sample ID	MPa	% inc.	% cov	MPa	% inc	cov %	MPa	% inc.	% cov
Control	6.75	0.00	5.43	7.20	0.00	4.54	7.81	0.00	4.48
G-O2	11.05	63.73	2.04	11.52	60.00	2.36	12.12	55.3	2.10
GNH2	10.78	59.83	2.67	11.07	53.80	2.59	11.69	49.7	4.11
GCOOH	10.41	54.30	3.42	10.66	48.20	3.09	11.42	46.3	4.79

Compressive Strength									
	7days			14days			28days		
Sample ID	MPa	% inc.	% cov	MPa	% inc.	% cov	MPa	% inc.	% cov
Control	65.55	0.00	2.34	73.93	0.00	2.21	79.21	0.00	1.87
G-O2	82.51	25.88	1.03	92.49	25.10	1.05	94.05	18.74	0.11
GNH2	82.57	25.97	1.05	92.25	24.77	1.48	93.67	18.25	0.33
GCOOH	81.21	23.90	1.17	90.20	22.00	1.39	92.27	16.49	0.32

Tensile Strength									
	7days			14days			28days		
Sample ID	MPa	% inc.	% cov	MPa	% inc.	% cov	MPa	% inc.	% cov
Control	3.59	0.00	11.36	3.70	0.00	6.63	3.99	0.00	4.70
G-O2	4.52	26.13	8.36	4.80	27.20	4.92	4.88	22.20	2.27
G-NH2	4.40	22.56	10.80	4.63	22.66	4.98	4.81	20.60	4.20
G-COOH	4.30	19.77	9.32	4.52	19.79	6.41	4.58	14.85	4.15

For further comparison and to establish a relationship between strength and microstructural development, strength test values were plotted separately in the form of graphs shown in figure 6.14. In control cement composite, curves representing strength values (Fig. 6.14a) has shown an increased linear trend indicating a consistent but slow gain in strength with a maximum value at 28days. This relates to the slow hydration of C_3A, C_3S and C_2S encapsulated by C-S-H bundles. Whereas, in case of nanocomposites curves indicating high early strength at 7 days and then a steady increase in flexural and tensile strengths. Compressive strength showed a distinct behaviour in nanocomposite sample and sharply increased between 7 and 14 days and then showed a steady increasing trend.

The high early strength in the nanocomposites and a sharp increase in compressive strength between 7 and 14 days can also be visualised from the trend and shift of curves representing strength values in the graphs (Fig. 6.14b-d) at the age of 7 days compared with control cement composite. The increased strength values at the age of 7days are also in correlation with SEM, XRD, FTIR and RS results discussed in previous sections. This

indicates that G-Fnt influentially participated in the microstructure development of nanocomposites right from very early days of hydration where the nanoplatelets regulated the growth, shape and arrangement of cement hydration crystals responsible for increasing high early strength.
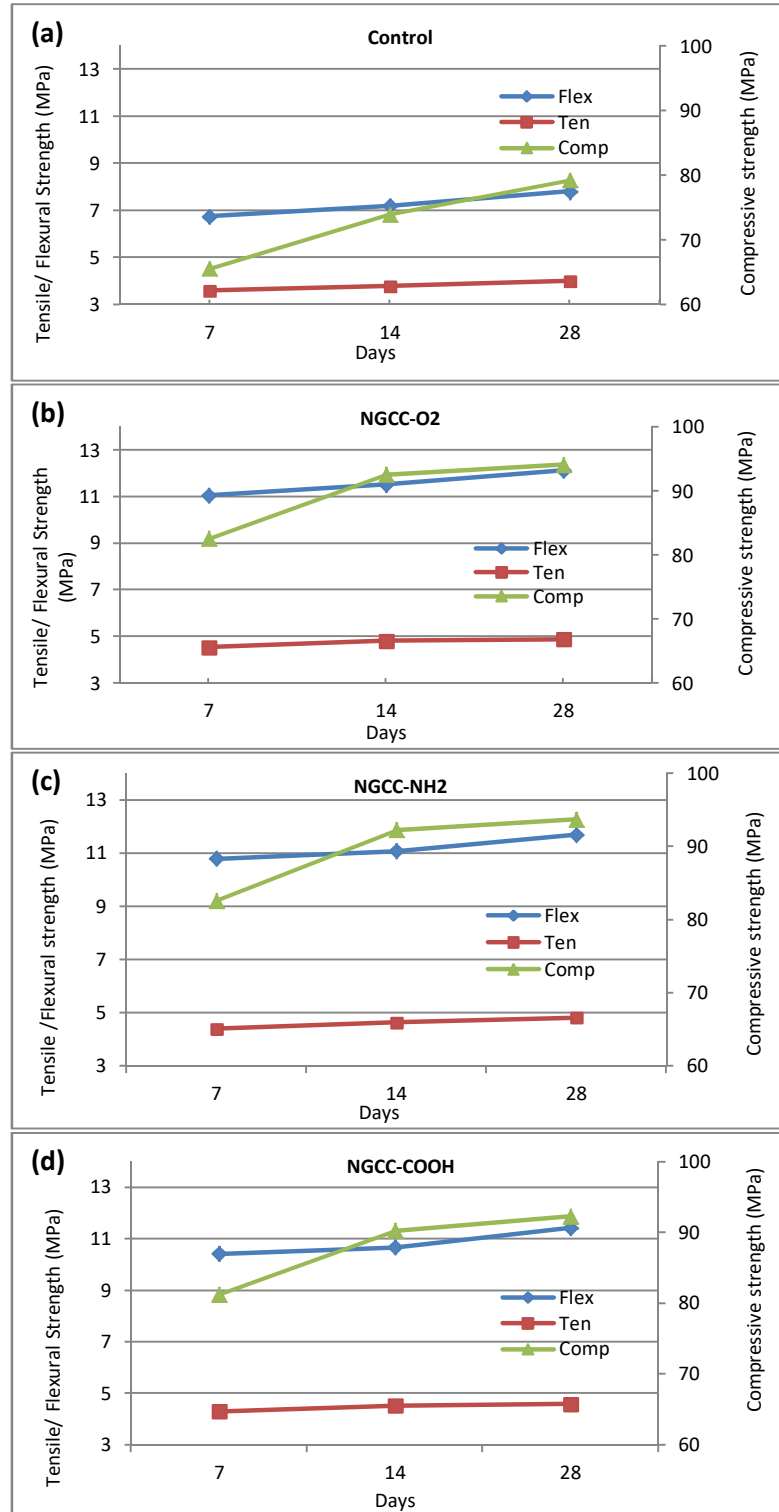
Figure 6.14 Mechanical strength test graphs of cement composites a) control cement b) NGCC-O$_2$ c) NGCC-NH$_2$ and d) NGCC-COOH

Moreover, G-Fnt nanoplatelets acted as nuclei for the growth of C-S-H around its shape to form a ribbed structure as shown in Fig. 6.11b-d. Increased compressive strength in nanocomposites indicated by the sharp curve between 7 and 14 days and can be linked to the increased growth of CH due to early hydration of C_3S and C_2S. This phenomenon could be related to the formation of densely packed polyhedral shaped CH crystals encased with C-S-H at this age discussed above in section 6.3.4 and shown in Fig. 6.12b.

Form the test data it has been observed that tensile strength increased with the almost linear trend in both control and all nanocomposites samples. Although, the tensile strength of nanocomposite prepared with $G-O_2$, $G-NH_2$ and G-COOH has increased by 26.13%, 22.56% and 19.7 % respectively at the age of 7 days. However, large variation in strength values has been observed in both control and nanocomposite samples. In contrast, cov % values for the flexural and compressive strengths of nanocomposites are well within the maximum recommended values of 5.7 % according to ASTM C8-02 and 2.37 % mentioned in the C39-99 ASTM respectively as shown in graphs (Fig. 6.15 a-b).

Higher strength deviation in tensile strength values at the age of 7 days seems to appear due to some procedural error and could not be identified during casting or testing. However, cov% values for tensile strength of nanocomposites at the age of 14 and 28 days (Fig. 6.15c) are well within the maximum limit of 5.0% mentioned in C39-99 ASTM. Therefore, overall strength deviation in flexural, compressive and tensile strength values of nanocomposite can be attributed with the uniform dispersion of G-Fnt nanoplatelets in the cement matrix resulting the higher degree of hydration and formation of denser microstructure leading to enhance mechanical properties intrinsically. Among three nanocomposites $NGCC-O_2$ showed consistent strength values outperformed other two due to its more dispersion capability and reactivity with cement particles. Moreover, in comparison nanocomposite prepared with G-Fnt nanoplatelets outperformed the one prepared with G-dot nanoplatelets (Chapter 5) in strength variations due to better dispersion capabilities.

A qualitative performance of nanocomposite (NGCC) in terms of stiffness (flexural modulus) and ductility was also compared with control cement composite. The typical stress-strain curves under flexure and compression stress for both control and nanocomposites NGCC-Fnt are shown in the (Fig.6.16). The relationship between flexural strength and displacement (Fig. 6.16a) for nanocomposites and control cement composites shows that nanocomposite samples undergoes to large deformation (approx. 0.27 mm)

before yielding to maximum stress values and cover the large area under the curves as compare to control cement composite.
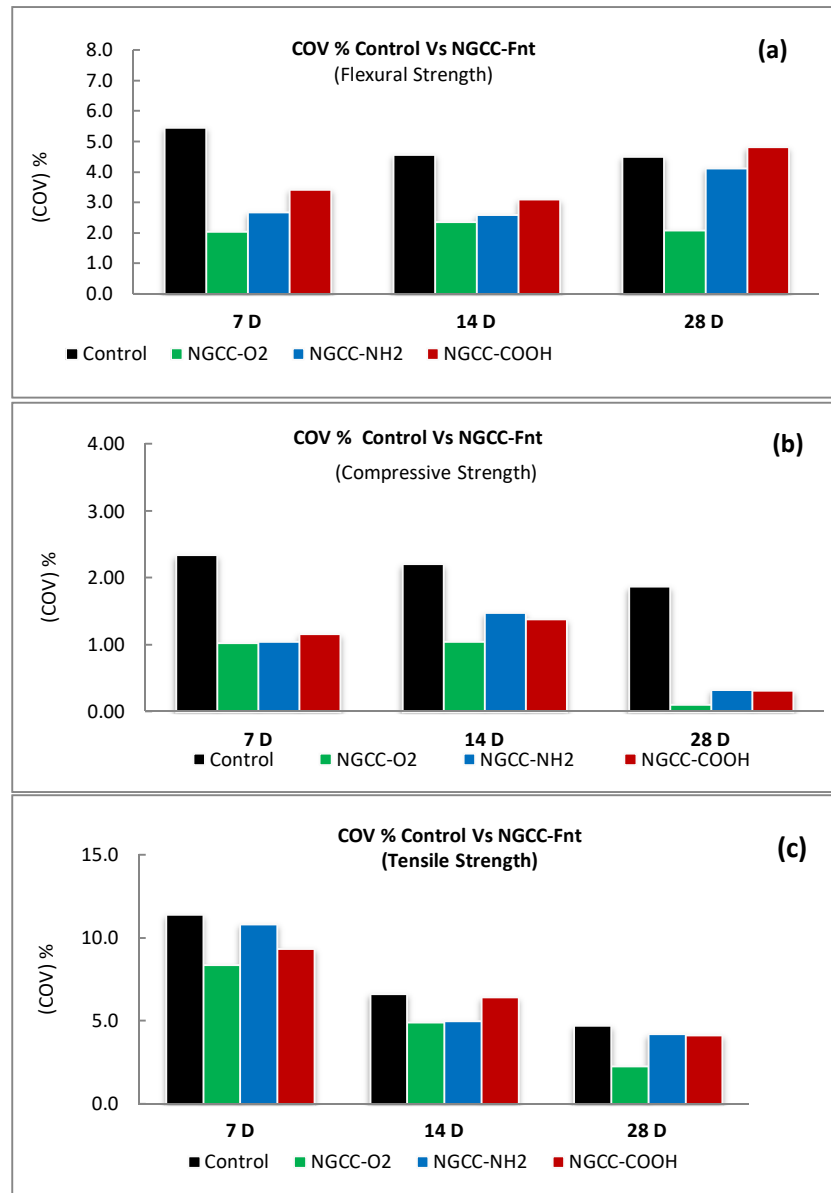
Figure 6.15 Coefficient of variation in strength values of control vs NGCC-Fnt at 7, 14 and 28 days for a) flexural strength b) compressive strength and c) tensile strength

It indicates that nanocomposite (NGCC-Fnt.) has more tendencies to bend with increased ductility and toughness due to reinforcing effect nanoplatelets. Further, curves representing stress displacement relationships for NGCC-Fnt are comparable with each other but distinct from the curve representing control cement composite exhibit higher stiffness (flexural modulus). It appears that G-Fnt nanoplatelets fairly influenced the mechanical properties of nanocomposite with better dispersion and reinforcement.

141
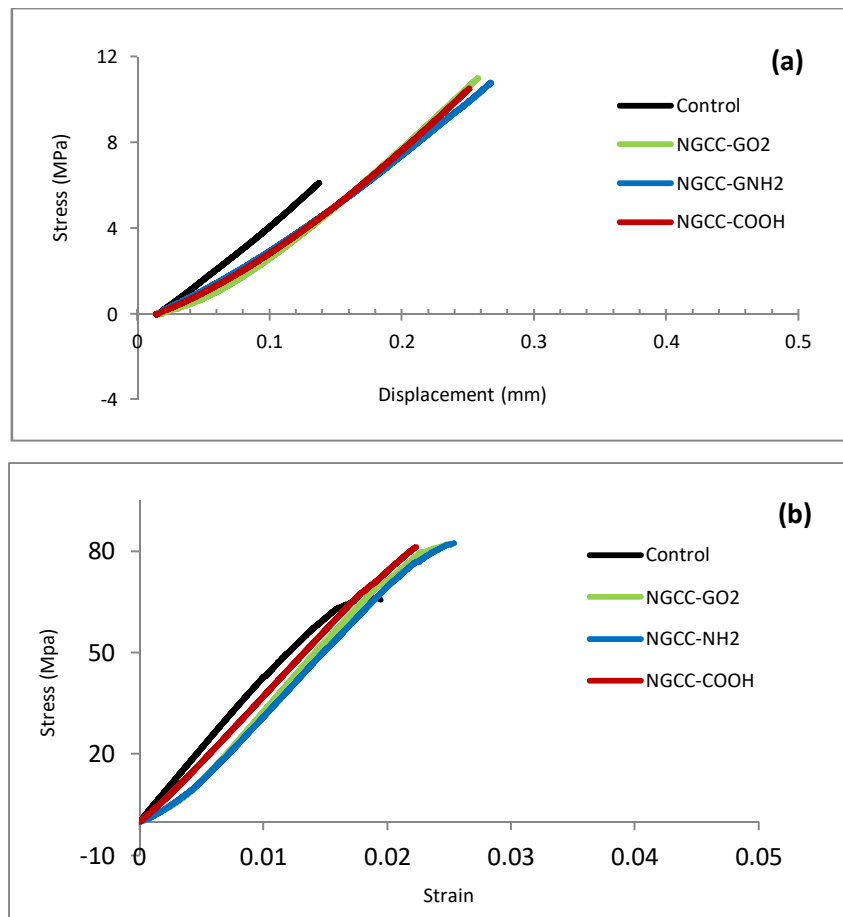
Figure 6.16 Curves showing stiffness and ductile properties of control and NGCC samples at 7days a) typical stress-displacement curves under flexure b) typical stress-strain curves under compression

A similar trend has been observed in the stress-strain relationship under compression (Fig. 6.16b) for nanocomposite and control cement composites, where nanocomposite yielded the higher strain capacity 0.0026 as compared to the control cement composite with 0.0018. A similar effect of graphene oxide on the strain capacity of nanocomposite has been reported (Pan et al., 2012) and suggested that increased strain capacity is due to the delayed initiation and propagation of microcracks due to presences of GO. The overall strength of nanocomposite prepared with 0.04 wt.% of G-Fnt has improved intrinsically as compared to control cement composite. Although the strength values among all three types of NGCC-Fnt are comparable but NGCC loaded with G-O_2 nanoplatelets exhibited higher, and consistent values outperformed the other two nanocomposites NGCC-NH_2 and NGCC-COOH. The flexural, compressive and tensile strength has increased by 63.73 %, 25.88% and 26.13% respectively as compared to the control cement composite at the age of 7 days. Moreover, an increased strain capacity has been observed in the NGCC-Fnt samples through stress-strain relationship.

6.4   Conclusions

GNPs functionalised via plasma exfoliation grafted with -O2, -NH$_2$ and -COOH to their surface with better dispersion capabilities were used in the development of three types of nanographene cement composites (NGCC-O$_2$, NGCC-NH$_2$ and NGCC-COOH). The effect of G-Fnt nanoplatelets on the chemical and phase composition, pore size distribution, microstructural development and mechanical strength of developed nanocomposites were tested using analytical characterization techniques XRD, FTIR, RS, MIP, EDAX and SEM. Analytical studies suggested that 2D shape GNPs did not react chemically to form a new compound but facilitated the chemical hydration process in the cement matrix by developing a unique network of nanoplatelets characterized by a system of pores, water molecules and liberated aligned ions from cement in the spaces between them. This suggested the initiation of nucleation effect of G-Fnt nanoplatelets in the cement matrix.

Analysis of XRD, FTIR and RS spectrums indicated the increased nucleation effect and activated growth of hydration products in NGCC-Fnt at an early stage of hydration. This suggested that the developed network of nanoplatelets at the initiation stage of hydration might have acted as an elementary skeleton to regulate the mechanism of crystal formation in the physical hydration process in the cement matrix. Through analytical studies in relation to SEM and EDAX characterization of NGCC-Fnt, more ettringite (AFt) formation in between and preferential growth of C-S-H solid around G-Fnt have been identified at the age of 7days. Whereas, the growth of CH crystals encased in C-S-H gel increased between 7-14 days of hydration with the activation of G-Fnt in the cement matrix. Moreover, the presence of G-Fnt nanoplatelets significantly improved the pore structure by reducing porosity and increasing the surface area from 20.55 m^2/g to 40.24 m^2/g in the cement matrix. This suggested the formation of denser and distinctive microstructure that might have led to enhance the mechanical properties of the cement matrix. NGCC-O$_2$ nanocomposite with enhanced toughness and ductility instigated in its microstructure as the better interaction of G-O$_2$ nanoplatelets with cement hydration crystal has outperformed the other two types of nanocomposites.

CHAPTER 7 Development of NGCC-CNF

7.1 Introduction

The development of NGCC-Fnt has been discussed in chapter 6, and we came to know that in physical hydration process the cement hydration crystals were grown in spaces where they can attain certain shapes and can increase their proportion to form a denser microstructure. These growth spaces ideally contain nano-sized water molecules providing a suitable environment to attract nano-sized ions liberated from cement particles. Hydration crystals like AFt and CH have seen precipitated enormously in such growth spaces. It has also been observed that the functionalised GNPs provided such a favourable environment to cement hydration crystals by developing a pore system of water filled gaps in the cement matrix due to its unique 2D shape, structural and surface properties. Whereas in the chemical hydration process the formation of C-S-H gel was the major factor that might have affected the strength of cement composite largely. In the formation of microstructure for NGCC-Fnt it has been observed that due to the nucleation effect, C-S-H has grown peripherally along the 2D shape of graphene nanoplatelets and might have contributed to the strength development of cement composite by holding the cement matrix more strongly than the C-S-H structure itself.

Since nanoplatelets were smaller in linear dimension the C-S-H growth around them has been observed in segments forming a skeleton for denser microstructure. The C-S-H growth filled the pores and encapsulated the AFt and CH crystal which in return contributed much towards the flexural and compressive strength of the cement matrix. However, there are better chances to improve the tensile strength of cement matrix by incorporating nano-sized foreign materials of 1D shape with a longer linear dimension such as CNTs and CNFs, where C-S-H may grow linearly along the length and can provide a larger connection within the microstructure to resist tensile loads. Much of research has already been done on CNTs cement composite, and a remarkable increase in mechanical and other properties has been reported due to their bonding with cement matrix. This has been comprehensively reviewed in the section 2.7.3 of Chapter 2. The use of CNFs in the cement matrix has been reported less in previous research and mostly emphasised the enhanced mechanical properties (Vera et al., 2009). The effect of the shape of CNFs on the crystal formation and growth of hydration products has not been done in previous research. CNTs and CNFs are hydrophobic due to high Van der Waals forces between

them. They are hard to disperse into the aqueous medium and thus agglomerate into cement matrix resulting in porous misstructure with poor mechanical properties.

A new generation of nanomaterials known as graphited carbon nanofibers (G-CNFs) with a diameter of 100 nm and length of 20-200 μm, which composed of conically shaped graphite sheets anchored in hollow fibrous tube-like structure as discussed in section 4.4 of chapter 4, was used for the development of NGCC. The unique morphology of G-CNF due to conical shape graphited platelets and long fibrous skeleton makes it possible to disperse in aqueous solution. Moreover, with the help of surface modification via surfactants it provides a strong bond with cement hydration crystals, especially with C-S-H gel. G-CNF with their unique structure and conical morphology can develop a robust interaction with the cementitious matrix to form strong microstructure and can resist tensile loads. This hypothesis originated the motivation to investigate the interaction of G-CNF with cement matrix for the development of NGCC-CNF.

In this chapter, the development of NGCC-CNF by using G-CNFs with various contents has been discussed. The uniform dispersion of G-CNFs into the aqueous medium with the help of surface modification and dose optimisation to be mixed in the processing of NGCC-CNF were designed. The physical and chemical interaction of G-CNFs with cement hydration due to their unique 1D shape geometry products was observed. The experimental data obtained through XRD, FTIR, EDAX, SEM, MIP and UTM characterization techniques were analysed to correlate the possible mechanism of crystal formation and their reinforcing effect on the cement hydration products. Accelerated cement hydration due to nucleation effect, structural and surface properties leading to enhance mechanical properties were discussed to conclude.

7.2   Processing of NGCC-CNF

The G-CNFs used in the processing of NGCC characterized as very lightweight and hydrophobic. To check the dispersion compatibility of G-CNFs into the aqueous medium, they were first used in a trial mix with very small quantity approx. 0.0025 % wt. of cement (36.8 mg) in a small beaker with 50 ml of water and stirred manually to achieve dispersion. Despite sonication for a reasonable time (5-10 mins), after manual mixing the G-CNFs did not disperse and was found suspended forming clusters of fibres on the surface of the water as shown in the Fig. 7.1. Form the literature it was found that hydrophobic material like CNFs can be dispersed by using chemicals, surfactants and some organic solvents (O.S) such as isopropyl alcohol discussed in the section 3.2.5 of chapter 3.
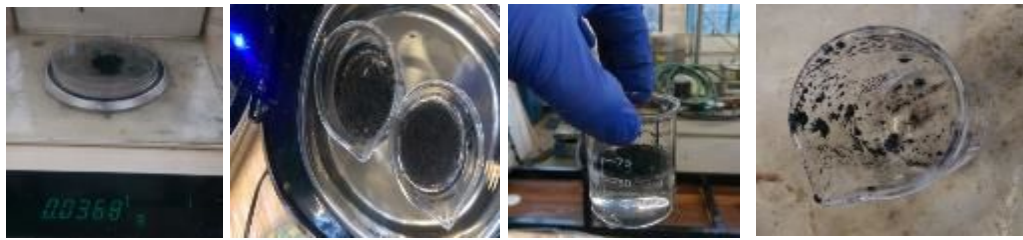
Figure 7.1 Trial mixes of G-CNFs into the water for processing of NGCC-CNF

It was found that G-CNFs were uniformly dispersed easily without manual stirring into the organic solvent otherwise clustered when mixed with water as shown in the Fig. 7.2. Therefore, economical and easily available organic solvent isopropyl alcohol was used in addition to the water to get a uniform dispersion of G-CNF in the aqueous medium. For this purpose, G-CNFs with increased contents were first mixed in 50 ml of organic solvent and then sonicated for 15 minutes with the same equipment and method used previously in the processing of other two cementitious composites. The amount of organic solvent was kept constant for all the mixes of G-CNFs because the addition of such chemicals can adverse the cement hydration reactions and result in the poor microstructure.
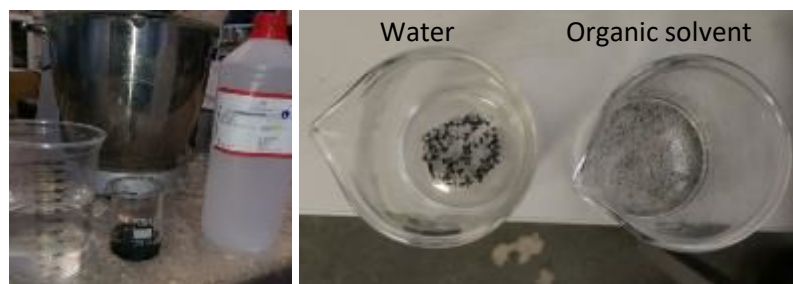
Figure 7.2 Comparison of G-CNFs dispersion into water and organic solvent (Isopropyl alcohol)

The constituents used for the mixing and processing of nanocomposite are mentioned in Table 7.1. To investigate the effect of G-CNFs on the cement hydration four types of NGCC were prepared with varied G-CNFs contents as mentioned in Table 7.1. NGCC with 0.0 % of G-CNFs was also prepared to investigate the sole effect of organic solvent on the cement hydration process, microstructure development and mechanical strength of cement composite. It was found while mixing increased contents (0.03 and 0.04 % wt.) of G-CNFs into the constant volume (50 ml) of organic solvent, these fibres again started to form clumps, clusters and thicken the solution as shown in Fig. 7.3. Through trial mixes G-CNFs contents up to 0.02% wt. were found optimum with 50 ml volume of organic solvent

regarding suitable dispersion. Therefore, four mixes of NGCC were designed with G-CNFs contents 0.00, 0.005, 0.01 and 0.02% wt. of cement.

Table 7.1 Mixing proportion of NGCC-CNF

Sr. No	Composite Name	Cement gm	G-CNFs Mg	% BWOC	Water ml	Organic solvent ml
1 ^	Control	1400	0.00	0.00	420	0.00
2	NGCC-CNF 0.00	1400	0.00	0.00	370	50.00
3	NGCC-CNF 0.005	1400	70.0	0.005	370	50.00
4	NGCC-CNF 0.01	1400	140.0	0.01	370	50.00
5	NGCC-CNF 0.02	1400	280.0	0.02	370	50.00

^ Control samples used for NGGC-G-Dot *BWOC=by weight of cement;

After the sonication of organic solvent with specific contents of G-CNFs, the obtained solution was further dissolved into the designed water contents and sonicated for another 30 minutes to ensure their homogenous dispersion into the aqueous medium. The aqueous solutions with varied contents of G-CNFs then used to process the NGCC adapting same procedure and methodology used for the processing of NGCC-Dot and NGCC-Fnt.

0.01% G-CNFs in water   0.01% G-CNFs in O.S   0.02% G-CNFs in O.S   0.03% G-CNFs in O.S
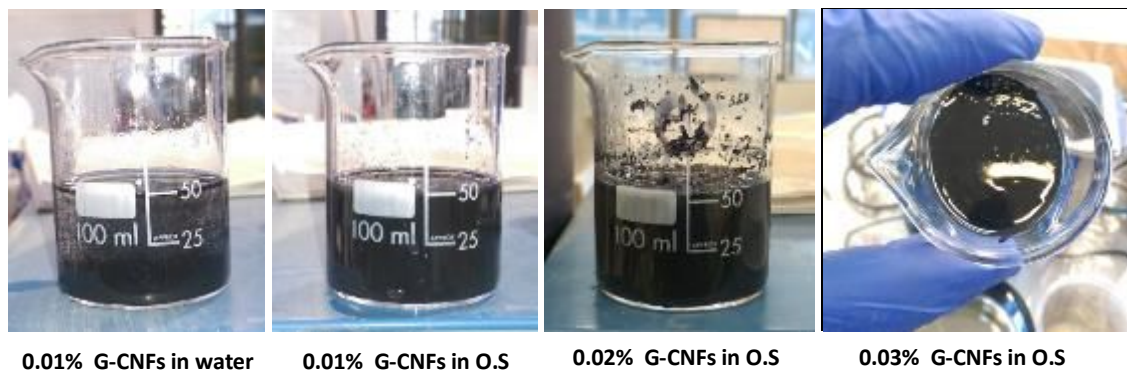
Figure 7.3 Trial mixes of G-CNFs with various contents into 50 ml of water and organic solvent (O.S)

7.3 Results and Discussion

The cured samples NGCC-CNF were tested and analysed for phase change, chemical composition, microstructural and development. The results obtained from characterization and testing were analysed, discussed and presented in the following sections

7.3.1 Effect of G-CNF on Phase & Chemical Composition of NGCC

To evaluate the effect of G-CNF on the mineralogy of hydration products of cement composite, samples were subjected to the XRD measurements using equipment, method and procedures mentioned in chapter 3. Combined XRD patterns of NGCC-CNF and control sample after 7 and 28 are days shown in Fig. 7.4a and Fig.7.4b respectively. A significant difference between XRD patterns of control and NGCC-CNF samples at the age 7 days (Fig. 7.4a) can be observed. In the control cement composite the expected hydration products, such as AFt (Ettringites), CH (Portlandite), poorly crystalised C-S-H and unreacted clinkers mostly calcium silicate (C_2S, C_3S), appeared at distinctive diffraction angles. More unreacted clinker phases such C_2S, C_3S and gypsum, were identified in the XRD patterns of NGCC composites with an organic solvent in the cement matrix. This suggests the slow hydration reaction and formation of fewer hydration products especially in NGCC with G-CNF contents 0.00 and 0.005 %. It seems that the presence of an organic solvent (Isopropyl alcohol) has retarded the hydration reaction in these composites.

Whereas, NGCC composites with G-CNF contents 0.01 and 0.02% showed an increased growth of CH crystals or perhaps amorphous C-S-H as well. This increased growth can be attributed to the nucleation effect introduced with increased contents of G-CNFs. The higher peak intensity of CH with corresponding accelerated hydration rate attributed to nucleation effect of CNTs and CNFs was also observed previously (Blandine et al., 2016). The presence of G-CNFs in cement matrix was mapped through small but distinctive graphite peaks near diffraction angle 26.5^o (Fig. 7.4a). In the XRD patterns of NGCC at the age of 7 days, less formation of AFt crystals has been identified as compared to the control cement composite. This might be due to the adverse effect of organic solvent, used for the dispersion of G-CNFs, on the hydration kinetics of the cement matrix. However, all the peaks related to CH can be seen distinctively intensified in the XRD patterns of NGCC composites especially with G-CNF contents 0.01 and 0.02 % at diffraction angles 18°, 29°,34°,47°,48.5^o and 54.5^o (Fig.7.4a). On the other hand, the C-S-H could not be mapped through clear diffraction peaks in the XRD patterns due to their amorphous structure or may be overlapped with some intense peaks of CH and unhydrated clinkers of C_3S and C_2S.
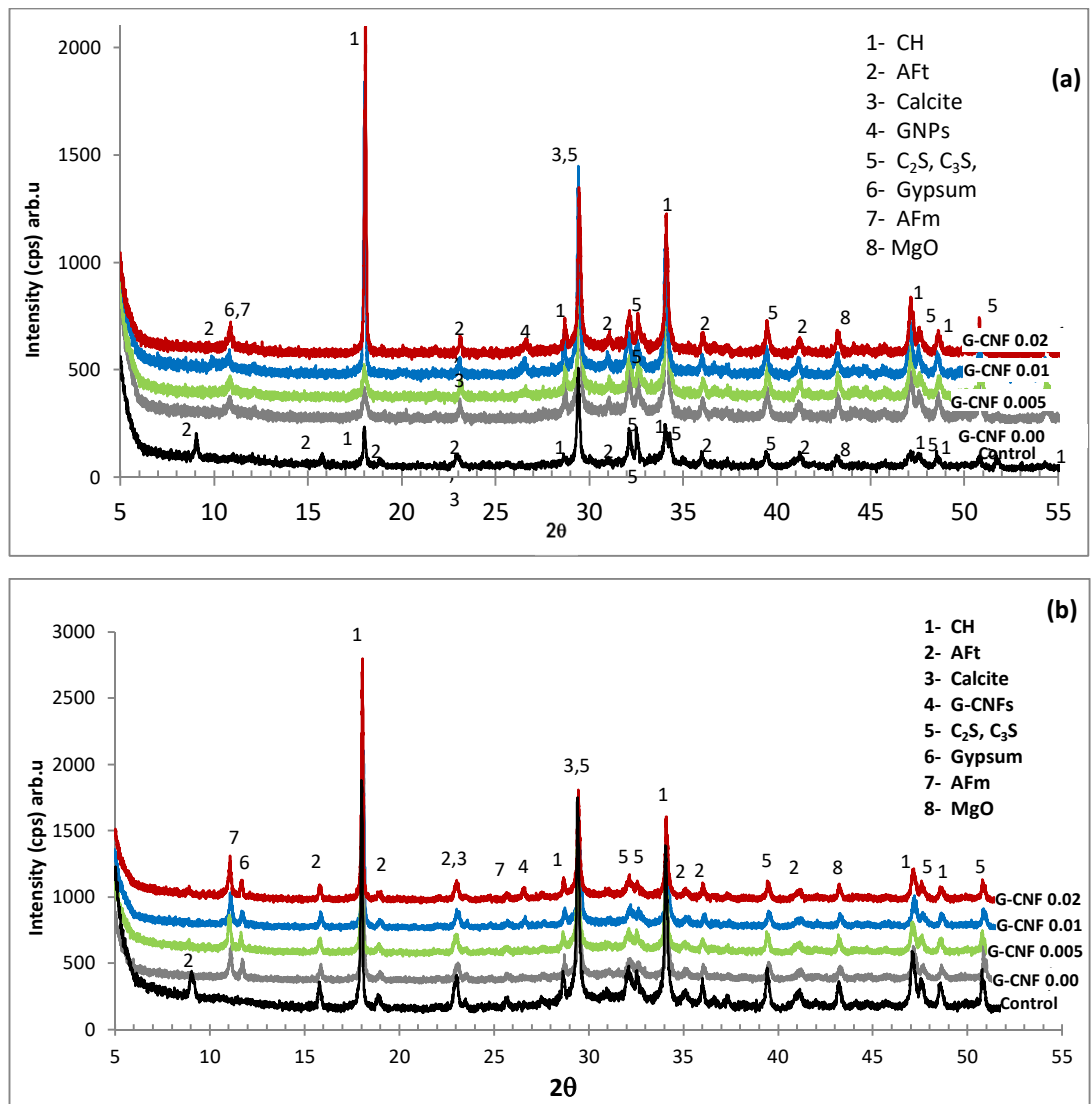
Figure 7.4 Combined XRD patterns of control and NGCC-CNF samples with varied contents at the age of a) 7days and b) 28 days

The XRD patterns of NGCC-CNF and control cement composite at the age of 28 days (Fig. 7.4b) indicate the reduction of diffraction peaks related to graphite C_3S and C_2S. This suggests that the consumption of cement particles in the progress of hydration may lead to increase the contents of hydration products especially CH and C-S-H, whereas, the reduction in graphite peak intensity may be due to diffraction affected by the growth of hydration products around the surface of nanofibers. The two peaks near diffraction angle 11.03° and 11.67° appeared in the samples are related to AFm phases and unreacted gypsum. It seems that organic solvent has slowed down the reaction of gypsum and hence the formation of AFt phases in the cement matrix. Moreover, C_3A reacted with AFt phases and transformed them into the AFm phases (Scrivener, 2004). It has been discussed in the previous chapter that in XRD measurements various diffraction peaks of hydration products especially AFt and C-S-H may be overlapped with higher intensities of water

149

bands and diffraction peaks of anhydrous cement clinkers such as CaCO3, C_3S, and C_2S. Therefore, FTIR measurements were employed to further reveal the chemical composition and bond formation in the NGCC-CNF composites.

The resulting FTIR spectrum obtained from NGCC-CNF and control composite at the age of 7 and 28 days is depicted in the Figure 7.5a and 7.5b respectively. FTIR spectrum of NGCC composite with varied contents of G-CNF can be distinguished clearly from the spectrum of control composite especially near area of water bands (3450cm^{-1} and 1650 cm^{-1}) and a characteristic band of C-S-H (957 cm^{-1}). It can be seen from the combined spectrums of 7days (Fig.7.4a) that major absorption band present in control composite near 3450 cm^{-1} due to stretching and bending vibrations of H-O-H in the compounds (AFt) is missing in the spectrums of all NGCC-CNF composites. Moreover, the water band near 1650 cm-1 in the spectrums of NGCC-CNF composites exhibits less absorption intensity as compared to the band present at the same position in the control composite. This suggests the less formation of compounds such as AFt in the NGCC-CNF composites. Further, the presence of CH compound in both control and NGCC-CNF composites can be mapped through the absorption band at 3647cm^{-1} due to the stretching of OH bond, and this band is more intense in case of NGCC with G-CNF 0.01 and 0.02 %. The similar trend of these bands near 3450cm^{-1}, 1650 cm^{-1} and 3647 cm^{-1} has been observed in the spectrums of both control and NGCC-CNF composites at the age of 28 days as shown in Fig.7.5b.

The FT-IR bands related to other hydration compounds such as calcium carbonate, AFt, AFm and C-S-H present in spectrums of 7days (Fig.7.4a) can be observed more clearly in the expanded view drawn separately (Fig.7.5c) between the range 1850-650 cm^{-1}. In the Fig.7.5a the strong characteristic bands related to calcium carbonate ($CaCO_3$) can be seen in the range of 1426-1430 cm^{-1} due to combined bending of v_2 and v_3 and at 871cm^{-1}due to bending of v_4. This may be due to the carbonation of samples during handling and storing for a longer duration before characterization. The sharp band of absorption at 1117 cm^{-1} due to the stretching vibration (v_3) of SO_4 indicates the presence of ettringites (AFt) in the control composite whereas this band stretched upwards in case of NGCC-CNF composites this might be indicating the transformation of AFt into AFm phases. The strong characteristic band centred at 950-960 cm^{-1} indicates the presence of C-S-H gel due to strong asymmetrical stretching vibration (v_3) of Si-O. This band is more intensified due to bending vibration of Si-O in case of NGCC loaded with G-CNF. This suggests that G-CNF triggered the growth of C-S-H in the nanocomposites.
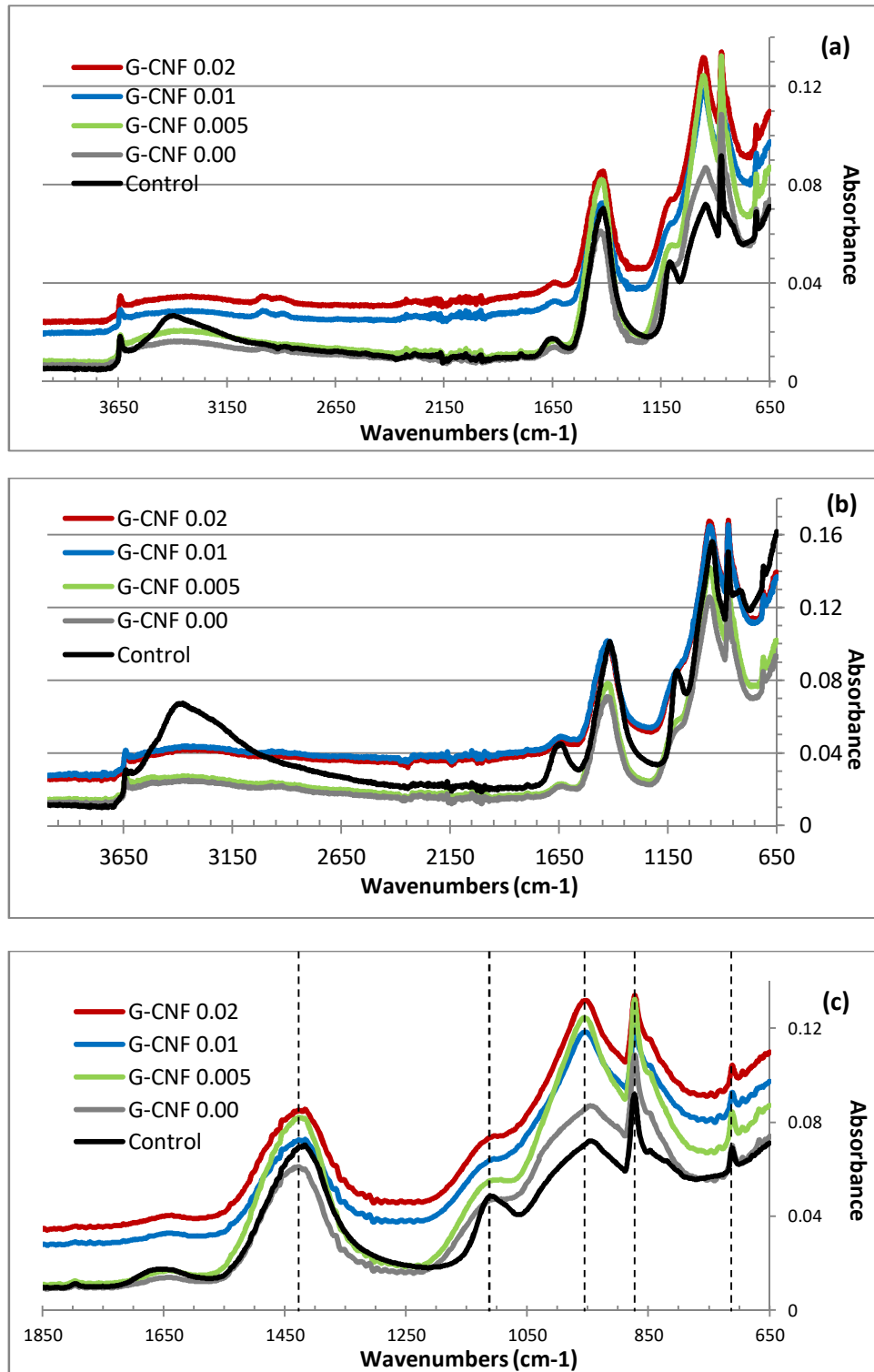
Figure 7.5 Combined FTIR spectrums of control and NGCC-CNF samples a) at the age of 7 days b) at the age of 28 days and c) expanded the view of Fig 7.6a between 1850 and 650 cm^{-1}

From the analysis of XRD and FTIR results, it is suggested that presence of G-CNFs itself has triggered the growth of CH and C-S-H hydration products in the cement matrix, that might be due to the nucleation effect of nanofibers. However, the addition of organic solvent used for the dispersion of G-CNFs has retarded the chemical hydration process and

might have resulted in less growth of AFt crystals. In the progress of hydration, the AFt crystals then transformed into AFm crystals. Further, no diffraction peak and absorption band related to the formation of the new compound has been observed in the XRD pattern and FT-IR spectrum of NGCC-CNF. This suggests that G-CNFs did not react chemically with the cement matrix but acted as a catalyst to accelerate the hydration process and might have interacted physically in the formation of hydration products due to their high aspect ratio and unique conical shape features.

7.3.2   Mechanism of Crystal Formation with G-CNF

To investigate the mechanism of crystal formation, regulated by G-CNFs in the cement matrix, high-resolution SEM and EDS measurements of un-fractured parts of samples were taken using the equipment, procedure and method already mentioned in chapter 3. The G-CNF contents of 0.005% were too low to observe in the representative samples. Therefore, NGCC composite with G-CNF contents of 0.01% and 0.02% were examined under SEM for crystal formation and EDS analysis.   Fig.7.6 depicts the growth mechanism of hydration products of control and NGCC with G-CNF 0.01% at the age of day 1. The irregular growth of rod-like AFt crystals with the mix proportion of other hydration products, such as CH, C-S-H gel and C-S-H amorphous solid, can be seen in SEM micrograph of control composite (Fig7.6a). Whereas, in SEM micrograph (Fig.7.6b), primarily C-S-H solid in amorphous form possibly encasing CH crystals has grown up in NGCC-CNF composite in bulk proportion. Moreover, the dense growth of C-S-H along the entire length of G-CNF surface initiated at this early stage.

It appears that G-CNFs are bonded strongly and secured better anchorage with C-S-H structure due to the unique conical shape features built upon their surface. Further, the high aspect ratio (~1300) and large surface area (24 m^2/g) with build-up features consisting conical graphited nanoplatelets of G-CNF might have provided the increased number of interaction points and initiated the nucleating effect for the hydration of C$_3$S as shown by arrows in the Fig. 7.6b. The improved microstructure and strength due to peripheral growth, strong covalent bonding, reinforcing and nucleating effect of CNTs and MWCNTs on the cement hydration products have also been reported previously (Li et al.,2007; Makar and Chan, 2009).
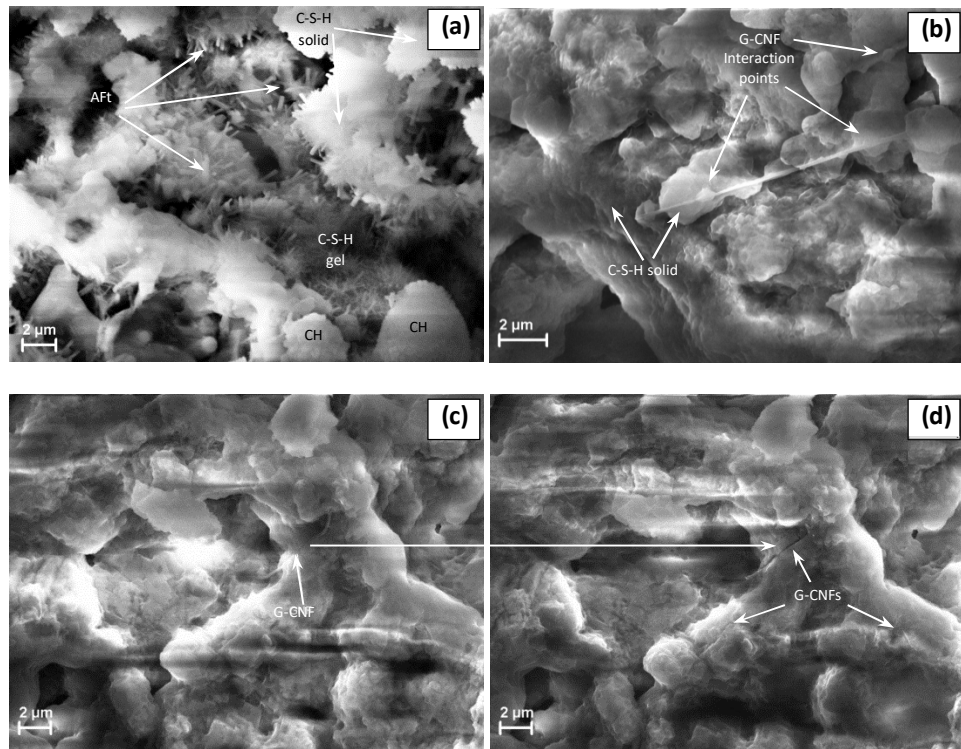
Figure 7.6 Growth mechanisms of hydration products day 1 a) control cement composite b) NGCC-CNF with 0.01 % G-CNF nucleating C-S-H c) C-S-H encasing G-CNF and d) G-CNF fully penetrated into C-S-H while taking measurements

The physical interaction of G-CNFs with the cement hydration products can be observed in the above SEM micrograph (Fig.7.6c) and accelerated the denser growth of C-S-H encasing the G-CNF and within a short period. While taking SEM measurements, the entire fibre has been penetrated fully into the C-S-H structure pointed by the arrow in Fig. 7.6d. From the SEM micrographs, it appears that the presence of G-CNF in the cement matrix reinforced the C-S-H structure with its 1D geometry and accelerated the hydration reaction due to its nucleating effect.

To investigate the chemical composition of cement hydration products near the G-CNFs, EDS measurements and spectrums were collected for the areas spotted in the Fig. 7.7. The EDS spot 1 and 2 were selected exactly on the G-CNF profile whereas hydration products grown near G-CNF were focused through EDS spot 3. The spectrums and elemental percentage % of EDS spots were collected through EDX TEAM software presented in the Fig. 7.7 and table 7.2 respectively. The elemental percentage % data of EDS spot 1 and 2 with carbon contents indicates the presence of G-CNF in the cement matrix. Whereas, higher contents of Ca and Si suggest the formation of a bulk amount of CH and C-S-H hydration products. Moreover, a small amount of elements whose composition close to AFt phases were also found in these spotted areas along the profile of nanofiber. This suggests

that less formation of AFt and a large number of CH crystals. However, they cannot be mapped through SEM micrographs at this stage and might be encased with the C-S-H. The formation of a large amount of CH crystal alone is not regarded beneficial for the strength and durability because of their poor strength and tendency to increase the alkalinity of cement microstructure (Stutzman, 2001). The increased contents of Na and K in the elemental composition of NGCC-CNF might be due to the increased growth of CH.
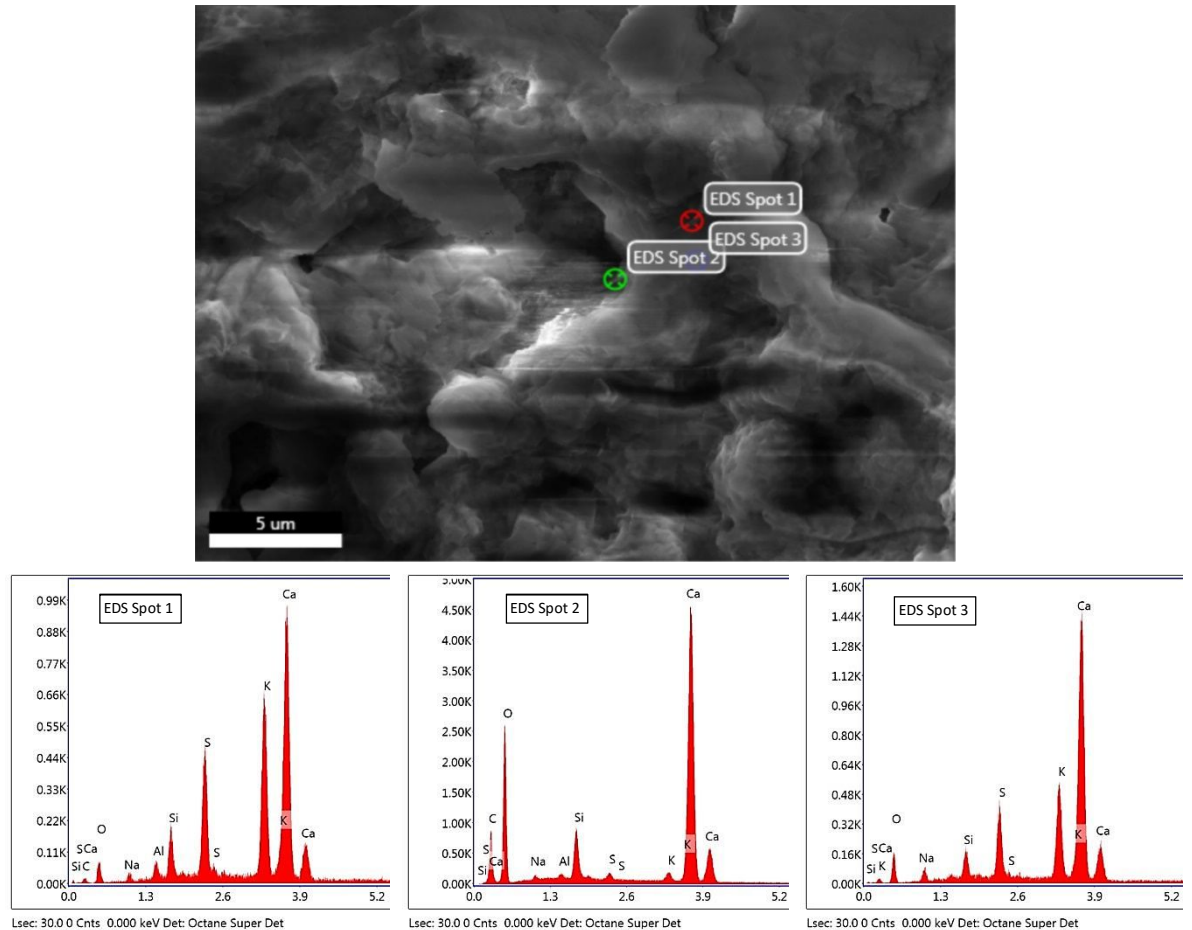
Figure 7.7 EDS spectrums of spotted areas of NGCC-CNF composite at day1 by operating SEM at 20.0 KEV

It seems that the presence of organic solvent used for the dispersion of G-CNF into the cement matrix might have retarded the reaction of sulphate ions with C_3A resulting less formation of AFt crystals. The higher contents of sulphur S measured at spot 2 and 3 suggest the presence of unreacted gypsum, whose traces were also detected in XRD patterns at 7 days of (Fig.7.4). Isopropyl alcohol also known as dimethyl carbinol is a chemical compound (C_3H_8O) miscible in water but not with a salt solution and forms separate layers in aqueous solution in the presence of salts (Rahway, 1983). The isopropyl alcohol might have separated from water due to the increased contents of Na and K in the NGCC composites introduced with a large growth of CH crystals.

154

Table 7.2 Chemical composition of C-S-H in NGCC with G-CNF 0.01 %

C-S-H Formation	Element percentage (%)							
	C	O	Ca	Al	Si	S	Na	K
(EDS Spot 1)	11.51	51.61	31.91	0.26	3.15	0.48	0.30	0.76
(EDS spot 2)	4.74	15.85	40.91	0.56	3.88	11.13	0.33	22.61
(EDS spot 3)	0.0	25.31	51.87	0.0	2.17	7.05	0.41	13.19

Further to observe the formation of hydration crystals regulated by the physical interaction of G-CNF in the progress of hydration, the SEM micrographs of NGCC were also taken at the age of 3,7 and 28 days and shown in Fig 7.8, 7.9 and 7.10 respectively. Figure 7.8 represents the SEM micrographs of NGCC with G-CNF contents of 0.01 % at the age of 3 days. It can be seen in the SEM micrograph (Fig.7.8a) that G-CNF provided the bridging mechanism to reinforce the C-S-H structure and paved the way for the denser growth of C-S-H in between the pores as shown in the Fig.7.8b. This bridging mechanism of G-CNF between the pores and C-S-H structures can be favourable to enhance the flexural and tensile strength of the cement microstructure. However, the rod-like AFt crystals were not observed in the NGCC composites due to their less formation.
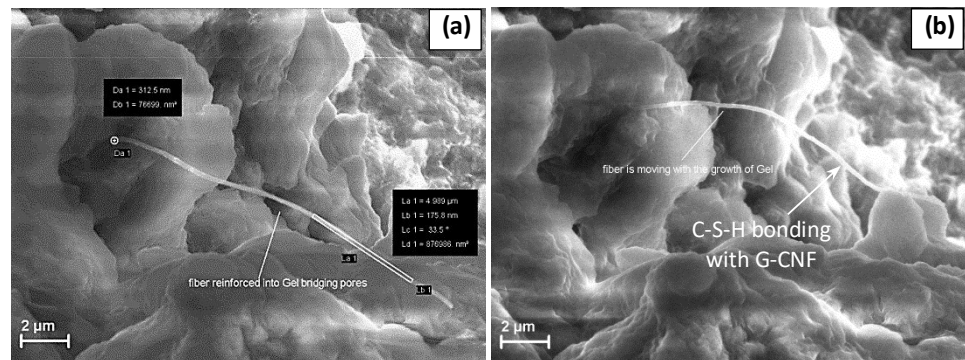
Figure 7.8 Growth of hydration products in NGCC- with G-CNF 0.01% at day 3 a) C-S-H growing along G-CNF profile and b) G-CNF reinforcing C-S-H structure and bridging the between the pores

It seems that 1D geometry and hydrophobic nature of G-CNFs were not able to generate a pore system within the cement matrix that can attract nano-sized water molecules near its surface to provide a favourable environment for the growth of AFt crystals. Since gypsum is highly soluble in water and releases Ca^+ and Sul^+ ions in the pores and causes C_3A to

form ettringites (AFt) (Taylor, 1992). Further, the presence of an organic solvent (Isopropyl alcohol) may also retard the hydration reaction of C_3A.

However, the formation of capillary pores has been observed in some areas of NGCC composite with G-CNF 0.02% at the age of 7 days. The formation of these pores can be associated with the columnar growth of C-S-H and CH crystals (Fig.7.9a and 7.9c), perhaps where the G-CNFs were present in more numbers in small bundles. This might be due to uneven dispersion with higher contents of G-CNF. These pores are most likely to be filled up with the potential growth of hydration products such as AFt and C-S-H in the progress of hydration. The C-S-H turning to the solid structure at this stage seems to have tobermorite-like sheets in its structure (Fig.7.9b) similar to those presented in Feldman and Sereda C-S-H model (Raki et al., 2010). The presence of AFt and CH crystals along with the denser growth of C-S-H structure can be observed in the high-resolution SEM measurements at the nanoscale (Fig.7.9b and 7.9d).
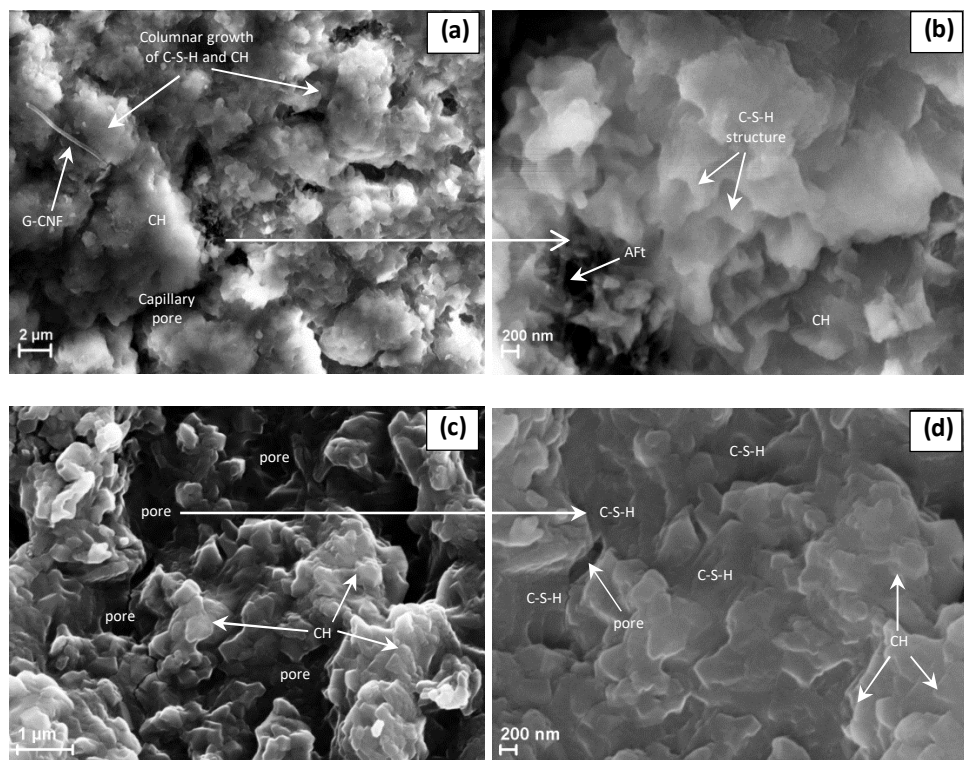
Figure 7.9 Growth of hydration products in NGCC with G-CNF 0.02% at day 7a) columnar growth of C-S-H and CH along fibre profile b) C-S-H turning to solid tobermorite like structure and AFt crystals in pores c) CH crystals with C-S-H developing pores in microstructure and d) C-S-H resin filling the pores

The characteristic morphology of AFt, AFm and CH appeared in pores at early days are not visible at the age of 28 days due to the excessive growth and dense packing of C-S-H around them. The cement matrix at this stage undoubtedly contains these hydration products but surrounded by solid C-S-H structures as shown in Fig.7.10a. Presence of these hydration products was also detected in XRD and FTIR spectrums. The combined growth of these hydration products reinforced with G-CNFs leads to shape up the crystals resembling with the red maple leaf as shown in Fig. 7.10b.

Through the observation of EDS measurements and SEM micrograph, it appears that G-CNFs regulated the formation of crystals in two ways in the cement matrix. First with the nucleation effect and accelerated the rate of hydration secondly, they provided the strong physical reinforcement to the cement matrix due to their unique surface features. Though the columnar growth of C-S-H and CH crystals generated some pores in the microstructure, this provided the strong connections between the hydration products.
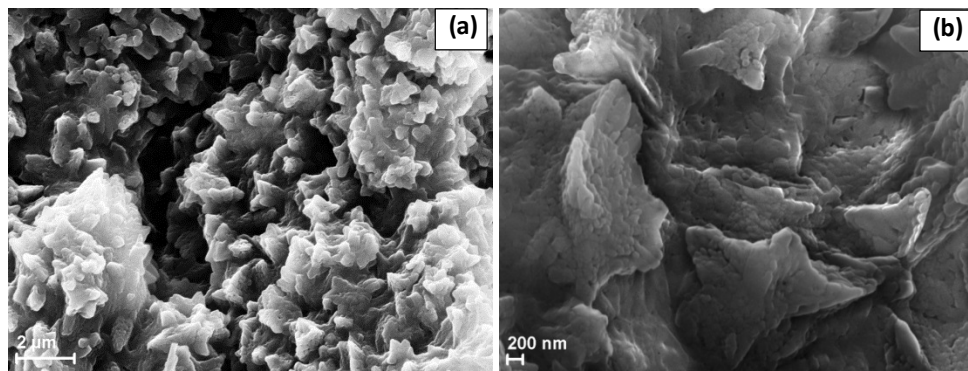
Figure 7.10 Growth of hydration products regulated by G-CNFs at day 28 a) hydration crystals surrounded by C-S-H products and b) C-S-H structure resembling maple leaf

7.3.3 Effect on G-CNF Pore Size Distribution of NGCC

In order to investigate the effect of G-CNFs on the pore structure of cement matrix, MIP and nitrogen gas absorption/adsorption test were employed in both control and NGCC-CNF composites at the age of 28 days. For the comparison, test parameters of control and NGCC composite with G-CNF contents of 0.02% are presented in Table 7.3. It can be seen from the test data that total volume of mercury intruded into NGCC composite is slightly increased (0.2872 ml/g) as compared to the intruded volume in control composite (0.2745 ml/g). This suggests that there is a slight increase in the porosity of NGCC-CNF composite. With the slight increase in the porosity in control composite 39.80% to 40.72%

in NGCC composite, there is the corresponding decrease in bulk density from 1.45 g/ml to 1.42 g/ml. However, average pore diameter (4V/A) measured 59.59 nm in control composite decreased to 50.52 nm in NGCC-CNF composite. Further, surface area measured through BET analysis has increased from 20.55m^2/g to 30.40 m^2/g. This suggests the increased growth of C-S-H in the cement matrix to develop such pore structure. It is widely accepted that the increased surface area of cement microstructure is associated with the increased degree of hydration (Thomas et al., 1998).

From the pore size distribution and SEM observation, it can be seen that the results of control composite are comparable with the NGCC composite. This suggests that G-CNF could not improve the pore structure of cement matrix as much rather there is a marginal increase in the porosity of NGCC composite due to capillary pores generated with the columnar growth of hydration products along fibre profile as discussed in the previous section.

Table 7.3 Intrusion data and nitrogen gas adsorption/desorption summary

Parameters	Samples	
MIP Test		
	Control	**NGCC-CNF 0.02**
Total Intrusion volume ml/g	0.275	0.287
Total pore area m^2/g	18.430	22.736
Average pore diameter (4V/A) nm	59.590	50.520
Median pore diameter nm	13.040	13.130
Bulk density g/ml	1.450	1.418
Apparent (skeletal) density g/ml	2.408	2.392
Porosity %	39.804	40.720
Nitrogen gas absorption/adsorption Test		
Surface area (BET) m^2/g	20.548	30.407
Cumulative volume of pores between 5 Å and 3000 Å width (cm^3/g)	0.050	0.072
BJH Adsorption average pore width (4V/A) Å	81.673	73.036
BJH Desorption average pore width (4V/A) Å	43.982	42.210

7.3.4   Effect of G-CNF on Microstructure of NGCC

To further investigate the interaction of G-CNFs with cement microstructure, SEM micrographs of fractured parts of NGCC-CNF samples were taken at the age of 7 and 28 days and compared with the micrographs of control composites. Fig. 7.11 depicts the SEM micrographs of control and NGCC composites with the increased contents of G-CNF at the age of 7 days. It can be seen in the control composite (Fig.7.11a) that rod-like AFt crystals are less in number but visible and irregularly interwoven with C-S-H and CH crystals. However, CH crystals and C-S-H amorphous solid are observed without AFt (Fig.7.11b) in

the NGCC composite prepared without G-CNF but mixed with an organic solvent. As discussed in the above section, the presence of organic solvent might have retarded the reaction of C_3A resulting less formation of AFt crystals.

Figure 7.11 SEM micrographs of 7days cement composites a) control b) NGCC-CNF 0.00 c) NGCC-CNF 0.005 d) NGCC-CNF 0.01 e) NGCC-CNF 0.02 and f) expanded view of marked area in 7.10e

It can be seen in the Fig 7.11c that G-CNF arrested the propagation of a crack through bridging mechanism but very small amount of G-CNF (0.005%) might not be able to resist the large cracks. However, less formation of very small cracks has been observed in the NGCC with GCNF 0.01% (Fig.7.11d). It seems that with increased contents of G-CNF

columnar growth of CH and C-S-H along fibre profile physically reinforced the cement microstructure and arrested the propagation of large cracks. From the XRD, FTIR and HR-SEM micrographs discussed in previous sections the increased growth of CH and C-S-H has been observed with increased contents of G-CNF in the cement matrix. However, traces of AFt and AFm phases were also detected in the XRD pattern at the age of 7 days.

The presence AFt and AFm crystals along CH and C-S-H can also be seen in the SEM micrograph of NGCC with 0.02% at the age of 7 days (Fig.7.11e-f). The presence of AFt and AFm crystals densifies the microstructure and could be responsible for increasing the flexural strength of the cement matrix. An improved microstructure with fewer cracks in NGCC with G-CNF contents 0.01% and 0.02% have been observed as compared to others and control composite. However, a few capillary pores have been observed in NGCC with G-CNF 0.02% composites due to the columnar growth of CH and C-S-H along the fibres. Most of the pores were filled with the massive growth of C-S-H in the progress of hydration as discussed in the previous section and shown in the Fig. 7.8d.

Microstructure developed in the control and NGCC-CNF composites at the age of 28 days was examined through the SEM micrographs shown in Fig. 7.12 (a-f). It can be seen in the SEM micrograph of control (Fig.7.12a) and composite with an organic solvent (without G-CNF) (Fig.7.12b) that cracks are passing through areas of dense hydration products in a straightforward manner. Whereas, NGCC-CNF cement composite showed (Fig.7.12c-e) comparatively fine cracks with considerable discontinuity. Moreover, G-CNF exhibited unique surface feature and strongly bonded with hydration products providing a large connection in the microstructure which can be seen pointed by arrows in Fig. 7.12d and 7.12e. This suggests that presence of G-CNF strongly bonded with C-S-H not only provided the physical reinforcement to microstructure to resist tensile loads but also deflected the propagation of cracks effectively to increase the peak loads. Further, the formation of AFm phases was observed in the NGCC-CNF composites and can be seen in the Fig. 7.12d and 7.12e pointed by arrows. AFm crystals usually formed with the transformation of AFt crystals when sulphate ion are not present or could not react with C_3A. The unreacted sulphur contents measured through XRD and EDS spectrums suggest that organic solvent obstruct the reaction of sulphate ions with C_3A. Therefore, AFt crystal developed were transformed into AFm crystals. AFm crystals are layered or lamellar shape penetrated into cement microstructure and might be helpful in further reinforcing the microstructure leading to enhance mechanical properties.
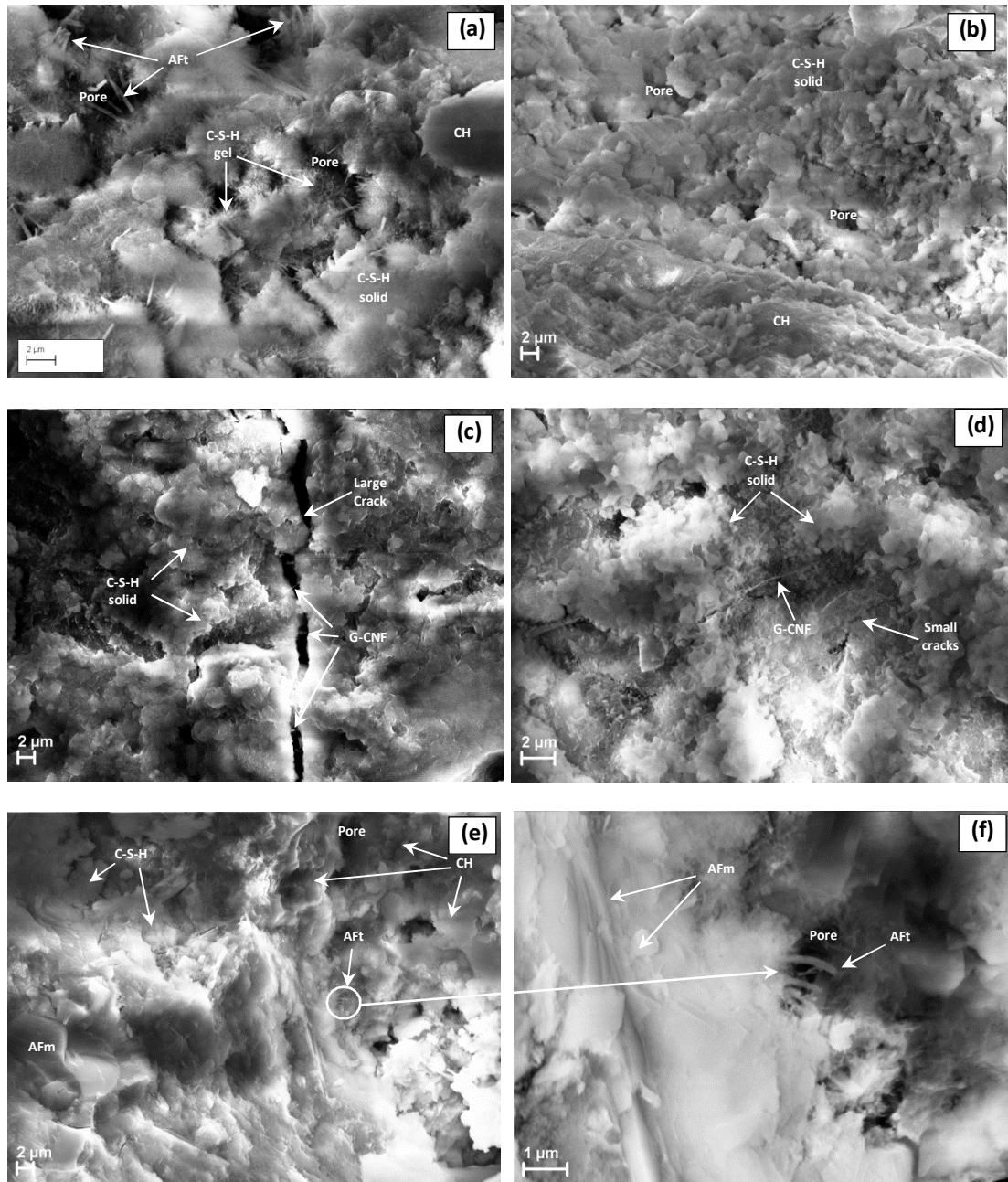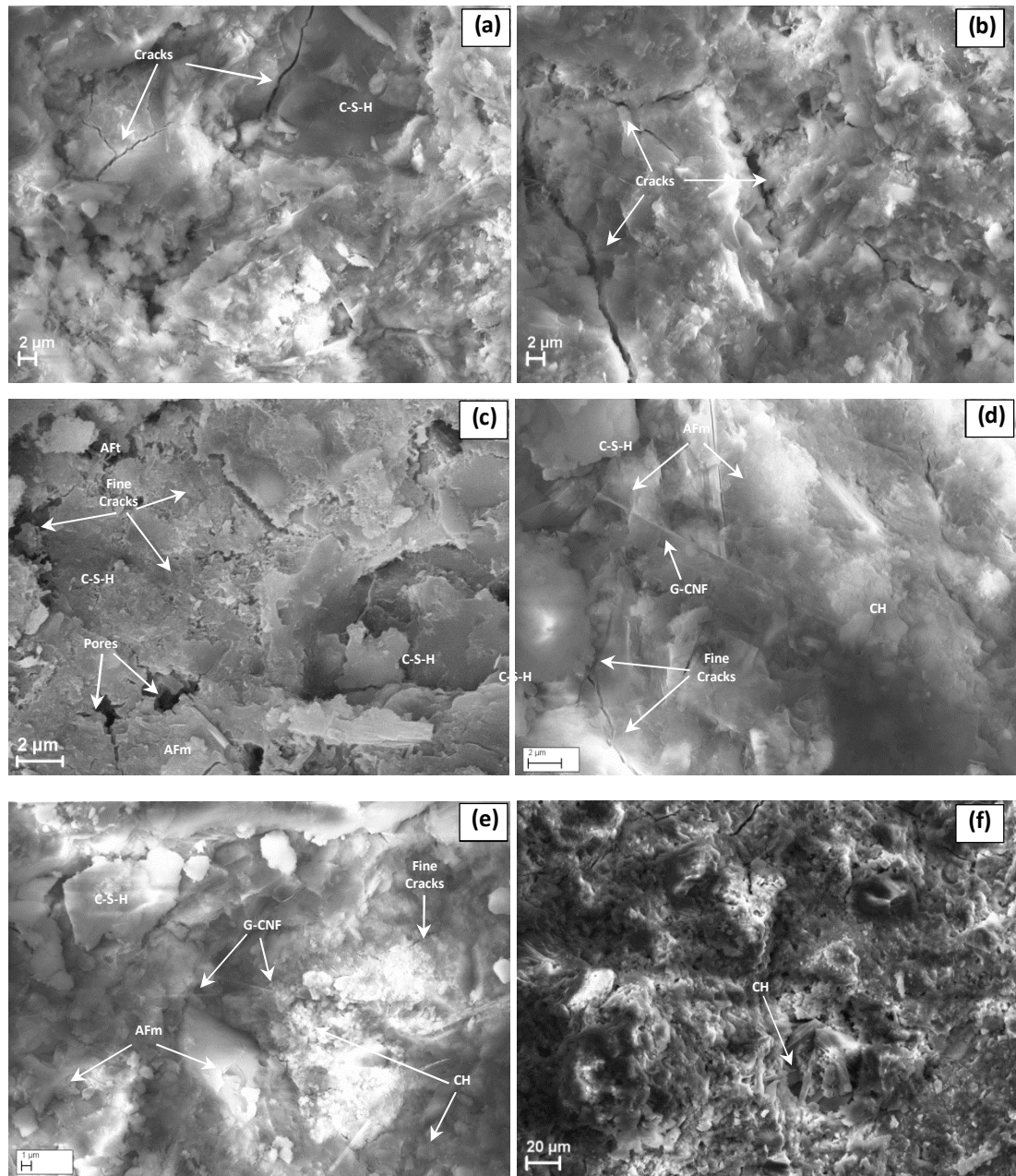
Figure 7.12 SEM micrographs of 28 days cement composites a) control b) NGCC-CNF 0.00 c) NGCC-CNF 0.005 d) NGCC-CNF 0.01 e) NGCC-CNF 0.02 and f) CH crystals in pore

7.3.5 Effect of G-CNF on the Mechanical Properties of NGCC

To investigate the effect of G-CNFs on the mechanical properties of NGCC, the samples with standard dimensions cured for 7, 14 and 28 days were tested for flexure, compression and tensile strength using the universal testing machine (UTM). The standard and procedures used for testing the samples are mentioned in section 3.5 of chapter 3. The mechanical strength results of control and NGCC composites with varied contents of G-CNFs were plotted in the form of graphs as shown in the Fig.7.13 a-c. Variation in the strength values was also analysed statistically by calculating the coefficient of variance

percentage (COV %) and plotted graphically as shown in Fig. 7.14 a-c. Detailed result data of 7, 14 and 28 days for strength values, percentage increase (% inc.) and (COV %) for all the samples are presented in Table 7.4 for reference.
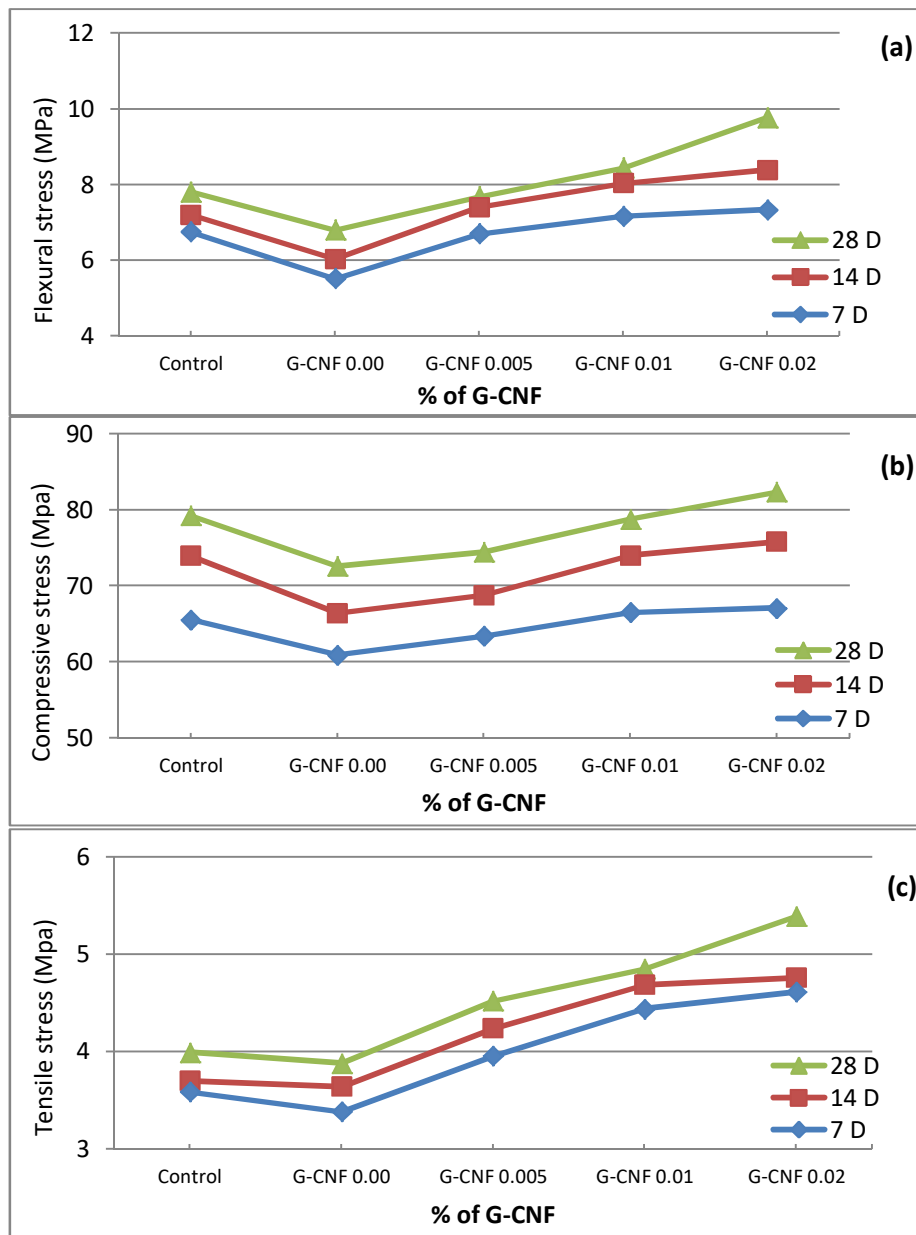
Figure 7.13 a) Mechanical strength graphs of control and NGCC with varied contents of G-CNF representing a) flexural b) compressive and c) tensile strengths at the age of 7, 14 and 28 days

It can be seen in the graphs (Fig. 7.13a-c) that the strength values of cement composite with G-CNF 0.00% decreased overall at 7, 14 and 28 days. The decrease in the strength of NGCC composite with G-CNF 0.00% and also in some samples of 0.005% were observed and mentioned with a negative sign in test data (Table 7.4). As discussed above, the NGCC with G-CNF 0.00% was prepared without any carbon nanofibers but mixed with organic

solvent similar to other composites to investigate its explicit effect on the cement hydration process.

Table 7.4 Mechanical strength test data

Flexural Strength									
Sample ID	**7days**			**14days**			**28days**		
	MPa	**% inc.**	**% COV**	**MPa**	**% inc**	**% COV**	**MPa**	**% inc.**	**% COV**
Control	6.75	0.00	5.43	7.20	0.00	4.54	7.81	0.00	4.48
GCNF 0.00	5.51	-18.38	8.91	6.02	-16.3	9.15	6.80	-12.9	10.07
GCNF 0.005	6.70	-0.74	14.89	7.40	2.8	9.86	7.68	-1.7	6.65
GCNF 0.01	7.16	6.17	10.25	8.03	11.6	8.12	8.44	8.1	5.72
GCNF 0.02	7.33	8.69	10.31	8.38	16.5	8.82	9.77	25.1	5.73
Compressive Strength									
Sample ID	**7days**			**14days**			**28days**		
	MPa	**% inc.**	**% COV**	**MPa**	**% inc.**	**% COV**	**MPa**	**% inc.**	**% COV**
Control	65.55	0.00	2.34	73.93	0.00	2.21	79.21	0.00	1.87
GCNF 0.00	60.91	-7.07	7.40	66.35	-10.2	8.32	72.56	-8.39	7.62
GCNF 0.005	63.37	-3.32	6.30	68.73	-7.03	5.74	74.41	-6.06	4.42
GCNF 0.01	66.50	1.46	6.50	73.96	0.04	6.55	78.75	-0.58	5.64
GCNF 0.02	67.04	2.27	7.14	75.78	2.50	6.38	82.34	3.96	5.87
Tensile Strength									
Sample ID	**7days**			**14days**			**28days**		
	MPa	**% inc.**	**% COV**	**MPa**	**% inc.**	**% COV**	**MPa**	**% inc.**	**% COV**
Control	3.59	0.00	11.36	3.70	0.00	6.63	3.99	0.00	4.70
GCNF 0.00	3.38	-5.67	4.68	3.64	-1.62	6.08	3.88	-2.81	5.26
GCNF 0.005	3.96	10.30	7.80	4.24	14.56	10.03	4.52	13.24	10.30
GCNF 0.01	4.44	23.76	9.23	4.68	26.66	11.62	4.85	21.54	7.50
GCNF 0.02	4.61	28.61	13.99	4.76	28.60	11.37	5.39	35.03	10.23

The test results in relation to the EDS and SEM measurements (Fig.7.7 and 7.10b) suggest that the organic solvent in the cement matrix retarded the hydration of C_3A and poor microstructure was developed due to the unequal proportion of AFt and CH crystals, this may be responsible for the decrease in the strength. It seems from the test data that the growth of hydration products increased with the introduction of nanofibers in the cement matrix, even with very fewer contents (0.005%) of G-CNF the flexural and compressive strengths improved although still below the strength of control composite (Fig. 7.13a and 7.13b). This suggests an increased hydration rate due to the presence of G-CNFs.

Moreover, increase of about 10-14% in the tensile strength of NGCC with G-CNFs contents of 0.005% (Fig. 7.13c) suggests that the unique shape of G-CNFs bonded strongly with the cement hydration products. The stronger interlocking to the cement microstructure with G-CNFs resisted the propagation of large cracks (Fig. 7.10c) and increased the peak tensile loads.

Similarly, a considerable increase in the tensile strength of NGCC with G-CNF 0.01% and 0.02% was also observed (Fig.7.13c) at the age of 7,14 and 28 days as compared to the control composite. Also, a reasonable increase in the flexural strength of NGCC with G-CNF 0.02% was consistent with the increased tensile strength. However, compression strength values of these nanocomposites were just comparable with control composites as shown in the Fig. 7.13b. For example, the flexural, compressive and tensile strength of NGCC with G-CNF 0.02% was increased by 8.69 %, 2.27% and 28.61% respectively at the age of 7 days as compared to control composite. The corresponding increase in strength at the age 14 and 28 days were 16.5%, 2.50%, 28.60% and 25.1%, 3.96 %, 35.03% respectively (Table7.4).
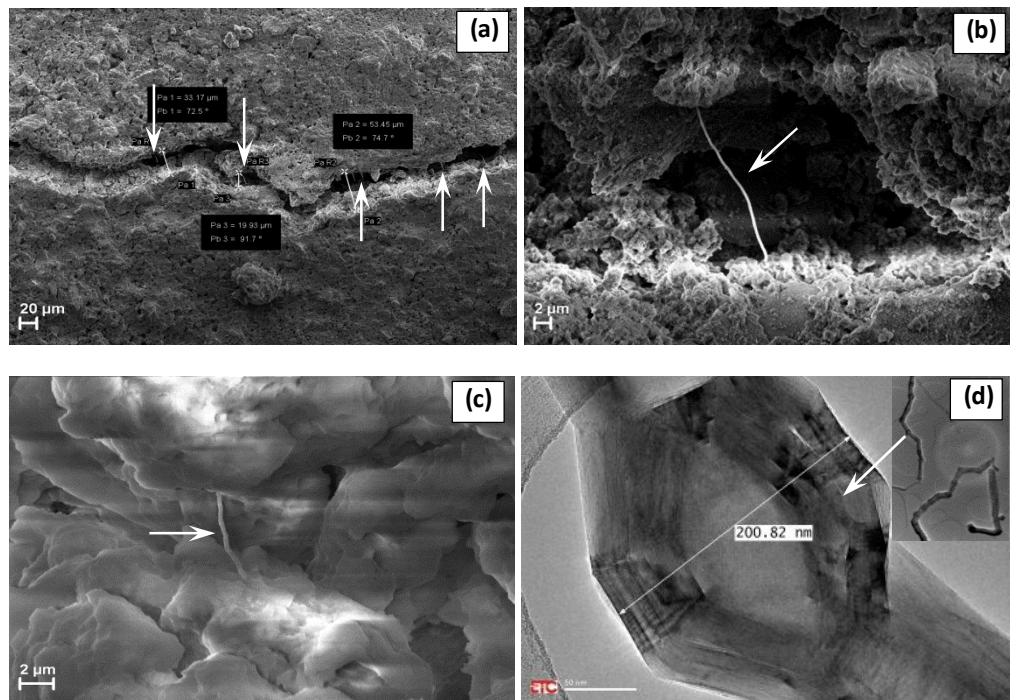

Figure 7.14 a) G-CNF bridging the cracks in NGCC-CNF 0.02 c) G-CNF bridging pores d) c) G-CNF providing interlocking with hydration products and d) nanoscale conical shape features of G-CNF

The test data suggests that considerable increase in the tensile strength of 35.03 % in NGCC composite with G-CNF contents 0.02% at the age of 28 days could be mainly due

to the physical reinforcement of G-CNFs. This reinforcement bonded strongly with C-S-H and connected the pores and cracks through the bridging mechanism as shown in the Fig.7.14a-c. It seems that unique nanoscale conical shape features of G-CNF (Fig. 7.14d) provided the better anchorage and interlocking with cement hydration products. Moreover, they not only provided physical reinforcement to resist direct tensile loads but also regulated the formation of hydration products responsible for resisting the flexural loads. A bridging action of CNTs influencing the tensile and flexural loads in the cement matrix has also been observed in the previous research work (Wang et al., 2013).

It can be seen in the graphs (Fig. 7.13c) that there is a linear increase in the tensile strength values of NGCC composites with the increased contents of G-CNF up to 0.01% at the age 7 and 14 days. Also, there is a marginal increase in the rate of gain of strength with G-CNF 0.02 % in the cement matrix. However, strength values considerably increased in NGCC with G-CNF contents 0.02% at the age of 28 days. It seems that the microstructure of NGCC strengthened with the formation of maple leaf shaped and AFm lamellar structures at the age of 28 days (Fig 7.9 and 7.11d-e).

Despite the presence of hydration products CH and C-S-H in large quantities, mapped through XRD, FTIR, and SEM micrographs of NGCC-CNF composites, the only reason for not much gain in compressive strength could be the columnar growth of these hydration products along the fibre profile leaving capillary pores around them (Fig.7.8c). Though the capillary pores seem filled up with C-S-H hard resin (Fig.7.8d) yet there could be chances for random leftover pores in the build-up microstructure. Increase in the porosity and corresponding decrease in the bulk density of NGCC-CNF composite discussed above in the section 7.3.3 can be related to the formation of comparatively porous microstructure as compared to control composite. Moreover, the adverse effect of organic solvent on the cement hydration might have led the formation of weak microstructure in some areas of nanocomposite and couldn't develop strength intrinsically. The large variations in the strength values of all NGCC-CNF were also observed as compared to control cement composite.

The variation in strength values was statically analysed by calculating the coefficient of variation percentage (COV%) and presented in the form of graphs in Fig. 7.15.
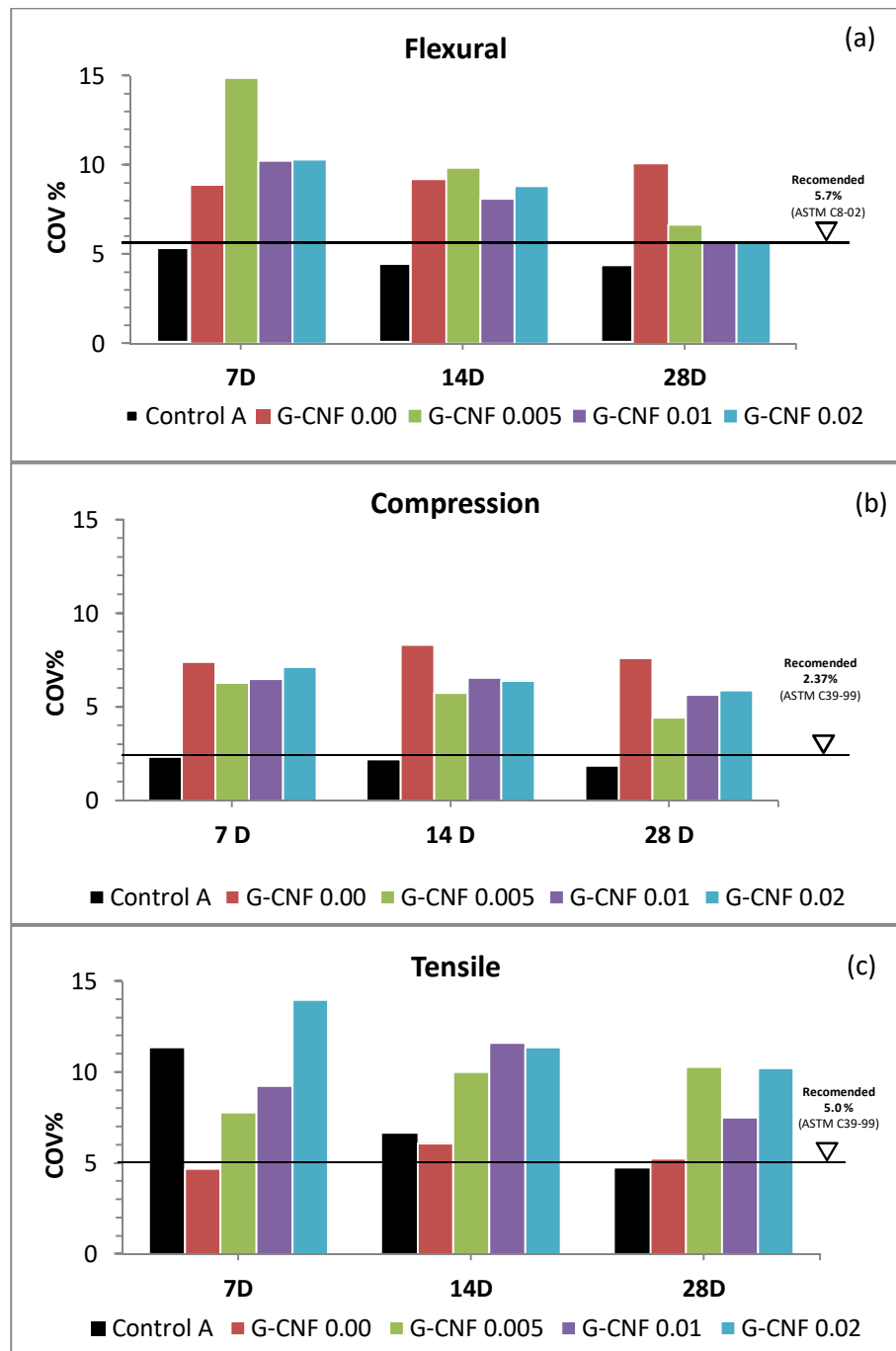
Figure 7.15 Variation in strength values of control and NGCC-CNF as COV% at 7, 14 and 28 days for a) flexural strength values b) compressive strength values and c) tensile strength values

It has been observed from the graphical data that COV% values of all NGCC-CNF were above the recommended values for flexural (5.7%, ASTM C8-02), compression (2.37%, ASTM 39-99) and tensile strengths (5.0%, ASTM 39-99). This suggests the development of poor microstructure due to the adverse effect of an organic solvent, or it could be due to agglomeration of G-CNFs caused by dispersion issues in some samples. It is suggested that chemical surface modification of these GCNFs via plasma exfoliation may develop better

166

dispersion capabilities in the aqueous medium without using organic solvent and enhanced properties can be achieved intrinsically when mixed with cement matrix.
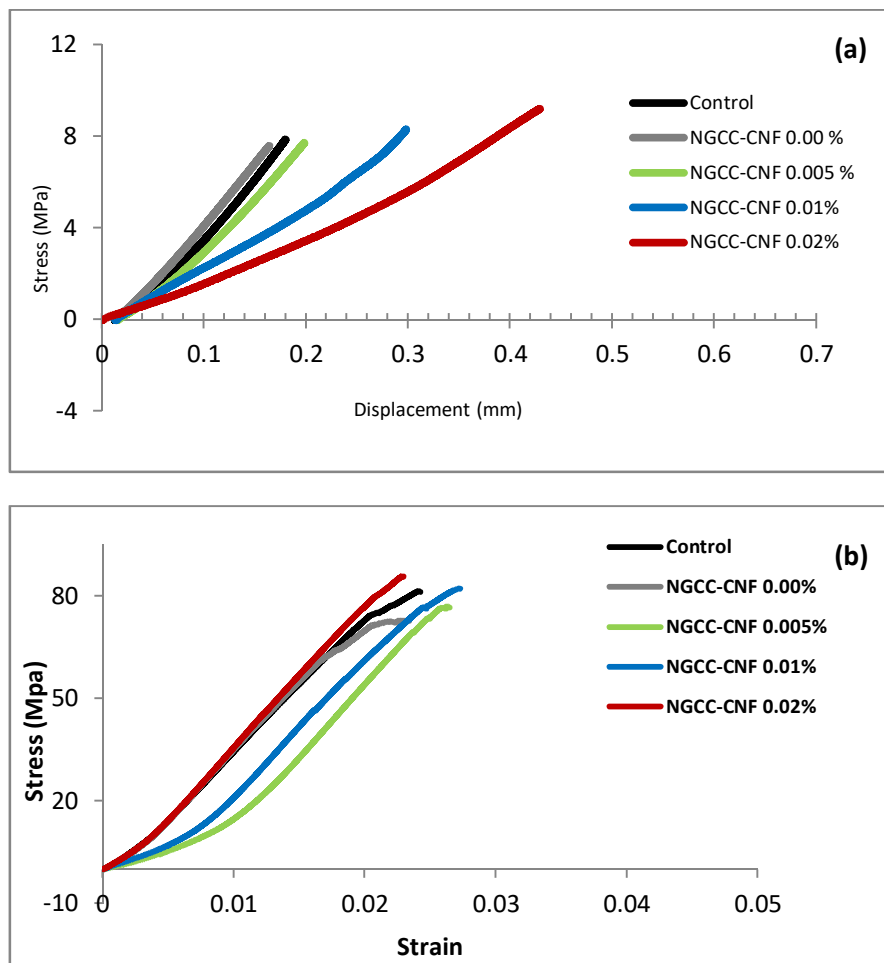
Figure 7.16 Curves showing stiffness and ductile properties of control and NGCC-CNF samples at 28 days a) typical stress-displacement curves under flexure and b) typical stress-strain curves under compression

The performance of NGCC-CNF regarding stiffness and ductility was also compared with the control cement composites. The typical stress-strain curves under flexure and compression stress for control and NGCC samples with varied contents of G-CNFs at the age of 28 days are shown in the (Fig.7.16). The relationship between flexural strength and displacement (Fig. 7.16a) for NGCC and control cement composites shows that NGCC with G-CNFs contents 0.01 wt.% and 0.02wt.% samples undergo large deformation approx. 0.30 mm and 0.43 mm respectively before yielding to maximum stress values, and covers the large area under the curves as compared to control cement and composites with less contents of G-CNFs.

This indicates that NGCC-CNF 0.01% and 0.02% has more tendencies to bend with the increased ductility and toughness due to the reinforcing effect of G-CNFs into the cement matrix. It appears that G-CNFs greatly influenced the elastic properties of nanocomposite by providing physical reinforcement and interlocking the hydration products, and delayed the propagation of microcracks. The almost comparable trend has been observed in the stress-strain relationship under compression (Fig. 7.16b) for NGCC and control cement composites. This indicates that there is no significant improvement in the NGCC in terms of compressive strength due to the increased porosity as discussed in above sections.

7.4 Conclusions

The high-performance cementitious composite of graphited carbon nanofibers (NGCC-CNF) was developed with varied contents of G-CNFs (0.00% to 0.02%) dispersed through organic solvent (Isopropyl alcohol) into the cement matrix. From the analysis of various characterization data and mechanical test results, the 0.02% contents of G-CNFs found optimum in the cement matrix. The higher diffraction peaks of CH in XRD patterns and higher absorbance bands related to C-S-H in FTIR spectrums suggested that G-CNFs not react chemically to form a new compound but accelerated the hydration of C_3S and C_2S. This suggested that G-CNFs with high aspect ratio acted as a catalyst for nucleation effect. Through EDAX characterization at detailed measurements of HR-TEM micrographs at nano-scale, enormous growth of C-S-H has been observed along the fibre profile. This indicated that high surface energy and unique 1D morphology of G-CNFs coupled with conical features of graphited nanoplatelets provided the more interaction points for the growth of C-S-H along its surface. However, columnar growth of C-S-H along the fibre profile might have developed capillary pores in some areas with higher contents of G-CNF and less formation of AFt crystals due to the adverse effect of an organic solvent which couldn't fill up all the pores (consequently porous microstructure) developed in these specific areas. Despite a marginal increase in porosity investigated through MIP test and nominal increase in the compressive strength, the NGCC with 0.02% G-CNFs contents outperformed in tensile strength test with a considerable increase of 35.03% at 28 days as compared to control composite. This suggested the G-CNFs acted as physical reinforcement and exhibited strong interfacial bonding with the cement matrix due to its unique conical features to resist tensile loads. Moreover, better anchorage and interlocking of hydration products through the bridging mechanism of G-CNFs arrested the cracks propagation and such increased the peak loads.

CHAPTER 8   Microstructure Regulated by Graphene Nanomaterials (GNMs)

8.1   Introduction

It has been discussed in previous chapters that cement hydration is a complex chemical process and produces various hydration products mainly C-S-H, CH, AFt and AFm. Among these hydration products AFT, CH and AFm exhibit perfect crystalline forms including rod-like, plate-like, and lamellar shapes respectively, while C-S-H initially formed as a gel and when cured become amorphous solid. The crystal shape and proportion of these hydration products depend on many factors and significantly influence the formation of microstructure, thus have a vital impact on mechanical properties of cement composite. In fact, there is a possibility to modify the microstructure of final hydration products of cement matrix using chemical admixtures, pozzolans, supplementary cementing components, adding nanomaterials and nano-fibres.

The effect of GO on cement microstructure has been investigated by many researchers, but its effect on shape change and formation crystals are very limited and in its infancy. The research work of Lv et al. is one of them in which they investigated the effect of GO nanosheets on the cement microstructure and mechanical properties influenced by shape change and growth pattern of hydration crystals (Lv et al., 2013). Through SEM characterization they proposed a possible mechanism regulated by GO shown in Fig. 2.37 and thought that GO nano-sheets could regulate the formation of hydration crystals by providing growth points on its surface and they called it a template effect. This template effect is equivalent to nucleation effect mentioned by others in their work (Table.2.6). According to their proposal, the GO stitched with active functional groups (-OH, -COOH, -SO_3H) at the edges reacts with C_3S, C_2S and C_3A and provides growth points for hydration products. They proposed further that with GO contents less than 0.04 wt.% in the cement matrix transformed the initially formed rod-like crystals (AFt) into flower-like crystals. While with higher contents (0.05 and 0.06 wt.%) of GO nanosheets these rod-like crystals transformed into regular or irregular polyhedrons shape crystals.

They used an admixture in the processing of GO cement composite and therefore, it may be possible that transformation of rod-like crystals into flowers shape crystals was due to the presence of polycarboxylate admixture in the cement matrix. Further, through SEM images they were unable to scale out the physical interaction of GO sheets with the cement

hydration products. Therefore, the proposed mechanism of cement hydration crystals regulated by GO needs further investigation in light of cement hydration chemistry.
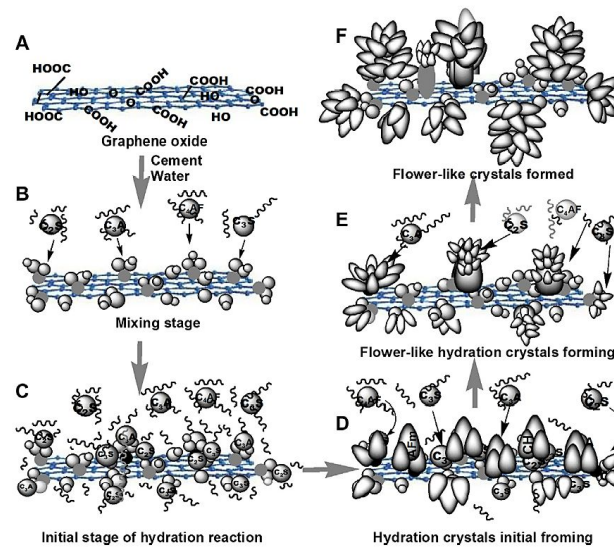
Figure 8.1 Proposed mechanisms of hydration cement crystals regulated by GO for by (Lv et al., 2013)

Moreover, the explicit effect of GO sheets on cement hydration for promoting the formation of rod-like hydration crystals on its surface and their further transformation into other forms of crystals such as flower or polyhedron crystals shapes needs scientific evidence through characterization techniques such as XRD, FTIR, EDAX. It would be suitable to propose a physical model by observing the physical interaction of graphene sheets with cement hydration products at nanoscale through SEM characterization.

In this chapter, the formation mechanism of different hydration products regulated by graphene nanomaterials (GNMs) has been discussed. SEM micrographs of un-fractured parts of samples of NGCC were examined under the controlled conditions to observe the growth of hydration products at early stages. Based on HR-SEM micrographs EDAX analysis and other characterization data, a possible mechanism of hydration crystal formation regulated by GNPs and GCNFs are presented.

8.2 Microstructure Regulated by GNPs

The cement hydration includes chemical and physical processes through a reaction between main constitutes (C_3A, C_3S, C_2S and C_4AF) of cement and water. The microstructure development of cement is not straightforward and has to go through complex chemical process mainly involving the hydration of aluminates and silicates.

Analytical studies conducted in the development of NGCC suggest that 2D shape GNPs acted as a catalyst rather than reactant and accelerated the hydration process through a unique network of nanoplatelets containing a system of pores, water molecules and liberated cement ions aligned in the spaces between them. Further GNPs forming an elementary skeleton provided the growth spaces to grow rod-like and plate-like hydration crystals with C-S-H gel in the physical hydration process. The Increased growth and their transformation into lamellar and polyhedral shapes took place in the favourable environment of Ca^{2+}, OH^- and Al_4O^- ions liberated from C_3S and C_3A in the water-filled gaps developed by GNPs. In the progress of hydration, the microstructure regulated by the GNPs further densified filling the pores with increased solid contents of CH and C-S-H. The mechanism of microstructure formation regulated by GNPs is mainly divided into four stages which includes i) Nucleation, ii) Formation, iii) Transformation and iv) Solidification, and explained in the following sections. The graphical representation of microstructure regulated by GNPs is presented in the Fig. 8.8.

8.2.1 Nucleation Stage

In general, when water is added to start the hydration in normal cement it becomes an ionic solution of high strength and generates the flocculated system of large water molecule surrounded by much smaller particles of cement as shown in the Fig. 8.2a. Cement particles remained unhydrated due to a large amount of water remained encapsulated in these flocs leading to slow hydration process.

(a)   **(b)**
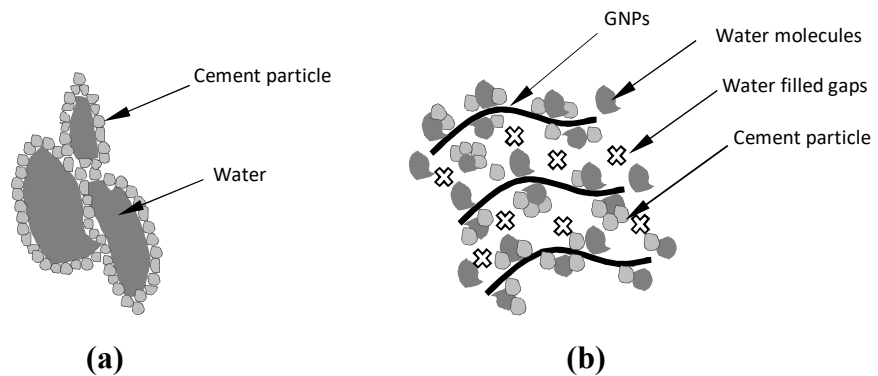
Figure 8.2 a) Flocculated system of water molecules in normal cement paste and b) network of pore systems of water filled gaps regulated by GNPs

From the XRD, FTIR, EDAX and SEM characterization it was suggested that GNPs due to its unique 2D shape, structural and surface properties induced the nucleation effect in the cement matrix and regulated the hydration process by developing a network of pore system of water filled gaps between GNPs as illustrated in Fig. 8.2b. In the high strength ionic

solution, the mobile ions such as Ca^{2+}, K^+, Na^+, OH^-, $SO4^{2-}$ and Al_4O^- liberated from the cement particles and small water molecules were attracted by oxygen-containing highly reactive sites on the surface of GNPs. With this nucleation effect, the attracted cement particles easily reacted with water molecules available near the surface in the water-filled gaps and accelerated the hydration process. The accelerated growth of hydration products observed through the SEM micrographs was in correlation with XRD and FTIR data.
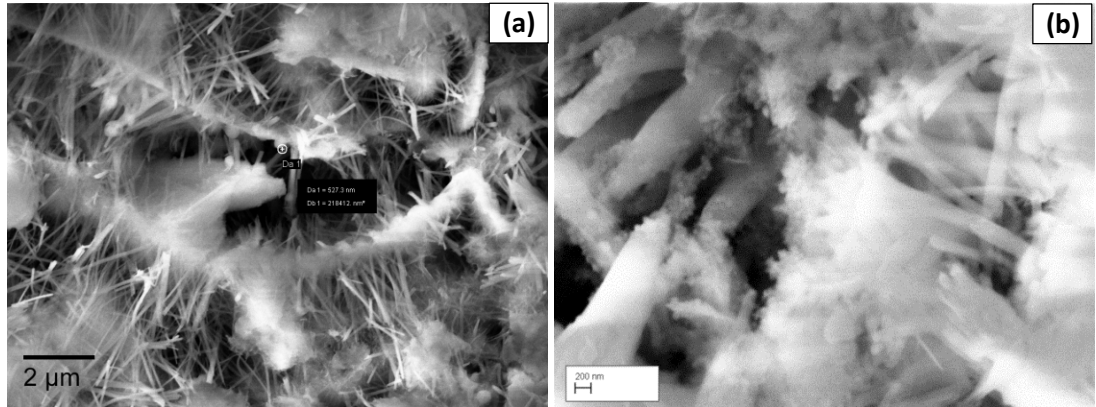
Figure 8.3 a) Nucleation of GNPs attracted to water molecules and cement ions of 500-600 nm range and b) cluster of cement ions in the range of nm-scale in the 3 to 4 µm wide water-filled gaps generated by GNPs

8.2.2 Formation Stage

In the next stage, the accelerated hydration of cement particles due to the nucleation of GNPs led to the formation of hydration crystals on its surface and in water-filled gaps in between the GNPs. C_3A hydrated quickly, reacting with sulphate ions to form AFt crystals. The aggressive growth of AFt crystals in large quantities took place in the suitable environment provided by GNPs hosting cement particles in a platelet arrangement. While in normal cement hydration AFt crystal could have been formed in less quantity due to dense packing with the stack-over arrangement of crystals where most of the cement particles remained unhydrated as illustrated in Fig.8.4.

Through the SEM micrographs, it was observed that with the progress in hydration GNPs encapsulated with C-S-H amorphous solid around its surface and a large number of rod-like AFt crystals out of the surface on both sides (Fig.8.3a). This arrangement suggests that the cement particles attracted in nucleation stage are now growing in the suitable environment provided by 2D shape morphology of GNPs. The integrated growth of AFt and C-S-H around the GNPs provided the elementary skeleton for further growth of hydration crystals and development of denser microstructure. More plate-like CH and C-S-H gel precipitated in the water-filled gaps due to the hydration of C_3S and C_2S at this stage.

Whereas, in normal cement paste most of the cement grains might have remained unhydrated due to the stake-up arrangement of cement particles and excessive growth of C-S-H around them (Fig. 8.4).
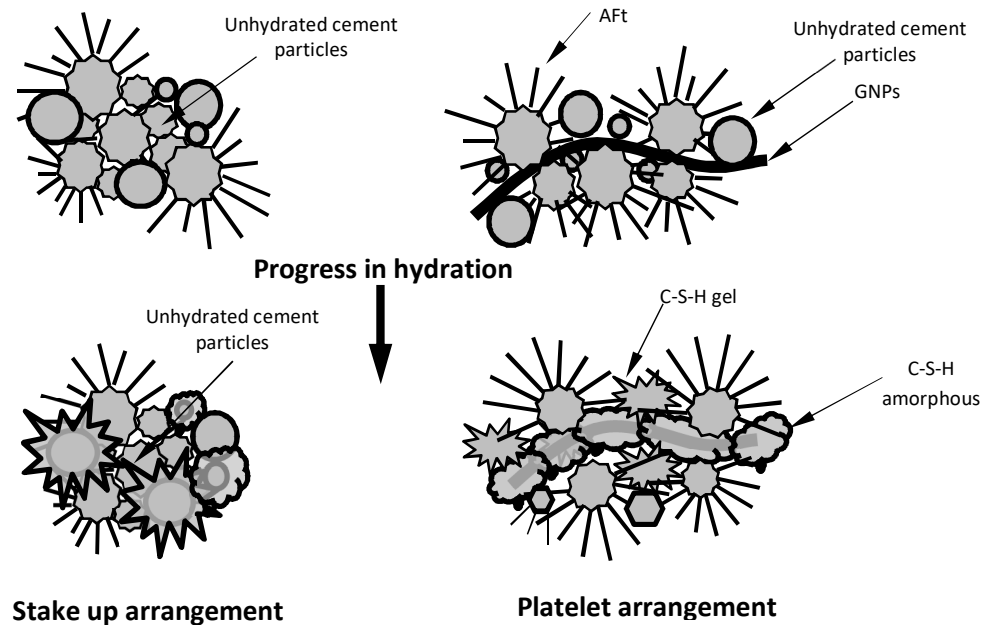
Figure 8.4 Formation of hydration crystals in stake up arrangement vs platelet arrangement
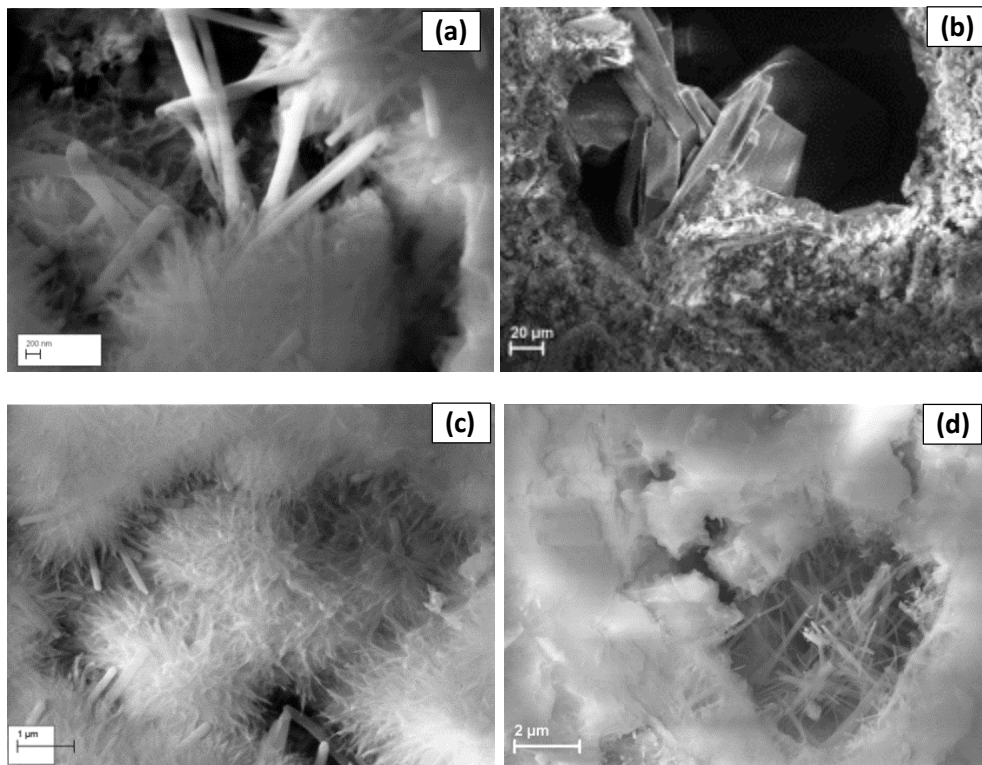
Figure 8.5 Formation of cement hydration products a) rod-like AFt crystals b)plate-like CH crystals c) C-S-H gel and d) C-S-H amorphous solid

The rod-like AFt crystals are seen as the interwoven network surrounded by CH and C-S-H filling the pores and gaps. AFt crystals approximately 6 μm long and 120-200 nm in diameter were observed twisted around C-S-H gel structures of 300-500 μm diameter. This microstructure development indicates that AFt reinforced the C-S-H structure towards the development of stronger microstructure. The formation of rod-like AFt, plate-like CH crystals, C-S-H gel and C-S-H solid has shown in the Fig. 8.5.

8.2.3 Transformation Stage

The denser growth of hydration products especially CH and C-S-H were observed around the elementary skeleton build up by GNPs. Most of the water-filled gaps were filled up with the interwoven growth of AFt, CH and C-S-H hydration products but still contained suitable environment of water molecules and Ca^{2+}, OH^- and Al_4O^- ions liberated from C_3S, C_2S and C_3A. Some of the rod-like AFt crystals reacted with C_3A after the consumption of sulphate ions and transformed into layered or lamellar crystal structures of AFm. The typical shape of AFm crystals observed can be seen in the Fig. 8.6 a-b. The presence of AFm crystals in the cement matrix was also mapped through XRD diffraction peaks.

Figure 8.6 Transformation of cement hydration products a,b) rod-like AFt crystals into layered or lamellar crystals of AFm. c,d) plate-like CH crystals into polyhedral shape

In the SEM micrographs, the polyhedral shape crystals of CH encased with C-S-H were observed with the hydration of C_2S, C_3S. From the EDAX analy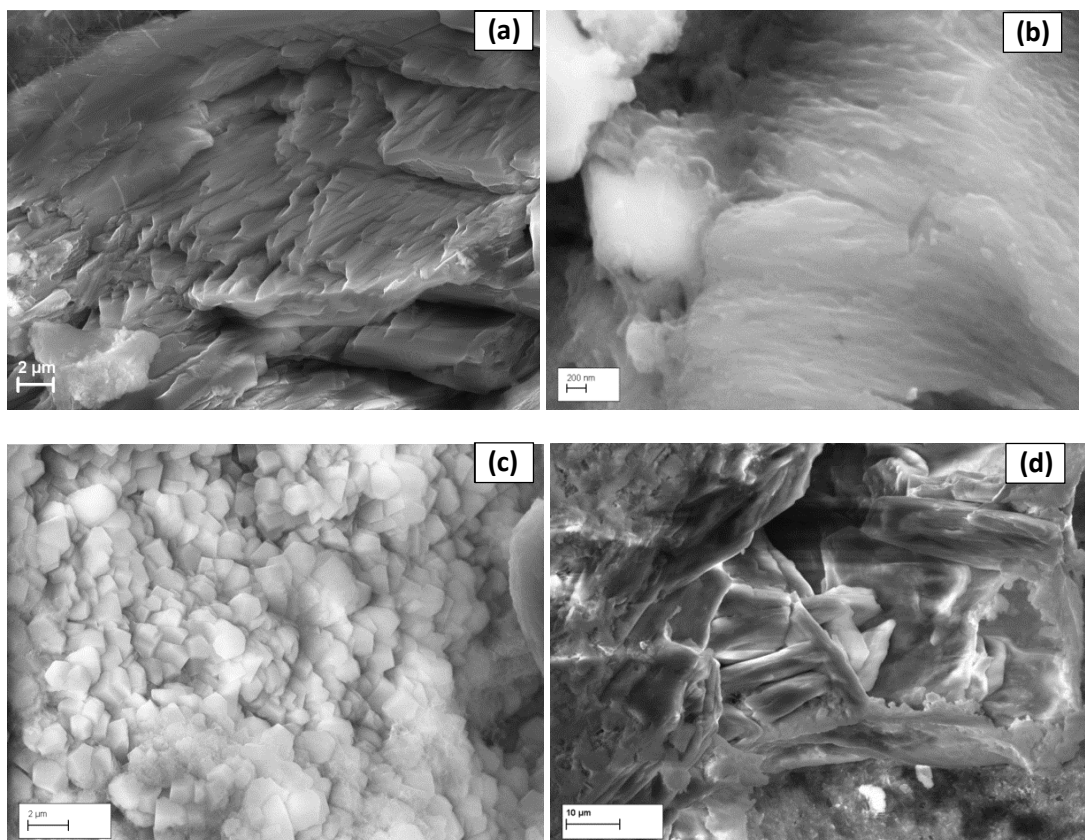sis it was found that elemental composition of polyhedral crystals contains Al and Fe contents but at higher contents of Ca relate them to CH crystals. Moreover, through mechanical testing, it was suggested that the polyhedral shape crystals might be responsible for increasing the compressive strength while rod-like AFt and lamellar shape AFm crystals contributed to the increase in the flexural strength of microstructure. The typical shape of the polyhedral and thick plate-like structures transformed from CH can be seen in the SEM micrographs presented in Fig. 8.6c and 8.6d respectively. The elementary skeleton of GNPs with further growth of denser C-S-H solids around them turned up to stiffer ribs like structures, and water-filled gaps were densely occupied by AFt, AFm, CH and C-S-H hydration products to represent as a whole solid mass.

8.2.4 Solidification Stage

In the progress of hydration, the microstructure developed earlier further densified with the solid contents of CH and C-S-H with the hydration of C_2S. There might be a formation of few more AFt crystals with the hydration of C_4AF, but this could not be detected in the dense and solid mass of C-S-H. It was difficult to observe the microstructure of cement matrix at this stage when the hydration products turned into solid masses. However, at some places with less C-S-H growth, the interaction of GNPs was observed. The ribbed GNP structure, encased with solid C-S-H integrated with dense and hardened masses of AFt, AFm and CH, representing a distinctive microstructure of cement hydration products, can be seen in the SEM micrograph in Fig.8.7. This phenomenon suggests that GNPs not only regulated the formation of the microstructure of cement hydration products but also acted as nano, reinforcement bonded strongly with C-S-H to resist the propagation of cracks.
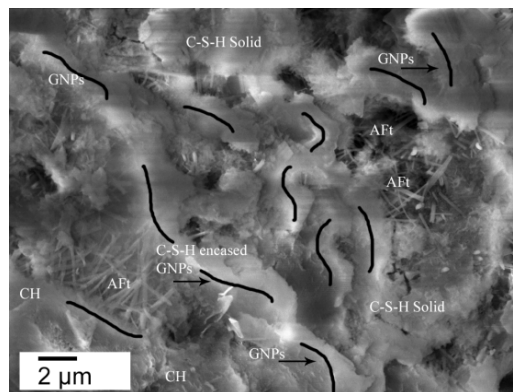

Figure 8.7 Distinctive microstructure of hardened cement paste with ribbed GNPs

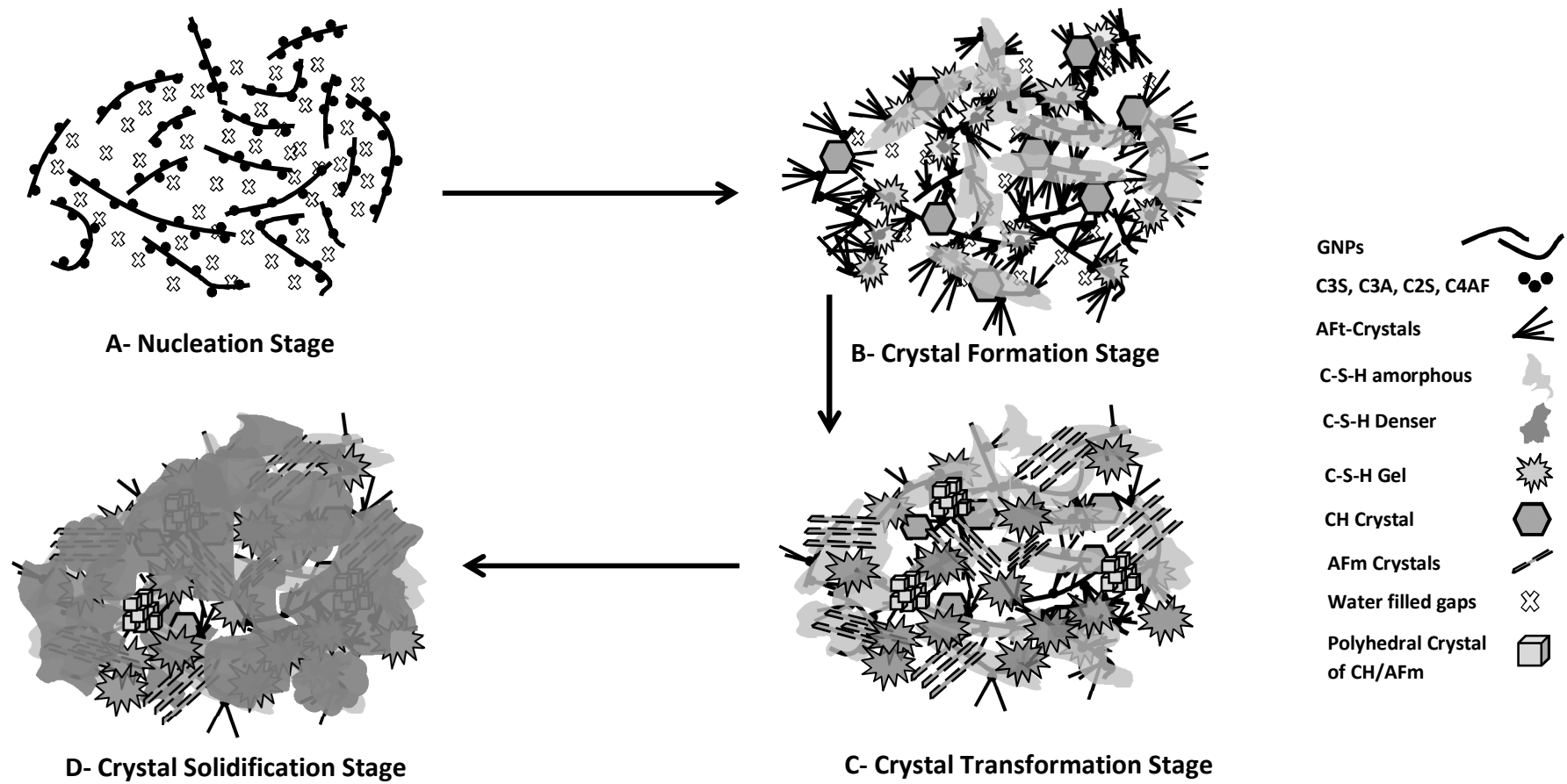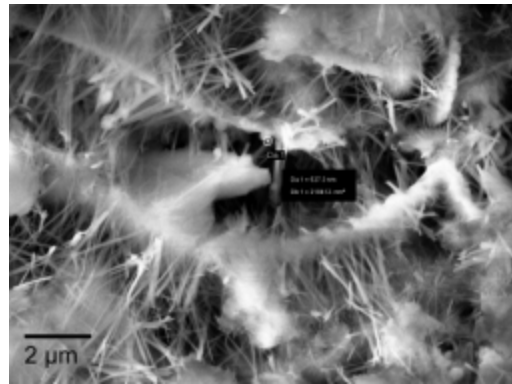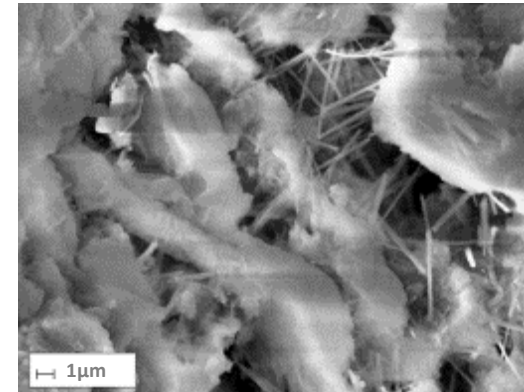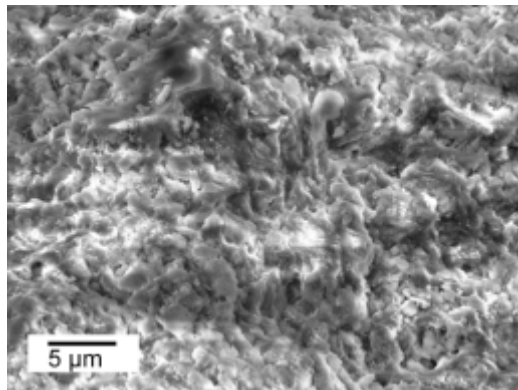**Figure 8.8 Microstructure of cement hydration regulated by GNPs**

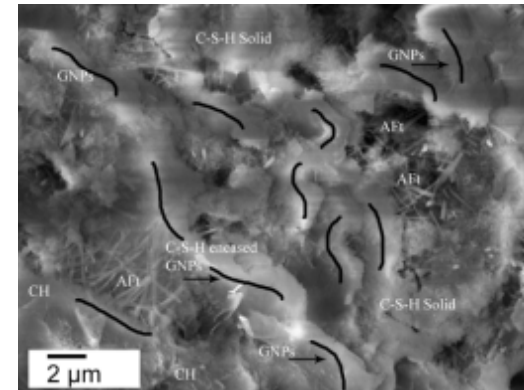**A- Nucleation Stage**

B- Crystal Formation Stage

D- Crystal Solidification Stage

C- Crystal Transformation Stage

Figure 8.9 Corresponding SEM micrographs of microstructure regulated by GNPs

8.3 Microstructure Regulated by GCNFs

As aforementioned, the kinetics of cement hydration and formation of the resulting microstructure is a complex process and depends on driving factors. It was observed that 2D shape of GNPs regulated the growth, formation and development of cement hydration crystals to form distinctive microstructure discussed above. Interestingly, 1D shape and unique morphology of GCNFs regulated the microstructure development of cement hydration products differently. The unique conical features of nanoplatelets provided the interaction points to initiate the nucleation effect in the cement matrix. The high aspect ratio, high surface area and linear morphology of GCNFs accelerated the hydration process and led to the formation of a bulk amount of CH and CSH in the amorphous solid along the fibre profile. However, the presence of organic solvent affected the hydration of C_3A resulting in less formation of AFt and AFm. In the progress of hydration CH and C-S-H amorphous solid transformed into polyhedral crystals encased in the hard resin of C-S-H in the form of columnar structures. These columnar structures reinforced with GCNFs finally solidified with a shape resembling a red maple leaf and developed the microstructure capable of resisting tensile loads. The stages of microstructure development regulated by GCNFs are explained in following sections and represented graphically in the Fig. 8.14.

8.3.1 Nucleation Stage

Contrary to GNPs, GCNFs possess hydrophobic nature and hard to disperse into the aqueous medium. Therefore, the organic solvent was used for ultimate even dispersion of GCNFs into the cement matrix. It was observed through HR-SEM micrographs that GCNFs due to 1D shape and hydrophobic nature could not develop a network of pores similar to GNPs. Instead of it, flocs containing a large amount of water surrounded by cement particles might have been developed. However, the high surface energy and unique conical features of 200 nm sized nanoplatelets inserted into GCNFs initiated the nucleation effect in the cement matrix and provided the interaction sites to make a bond with cement hydration products as shown in the Fig.8.10. The C-S-H floc structures bonded strongly with the fibre surface started to grow along the fibre profile. The high aspect ratio (~1300) and high surface area (24 m^2/g) of GCNFs accelerated the hydration process and increased the growth of CH and C-S-H in amorphous solid form. The accelerated hydration was confirmed through EDAX, SEM, XRD characterization and higher absorbance bands of FTIR spectrums.
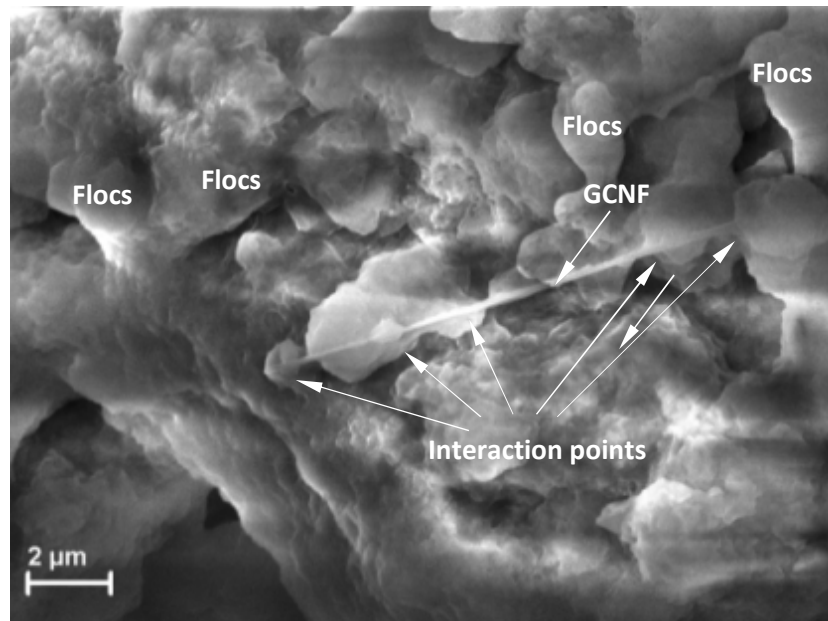
Figure 8.10 Nucleation effects of GCNFs into the cement matrix, C-S-H interacting with CNFs

8.3.2 Formation Stage

The GCNFs bonded strongly with the C-S-H structure not only provided the physical reinforcement but also accelerated the growth of hydration products due to the nucleation effect and regulated the formation of hydration products. With the accelerated hydration of C_3S and C_2S, the formation of CH and C-S-H along the fibre profile can be seen in the Fig. 8.11. Moreover, the GCNFs reinforced into the C-S-H structure also provided the bridging mechanism to interlock hydration products at this stage and arrested the cracks at a later stage of hydration. However, due to the adverse effect of organic solvent on the hydration of C_3A, less formation of AFt crystals was observed.
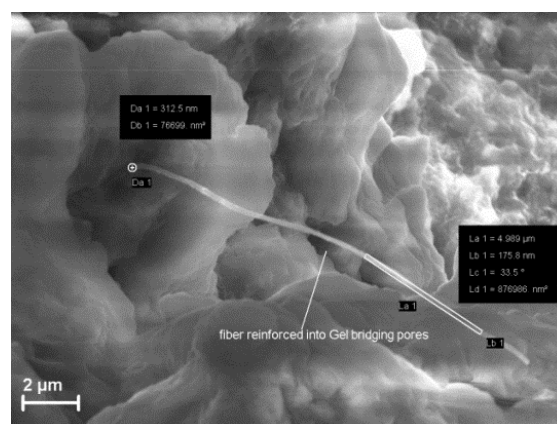
Figure 8.11 Formation of CH and C-S-H hydration products in amorphous form along the fibre profile

179

Further, with the hydration of C_2S more formation of CH was observed along the fibre profile in the SEM micrographs as well as in XRD patterns obtained.

8.3.3 Transformation Stage

The columnar structures consisting CH polyhedral shape crystals covered with the hard resin of C-S-H were observed at this stage as shown in the Fig. 8.12. It seems that amorphous form of CH developed earlier now transformed into the polyhedral shape crystals also with the hydration of C_2S, the flocs liberated the encased water molecules to form C-S-H hard resin. Moreover, C-S-H amorphous turned to more solid with tobermorite-like sheets in its structure. The columnar structures reinforced with GCNFs acted as a skeleton, and C-S-H hard resin filled into the pores between them further developed the denser microstructure. However, porous microstructure was observed locally due to unfilled pores also verified by MIP test data. Moreover, AFt formed earlier were seen transformed into AFm phase also correlated with the peaks appeared in XRD patterns.
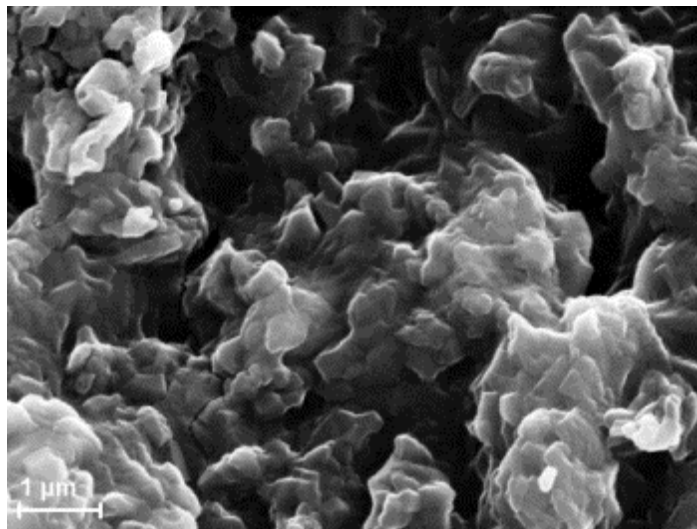
Figure 8.12 Transformation of CH and C-S-H amorphous hydration products into polyhedral and hard resin

8.3.4 Solidification Stage

In the progress of hydration, the CH in columnar structures, AFt, AFm and excessive growth of C-S-H filled the pores further transformed into solid crystals of a shape similar to the red maple leaf as shown in Fig.8.13. These solid crystals reinforced with GCNFs provided the large and strong connections between the hydration products, leading to develop a strong microstructure capable of resisting flexural and tensile loads. Moreover,

these solid crystals also deflected the propagation of cracks and increased the flexural and tensile strengths observed from the mechanical test data.
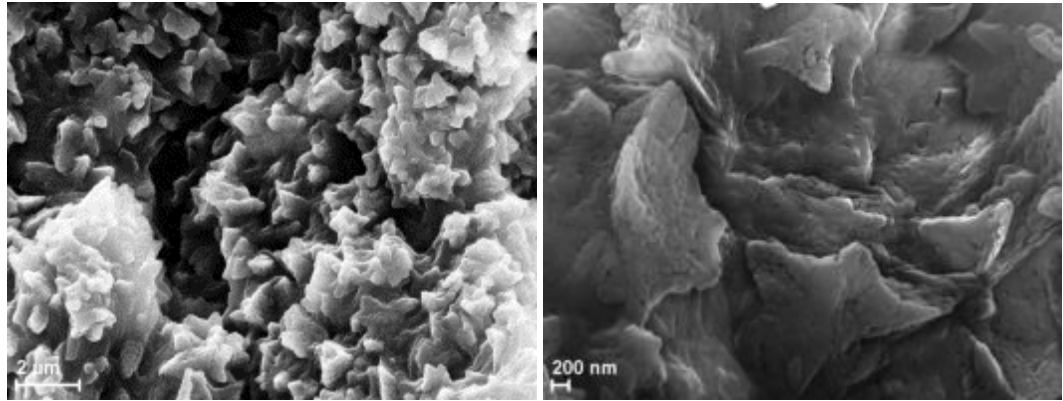
Figure 8.13 Solid crystals resembling the shape of red maple leaf in the microstructure regulated by GCNFs

8.4 Conclusions

The formation mechanism of cement hydration products regulated by GNPs and GCNFs detailed in previous chapters are summarised here with graphical model representations. GNPs and GCNFs regulated the cement microstructure differently. The shape (2D and 1D) of these nanomaterials played a vital role in the formation of cement hydration products and development of microstructure ultimately responsible for increasing toughness. The GNPs with 2D shape regulated the formation of hydration products by developing a network of pore system of water filled gaps where rod-like crystal AFt developed in large quantities helpful to densify the microstructure. Moreover, C-S-H grown on the surface of GNPs due to the nucleation effect provided the skeleton for further development of microstructure. Whereas, GCNFs regulated the microstructure in two ways, accelerating the hydration process through nucleation and providing the physical reinforcement through the enormous growth of C-S-H along fibre profile. The unique conical features of GCNFs morphology provided the interaction points or reactive sites for C-S-H in the nucleation stage and strong interlocking between hydration products at formation stage. The hardened microstructure regulated by both GNMs was apparently similar due to the denser growth of C-S-H around the elementary microstructures but different in properties.
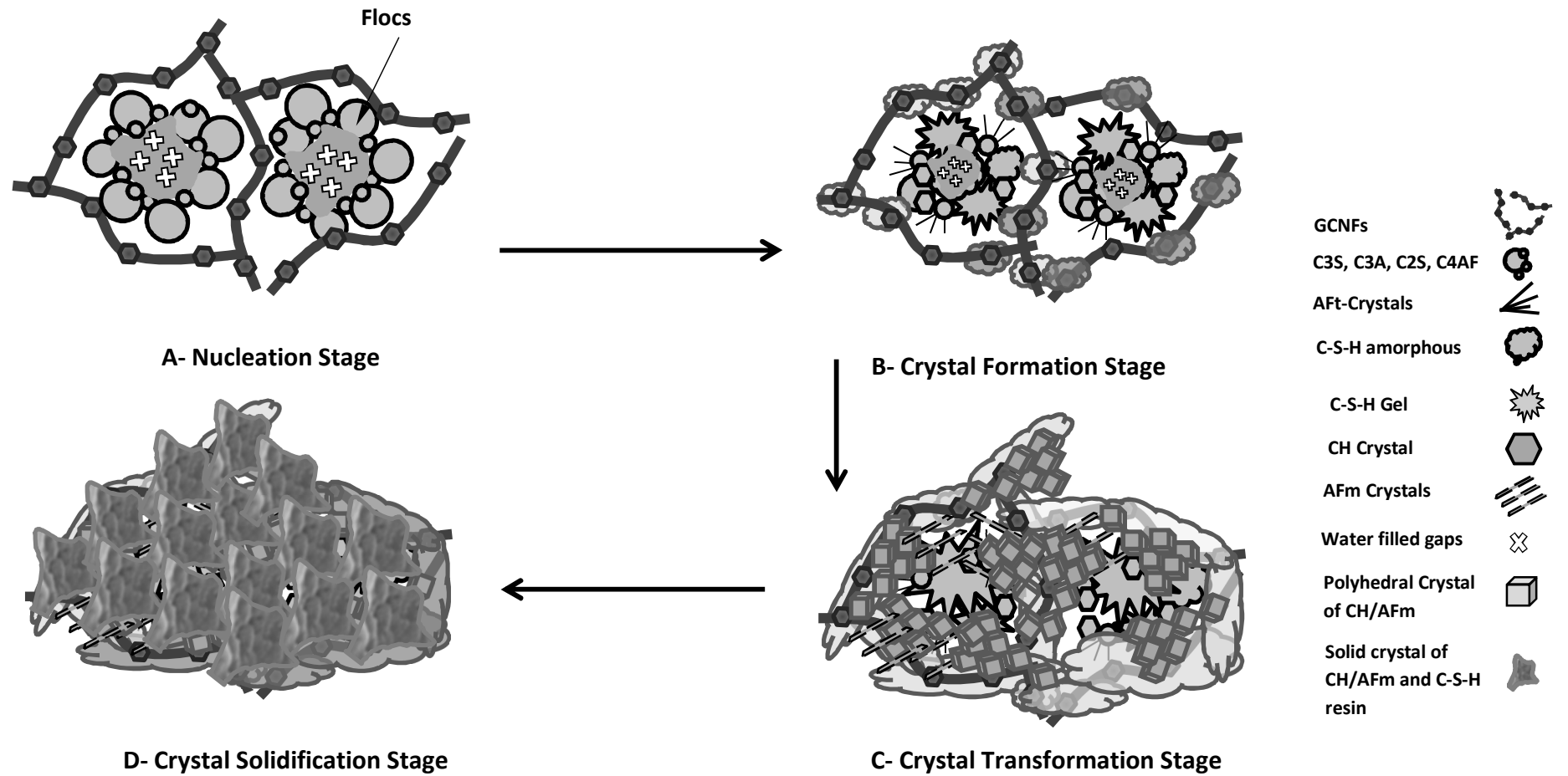
Figure 8.14 Microstructure of cement hydration regulated by GCNFs
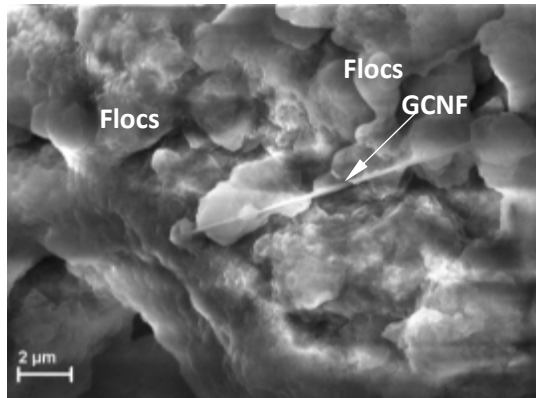
A- Nucleation Stage
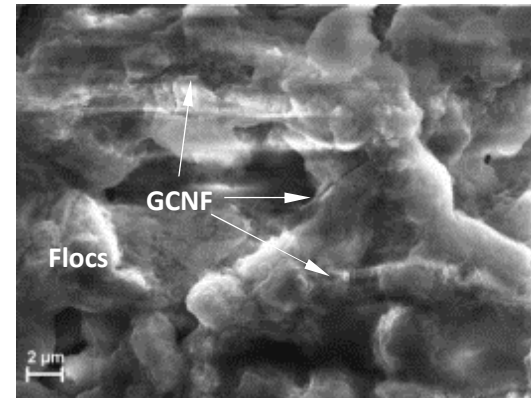
B- Crystal Formation Stage
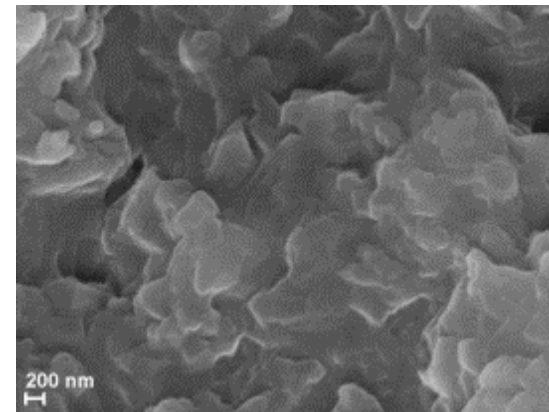
D- Crystal Solidification Stage
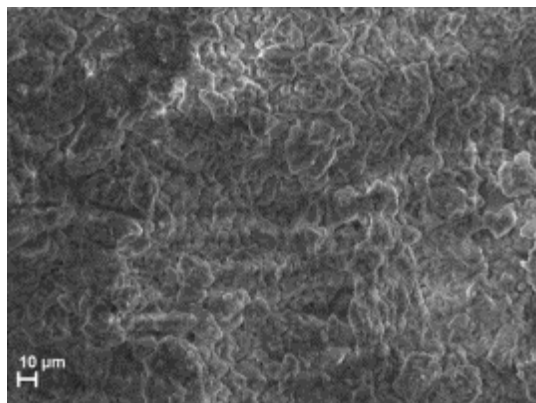
C- Crystal Transformation Stage

Figure 8.15 Corresponding SEM micrographs of microstructure regulated by GCNFs

CHAPTER 9   Conclusions and Future Research

9.1   Introduction

In the recent years, many successful efforts have been made to improve mechanical properties, especially flexural and tensile strength of cementitious composites by using physically and chemically modified nanomaterials. Graphene oxide (GO) is the most widely used nano technologically enhanced precursor material used to enhance durability and mechanical properties of cementitious composites. However, it is expensive to synthesis it via chemical dispersion using extensive sonication. Wrinkled morphology, variation in strength values and unknown physical interaction with cement hydration products are also the drawbacks of GO cementitious composites mentioned by the researchers. To address these issues, newly emerged graphene nanomaterials (GNMs) synthesised via technologically advanced methods has been used to develop nanographene cementitious composites (NGCC). Three different types of NGCC has been developed, namely NGCC-Dot, NGCC-Fnt and NGCC-CNF by using pristine GNPs (G-Dot), functionalised GNPs (G-Fnt) and graphited nanofibers (G-CNFs) into the cement matrix respectively.

The main objective of this PhD research work is to develop nano graphene cementitious composite (NGCC) using low-cost 2D GNPs and 1D GCNFs; synthesised in an environmentally friendly way and to investigate the effect of these nanomaterials in the development of distinctive microstructure lead to enhance its mechanical properties. The research work presented in this thesis is summarised as follows:

- The Genome of graphene nanomaterials (GNMs) used in the research work has been investigated for lattice structure, surface morphology and chemical structure through sophisticated characterization techniques.

- The optimum contents of GNPs to enhance mechanical properties of the cement matrix using G-Dot has been designed, and through analytical techniques, the hydration crystals and their arrangement has been investigated in the development of distinctive microstructure led to develop high-performance NGCC.

- The high-performance NGCC developed using functionalised GNPs has been experimentally investigated for flexural, compressive and tensile strength. The accelerated hydration, pore structure development, mechanism of crystal formation and physical interaction of 2D GNPs in NGCC has been evaluated analytically.

- The nucleation effect accelerated hydration, and strong interlocking of cement hydration products due physical reinforcement provided by the 1D shape of GCNFs in the cement matrix has been investigated through characterization techniques. The increased tensile strength are evaluated through mechanical testing.

- Based on experimental, analytical and characterization, the possible mechanism of crystal formation and microstructure development regulated by GNMs has been presented as physical models.

In this chapter, conclusions derived from the research work mentioned above with future recommendations are presented.

9.2   Conclusions

1)   A comprehensive review of basic cement chemistry related to the hydration process, crystals formation and microstructure development has been presented. The use of various nanomaterials in the cement matrix has been discussed and it is found that in recent years graphene oxide (GO) nanosheets with excellent mechanical properties have been used extensively for the enhancement of mechanical properties of cementitious composites. However, other forms of graphene such as graphene nanoplatelets (GNPs) were rarely used. Moreover, graphene nanosheets mostly functionalised with oxygen group (-O, -OH) were used for better dispersion whereas the effect of others forms such as carboxylic (-COOH) and amine ($-NH_2$) functional groups has been observed rarely. A remarkable enhancement in the flexural and compressive strength in GO cementitious composites prepared with admixtures such as polycarboxylate (PC) has been reported previously, while the research work for improvement in tensile strength and formation of microstructure without using admixtures is very limited. Further, the enhanced mechanical properties of GO cement composites has been linked to the formation of denser microstructure due to increased nucleation and improved pore structure by the GO nanosheets. In the previous research the effect of shape and physical interaction of nanomaterials with hydration products is not present. Therefore, high-performance

nanographene cementitious composite (NGCC) has been developed to investigate the mechanism of hydration crystal formation regulated by shape and geometry (2D or 1D) of graphene nanomaterials and their ultimate effect on the microstructure development leading to enhance the mechanical strength of NGCC.

2)   The material genome (fundamental structural and other important features) of GNMs used in this research are investigated through various characterization techniques. Plasma exfoliated GNPs has been structurally analyzed through HR-TEM images. The condensed hexagonal honeycombed lattice structure has been measured having hexagon width of 0.178 to 0.200 nm and an interlayer spacing of 0.335 nm. Through SEM and AFM measurements, irregular shape functionalised GNPs (G-Fnt) with lateral dimensions 5-10 μm and thickness of 35-40 nm are found uniformly dispersed in the aqueous medium. The presence of more reactive sites and high surface energy has been estimated from RAMAN spectrums of G-Fnt with I_D/I_G ratio equal to 0.304 as compared to 0.121in G-Dot. The crystal structure of both GNPs has been characterized as similar to the pure graphene with the identification of main IR bands at 1597 cm^{-1}, 897 cm^{-1} and XRD diffraction peak near 2θ = 26.40°. From the characterization data, GNPs appeared as a promising candidate for the development of nano cementitious composite due to their well-defined lattice structure, wrinkle free 2D shape morphology, high surface energy and well dispersion capabilities in the aqueous solution. Whereas, vapour grown graphited carbon nano fibres (GCNFs) has been characterized through HR-TEM images having 200 nm wide unique conical features of nanoplatelets and 20-200 μm long fibrous 1D morphology.

3)   NGCC-Dot has been developed by dispersing the varied contents 0.01 % to 0.05 % of plasma exfoliated G-Dots bwoc into water using simple sonication for 30 mins. Through analytical and mechanical testing the concentration of 0.04% has been found optimum and has also been used for the development NGCC-Fnt. Functionalised GNPs exhibited the better dispersion into the aqueous solution due to the chemical groups (-O_2, -NH_2 and -COOH) grafted on their surface via plasma exfoliation. Among three types of functionalised GNPs, the G-O_2 outperformed the other two by dispersing quickly and uniformly into the water. However, the GCNFs with hydrophobic characteristics due to strong Van der Waal's forces were found difficult to disperse into water. Therefore, they were first dispersed in an organic solvent and sonicated for 15 mins and then for another 30 mins adding the solution into a desired quantity of water. The concentration of 0.02 % was found optimum as with higher contents clusters and lumps of GCNFs were observed.

4)   The nucleation effect of GNPs and GCNFs in cement matrix was quite distinctive due to their shape and other structural and morphological properties. It was observed through HR-SEM micrographs in correlation with analytical characterization data (XRD, EDAX, FTIR, and RAMAN), that the plasma exfoliated GNPs with an optimum concentration of 0.04 % initiated the nucleation effect. The nucleation effect was more profound in the NGCC-Fnt as compared to NGCC-Dot when examined at nanoscale through HR-SEM micrographs. The functionalised nanoplatelets due to its unique 2D shape, structural and surface properties were able to develop a unique network system of pores of water filled gaps. Moreover, aligned ions such as Ca^{2+}, K^+, Na^+, OH^-, $SO4^{2-}$ and Al_4O^- liberated from cement particles in the spaces between them. The uniformly dispersed $G-O_2$ exhibited the increased nucleation effect as compared to the $G-NH_2$ and G-COOH. Whereas, high surface energy and unique 1D morphology of G-CNFs coupled with conical features of graphited nanoplatelets initiated the nucleation effect by providing the interaction points to grow C-S-H along the fibre profile. Although, GCNFs due to their hydrophobic nature were not able to attract water molecule near their surface rather the flocs of large water molecules surrounded by cement particles were observed in the nucleation stage.

5)   Both GNPs and GCNFs did not work as reactant but performed as a catalyst and accelerated the hydration process differently. The increased formation of AFt hydration crystals suggested that the G-Dot accelerated the hydration of C_3A due to its high surface energy. Moreover, the increased growth of C-S-H in the amorphous solid form along the surface of G-Dot has also been observed due to the hydration of C_3S and C_2S. Compared to NGCC-Dot more profound growth of AFt crystals has been observed in the NGCC-Fnt nanocomposite due to more nucleation effect and availability of water molecules in the water-filled gaps. In the XRD, FTIR and RAMAN no new peaks has been observed suggested that GNPs not acted as a reactant to form a new compound but accelerated the hydration of cement constituents as a catalyst. The catalytic behaviour of GCNFs in the cement matrix was quite distinctive in XRD patterns and in FTIR spectrums. Increased interaction points due to conical features during nucleation, high aspect ratio (~1300) and high surface area ($24m^2/g$) of GCNFs has contributed to accelerating the hydration process. However, the presence of organic solvent retarded the hydration of C_3A. Consequently, less formation of AFt crystals has been observed in NGCC-CNF.

6)   GNPs and GCNFs regulated the cement microstructure differently. In fact, the shape (2D and 1D) of these nanomaterials has played a vital role in the formation of cement hydration products and development of microstructure ultimately responsible for the increased toughness. The GNPs with 2D shape has regulated the formation of hydration products with the platelet arrangement of cement particles and by developing a network of pore system of water filled gaps. The rod-like crystal AFt approximately 6 μm long and 120-200 nm in diameter interwoven in large quantities in the water-filled gaps has significantly improved the pore structure by reducing porosity and increasing the surface area from 20.55 m^2/g to 40.24 m^2/g in the cement matrix. Moreover, the C-S-H grown on the surface of GNPs due to nucleation effect provided the elementary skeleton for further development of microstructure. In comparison the GCNFs regulated the microstructure in two ways, first accelerated the hydration process through nucleation and secondly provided the physical reinforcement through the enormous growth of C-S-H along fibre profile.

7)   The activation of GNPs and GCNFs into the cement matrix has not only regulated the microstructure development through nucleation and accelerated hydration but also provided the nano reinforcement to the microstructure by bridging the pores, arresting the cracks and resisting the tensile loads. The GNPs has been observed strongly bonded with the peripheral growth C-S-H structures around them. The strong interfacial bonding of GNPs with cement matrix has provided the nanoreinforcement and contributed in bringing the cracks initiated at the nanoscale. GNPs smaller in lateral dimension could have increased the toughness of NGCC by arresting the cracks initiated at the nanoscale. Whereas, GCNFs strongly bonded with C-S-H has provided the physical reinforcement and larger connections by interlocking the hydration products.

8)   The 2D shape GNPs enhanced the mechanical properties of cementitious composite quite differently as compared to the 1D shape GCNFs. The NGCC-Dot and NGCC-Fnt with GNPs concentration of 0.04 wt. % exhibited the similar characteristics of strength development. Despite strength variations in some NGCC-Dot samples, a remarkable increase in flexural strength by 55.60 % and 63.73 % has been observed in the NGCC-Dot and NGCC-Fnt samples respectively. This strength enhancement can be linked primarily to the increased formation of AFt crystals and reinforcement provided by GNPs. While, the increase in compressive strength can be linked to the formation of polyhedral shape crystals of CH and overall compact microstructure regulated by GNPs. The NGCC-Fnt samples have also been tested for tensile strength, and an increase of 26.13 % has been

observed at the age of 7 days as compared to the control samples. The increase in the flexural, compressive and tensile strength of NGCC-Fnt samples by 55.30 %, 18.74 % and 22.20 % has been observed respectively at the age of 28 days as compared to control samples. Also, a remarkable increase in tensile strength by 35.03 % at the age of 28 days has been observed in NGCC-CNF and can be related to larger connections of hydration products with physical reinforcement of GCNFs. Importantly, the relationship between flexural strength and displacement revealed that NGCC-CNF has more tendencies to bend with increased ductility and toughness due to the reinforcing effect of strongly bonded GCNFs with cement matrix.

9.3   Future Research and Recommendations

Plasma Functionalization of GCNFs: The activation of GCNFs remarkably enhanced the tensile strength and ductility of cement matrix but physical modification to achieve dispersion using organic solvent worked an adverse effect on microstructure development. Therefore, chemical modification of GCNFs with functionalised groups of $-O_2$, -COOH, and $-NH_2$ using plasma exfoliation can produce excellent results.

Hybrid NGCC (GNPs and GCNFs): The shape of nanomaterials has great influence in regulating the microstructure. It has been observed that 2D shape GNPs and 1D shape GCNFs regulated the cement microstructure distinctively. The 2D shape GNPs developed the denser and strong microstructure leading to enhance flexural and compressive strength while the 1D shape of GCNFs primarily enhanced the tensile strength and ductility by providing physical nanoreinforcement. The co-effect of both 2D shape GNPs and 1D GCNFs can produce a synergic effect on the strength and ductility of cementitious composites.

Electrical and Thermally Conducted NGCC: The graphene nanomaterials no doubt possess excellent electrical and thermal conductivity properties along with high mechanical strength. Therefore, NGCC with enhanced mechanical properties can also be gauged experimentally for enhanced electrical and thermal properties.

Corrosion Resistant NGCC: Graphene nanomaterials one atom thick layer of strongly bonded carbon atoms also has excellent surface and barrier properties due to which they can be bonded strongly with cement matrix and can reduce permeability and transportation of harmful slats from the environment into the cement microstructure.

Nano-Engineered Concrete: Using Nano-engineered concrete with high strength and high strain capabilities, reduced sections of structural reinforced concrete members can be designed efficiently. To get ultimate benefits of NGCC at nano level in the development of nano-engineered concrete there is a need to introduce a bridging material between cement matrix (nano level) and aggregate interfacial transition zone (ITZ) (micro level). This bridging material could be graphene micro fibres (GMF) developed through graphene and polymeric composite.

Bibliography

Abu Al-Rub, R.K., Ashour, A.I. and Tyson, B.M. (2012) 'On the aspect ratio effect of multi-walled carbon nanotube reinforcements on the mechanical properties of cementitious nanocomposites', *Construction and Building Materials*, 35, pp. 647–655.

Akhtar, S. (2012) *Transmission electron microscopy of Graphene and hydrated Biomaterial Nanostructures novel techniques and analysis*. Acta Universitatis Upsaliensis.

Aldrich, S. (2016) *Carbon Nanofibers- processing and dispersing*. Available at: http://www.sigmaaldrich.com/technical-documents/protocols/materials-science/carbon-nanofibers.html (Accessed: 28 September 2016).

Alkhateb, H., Al-Ostaz, A., Cheng, A.H.. and Li, X. (2013) 'Materials genome for Graphene-Cement Nanocomposites', *Journal of Nanomechanics and Micromechanics*, 3(3), pp. 67–77.

Altoubat, S. and Yazdanbakhsh, A. (2009) 'Shear behaviour of Macro-Synthetic fibre-reinforced concrete beams without stirrups', *ACI Materials Journal*, 106(4).

Babak, F., Abolfazl, H., Alimorad, R. and Parviz, G. (2014) 'Preparation and mechanical properties of Graphene oxide: Cement Nanocomposites', *The Scientific World Journal*, 2014, pp. 1–10.

Black, L., Breen, C., Yarwood, J., Deng, C.., Phipps, J. and Maitland, G. (2006) 'Hydration of tricalcium aluminate (C3A) in the presence and absence of gypsum—studied by Raman spectroscopy and x-ray diffraction', *Journal of Materials Chemistry*, 16(13), p. 1263.

Blandine, F., Habermehi-Cwirzen, K. and Cwirzen, A. (2016) 'Contribution of CNTs/CNFs morphology to the reduction of autogenous shrinkage of Portland cement paste', *Frontiers of Structural and Civil Engineering*, 10(2), pp. 224–235.

Bonaccorso, F., Lombardo, A., Hasan, T., Sun, Z., Colombo, L. and Ferrari, A.C. (2012) 'Production and processing of graphene and 2d crystals', *Materials Today*, 15(12), pp. 564–589.

Campillo, I., Dolado, J. and Porro, A. (2004) 'High-performance nanostructured materials for construction.',*Special Pub-R Soc Chem*, (292), pp. 215–26.

Cement CEMEX UK (2016) Available at: http://www.cemex.co.uk/cement.aspx (Accessed: 31 August 2016).

Chuah, S., Pan, Z., Sanjayan, J.G., Wang, C.M. and Duan, W.H. (2014) 'Nano reinforced cement and concrete composites and a new perspective from graphene oxide', *Construction and Building Materials*, 73, pp. 113–124.

Coleman, J.N., Khan, U., Blau, W.J. and Gun'ko, Y.K. (2006) 'Small but strong: A review of the mechanical properties of carbon nanotube-polymer composites', *Carbon*, 44(9), pp. 1624–1652.

Cooper, D.R., D'Anjou, B., Ghattamaneni, N., Harack, B., Hilke, M., Horth, A., Majlis, N., Massicotte, M., Vandsburger, L., Whiteway, E. and Yu, V. (2012) 'Experimental review of Graphene', *ISRN Condensed Matter Physics*, 2012, pp. 1–56.

Cwirzen, A., Habermehl-Cwirzen, K. and Penttala, V. (2008) 'Surface decoration of carbon nanotubes and mechanical properties of cement/carbon nanotube composites', *Advances in Cement Research*, 20(2), pp. 65–73.

Davalos, J.F. (2012) 'Advanced materials for civil infrastructure rehabilitation and protection', Seminar at The City College of New York: New York.

Delhaes, P. (ed.) (2000) *Graphite and precursors*. Amsterdam: Taylor & Francis.

Garci Juenger, M.C. and Jennings, H.M. (2001) 'The use of nitrogen adsorption to assess the microstructure of cement paste', *Cement and Concrete Research*, 31(6), pp. 883–892.

Garg, A. and Sinnott, S.B. (1998) 'Effect of chemical functionalization on the mechanical properties of carbon nanotubes', *Chemical Physics Letters*, 295(4), pp. 273–278.

Gastaldi, D., Canonico, F. and Boccaleri, E. (2009) 'Ettringite and calcium sulfoaluminate cement: Investigation of water content by near-infrared spectroscopy', *Journal of Materials Science*, 44(21), pp. 5788–5794.

Geim, A.K. and Novoselov, K.S. (2007) 'The rise of graphene', *Nature Materials*, 6(3), pp. 183–191.

Geng, Y., Wang, S.J. and Kim, J.-K. (2009) 'Preparation of graphite nanoplatelets and graphene sheets', *Journal of Colloid and Interface Science*, 336(2), pp. 592–598.

Ghosh, S.N. and Handoo, S.K. (1980) 'Infrared and Raman spectral studies in cement and concrete (review)', *Cement and Concrete Research*, 10(6), pp. 771–782.

Goncalves, G., Marques, P.A.A.P., Granadeiro, C.M., Nogueira, H.I.S., Singh, M.K. and Grácio, J. (2009) 'Surface modification of Graphene Nanosheets with gold Nanoparticles: The role of oxygen Moieties at Graphene surface on gold Nucleation and growth', *Chemistry of Materials*, 21(20), pp. 4796–4802.

Gong, K., Pan, Z., Korayem, A.H., Qiu, L., Li, D., Collins, F., Wang, C.M. and Duan, W.H. (2015) 'Reinforcing effects of Graphene oxide on Portland cement paste', *Journal of Materials in Civil Engineering*, 27(2), p. A4014010.

Haydale Graphene industries plc (2016) Available at http://www.haydale.com/media/1182/jec-reach-14-3-2016-final.pdf (Accessed: 31 August 2016).

He, T., Shi, C., Li, G. and Song, X. (2012) 'Effects of superplasticizers on the carbonation resistance of C3S and C3A hydration products', *Construction and Building Materials*, 36, pp. 954–959.

Horszczaruk, E., Mijowska, E., Kalenczuk, R.J., Aleksandrzak, M. and Mijowska, S. (2015) 'Nanocomposite of cement/graphene oxide – impact on hydration kinetics and Young's modulus', *Construction and Building Materials*, 78, pp. 234–242.

Hughes, T. (1995) 'Determining cement composition by Fourier transform infrared spectroscopy', *Advanced Cement-Based Materials*, 2(3), pp. 91–104.

Hummers, W.S. and Offeman, R.E. (1958) 'Preparation of Graphitic oxide', *Journal of the American Chemical Society*, 80(6), pp. 1339–1339. doi:

Jo, B.-W., Kim, C.-H., Tae, G. and Park, J.-B. (2007) 'Characteristics of cement mortar with nano-siO2 particles', *Construction and Building Materials*, 21(6), pp. 1351–1355.

Kalbac, M., Farhat, H., Kong, J., Janda, P., Kavan, L. and Dresselhaus, M.S. (2011) 'Raman spectroscopy and in situ Raman Spectroelectrochemistry of Bilayer 12 C/ 13 C Graphene', *Nano Letters*, 11(5), pp. 1957–1963. doi: 10.1021/nl2001956.

Kang, Z., Wang, E., Gao, L., Lian, S., Jiang, M., Hu, C. and Xu, L. (2004) 'One-Step water-assisted synthesis of high-quality carbon Nanotubes directly from graphite', *ChemInform*, 35(3).

Kawashima, S., Hou, P., Corr, D.J. and Shah, S.P. (2013) 'Modification of cement-based materials with nanoparticles', *Cement and Concrete Composites*, 36, pp. 8–15.

Kim, Y.-Y., Lee, K.-M., Bang, J.-W. and Kwon, S.-J. (2014) 'Effect of W/C ratio on durability and porosity in cement mortar with constant cement amount', Advances in Materials Science and Engineering, 2014, pp. 1–11

Kloprogge, J.T., Schuiling, R.D., Ding, Z., Hickey, L., Wharton, D. and Frost, R.L. (2002) 'Vibrational spectroscopic study of syngenite formed during the treatment of liquid manure with sulphuric acid', *Vibrational Spectroscopy*, 28(2), pp. 209–221.

Kongkhlang, T., Reddy, K.R., Kitano, T., Nishu, T. and Tashiro, K. (2010) 'Cocrystallization phenomenon of polyoxymethylene blend samples between the deuterated and hydrogenated species', *Polymer Journal*, 43(1), pp. 66–73.

Konsta-Gdoutos, M.S., Metaxa, Z.S. and Shah, S.P. (2010) 'Highly dispersed carbon nanotube reinforced cement-based materials', *Cement and Concrete Research*, 40(7), pp. 1052–1059.

Kontoleontos, F., Tsakiridis, P., Marinos, A., Katsiotis, N., Kaloidas, V. and Katsioti, M. (2013) 'Dry-grinded ultrafine cement hydration. Physicochemical and microstructural characterization', *Materials Research*, 16(2), pp. 404–416.

Kostić, R., Mirić, M., Radić, T., Radović, M., Gajić, R. and Popović, Z.V. (2009) 'Optical characterization of Graphene and highly oriented Pyrolytic graphite', *Acta Physica Polonica A*, 116(4), pp. 718–721.

Kuilla, T., Bhadra, S., Yao, D., Kim, N.H., Bose, S. and Lee, J.H. (2010) 'Recent advances in graphene based polymer composites', *Progress in Polymer Science*, 35(11), pp. 1350–1375.

Lahiri, J., S Miller, T., J Ross, A., Adamska, L., Oleynik, I.I. and Batzill, M. (2011) 'Graphene growth and stability at nickel surfaces', *New Journal of Physics*, 13(2), p. 025001.

Lee, H., Bratescu, M.A., Ueno, T. and Saito, N. (2014) 'Solution plasma exfoliation of graphene flakes from graphite electrodes', *RSC Adv.*, 4(93), pp. 51758–51765.

Li, G.Y., Wang, P.M. and Zhao, X. (2005) 'Mechanical behaviour and microstructure of cement composites incorporating surface-treated multi-walled carbon nanotubes', *Carbon*, 43(6), pp. 1239–1245.

Li, G.Y., Wang, P.M. and Zhao, X. (2007) 'Pressure-sensitive properties and microstructure of carbon nanotube reinforced cement composites', *Cement and Concrete Composites*, 29(5), pp. 377–382.

Li, H., Xiao, H., Yuan, J. and Ou, J. (2004) 'Microstructure of cement mortar with nano-particles', *Composites Part B: Engineering*, 35(2), pp. 185–189.

Li, X., Wei, W., Qin, H. and Hang Hu, Y. (2015) 'Co-effects of graphene oxide sheets and single wall carbon nanotubes on mechanical properties of cement', *Journal of Physics and Chemistry of Solids*, 85, pp. 39–43.

Li, Z. and Liang, W. (2011) *Advanced concrete technology, Chapter 2*. online Chapter 2 edn. Oxford, United Kingdom: Wiley, John & Sons.

Lin, C., Wei, W. and Hu, Y.H. (2016) 'Catalytic behaviour of graphene oxide for cement hydration process', *Journal of Physics and Chemistry of Solids*, 89, pp. 128–133.

Liu, F., Sun, Z. and Qi, C. (2015) 'Raman spectroscopy study on the hydration behaviours of Portland cement pastes during setting', *Journal of Materials in Civil Engineering*, 27(8), p. 04014223.

Lv, S., Liu, J., Sun, T., Ma, Y. and Zhou, Q. (2014) 'Effect of GO nanosheets on shapes of cement hydration crystals and their formation process', *Construction and Building Materials*, 64, pp. 231–239.

Lv, S., Ma, Y., Qiu, C., Sun, T., Liu, J. and Zhou, Q. (2013) 'Effect of graphene oxide nanosheets of microstructure and mechanical properties of cement composites', *Construction and Building Materials*, 49, pp. 121–127.

Madani, H., Bagheri, A. and Parhizkar, T. (2012) 'The pozzolanic reactivity of monodispersed nano silica hydrosols and their influence on the hydration characteristics of Portland cement', *Cement and Concrete Research*, 42(12), pp. 1563–1570.

Makar, J., Margeson, J. and Luh, J. (2005) 'Carbon nanotube/cement composites-early results and potential applications', Vancouver, Canada: Proceedings of 3rd international conference on construction materials: performance, innovations and structural implications.

Makar, J.M. and Chan, G.W. (2009) 'Growth of cement hydration products on single-walled carbon Nanotubes', *Journal of the American Ceramic Society*, 92(6), pp. 1303–1310.

Matschei, T., Lothenbach, B. and Glasser, F.P. (2007) 'The role of calcium carbonate in cement hydration', *Cement and Concrete Research*, 37(4), pp. 551–558.

Mehta, P.K., Monteiro, P.J.M., Mehta, K.P. and Monteiro, J.M. (2013) *Concrete: Microstructure, properties, and materials*. 4th edn. New York: McGraw-Hill Professional.

Melo, V. et al. (2011) 'Macro- and micro-characterization of mortars produced with carbon Nanotubes', *ACI Materials Journal*, 108(3).

Mohammed, A., Sanjayan, J.G., Duan, W.H. and Nazari, A. (2015) 'Incorporating graphene oxide in cement composites: A study of transport properties', *Construction and Building Materials*, 84, pp. 341–347.

Mollah, M.Y.A., Yu, W., Schennach, R. and Cocke, D.L. (2000) 'A Fourier transform infrared spectroscopic investigation of the early hydration of Portland cement and the influence of sodium lignosulfonate', *Cement and Concrete Research*, 30(2), pp. 267–273.

Nadeem, R., Ansari, T.M., Akhtar, K. and Khalid, A.M. (2009) 'Pb(II) sorption by pyrolysed Pongamia pinnata pods carbon (PPPC)', *Chemical Engineering Journal*, 152(1), pp. 54–63.

Naebe, M., Wang, J., Amini, A., Khayyam, H., Hameed, N., Li, L.H., Chen, Y. and Fox, B. (2014) 'Mechanical property and structure of Covalent Functionalised Graphene/epoxy Nanocomposites', *Scientific Reports*, 4.

Nasibulin, A.G., Shandakov, S.D., Nasibulina, L.I., Cwirzen, A., Mudimela, P.R., Habermehl-Cwirzen, K., Grishin, D.A., Gavrilov, Y.V., Malm, J.E.M., Tapper, U., Tian, Y., Penttala, V., Karppinen, M.J. and Kauppinen, E.I. (2009) 'A novel cement-based hybrid material', *New Journal of Physics*, 11(2), p. 023013.

Nazari, A. and Riahi, S. (2011) 'The effects of SiO2 nanoparticles on physical and mechanical properties of high strength compacting concrete', *Composites Part B: Engineering*, 42(3), pp. 570–578.

Novoselov, K.S. (2004) 'Electric field effect in Atomically thin carbon films', *Science*, 306(5696), pp. 666–669.

Oltulu, M. and Şahin, R. (2013) 'Effect of nano-siO2, nano-al2O3 and nano-fe2O3 powders on compressive strengths and capillary water absorption of cement mortar containing fly ash: A comparative study', *Energy and Buildings*, 58, pp. 292–301.

Omotoso, O.E., Ivey, D.G. and Mikula, R. (1998) 'Containment mechanism of trivalent chromium in tricalcium silicate', *Journal of Hazardous Materials*, 60(1), pp. 1–28.

Palomo, A., Blanco-Varela, M.T., Granizo, M.L., Puertas, F., Vazquez, T. and Grutzeck, M.W. (1999) 'Chemical stability of cementitious materials based on metakaolin', *Cement and Concrete Research*, 29(7), pp. 997–1004.

Pan, Z., Collins, F., Li, D. and Duan, W.H. (2013) 'Graphene oxide reinforced cement and concrete wo patent app.', *WO Patent App.*, (PCT/AU2012/001,582.).

Pan, Z., He, L., Qiu, L., Korayem, A.H., Li, G., Zhu, J.W., Collins, F., Li, D., Duan, W.H. and Wang, M.C. (2015) 'Mechanical properties and microstructure of a graphene oxide–cement composite', *Cement and Concrete Composites*, 58, pp. 140–147.

Peyvandi, A., Soroushian, P., Abdol, N. and Balachandra, A.M. (2013) 'Surface-modified graphite nanomaterials for improved reinforcement efficiency in cementitious paste', *Carbon*, 63, pp. 175–186.

Pu, N.-W., Wang, C.-A., Liu, Y.-M., Sung, Y., Wang, D.-S. and Ger, M.-D. (2012) 'Dispersion of graphene in aqueous solutions with different types of surfactants and the production of graphene films by spray or drop coating', *Journal of the Taiwan Institute of Chemical Engineers*, 43(1), pp. 140–146.

Qing, Y., Zenan, Z., Deyu, K. and Rongshen, C. (2007) 'Influence of nano-siO2 addition on properties of hardened cement paste as compared with silica fume', *Construction and Building Materials*, 21(3), pp. 539–545.

Qiu, L., Yang, X., Gou, X., Yang, W., Ma, Z.-F., Wallace, G.G. and Li, D. (2010) 'Dispersing carbon Nanotubes with Graphene oxide in water and synergistic effects between Graphene derivatives', *Chemistry - A European Journal*, 16(35), pp. 10653–10658.

R.F. Feldman and P.J. Sereda. A model for hydrated portland cement paste as deduced from sorption-length change and mechanical properties. Matriaux et Construction, 1(6):509–520, 1968.

Rafiee, M.A., Rafiee, J., Wang, Z., Song, H., Yu, Z.-Z. and Koratkar, N. (2009) 'Enhanced mechanical properties of Nanocomposites at low Graphene content', *ACS Nano*, 3(12), pp. 3884–3890.

Rahway, N. (1983) 'The Merck index, 10th Ed. Merck & Co.', *Journal of Pharmaceutical Sciences*, 73(6), pp. pp–749.

Raki, L., Beaudoin, J., Alizadeh, R., Makar, J. and Sato, T. (2010) 'Cement and concrete Nanoscience and Nanotechnology', *Materials*, 3(2), pp. 918–942.

Rashad, M., Pan, F., Tang, A., Lu, Y., Asif, M., Hussain, S., She, J., Gou, J. and Mao, J. (2013) 'Effect of graphene nanoplatelets (GNPs) addition on strength and ductility of magnesium-titanium alloys', *Journal of Magnesium and Alloys*, 1(3), pp. 242–248.

Reich, S. and Thomsen, C. (2004) 'Raman spectroscopy of graphite', *Philosophical Transactions of the Royal Society A: Mathematical, Physical and Engineering Sciences*, 362(1824), pp. 2271–2288.

Romani, A. and Gronchi, P. (2015) *Graphene Oxide as a cement reinforcing additive preliminary study*.

Roy, D., Chhowalla, M., Wang, H., Sano, N., Alexandrou, I., Clyne, T.W. and Amaratunga, G.A.J. (2003) 'Characterisation of carbon nano-onions using Raman spectroscopy', *Chemical Physics Letters*, 373(1-2), pp. 52–56.

Said, A.M., Zeidan, M.S., Bassuoni, M.T. and Tian, Y. (2012) 'Properties of concrete incorporating nano-silica', *Construction and Building Materials*, 36, pp. 838–844.

Sakai, E., Nikaido, Y., Itoh, T. and Daimon, M. (2004) 'Ettringite formation and microstructure of rapid hardening cement', *Cement and Concrete Research*, 34(9), pp. 1669–1673.

Sanchez-Valencia, J.R., Dienel, T., Gröning, O., Shorubalko, I., Mueller, A., Jansen, M., Amsharov, K., Ruffieux, P. and Fasel, R. (2014) 'Controlled synthesis of single-chirality carbon nanotubes', *Nature*, 512(7512), pp. 61–64.

Sarkar, S.K., Raul, K.K., Pradhan, S.S., Basu, S. and Nayak, A. (2014) 'Magnetic properties of graphite oxide and reduced graphene oxide', *Physica E: Low-dimensional Systems and Nanostructures*, 64, pp. 78–82.

Scrivener, K.L. (2004) 'Backscattered electron imaging of cementitious microstructures: Understanding and quantification', *Cement and Concrete Composites*, 26(8), pp. 935–945.

Scrivener, K.L. and Kirkpatrick, R.J. (2008) 'Innovation in use and research on cementitious material', *Cement and Concrete Research*, 38(2), pp. 128–136.

Shang, Y., Zhang, D., Yang, C. and Liu, Y. (2015) 'Effect of graphene oxide on the rheological properties of cement pastes', *Construction and Building Materials*, 96, pp. 20–28.

Siddique, R. and Mehta, A. (2014) 'Effect of carbon nanotubes on properties of cement mortars', *Construction and Building Materials*, 50, pp. 116–129.

Sobolev, K., Flores, I., Hermosillo, R. & Torres-Martínez, L.M. 2008, "Nanomaterials and nanotechnology for high-performance cement composites", American Concrete Institute (ACI) SP-254, 2008, pp 93-120

Stankovich, S., Dikin, D.A., Piner, R.D., Kohlhaas, K.A., Kleinhammes, A., Jia, Y., Wu, Y., Nguyen, S.T. and Ruoff, R.S. (2007) 'Synthesis of graphene-based nanosheets via chemical reduction of exfoliated graphite oxide', *Carbon*, 45(7), pp. 1558–1565.

Steven, E., Saleh, W.R., Lebedev, V., Acquah, S.F.A., Laukhin, V., Alamo, R.G. and Brooks, J.S. (2013) 'Carbon nanotubes on a spider silk scaffold', *Nature Communications*, 4.

Supermarket, G. (2009) *Graphene supermarket*. Available at: https://graphene-supermarket.com/home.php (Accessed: 17 August 2016).

Stutzman, P.E. (2001). "Scanning Electron Microscopy in Concrete Petrography."Calcium Hydroxide in Concrete, J. Skalny, J. Gebauer, I. Odler, editor, American Ceramic Society, Westerville, 59-72.

Taylor, H. F. W. (1992) *Properties of Portland clinker and cement, Cement Chemistry,* London, Academic Press,

Thomas, J.J., Jennings, H.M. and Allen, A.J. (1998) 'The surface area of cement paste as measured by neutron scattering: Evidence for two C-S-H morphologies', *Cement and Concrete Research*, 28(6), pp. 897–905.

Treval Clifford Powers and Theodore Lucius Brownyard. Studies of the physical properties of hardened Portland cement paste. 43(9), 1946.

Tuinstra, F. (1970) 'Raman spectrum of graphite', *The Journal of Chemical Physics*, 53(3), p. 1126.

Vera-Agullo, J., Chozas-Ligero, V., Portillo-Rico, D., García-Casas, M.J., Gutiérrez-Martínez, A., Mieres-Royo, J.M. and Grávalos-Moreno, J. (2009) 'Mortar and Concrete Reinforced with', *ACCIONA Infraestructuras*, .

Wang, B., Han, Y. and Liu, S. (2013) 'Effect of highly dispersed carbon nanotubes on the flexural toughness of cement-based composites', *Construction and Building Materials*, 46, pp. 8–12.

Wang, C., Li, K.-Z., Li, H.-J., Jiao, G.-S., Lu, J. and Hou, D.-S. (2008) 'Effect of carbon fibre dispersion on the mechanical properties of carbon fibre-reinforced cement-based composites', *Materials Science and Engineering: A*, 487(1-2), pp. 52–57.

Wang, Q., Wang, J., Lu, C., Liu, B., Zhang, K. and Li, C. (2015) 'Influence of graphene oxide additions on the microstructure and mechanical strength of cement', *New Carbon Materials*, 30(4), pp. 349–356.

Wani, I.A., Ganguly, A., Ahmed, J. and Ahmad, T. (2011) 'Silver nanoparticles: Ultrasonic wave assisted synthesis, optical characterization and surface area studies', *Materials Letters*, 65(3), pp. 520–522.

Winter, N.B. (2009) *Understanding cement, An introduction to cement production, cement hydration and deleterious process in concrete., Page 64*. Online edn. UK:

Xiong, Y., Xie, Y., Li, X. and Li, Z. (2004) 'Production of novel amorphous carbon nanostructures from ferrocene in low-temperature solution', *Carbon*, 42(8-9), pp. 1447–1453.

Yazdanbakhsh, A., Grasley, Z., Tyson, B. and Abu Al-Rub, R. (2010) 'Distribution of carbon Nanofibers and Nanotubes in Cementitious composites', *Transportation Research Record: Journal of the Transportation Research Board*, 2142, pp. 89–95.

Yousuf, M., Mollah, A., Hess, T.R., Tsai, Y.-N. and Cocke, D.L. (1993) 'An FTIR and XPS investigations of the effects of carbonation on the solidification/stabilization of cement based systems-portland type V with zinc', *Cement and Concrete Research*, 23(4), pp. 773–784.

Yousuf, M., Mollah, A., Palta, P., Hess, T.R., Vempati, R.K. and Cocke, D.L. (1995) 'Chemical and physical effects of sodium lignosulfonate superplasticizer on the hydration of portland cement and solidification/stabilization consequences', *Cement and Concrete Research*, 25(3), pp. 671–682.

Zhang, M.-H. and Islam, J. (2012) 'Use of nano-silica to reduce setting time and increase early strength of concretes with high volumes of fly ash or slag', *Construction and Building Materials*, 29, pp. 573–580.

Zou, G., Zhang, D., Dong, C., Li, H., Xiong, K., Fei, L. and Qian, Y. (2006) 'Carbon nanofibers: Synthesis, characterization, and electrochemical properties', *Carbon*, 44(5), pp. 828–832.